

THESIS ON POWER ENGINEERING,
ELECTRICAL ENGINEERING, MINING ENGINEERING D77

**Research and Development of Exterior-
Rotor Permanent Magnet Synchronous
Machines for Light Aerial Vehicles**

RENÉ NUKKI

TUT
PRESS

Tallinn University of Technology
Faculty of Power Engineering
Department of Electrical Engineering

This dissertation was accepted for the defence of the degree of Doctor of Philosophy in Engineering on May 9, 2016.

Supervisors: Prof. Tõnu Lehtla, Department of Electrical Engineering, TUT

Assoc. Prof. Aleksander Kilk,
Department of Electrical Engineering, TUT

Opponents: Assoc. Prof. Pia Lindh, Lappeenranta University of Technology,
Finland

Prof. Andres Annuk, Estonian University of Life Sciences, Estonia

Defence of the thesis: June 21, 2016

Declaration:

Hereby I declare that this doctoral thesis, my original investigation and achievement, submitted for the doctoral degree at Tallinn University of Technology, has not been submitted for any academic degree.

René Nukki

Copyright: René Nukki, 2016

ISSN 1406-4731

ISBN 978-9949-23-972-6 (publication)

ISBN 978-9949-23-973-3 (PDF)

ENERGEETIKA. ELEKTROTEHNIKA. MÄENDUS D77

**Välisrootoriga püsomagnet-
sünkroonmasinate uurimine ja
väljatöötamine kergetele õhusõidukitele**

RENÉ NUKKI

CONTENTS

ACKNOWLEDGEMENTS	7
LIST OF ABBREVIATIONS	8
SYMBOL INDEX.....	10
1 INTRODUCTION.....	16
1.1 Background.....	16
1.2 History and Current Situation	18
1.3 New Developments and Trends	20
1.4 Research Objects of the Thesis	24
1.5 Main Objectives and Tasks of the Thesis	27
1.6 Contribution of the Thesis and Dissemination.....	27
1.7 Outline of the Thesis.....	28
2 DESIGN PROCESS OF EXTERIOR-ROTOR PM MACHINES FOR LIGHT AERIAL VEHICLES	30
2.1 Machine types	30
2.2 Determination of Application and Requirements	31
2.3 Choice of Rotor Geometries	33
2.4 Initial Sizing.....	35
2.5 Poles and Stator Geometry.....	37
2.6 Soft Magnetic Materials.....	45
2.6.1 Analysis of HPSMG stator material.....	47
2.6.2 Analysis of FESM stator material	50
2.7 Permanent Magnets.....	52
2.7.1 HPSMG and FESM permanent magnets.....	54
2.8 Windings.....	56
2.8.1 HPSMG Gramme or toroidal winding	56
2.8.2 FESM concentrated winding.....	58
2.9 Conclusion	63
3 ELECTROMAGNETIC DESIGN	64
3.1 Possibilities of PM Machine Description and Analysis.....	64
3.2 Analysis of the Primary Magnetic Field	67
3.2.1 Magnetic circuit of HPSMG	67
3.2.2 Magnetic circuit of FESM.....	75
3.3 Armature Reaction and Demagnetization	78
3.3.1 Special case of armature reaction – sudden short circuit	79
3.4 Resultant Magnetic Field	83
3.5 Comparative Analysis of Gramme’s and Concentrated Winding.....	88
3.6 EMF and Back-EMF	96
3.7 Electromagnetic Force and Torque.....	102
3.8 Cogging Torque	106
3.9 Output Power and Efficiency	108
3.10 Conclusion	114
4 THERMAL ANALYSIS.....	116

4.1	Thermal Modelling	121
4.1.1	HPSMG with the toroidal winding	122
4.1.2	HPSMG with the concentrated winding	124
4.1.3	Analysis of FESM temperature fields	127
4.2	Conclusion	131
5	EXPERIMENTAL VERIFICATION	132
5.1	Overview of Laboratory Test Benches	132
5.2	Distribution of the Magnetic Field in the Air Gap.....	133
5.3	Generator Mode	135
5.3.1	Open-circuit test.....	135
5.3.2	Load test.....	137
5.3.3	Short circuit test	139
5.3.4	Temperature measurements	140
5.3.5	Losses.....	141
5.4	Motor Mode	145
5.4.1	Batteries	145
5.4.2	Open-circuit test.....	147
5.4.3	Load test.....	150
5.4.4	Temperature measurements	158
5.5	Power and Torque Density.....	160
5.6	Conclusion	162
6	FUTURE RESEARCH	164
	REFERENCES.....	165
	ABSTRACT	172
	KOKKUVÕTE.....	174
	ELULOOKIRJELDUS.....	176
	CURRICULUM VITAE	177
	APPENDIX	178
	AUTHOR'S PUBLICATIONS	183

ACKNOWLEDGEMENTS

I would like to express my gratitude to everyone who have motivated me all through the strenuous periods towards my research goals.

First, I would like to thank Enno Lend, Rector of TTK University of Applied Sciences, and Vello Vainola, Dean of the Faculty of Mechanical Engineering for creating me an opportunity and desire to quest for doctoral studies.

Secondly, I would like to thank my supervisors, professor Tõnu Lehtla and especially associate professor Aleksander Kilk from Tallinn University of Technology for helping and guiding me with their expertise through the complexities of research.

Special thanks are due to Mr. Kristjan Tiimus Sr for leading the construction of the first prototype of the first machine. His further expertise and instructions were also invaluable.

I am grateful to my colleagues in TTK University of Applied Sciences, including associate professor Heljut Kalda, lecturers Samo Saarts, Anton Rassõlkin, Anne Uukkivi and others who have also contributed to my research. Additionally, Dr. Ants Kallaste, Dr. Toomas Vaimann and Professor Lauri Kütt from Tallinn University of Technology have given their hand.

My greatest thanks are due to Dr. Dave Staton, Dr. Mircea Popescu and Dougie Hawkins from Motor Design Ltd; also to Johann Kott from MACCON GmbH for consulting me on modelling.

Finally, my sincere gratitude goes to my partner Gaily and my sons Reeno and Kristen who showed continuous patience and understanding and who aroused my enthusiasm and supported my will.

René Nukki

LIST OF ABBREVIATIONS

A.D.	Anno Domini
AC	Alternating Current
AFC	Alkaline Fuel Cell
AgZn	Silver-Zinc Battery
AlNiCo	Aluminium, Nickel, Cobalt Magnets
API	American Petroleum Institute
B6U	Rectifier Bridge
BH _{max}	Maximum Energy Product
BLDC	Brushless Direct Current Machine
BLV Method	Analytical Calculation Method based on Faraday's Law
CCTV	Closed Circuit Television
CNC	Computer Numerical Control Machine
DC	Direct Current
DCM	Direct Current Machine
EM	Electrical Machine
EMF	Electromotive Force
EMI	Electromagnetic Interference
EN	European Norms
FEA	Finite Element Analysis
FEM	Finite Element Method
FES	Full Electric System
FESM	Full Electric System Machine
FPM	Fixed Permeability Method
HDS	Hybrid Drive System
HPS	Hybrid Propulsion System
HPSMG	Hybrid Propulsion System Motor-Generator
ICE	Internal Combustion Engine
IEC	International Electrotechnical Commission
IEEE	Institute of Electrical and Electronics Engineers
IM	Induction Machine
JFET	Junction Field Effect Transistor
LAV	Light Aerial Vehicle
LiPo	Lithium Ion Polymer Battery
NdFeB	Neodymium Iron Boron Magnet
NiCr	Nickel Chrome
NiCu	Nickel Copper
NO	Non-Grain-Oriented Electrical Steel
ODP	Over Discharge Protection
OICA	International Organization of Motor Vehicle Manufacturers
PEMC Group	Power Electronics, Machines and Control Group
PM	Permanent Magnet
PMSM	Permanent Magnet Synchronous Machine

P-to-V	Power-to-Volume ratio (power density)
P-to-W	Power-to-Weight ratio (specific power)
RMS	Root Mean Square
RPM	Revolutions Per Minute
SMC	Soft Magnetic Composites
SmCo	Samarium-Cobalt Magnets
SRM	Synchronous Reluctance Machine
TCE	Magnetic Co-Energy Method
TMSI	Maxwell's Stress Tensor Surface Integral Method
T-to-V	Torque-to-Volume ratio (torque density)
UAV	Unmanned Aerial Vehicle
UL	Underwriters Laboratories Inc
VW	Virtual Work Method

SYMBOL INDEX

a	acceleration, number of parallel path
A	stator linear current density
A_{coil}	external surface area of the coil
A_{con}	cross sectional area of one conductor
A_p	area of the magnet pole
A_{ry}	cross sectional area of the rotor yoke
A_{sl}	slot area
b_c	conductor strand width
b_{ew}	axial length of the end winding
B_g	air gap flux density
BH_{max}	energy density
B_{kp}	flux density in knee point
B_{min}	flux density before total demagnetization
B_r	remanent flux density, radial components of flux density
B_{ry}	flux density in the rotor yoke
B_s	average flux density in the stator
B_{sat}	saturation flux density
b_{sl}	slot width
B_{sy}	flux density in the stator yoke
B_{tan}	tangential components of the flux density
B_{th}	tooth magnetic flux
C_E	constant of electromotive force
C_M	mechanical constant
c_p	specific heat of air at constant pessure
c_φ	flux concentration factor
D_{con}	conductor diameter
D_r	external diameter of rotor
D_{rin}	internal diameter of rotor
D_s	external diameter of stator
E	electromotive force (rms)
e_{phmax}	peak back EMF in phase
f	operating frequency
F_{dem}	demagnetizing magnetomotive force

F_{em}	electromagnetic force
F_m	magnetomotive force
G	permeance of magnetic circuit
G_{Σ}	summarized permeance
G_f	fringing permeance
G_g	air gap permeance
G_l	permeance of flux leakage path
G_m	permanent magnet permeance
G_{ry}	permeance of rotor yoke
G_{sy}	permeance of stator yoke
G_{th}	permeance of teeth
H	magnetic field strength
h_c	conductor strand thickness
H_c	coersivity
H_{ci}	intrinsic coercivity
h_{coil}	height of winding coil
H_g	barometric height of mercury
h_m	magnet height
H_m	internal magnetizing force
h_{ry}	height of rotor yoke
h_s	total height of stator
h_{sy}	height of stator yoke
h_{tip}	radial height of the tooth tip
I_0	no-load current
I_a	armature current
I_{con}	current in a conductor
I_k	short-circuit current
I_{kl}	inrush current
I_n	nominal current
I_{ph}	phase current
\dot{I}_{res}	resultant current
I_{sup}	supply current
J	current density
J_{in}	moment of inertia
k_l	winding factor

k_2	air gap factor
k_c	Carter's coefficient
k_l	leakage factor
k_m	coverage factor
k_r	reluctance factor
k_{sl}	slot fill factor
k_{stk}	stacking factor
K_{trv}	torque per rotor volume
k_v	speed constant
L	self-inductance
l'_g	air gap length without magnets
$L_{\Sigma l}$	total inductance
L_{ew}	end winding leakage inductance
l_g	air gap length
l_m	length of magnets
L_n	the n -th space harmonic
L_{sl}	slot leakage inductance
L_{stk}	machine axial length
L_{sy}	axial length of stator
l_{th}	length of the tooth perimeter
L_{th}	tooth tip leakage inductance
m	number of phases
M	mutual inductance
m_i	point mass
m_{sy}	weight of stator core
n	rotational speed
N	cables per slot
n_0	speed limit for zero torque
N_{con}	number of active conductors in a slot
n_{const}	speed limit for constant torque
N_{cp}	turn per coil pair
n_{cp}	number of coil pairs
n_n	nominal rotational speed
P	power
p	number of polepairs
P_l	nominal power

P_2	mechanical output power
P_{add}	additional loss
p_{air}	air pressure
P_{Cu}	copper loss
P_{eddy}	eddy current loss in the stator
P_{el}	electrical power
P_{Fe}	iron loss
P_{hys}	hysteresis loss in the stator
P_k	short-circuit power
p_k	dissipated power in the construction elements
P_{loss}	power loss
P_{PM}	magnet loss
P_{sup}	input power
P_{vent}	power of a ventilator
q	slots per pole and phase, heat flux density
Q	quantity of air
Q'_{con}	power loss due to the conduction
Q'_{cv}	power loss due to the convection
Q'_{rad}	power loss due to the radiation
Q_s	number of stator slots
q_{sb}	Stefan-Boltzmann constant
Q'_T	total thermal loss
Q'_v	heat flow by volume
R_{Σ}	total internal resistance
R_{con}	active resistance of a conductor
r_i	inertial radius
R_{in}	internal resistance
r_k	active resistance during short-circuit
R_{out}	external resistance
r_r	radius of the rotor
R_{win}	active resistance in windings
\mathcal{R}_{Σ}	total magnetic reluctance
S	apparent power
t	time
T	torque

THD_e	total harmonic distortion of back-EMF
THD_u	total harmonic distortion of phase voltage
T_k	thermodynamic temperature
T_{cog}	cogging torque
T_{em}	electromagnetic torque
T_{ICE}	torque of an internal combustion engine
T_m	mechanical torque
t_p	pole pitch
T_{pr}	counter torque of a propeller
t_{sl}	slot pitch
T_{sum}	total torque
U_{DC}	rectified voltage
U_l	line voltage
U_{ph}	phase voltage
U_{sup}	supply voltage
v	velocity of a cooling element
V_r	rotor volume
V_{sy}	stator volume
W_c	co-energy
w_{coil}	width of a winding coil side
w_{ew}	width of the end winding
w_m	width of magnet
w_{sl}	width of slot opening
w_{th}	width of tooth
α	electrical offset angle
α_{con}	thermal conduction coefficient
α_{cv}	specific heat dissipation factor in convection
α_f	empiric specific heat dissipation factor
α_{rad}	specific heat dissipation factor in radiation
γ	coefficient of the air gap
η	efficiency
ϑ	temperature
ϑ_0	initial temperature
θ_e	electrical position angle of the rotor
ϑ_{in}	air ingoing temperature
θ_{ph}	phase advance

ϑ_{win}	winding temperature
λ_{lew}	end winding permeance factor
λ_{sl}	permeance factor of the whole slot
λ_{th}	tooth permeance factor
λ_w	winding permeance factor
μ_0	permeability of vacuum
μ_a	absolute magnetic permeability
μ_r	relative permeability of magnets
ρ	material density
σ	skew angle
σ	air gap shear stress
σ_c	conductivity of conductor strand
σ_{Fr}	radial stress component
σ_{Ftan}	tangential stress component
τ_u	winding pitch
Φ_{ew}	end winding leakage flux
Φ_m	main magnetic flux
Φ_p	pole leakage flux
Φ_{sl}	slot leakage flux
Φ_{th}	tooth tip leakage flux
Ψ	flux linkage
ω	angular velocity

1 INTRODUCTION

1.1 Background

Consumption of fossil resources is an increasing trend in the present society. This is also related to transportation means which consume different fuels based on natural raw materials. According to OICA (International Organization of Motor Vehicle Manufacturers), more than 87 million vehicles were produced in 2013, and this is a growing trend. On the one hand, daily world consumption is approximately 85 million barrels of oil; on the other hand, the proven oil reserves compose only of 1300 billion barrels [1]. At the current rate of consumption, the world will run out of oil approximately in the next 40 years [2].

Thus, alternative solutions are being sought aside of internal combustion engines (ICE) mostly used in the transport vehicles today as the main traction source. Latest discussions have focused more and more on electrical machines (EM), as their advantages are: simpler construction, higher reliability, smaller size at the same rated power, lighter weight, higher efficiency, better environmental cleanliness, lower noise level, and lower price.

Additionally, electrical machines are reversible. Functioning as a motor and consuming electrical energy, they transform electrical energy into mechanical energy, thus actuating several mechanisms.

Electrical machines are able to transform mechanical energy into electrical energy. This quality applies also to asynchronous machines, which should be connected to mains for operating as a generator; also, a capacitor battery can be connected to its output terminals and parallel to a load, enabling operation of the asynchronous generator also in autonomic conditions [3].

In general, EMs consume more than 65% of electrical energy produced in different applications worldwide. Also they produce almost all energy necessary for consumption if operated as generators.

Usage of electrical machines in autonomous transport vehicles is significantly lower. In history, several tests have been performed to increase the usage of electrical machines in this area, however, without any breakthrough. Energy storage units, mostly rechargeable batteries, capable of making the transport means autonomously mobile and independent of power network are among main obstacles. While low-power electrical machines have their important role in most of transportation vehicles, the EMs as traction motors are only now making their way into commercial vehicles. Miscellaneous hybrid solutions have been used quite successfully, in which an electrical machine operates with an ICE as an integrated single system, which uses mostly ICE and EM combinations to move the vehicle. However, pivotal solutions are still sought for power supply units of fully electrical drives. A HDS combines the strengths of both motors [4]. This conception allows a decrease in ICE dimensions, which also decreases fuel consumption, emissions, noise, as well as power and torque. To compensate this,

EM is added, giving additional power and torque if necessary. An electrical generator is commonly used with ICE to charge power supply units.

The weakness of this solution is an additional weight resulting from EM and its power supply units. The latter is not of major importance in shipping, train industry, heavy vehicles where HDS have been used for decades. But the weight of the power supply unit is of importance in areas where high specific power $P\text{-to-}W$ (kW/kg) and torque density $T\text{-to-}V$ (kNm/m³) are important. These areas are, for example, small transport vehicles including sport and racing cars, space technology and light aviation. Thus, the importance of EMs in these fields is constantly increasing.

This dissertation focuses on light aerial vehicles (LAV) where drive systems similar to those in the modern car industry can be used.

Full electric system (FES) can be considered the simplest, effective, versatile and cost-effective propulsion system in light aerial vehicles where an electrical machine with the power supply unit operates as an independent power supply unit working by the same principles as all electric cars.

Table 1.1 compares the mean efficiency characteristics of the most frequently used petrol based turbo propeller and the turbo fan engines to alternative electrical motors in light aerial vehicles.

Table 1.1. Comparison of machines used in electric vehicles [5]

No.	Name	Parameters with the average efficiency			
		Turbo-propeller	Turbofan	Fully electric	Fully electric
1	Engine type	Turbo-propeller	Turbofan	Fully electric	Fully electric
2	Energy source	Kerosene	Kerosene	LiPo battery	AFC Fuel cell
3	Physical process	Thermodynamics (50%)	Thermodynamics (50%)	Electro-chemical (99%)	Electro-chemical (60%)
4	Transmission type	Gearbox (98%)	-	Gearbox (98%)	Gearbox (98%)
5	Propulsion element	Propeller (80%)	Fan and nozzles (65%)	Propeller (80%)	Propeller (80%)
6	Additional devices	-	-	Electric controller (98%)	Electric controller (98%)
7	Total efficiency	~40%	~35%	~75%	~45%

It is obvious that only fully electrical propeller drive based on an electrical engine and a battery unit is superior to turbo ventilator drives and turbo propeller drives, being twice as effective. Thus, it is reasonable to develop fully electrical engines for airplane engines.

The development is limited by size and amount of the power supply unit necessary for a desired flight time, which also has a direct effect on the total weight of the aerial vehicle, increasing the necessity for higher power and thus for a heavier drive of a larger size.

Increasing use of the Hybrid Propulsion System (HPS) for charging power supply units provides a more convenient and feasible solution also in light aerial vehicles. This kind of a hybrid drive allows longer flight mode compared to FES, which can also be controlled precisely and flexibly, enabling reduction of noise, exhaust fumes and fuel consumption [6]. Higher safety in emergency situations where ICE stops is also essential, for example, because of run-out of fuel; an electrical motor in the same drive can be used for landing.

1.2 History and Current Situation

Usage of electrical motors for aircraft propulsion is not new. In 1883, Gaston Tissandier from France was the first to use an electrical motor as a propulsion system for an aerial vehicle. In 1884, Charles Renard and Arthur Krebs from France used a more powerful motor on their dirigible "La France", flying a total period of 23 min [7]. At the same time, Croatian inventor Nikola Tesla designed his aerial vehicle with an electric propulsion unit [8], [9].

In unmanned aeroplanes, electrical machines were first used in 1957 when H. J. Taplin from UK performed officially the first radio-controlled flight with his prototype of the light aerial vehicle "Radio Queen". Permanent magnet motor and AgZn battery were used in the aerial vehicle. Aircraft designed by Fred Miltky also made its first flight in the same year [10].

Almost a century later, on April 29th, 1979, the first manned airplane equipped only with electrical power supply unit "Solar Rise" receiving its energy from solar panels, piloted by Larry Mauro, took off from the Flabob aviation field in California [10].

Further developments of electrical airplanes were made during the following decades, the most notable of which is the fully electrical glider "Antares 20E" constructed in 1999.

In 2009, an American enterprise Yuneec introduced a first revolutionary electrical light aerial vehicle E430 with the rated power of 40 kW, the target group of which were civilians [11].

In January 2015, an electrical plane "Solar Impulse" using four brushless permanent magnet machines of the total rated power of 52 kW as motors and only solar energy, took off from Abu Dhabi for circumnavigation [12].

The first hybrid electrical drives were constructed in 1890–1900. In 1899, a Belgian Henri Pieper demonstrated a vehicle with a hybrid drive in Paris where an internal combustion motor operated in parallel to an electrical engine. In 1909, the inventor was granted the first patent in the world in this area by the US Patent and Trademark Office [13].

Hybrid drives were not used publicly before Toyota introduced a new model Prius in 1997, which was marketed all over the world within only a couple of years [14].

Hybrid drive is still making its way to aviation. In 2009, German airplane manufacturer introduced a "Flight Design" drive, in which internal combustion engine Rotax 914 of the airplane and electrical drive were interconnected with belts, rated powers were 86 kW and 30 kW, respectively (Fig. 1.1) [15].

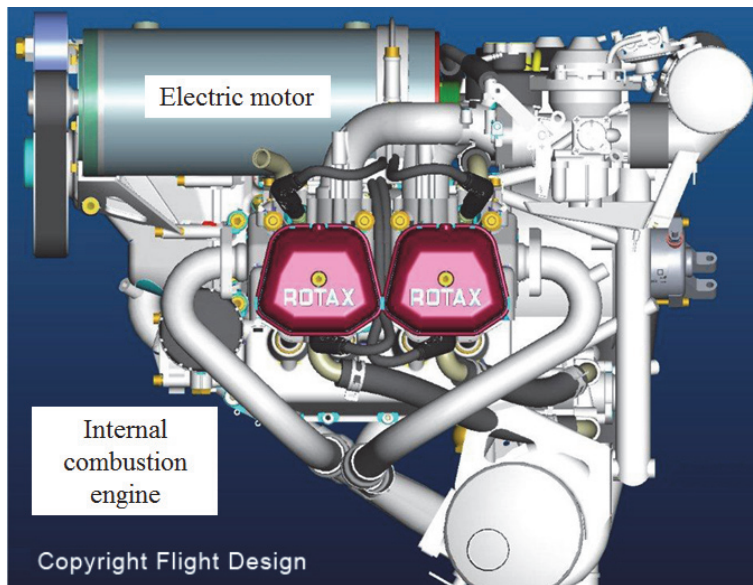


Fig. 1.1. Outside view of the hybrid drive by Flight Design [15].

Maximum power resulting from the parallel operation of the two machines was used on takeoff. Additionally, an electrical motor can briefly be used for landing the airplane in emergency situations.

In 2012, Richard R. Glasscock from Queensland University of Technology, Australia, constructed an enhanced hybrid drive prototype for his master's thesis, which stipulated replacing a 25 cm³ four-stroke internal combustion engine (ICE) operating as a main propulsion element with a smaller, 10 cm³ and two-stroke ICE, giving enough torque and power for stable flight of a plane in initially unmanned plane "ScanEagle". Similar to the example described above, on takeoff or during ascending, the ICE would be supported by an electrical motor used concurrently [16].

Fig. 1.2 shows a test bench with the prototype of the hybrid drive built by Richard R. Glasscock.

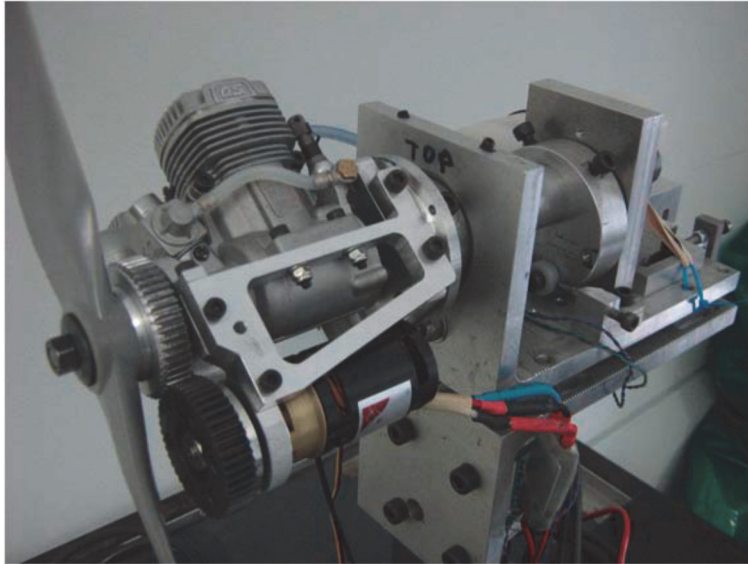


Fig. 1.2. Hybrid electric drive prototype by Richard R. Glasscock [16].

Glasscock's solution shows both advantages of the hybrid drive: parallel usage of both motors with a possibility to function together and alone, and a possibility to decrease size, weight and thus fuel consumption of the ICE.

1.3 New Developments and Trends

PM machines are currently the benchmark for high efficiency motors, but the tendency is to move away from rare earth materials, as usage of these is still expensive compared to usage of electromagnetic coils. In search of novel solutions, rotors made only from copper, synchronous reluctance machines (SRM) and their variations, and also non-rare earth machines are therefore under consideration [17], [18].

Efficiency of electrical machines presently manufactured is brought to limits of technological and constructional aptness. For example, according to international standards IEC 60034-30:2008 and IEC60034-21:2009, minimal efficiency of EMs using 1 kW 50 Hz local network by standard class IE₁ is 70%, but in 10 kW motors, the value is already 87% [19].

Nevertheless, problems with losses and material aging and elaborating even more effective solutions are in focus. Minimizing the losses allows higher effectiveness on higher frequencies and rotational speeds. For example, studies are conducted to laminate steel with high silicon content (~6.5%) to reduce iron losses and improve efficiency by up to 40%. Improved are also non-rare earth magnets as AlNiCo magnetic properties [17].

Based on new technologies, configurations and materials, one of the purposes is to rise significantly the power density $P\text{-to-}V$ of EMs up to 30 kW/l or 30000 kW/m³ [18]. In this regard, the PM machines have a guaranteed

advantage compared to SR and induction machines (IM), as even higher power density is among their strengths. For example, a PM synchronous machine has been developed by Power Electronics, Machines and Control Group (PEMC Group), the P -to- V of which is 33 kW/l or 33000 kW/m³ and the specific power P -to- W = 16 kW/kg at the rotational speed of 32 000 rpm [18]. Halbach array is used in the permanent magnets of the rotor of the machine (Fig. 1.3).

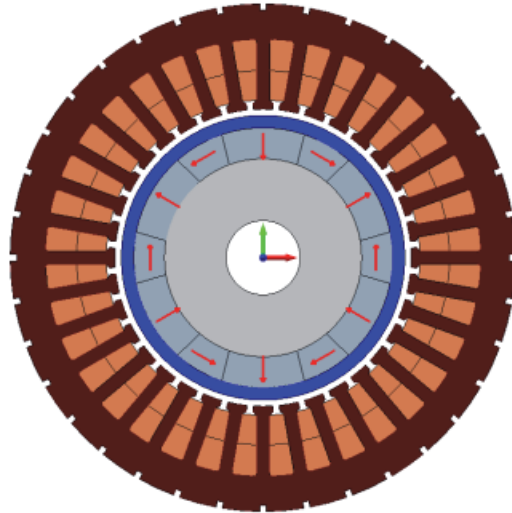


Fig. 1.3. High power density prototype by PEMC [18].

Limits of the torque density T -to- V have also been moved by PEMC Group. For example, maximum T -to- V of the PM exterior-rotor synchronous machine prototype developed by PEMC Group was measured at 270 kNm/m³ [18].

Fig. 1.4 shows the outer appearance of the motor and the internal view of the rotor.



Fig. 1.4. High torque density PMSM developed by PEMC [18].

Typically, higher power density is a concern not only for electrical machines, but also for power electronics used to control them. However, a new type of a controller uses Silicon Carbide JFETs with the switching frequency of 50 kHz as elements. Power density of a forced ventilated controller is 20 kW/l or 20000 kW/m³ [18].

Another development in power electronics control of electrical motors is their mechanical integration with an electrical machine that optimizes general size measurements of the propulsion system.

Fig. 1.5 shows an end-winding integrated modular converter.



Fig. 1.5. Integrated modular converter with a high power density by PEMC [18].

Regarding FES of light aircraft, in April 2015, Siemens published a 260 KW motor LUFO IV weighing slightly over 50 kg at the specific power of 5 kW/kg. At this performance, maximum take-off mass at the rotational speed of $n = 2500$ rpm without using an intermediate reduction gear is 1800 kg, which is enough for takeoff for most of lightweight planes [20].

Fig. 1.6 shows an exterior view of the abovementioned motor.

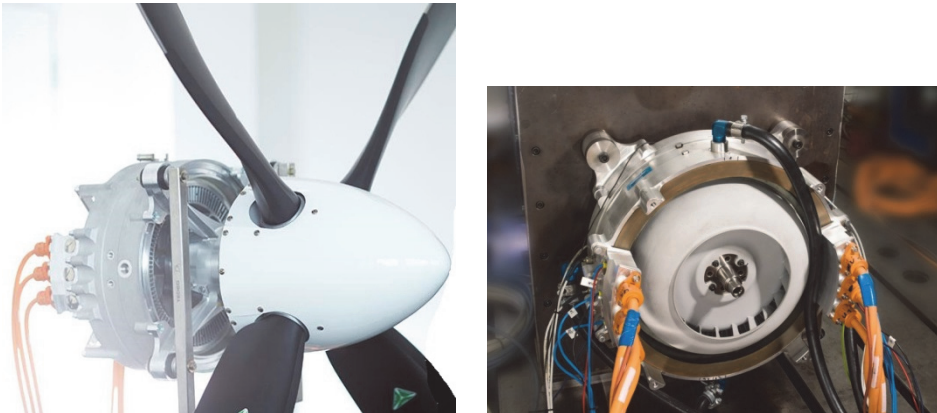


Fig. 1.6. LUFO IV light aircraft motor constructed by Siemens [20].

In the area of light aircraft, HPS has been developed mostly during the last decade. Several prototypes have been constructed based on these novel solutions, and several patents have been claimed. One of the differences compared to HDS used in cars is related to EM, one unit of which in aircraft can function as a motor and as a generator. In this form, separate as well as parallel functioning of ICE is possible.

One of the examples is the prototype patented by F. G. Harmon, R. M. Hiserote, M. D. Rippl and J. K. Ausserer in 2012, shown in Fig. 1.7 [21].

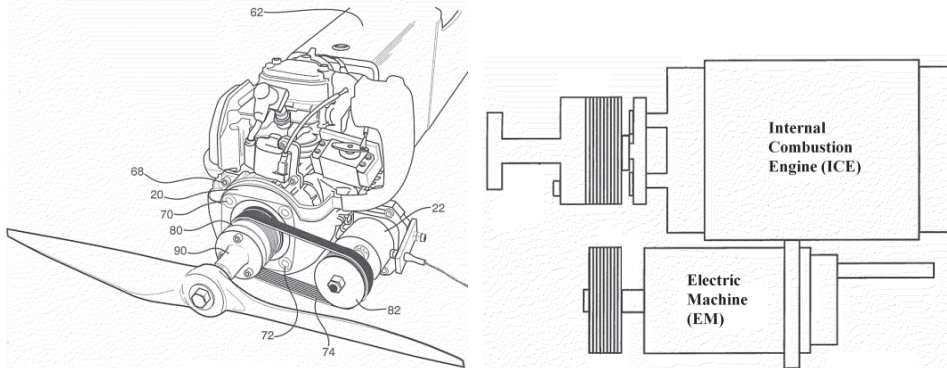


Fig. 1.7. A HPS prototype with a parallel placement of ICE and EM [21].

In this solution, the ICE is mechanically coupled with an electrical machine (EM) with a propeller connected to it. EM can function as a motor as well as a generator, also as a starter for the ICE. Additionally, EM can be used as a supplementary power source at the time of take-off or ascending when a short-term increase of power and rotational speed is necessary.

In this solution, EM's autonomous function of a motor independent of ICE is also possible.

In addition, EM may also function as a generator, the function of which is to generate power necessary to charge batteries on board of the aircraft [21].

In June 2015, a German engine manufacturer of Rotax Aircraft Engines presented a prototype of a hybrid propulsion system designed for light aircraft at Paris Air Show. Similar to the example described above, the propulsion system comprises an ICE but a permanent magnet synchronous machine, as an innovation, is added on the same shaft, functioning as a motor and as a generator, allowing usage of EM also for charging the batteries.

Additionally, EM functions as a starter. In emergency situations, e.g. in case ICE stops, it can be mechanically separated from the electrical machine. Both machines can function in parallel, giving short-time additional power on take-off or landing of the plane, using the braking torque of the propeller [22].

Fig. 1.8 shows the outer appearance of the described hybrid propulsion system.



Fig. 1.8. A hybrid-electric drive prototype by Rotax Aircraft Engines [22].

In summary, use of electrical machines in hybrid systems as well as in autonomous power sources in FESs is increasing. Hence, in a long-term perspective, hybrid solutions can be mostly considered as a certain stage in the EM development process. As outlined at the beginning of the introduction, usage of EMs in FESs in the area of light aviation is inhibited only by the limitations of battery capacity. Breakthrough in this area is expected already in the near future.

As both concepts are topical, the studies of EMs discussed in this doctoral thesis are based on the configurations of both HPS and FES.

1.4 Research Objects of the Thesis

In the main part of this doctoral thesis, HPS solution with equal torque and power of ICE and EM and use of full electric mode if necessary is discussed. Focus is on the Hybrid Propulsion System Motor-Generator (HPSMG) as part of the hybrid drive functioning both as a motor and as a generator. In case the machine functions as a motor, it is designed to operate as a main motor and starter in parallel with ICE.

The principal scheme of HPS is shown in Fig. 1.9.

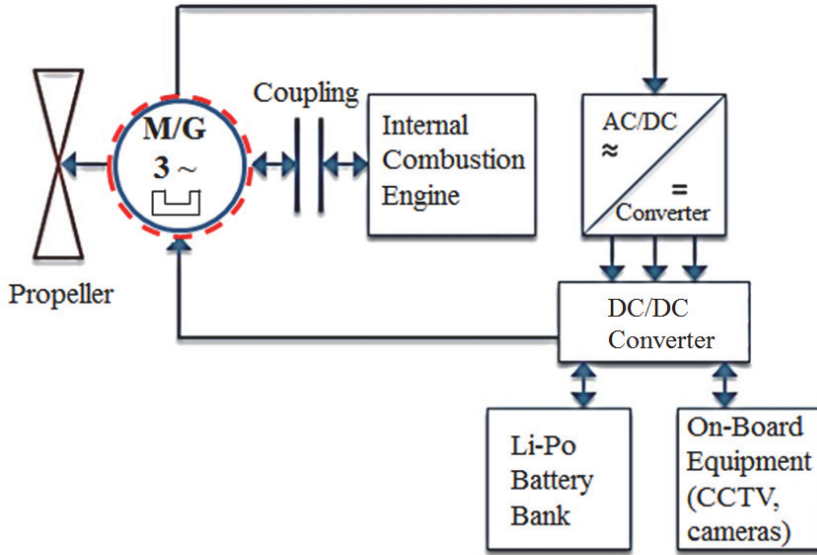


Fig. 1.9. Principal scheme of the UAV hybrid engine and energy storage system [23].

In terms of construction, HPSMG and ICE are located on the same shaft, which is a single-cylinder four-stroke engine Honda GX35. It is also the main engine starting the propeller of the light airplane, as shown in Fig. 1.10.

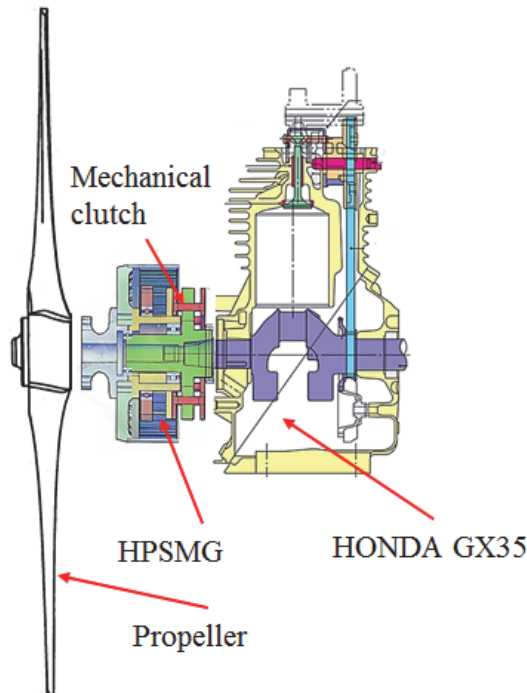


Fig. 1.10. A cross-sectional view of the studied HPS [24].

HPSMG is mechanically attached to the housing of the ICE, forming a compact system. Although both machines use the same traction axle, if necessary, they are separable by a clutch.

Similar to the examples in Sections 1.2 and 1.3 [21], [22], HPSMG functions both as a motor and a generator. In addition to functioning as a main propulsion device, parallel functioning of ICE and HPSMG increases the output power of the whole drive on take-off and on landing. Furthermore, HPSMG can also be used as a starter for restarting an ICE during flight and on land.

As current densities in HPSMG are untraditionally high compared to usual EMs, it is required to find solutions for thermal problems to ensure optimal cooling of the machine. Besides, one of the basic requirements in HPSMG design was to attain power-to-weight (W/kg) and power-to-volume (W/m^3) ratios as high as possible. This, in turn, raised electromagnetic problems.

In this context, the main focus of this thesis research is mostly on electromagnetic and thermal parameters of HPSMG.

In addition, a FES solution was addressed, applied on an electrical paraglider shown in Fig. 1.11.



Fig. 1.11. A typical appearance of an electric paraglider [25].

In this FES, the EM functioning as a drive of a paraglider was designed to work only on take-off; optimization of the number and weight of power supplies is possible, thus maximizing specific power of the aircraft. The paraglider is landed using an attached wing independent of the power supply.

Similar to HPSMG, hybrid propulsion exterior rotor geometry was used in this motor, but the configuration of the stator was different. A high specific power and resulting high current densities were common features of both of the

machines designed, which made the comparison possible. Additionally, mechanical parameters of the machines were compared, juxtaposing their torque densities (Nm/m^3).

Based on the detailed description of the design of the electromagnetic and thermal part of multipole exterior rotor PM electric machines, analytic results and values obtained in modelling of both machines were compared. The electrical machine of the paraglider was here used as reference to the analysis of the main subject of the thesis, i.e. HPSMG.

1.5 Main Objectives and Tasks of the Thesis

The main goal of this doctoral thesis is to develop a PM synchronous machine with high specific power and high efficiency to be used in light aircraft both as a motor and a generator, using a novel configuration of toroidal winding and stator geometry.

The main research tasks of the PhD thesis:

- Overview of types, geometries and operating modes of electrical machines used in hybrid and fully electrical drives of present-day light aircraft
- Overview of state-of-the-art technologies and development trends of electric propulsion
- Specification of initial parameters, such as stator and rotor geometries and dimensions for basic design
- Development of electromagnetic design
- Development of thermal design
- Practical testing of prototypes at the test bench and verification of analytical and modelling results
- Evaluation and comparative analysis of output parameters of prototypes in terms of power density, specific power and torque density

1.6 Contribution of the Thesis and Dissemination

Main positions of scientific and practical novelty are listed below.

Scientific Novelty

Scientific novelty of the doctoral thesis includes:

- Design process methodology of an exterior-rotor permanent magnet synchronous machine construction for a lightweight aircraft operating as a motor, starter and a generator in a hybrid electrical propulsion system
- Proposal of a novel type, low power loss, ergonomic stator geometry with high slot fill factor in combination with Gramme's toroidal winding in the studied machine
- Comparative electromagnetic and thermal analysis between new toroidally wound stator and more common concentrically wound stator

Practical Novelty

Practical novelty of the doctoral thesis includes:

- Electromagnetically and thermally modelled virtual models of three permanent magnet synchronous machines
- Two practically constructed full-size prototypes of permanent magnet synchronous machines
- Original test bench for practical testing of both of the machines
- Applying higher current densities than usual and obtaining high specific power and torque densities in each prototype

Dissemination of the Results and Publications

The author has presented the results of the doctoral thesis at four international conferences directly associated with the thesis. Three of them are available in the IEEE database and one has been published in an international peer-reviewed journal.

1.7 Outline of the Thesis

Chapter 2 outlines the design process of HPSMG and FESM with their application area and resulting requirements; topology of the rotor and the stator, dimensions and electrical and magnetic parameters are calculated.

Soft magnetic materials used in the stators of electrical machines are discussed separately, properties of most widely used materials are analyzed and compared and an optimal solution for machines to be designed, considering intended use of the machines, is found.

Permanent magnet materials are also discussed in detail. Their developmental stages and technical specifications are reviewed. Permanent magnets used in the machines to be developed and their specifications are described.

HPSMG and FESM windings are discussed in the last part of Chapter 2. Focus is on the construction and technical specifications of the windings of the two machines.

Chapter 3 contains the electromagnetic part of the HPSMG and FESM design. Parameters of primary and secondary magnetic field and resulting magnetic field generated by both of them are analyzed thoroughly. Results of calculations are compared to those obtained by modelling, using software applications SPEED PC-BDC and PC-FEA, Motor-CAD BPM-EMag, and FEMM 4.2.

As FESM is considerably more powerful and with bigger overall dimensions then this chapter includes also a description of an experimentally modelled machine with the identical rotor topology and dimensions as HPSMG, but has the concentrated winding and stator geometry as FESM. The main purpose of the experimental model was to create a direct and more exact reference object for the toroidally wound HPSMG which is based on the similar rotor geometry, volume and total mass of the machine, identical location and mass of permanent

magnets etc. The comparative analyses is focused to bring out the advantages and disadvantages of both types of windings and stator geometries.

The last part of the chapter covers the analysis of the calculated and modelled parameters of all three machines related to the electromotive force, the back electromotive force, electromagnetic torque and cogging torque, as well as to power.

Chapter 4 presents an analysis of the thermal parameters of the machines, which are measured in all three machines similar to measurements in the previous chapters. First, an overview of general physical principles of thermal energy conduction is given. Second, the virtual heating processes of different parts of the machines are discussed. In this case, software application Motor-CAD-BPM Thermal is used in modelling.

Chapter 5 gives an overview of practical testing of HPSMG and FESM and the results obtained and their analysis. The first part discusses generator tests of machines in no-load conditions as well as in load conditions.

The second part gives an overview of motor tests performed likewise in both no-load conditions and in load conditions.

In the tests, temperatures were measured and temperature constants were found.

In the last part of Chapter 5, HPSMG and FESM specifications are analyzed in the context of specific power and torque density. The results are compared to those of chosen products of known motor manufacturers in the area of light aviation.

Chapter 6 summarizes and evaluates the results of this thesis research. Additionally, future perspectives and the planned and related purposes are discussed.

References consist of 79 external and 4 author's publications.

2 DESIGN PROCESS OF EXTERIOR-ROTOR PM MACHINES FOR LIGHT AERIAL VEHICLES

This chapter gives a parallel overview of the design stages of two exterior-rotor PM synchronous machines. A machine designed for an electric paraglider FESM is used here as a reference for HPSMG, which operates as a motor and a generator in HPS. HPSMG is the main research object of the thesis.

2.1 Machine types

Designing of HPSMG and FESM was limited by the following requirements: simple construction, low cost, high power-to-weight ratio, and power-to-volume ratio, small dimensions, good characteristics of controlling and adjusting, and high torque at low speed. To fulfill the requirements, the first task was to find the right type of the machine. A wide variety of electrical machines are available that meet very different requirements and environments, thus they have technical parameters that are significantly different. As the research discussed in this doctoral thesis is related to light aviation, features comparable to those of other electrical vehicles can be identified.

Table 2.1 shows a comparison of main characteristics of electrical machines most commonly used in electrical vehicles [26].

Table 2.1. Comparison of machines used in electrical vehicles

Performance	Machine type				Unit
	DCM	IM	PM	SRM	
Power density	Low	Medium	High	Very high	-
Peak efficiency	< 90	90-95	95-97	< 90	%
Load efficiency	80-87	90-92	85-97	78-86	%
Controllability	Simple	Complex	Hard for field weakening	Complex	-
Reliability	Normal	Good	Excellent	Good	-
Heat dissipation	Bad	Bad	Good	Good	-
Size and weight	Large, heavy	Normal, normal	Small, light	Small, light	-
High-speed performance	Poor	Excellent	Good	Excellent	-
Construction	Slightly worse	Better	Slightly better	Excellent	-
Cost of motor	9	7-9	9-13	5-9	€/kW
Cost of controller	Low	High	High	Normal	-
Combination property	Slightly worse	Normal	Excellent	Better	-

The table shows that PM machines have advantages over other machine types, having high power density, high efficiency, low mass and low volume. SRMs have similar good characteristics but lower efficiency.

Among PM machines are Brushless DC machines (BLDC), a popular design from the recent decades thanks to their good characteristics and performance. The BLDC machine has starting characteristics of a series excitation DC machine and the speed regulation characteristics of a shunt excitation DC machine [26]. Electronically controlled BLDC has several advantages over brushed DC machine and induction motors, such as a better speed versus torque characteristics, high dynamic response, high efficiency and reliability, long operating life, noiseless operation, higher speed ranges, and low electromagnetic interference (EMI). Additionally, the ratio of delivered torque to the size of the motor is higher, making it useful in applications where space and weight are critical factors, especially in aerospace applications [27].

Although the BLDC is defined and classified under no unified standard, it has presently been looked at as an independent machine type, having many similarities with PMSM; one of their main differences is the shape of back-EMF, which in PMSM is a three-phase sinusoidal waveform and in BLDC a quasi-square waveform [26].

As the output voltage and output current of converters used for power supply and control of HPSMG and FESM provide the quasi-square shape of waveform, both of the machines can be looked at as BLDC machines, therefore machines of that type are focused on in this thesis.

2.2 Determination of Application and Requirements

Before designing a new machine, it is essential to determine its intended use and thus to define specific conditions and requirements. HPSMG and FESM are used in light aerial vehicles where each electrical machine with a propeller forms a propulsion system with similar operations. Differences are only in the operation modes of each machine. Thus, problems with the propulsion system and working environment are also similar.

Analysis of the standards for the machines designed reveals that in BLDC and PM electrical machines, no separate international standards have been established [26]. In the design of this type of machines, only standards for general rotating electrical machines are taken into account, i.e. IEC/EN 60034: "Rotating Electrical Machines" and IEC/EN 60072: "Dimensions and output series for rotating electrical machines" [28]. In USA, additionally, the following standards are adhered: API 546: "Brushless Synchronous Machines - 500 kVA and Larger", UL 1004: "Standard for Electric Motors" and similar to the other countries, several directives adjusted to local requirements are followed.

As an applicable standard for BLDC machines is missing, the common process for basic design rules were followed also in this doctoral thesis regarding HPSMG and FESM. The first of them is to determine mechanical

requirements like necessary torque, rotational speed and power. Technical specifications of propellers of HPSMG and FESM were used as a reference, including the propeller pitch and the counter torque at different rotational speeds, which were experimentally measured earlier. In HPSMG, specifications of ICE working in parallel to HPSMG were taken as reference in addition to parameters of the propeller. This requirement included starting the ICE as a starter, thus it was required to ensure sufficient starting torque and parallel operation of both machines on sharing torques on take-off of the aircraft.

In the determination of the output power, it is important to pay attention to the future operating mode of a machine to be designed. Choice of an operating mode is directly related to the dynamics of thermal processes inside the machine and at incorrect choice, this may result in overheating of the machine.

According to the standard IEC/EN 60034-1, operational cycles for mechanical devices, including electrical machines, are set to express their load operation in different time periods [29].

Duration of the operational cycles of HPSMG and FESM is generally at least $t = 15$ min. In this period, each machine develops constant working temperature.

One of HPSMG's operational modes is the starter mode in which ICE is started within some seconds. In this case, the working cycle is too short to develop constant temperature. Thus, both of the machines belong to class S_1 according to the classification of the standard, additionally HPSMG belongs to class S_2 .

The maximum values of output power and torque of an ICE [30] were considered as reference values for HPSMG. According to set criteria the power and torque of HPSMG should not be lower.

FESM as a BLDC machine is a slow speed motor the nominal rotation speed of which is $n = 3000$ rpm. Finding this value was necessary because of linear velocity of the top of the blade of the propeller during rotation; the value had to remain in calculated limits to avoid additional losses generated at speeds higher than optimal. As it was required to obtain the power and high torque at low rotation speed, the result was a high number of magnetic poles, high operating frequency and nominal current like in HPSMG. The requirements above and the resulting problems are the topics to be addressed in the design and construction of BLDC motors of high specific power and high torque. Commonly, such motors feature quite low operating voltages, but high magnetic frequencies and current densities, which is a direct indication to the importance of cooling as well as losses.

For FESM the low voltage and high current AC/DC converter with the electrical parameters of $U_{sup} = 51.8$ V_{DC} (14S) and $I_{sup} = 250$ A was selected [31]. In the calculation of voltage and capacity of the battery unit, these parameters are used as reference.

2.3 Choice of Rotor Geometries

Several types of electrical machines are used in light aerial vehicles, i.e. small unmanned airplanes and electrical paragliders having one pilot. Amongst them, BLDC machines are most widely used because of their simplicity, reliability, high specific powers and moment torque and allow autonomous operation of the aerial vehicle, i.e. the aerial vehicle is separated from the power network.

Problems with power supply units of light aerial vehicles are very similar to those that are faced with racing technologies used on water or on land. BLDC machines are very common in these areas, as one of the most important requirements is also power-to-mass ratio, and torque-to-volume ratio. Thus, similarities exist in types of electrical machines used in those areas, and also in their geometries.

BLDC machines can be divided into three main groups on the basis of geometries of their rotors: interior rotor, exterior rotor, and axial rotor (Fig. 2.1) [32].

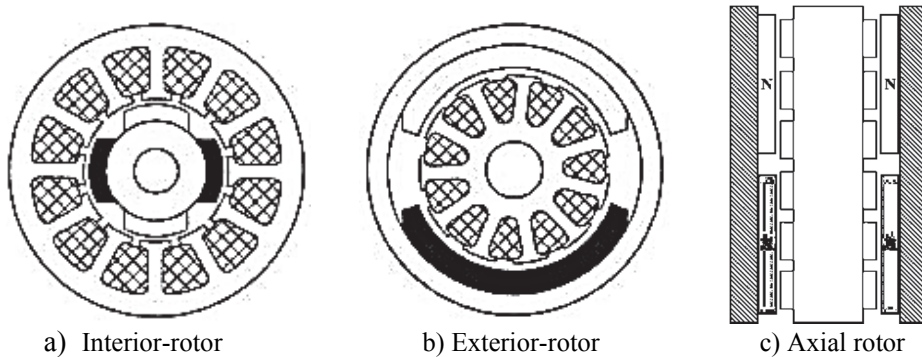


Fig. 2.1. Three basic brushless machine configurations [33].

Regarding geometry, an exterior rotor was chosen for HPSMG and FESM for miscellaneous reasons. With regard to HPSMG, the first reason was the necessity to place the coupling mechanism of HPSMG and ICE space-savings into the interior part of HPSMG. If an interior rotor or axial rotor had been used, this would have been made technologically more complicated. This solution did not concern FESM, which has an autonomous power supply without coupling. This solution allows housing of power electronic devices, e.g. a controller inside the stator in the future.

Another structural advantage derived from the choice of exterior-rotor geometry was allocation of permanent magnets on the rotor. As in both machines, the magnets are located on the surface of the inner diameter of the rotor, centrifugal force presses the magnets on the wall of the rotor and no special bandages are needed for fixation which, in contrast, is required in constructions with an interior rotor. This increases strength and reliability of both of the machines.

Additionally, an exterior rotor has other advantages over an interior rotor:

- exterior rotor allows usage of lower energy magnets [34];
- exterior rotor machine can have a larger air gap diameter with the same rated power and volume that allows higher torque density [35];
- a larger rotor diameter gives a larger moment of inertia [32], which is necessary for surpassing air resistance generated by the rotating propeller;
- overall reduced copper loss, reduced production costs [34].

Different studies conducted in the last decades reveal that machines with axial geometry have certain advantages over machines with cylindrical design and radial magnetic flux (e.g. induction machines), especially in terms of power and torque density [36], [37]. Comparison of the axial geometry of permanent magnet synchronous machines with that with radial geometry reveals that the two specifications above as well as their efficiency are quite similar [38].

Axial rotor machines have normally two stators or two rotors to achieve the necessary balance. Hence, the air gap length of an axial rotor machine is twice as wide as it is in radial rotor machines. The result is higher leakage of magnetic flux [32]. Also, the axial rotor machine requires more magnet mass and ball bearings, which creates larger losses [39]. Therefore, overall manufacturing costs of a radial rotor machine are lower than with the axial rotor machine [35]. Additionally, manufacturing costs are affected by the fact that manufacturing methods of machines with radial rotor have been developed during significantly longer time span. Considering the previous analysis, the exterior-rotor radial geometry for HPSMG and FESM as the most optimal was selected.

Combining interior rotor and exterior rotor geometries and designing a so-called dual rotor is also among solutions for construction. Several tests have shown that BLDC machines of this geometry show approximately twice as high torque density and the ratio of torque to weight as similar BLDC machines with an interior rotor. Differences in the efficiency of both machine types compared are marginal [40]. Dual-rotor construction of the prototype of a PMSM machine is shown in Fig. 2.2.

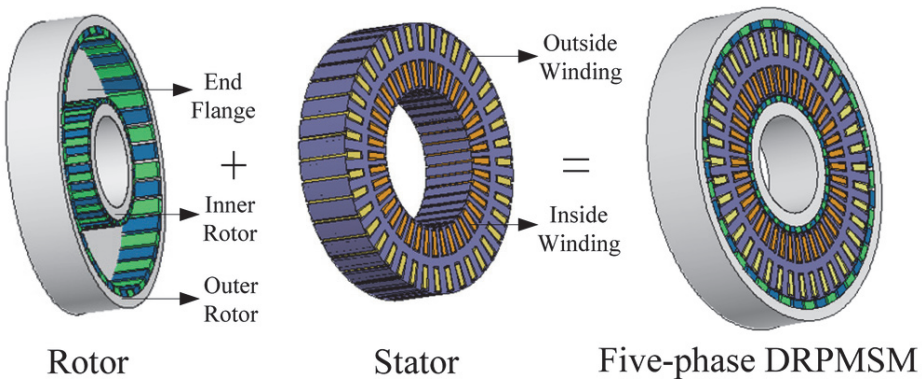


Fig. 2.2. The construction of dual-rotor PMSM [41].

Significantly higher complexity of this rotor type construction requires higher mechanical precision, higher mass and higher costs from additional magnetic material, more massive bearing assembly because of heavier rotor are the problems faced with this geometry compared to machine types with an interior rotor and an exterior rotor. Additionally, using the same stator yoke for both magnetic circuits causes problems with cooling the machine.

Resulting from the analysis of weaknesses and advantages of different structures and constructions, it was decided to use exterior rotor geometry in HPSMG and FESM.

Short rotor length L_{stk} compared to the large radial diameter D_r is characteristic of this geometry. This structure allows the rotor to obtain maximum mechanical torque T . An exterior rotor features a hollow cylinder where permanent magnets are placed onto the inner perimeter of the rotor, which form the major part of the mass inducing inertia. Thus, radial distance of magnets from the rotor's axis of rotation can be considered as the rotor's inertial radius r_i :

$$J_{in} = \sum m_i \cdot r_i^2, \quad (2.1)$$

where J_{in} is moment of inertia and m_i point mass.

Eq. (2.1) shows that the larger the r_i , the higher the moment of inertia that can be obtained. According to Newton's Second Law, J_{in} and T are directly related, obtained by placing m_i , i.e., permanent magnets as far as possible of the rotating axis (Eq. (2.2)):

$$T = J_{in} \frac{d\omega}{dt} = J_{in} \cdot a, \quad (2.2)$$

where $d\omega/dt$ is acceleration of the body (rad/s^2).

This pattern is also the cause of high D_r and low L_{stk} ratio in the exterior rotor.

The size of the rotational step is important in defining the number of rotor poles. Increasing the number of teeth and poles allows shorter steps and higher and more stable torque already at lower rotational frequencies. Additionally, this structure reduces the cogging torque, at the same time, significant increase of supply voltage frequency is required to attain higher rotational speeds. This, in turn, increases hysteresis loss in the stator yoke. To avoid this, the stator yoke was required to be constructed from a high property electrotechnical steel.

2.4 Initial Sizing

As Section 2.2 had initially defined maximum DC power P_l of battery units and controllers of both machines, the expected power P_2 on the shaft was

calculated using this value based on the power factor $\cos \varphi$ of both converters less than 95%. As a result, desired efficiency of both machines was set to 0.85 or 85%, which provided mechanical power of 0.8 kW in HPSMG and 11.0 kW in FESM. Then, mechanical torque at the shaft T_m was calculated:

$$T_m = \frac{P_2}{\omega} = \frac{P_2}{2\pi n / 60}, \quad (2.3)$$

where ω is angular velocity.

Additionally, 2-3% should be added due to friction, windage and drag torque [42]. Thus, the estimated T_m for HPSMG was 1.95 Nm and for FESM 36.0 Nm.

Based on the results, the torque per unit rotor volume K_{trv} was calculated, which describes the amount of torque available for a given rotor volume [43]:

$$K_{trv} = \frac{|T_m|}{\frac{\pi}{4} D_r^2 L_{stk}}, \quad (2.4)$$

where D_r is the rotor diameter and L_{stk} is the active stack length.

As in the beginning, the sizes of the machines were not available, K_{trv} value was taken from a handbook where an arithmetical average value for totally-enclosed motors with NdFeB magnets is 28 kNm/m³ [42].

The air gap shear stress or the tangential force per unit rotor surface area σ can be found by the following equation [43]:

$$\sigma = \frac{|T_m|}{\frac{\pi}{2} D_r^2 L_{stk}} = \frac{K_{trv}}{2} \quad (2.5)$$

Eq. (2.5) shows that σ is closely related to K_{trv} and is its half-value, i.e., 14 kN/m² (Pa).

To simplify the calculation process, the length and the diameter of the rotor was calculated according to the following equation, where the ratio of L_{stk} and D is 1.0 [42]:

$$D_r = \sqrt[3]{\frac{2T_m}{\pi\sigma}} \quad (2.6)$$

Total volume of the rotors is calculated below. While it was important to obtain the moment of inertia as high as possible in both machines, the radial diameter of rotors was increased based on the computed volume, decreasing the rotor length at the same time. Computed diameter/length ratio D_r/L_{stk} for both rotors was approximately 1/5. The diameter of HPSMG rotor's active part L_{stk} was 22 mm and in FESM, the same value was 40 mm. Resulting radiuses r_r of rotors were calculated according to Eq. (2.7):

$$r_r = \sqrt{\frac{V_r}{\pi \cdot L_{stk}}} \quad (2.7)$$

Based on the calculations, HPSMG rotor diameter was $D_{r(HPSMG)} = 98.0$ mm and the same value in FESM was $D_{r(FESM)} = 207.0$ mm.

Table 2.2 summarizes computational base parameters of HPSMG and FESM.

Table 2.2. Initial parameters of HPSMG and FESM

No.	Symbol	Description	HPSMG	FESM	Unit
1	U_{sup}	Supply voltage	21.0	51.8	V _{DC}
2	I_v	Maximum continuous current	43.0	250	A
3	P_1	Nominal power	0.9	13.0	kW
4	P_2	Estimated mechanical power	0.8	11.0	kW
5	n_n	Nominal speed	4000	3000	rpm
6	T_m	Estimated mechanical torque	1.95	36	Nm
7	K_{trv}	Torque per rotor volume	28	28	kNm/m ³
8	σ	Air gap shear stress	14	14	kN/m ²
9	D_r	Outer diameter	98	207	mm
10	L_{stk}	Axial length	22	40	mm
11	V_r	Rotor volume	0.00017	0.0014	m ³

2.5 Poles and Stator Geometry

The armature winding of PM machines is usually mounted in slots. In slotless windings, cogging torque can be minimized, higher efficiency can be attained at high speeds, lower torque ripple, and less acoustic noise can be obtained. These specifications were not of primary importance in HPSMG and FESM regarding their function, which had to meet the requirement of high power and torque density already at low rotational speed. These objectives are easier to be attained using winding with slots, which additionally allows higher efficiency at lower speeds, lower armature current, less PM material, and lower material costs [44]. Several tests have shown that for the same produced torque, a slotless machine needs higher magnetomotive force than a slotted machine. But this increases proportionally copper losses. A slotless machine heats up very fast with high currents and therefore it needs special heat sinks for dissipating the heat [32], [45].

Additionally, slots and their teeth ensure steadier fixation of the winding on the stator yoke, at the same time, they make the winding process more inconvenient in practice and create a necessity for additional isolation inside the slot to protect the winding.

Stators with a high number of slots are common in BLDC configurations with an exterior rotor used in light aircraft with electrical power supply. This is caused by a larger radial diameter of machines with an exterior rotor compared to machines with an interior rotor at the same volume of stator stack. With an interior rotor, the stator stack is longer.

The other practical reason for using exterior-rotor geometry is the comfortable and easy winding of the stator as its slots and teeth are located on the exterior surface of the stator of the electrical machine, which is important especially in the smaller diameter winding machines and with multiple slots.

Thus, stator geometry with exterior teeth was used also in HPSMG and FESM. The stators were different by the configuration of the slots. Fig. 2.3 illustrates the geometrical structure of the HPSMG magnetic circuit, showing also the location of teeth on the stator.

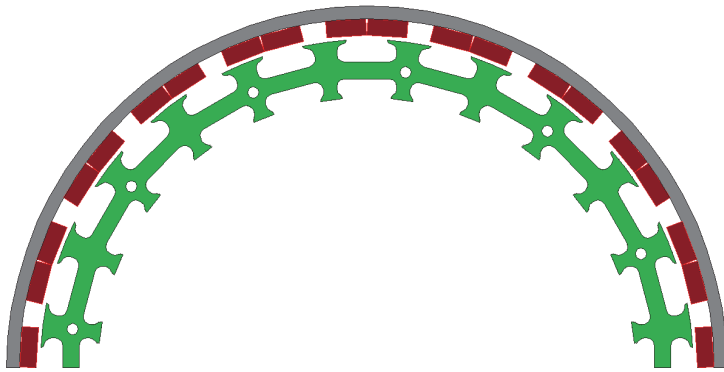


Fig. 2.3. The geometry of the stator and the rotor of HPSMG.

Location of slots at both sides of the stator yoke is characteristic of this geometry. This configuration allows fixing of coils of toroidal or Gramme's winding around the stator yoke, not around teeth as usual.

Conventional positioning of slots was followed in the FESM stator geometry (Fig. 2.4) where winding coils were planned to be wound around the teeth.

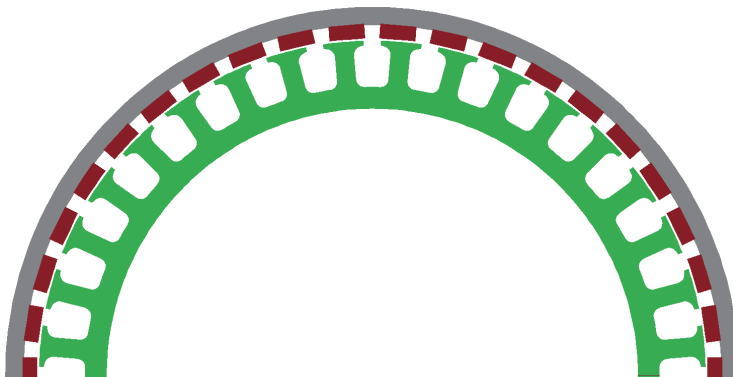


Fig. 2.4. The geometry of the stator of FESM.

It was planned to use two-layered concentrated windings as windings of both stator types where phase windings were made up from similar winding groups of two coils but their position on the stator was different.

The purpose was to allow comparison of the two stator geometries and mapping and analysis of electromagnetic parameters arising from these windings.

Finding stator's outer dimensions D_s is usually based on the geometrical correlation (Eq. (2.8)).

$$D_s = D_{rin} - 2l_g, \quad (2.8)$$

where D_{rin} is the inner diameter of the exterior rotor and l_g is the air gap length.

As outer diameters D_r (Section 3.1.3) of HPSMG and FESM rotors were previously found, calculating D_{rin} required finding the height of the rotor yoke h_{ry} , which is dependent on the density of magnetic flux B_{ry} of the rotor yoke. This value is affected by the dimensions of the rotor yoke and magnets used and the value of the air gap magnetic flux density B_g , the range of which is generally 0.85-1.05 T in PMSM [46]. Based on the data above, magnetic flux density in the rotor yoke was calculated (Eq. (2.9)) [42]:

$$B_{ry} = \frac{B_g \cdot A_{0.5p}}{A_{ry}}, \quad (2.9)$$

where A_{ry} is the cross-sectional area of the rotor yoke and $A_{0.5p}$ is the cross-sectional area of the half-width of the pole (Fig. 2.5).

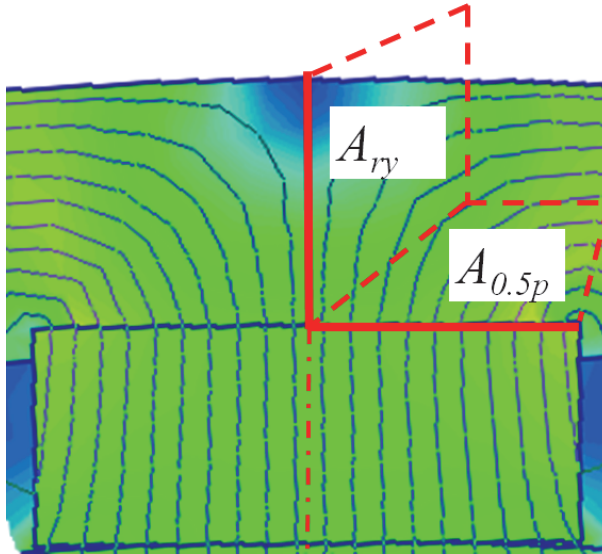


Fig. 2.5. A sectional view of the single magnetic pole and the rotor yoke of FESM.

To perform calculations, the chosen presumed values of B_g in HPSMG and FESM were 0.85 T [46]. As the length of the rotor yoke L_{stk} was already known (Section 2.4), to find A_{ry} and $A_{0.5p}$, it was required to find h_{ry} and the height of magnets h_m . This was done using the predetermined values limited by the dimensions of available magnets, mechanically optimal structure of rotors and the highest limit of B_{ry} , which in standard synchronous machines is between 1.0-1.6 T [46]. Finding suitable h_{ry} based on the condition that if it is necessary to change the value, it is also necessary to change h_m values so that differences between h_{ry} and h_m would be minimal. Hence, $h_{ry} = 2.55$ mm ($B_{ry} = 1.6$ T) in HPSMG and $h_{ry} = 5.0$ mm ($B_{ry} = 0.85$ T) in FESM and thus, respective D_{rin} values were 197.0 and 93.0 mm. Magnets to be used were chosen from magnets commercially available. Thus, further calculations based on magnets in which h_m conformed to previously calculated h_{ry} had the highest value. The height of magnets in HPSMG was $h_m = 2.2$ mm and in FESM, the value was 4.0 mm.

Subsequently, HPSMG and FESM air gap lengths l_g were calculated (Eq. (2.10)) [46]:

$$l_g = \gamma \cdot \tau_p \frac{A}{B_g}, \quad (2.10)$$

where γ is the coefficient of the air gap, τ_p is the pole pitch and A is the stator linear current density.

While in the designed HPSMG and FESM, the calculated current density was high, i.e. more than 10 A/mm², the value of A was measured to be 200 kA/m [46]. According to the calculations, air gap length of both machines was $l_g \sim 0.6$ mm.

Maximum resistance to demagnetization requires a small l_g . Still, larger l_g creates a good magnetic reluctance and slows the saturation process. In the case of very small BLDC machines, the range of l_g may be 0.10-0.30 mm, in medium-sized machines, the value range is 0.30-0.50 mm and in large BLDC machines, the value range is 0.60-0.90 mm [32].

Therefore, HPSMG can be considered a medium-sized machine and FESM a medium-sized or a large BLDC machine. Thus, the air gap length was designed at $l_g = 0.5$ mm in HPSMG and $l_g = 0.6$ mm in FESM.

Calculation results above allowed finding outer diameters D_s of HPSMG and FESM stators (Eq. (3.6)), which in the HPSMG stator was 87.5 mm and in the FESM stator was 188.0 mm. In the design of both machines, the common ratio of rotor length and stator length in practice was considered at $L_{stk}/L_{sy} = 4l_g$ [46]. Thus, the length of stators and rotors is as follows: $L_{stk(HPSMG)} = 22$ mm, $L_{sy(HPSMG)} = 20$ mm, $L_{stk(FESM)} = 42$ mm, $L_{sy(FESM)} = 40$ mm.

The number of poles chosen affects directly K_{trv} and σ values. Increasing the number of magnetic poles increases proportionally both of the parameters mentioned above (Eq. (2.11)) [43]:

$$K_{trv} = \frac{|T|}{\frac{\pi}{4} D_r^2 L_{stk}} = \frac{4p B_g F_m}{\pi r_r}, \quad (2.11)$$

where r_r is rotor radius and F_m is magnetomotive force.

As HPSMG and FESM require high torque at low rotational speed and the geometry of the exterior-rotor of large diameter, and based on the considerations above, both machines were designed to be multipolar, i.e., with more than 10 poles. According to the number of poles, the content value was chosen to be the ratio of the width of magnets w_m to the pole pitch of the rotor τ_p , i.e., the coverage factor k_m (Eq. (2.12)) [47]:

$$k_m = \frac{w_m}{\tau_p} \quad (2.12)$$

In practice, k_m value is usually in the range of 0.65-0.75. If k_m has a smaller value, then B_{ry} decreases too much, causing significant decrease of the torque in the machine (Eq. (2.11)). On the other hand, higher k_m value causes the saturation of the rotor yoke. Coverage factor value depends mostly on the dimensions of available magnets.

Initial value of k_m in HPSMG and FESM was chosen at 0.7. Finding w_m of magnets was limited by the predefined values like height of the magnets h_m , length of the magnets l_m (which was equal to the stator length L_{sy} in both cases), curvature of the rotor and maximum operating temperature because of high current densities. Thus, the FESM magnets were chosen with dimensions of $l_m = 40$ mm and $w_m = 10$ mm [48].

Through defining the dimensions of magnets of FESM, the pole pairs were found to be $p = 21$ (Eq. (2.13)):

$$p = \frac{k_m \cdot \pi D_{rin}}{2w_m} \quad (2.13)$$

Actual coverage factor of FESM was $k_m = 0.68$ (Fig. 2.6), which is in the same range with coverage factors used in practice.

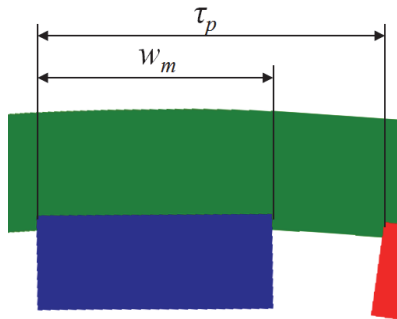


Fig. 2.6. FESM pole pitch [49].

Similarly, w_m and p of HPSMG were found, where k_m , l_m and h_m values were predefined. As D_{rin} value of HPSMG was approximately twice lower comparing to FESM, it was decided to decrease the number of pole pairs of HPSMG, i.e. up to 20. While $k_m = 0.7$, the result of w_m was 10.2 mm, which is similar to the same value in FESM. As the inner diameter of the HPSMG rotor curvature is twice as small as in FESM, several constructional and electromagnetic problems arise because of wide magnets placed into the small diameter of HPSMG, resulting in fragile fixation of magnets, increasing magnetic reluctance between the rotor yoke and magnet, deteriorating sinusoidal waveform of the magnetic flux and creating a need for a larger air gap. To solve the problem, HPSMG poles were constructed from magnet pairs with dimensions of $l_m = 20$ mm and $w_m = 10.8$ mm [50]. Based on the considerations above, HPSMG corrected coverage factor was calculated to be $k_m = 0.74$ (Fig. 2.7), which also remains in the range of coverage factors mentioned above.

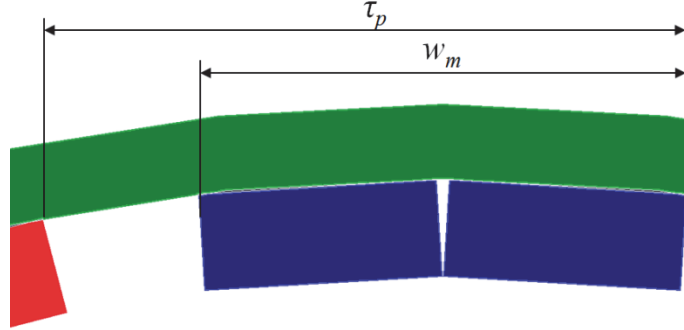


Fig. 2.7. HPSMG pole pitch.

The next step in the HPSMG and FESM development was the design of stator topologies.

Open slots are not very common in the stators of BLDC machines as their shape amplifies the cogging torque [32]. Neither are round-bottomed stator slots, which are mostly used in asynchronous machines, very common. Mostly square form slots are used in BLDC machines, which increases the cross-sectional area of the slot opening and allows inhibiting temperature rise, which is important in machines with high energy density like HPSMG and FESM [32]. On the other hand, cogging torque is lower in a smaller slot opening [51]. One possibility is to use half-closed slots where teeth tips are placed above the slot. This structure decreases the diameter of the slot opening but the cross-sectional area of the slot remains almost the same [32]. Radial height of the tips h_{tip} is an important aspect in the choice of the slots and teeth, as saturation is generated in the tooth tip in case the value is too high, resulting in an effect of an open slot. This, in turn, increases the cogging torque. In practice, the value of h_{tip} is chosen to be of the same magnitude as the length of the tooth tip w_{tip} to minimize saturation. Additionally, respective radiuses are given for tooth tips from the slot side [32].

The considerations above were taken into account on planning the HPSMG and FESM stators. Thus, the stators of both machines were designed to be half-

closed. Widths of magnets and magnet poles of each machine were the basis of further calculations. Width of one magnet of HPSMG was 5.4 mm. The half-value of this, 2.7 mm was used as an approximate width of a tooth. Width of the whole magnet was used as a basis for preliminary dimensioning of the tooth head width. Both parameters were divided by a coefficient 0.9 to increase the total cross-sectional area and to decrease saturation, resulting values of width of tooth w_{th1} and widths of tooth tip w_{th2} were 3.0 mm and 6.0 mm, respectively (Fig. 2.8).

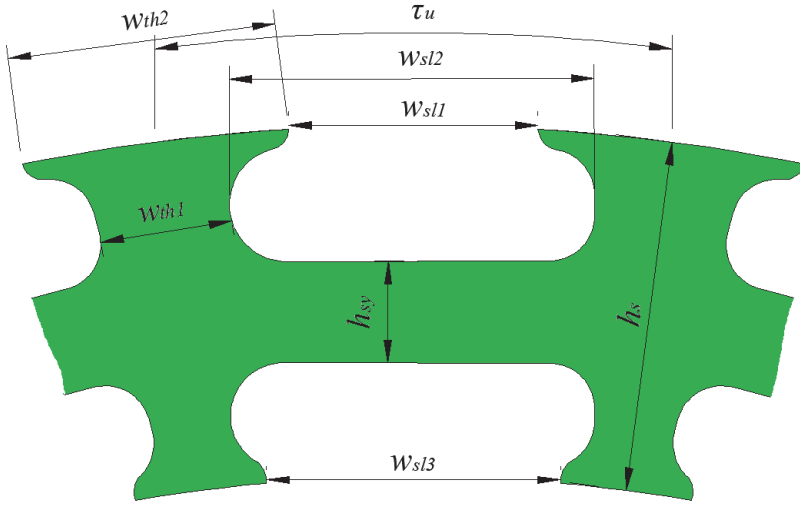


Fig. 2.8. HPSMG stator topology.

Width of slot opening w_{sl1} was found using the half-value of one pole (5.5 mm). Values of w_{th2} and w_{sl1} formed the slot pitch $\tau_u = 11.45$ mm of HPSMG, which was used to calculate the number of HPSMG slots $Q_s = 24$ (Eq. (2.14)):

$$Q_s = \frac{\pi D_s}{\tau_u} \quad (2.14)$$

Slot width on the outer perimeter was calculated to be $w_{sl2} = 8.0$ mm, which was found by the arithmetic subtraction of τ_u and w_{th1} .

As the structure of the HPSMG stator was designed considering Gramme's winding, similar calculations were performed for teeth located on the inner perimeter and for slot topology, using a similar slot width $w_{sl3} = 8.0$ mm. Smaller inner radius of the stator resulted in the smaller width of teeth and tooth heads. As in HPSMG, rotor magnets are placed only above the outer teeth layer, with the primary magnetic flux usually closing in this area. Thus, smaller width of teeth and tooth tips of the inner teeth layer is justified.

Regarding the stator yoke height, distribution of the resulting main magnetic flux was considered. Thus, the measure was chosen to be $h_{sy} = 2.25$ mm, which is smaller than the tooth height, but similar to the rotor yoke height h_{ry} . Depths

of slots h_{sl1} and h_{sl2} were designed proportionally to the tooth, the height of the yoke and the width of the slot, which resulted in the total height of the stator $h_s = 7.75$ mm and the inner diameter $D_{sin} = 72.0$ mm. Using this structure, the resulting ratio of the sum of average length of parallel slots of one winding coil w_{sl} and heights h_{sl1} and h_{sl2} was found at 1.3.

Similar calculations were performed for the structure of the FESM stator. To find the tooth width w_{th1} , half-value of one magnet width $w_{m0.5} = 5.0$ mm was used, and the width of the tooth head w_{th2} was calculated using the width of the whole magnet, which was divided by a coefficient 0.9. The results were $w_{th1} = 5.5$ mm and $w_{th2} = 11.1$ mm, and the number of slots $Q_s = 35.6$, i.e. 36 (Eq. (2.14)). The result of the integer Q_s gave the value of τ_u of 16.4. Dimensions w_{th2} were increased up to 11.5 mm, using the difference resulting from Q_s (Fig. 2.9).

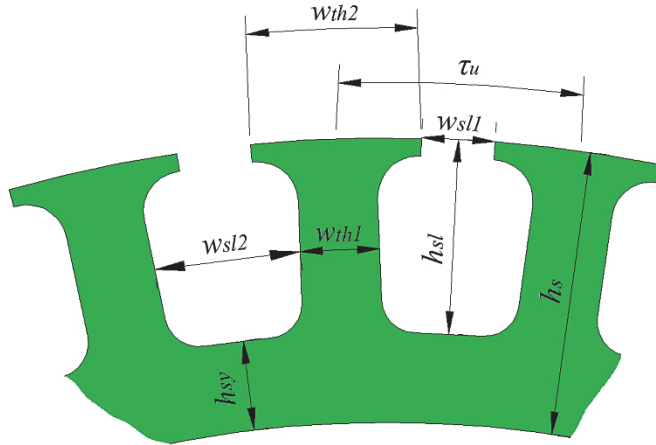


Fig. 2.9. FESM stator topology.

Ratio of the FESM slot opening to the width of the magnetic pole w_m is 0.5 like in HPSMG, which results in the w_{sl1} value of 5.0 mm. Width of the slot opening w_{sl2} was calculated likewise, using the mean value of 10.0 mm.

As different from the HPSMG winding structure where winding coils were designed to be located around the stator yoke, coils of the FESM winding were located on the teeth layer. Therefore, contrary to the calculation methods used for HPSMG, in the calculation of the depth of the FESM slot h_{sl} , its ratio to slot width w_{sl} was used, yet with the same ratio 1.3 of both parameters.

The design of the FESM stator yoke height h_{sy} was based on the values of tooth width w_{th1} and rotor yoke height h_{ry} like in the calculations made for HPSMG. To increase the mechanical strength, h_{sy} value was increased up to 6.0 mm, resulting in the stator height of $h_s = 19.0$ mm and the inner diameter of $D_{si} = 150$ mm.

The main dimensional data discussed and calculated in this section are summarized in Appendix 1.

2.6 Soft Magnetic Materials

Today, thin packets of ferromagnetic materials are mostly used for cores of the stator and in some cases also for rotor in electrical machines. They are typically classified into grain-oriented and non-grain-oriented electrical steels. Typically, grain-oriented steel is applied in a power transformer core. Non-grain-oriented steels are widely used in rotating electrical machines [52]. Most widely used of them is a so-called electrical steel, which contains 95-97% of iron and 1-3% of silicon [35]. On the one hand, the higher the silicon content, the higher is the resistance of the material, decreasing eddy current and hysteresis loss, on the other hand, decreases the magnetic permeance μ . Therefore, one solution would be to choose a material of lower silicon content and thickness, allowing minimizing iron losses due to its small cross-sectional area. Weaknesses of this solution are that it is expensive, the process is time-consuming and it requires special equipment.

In addition to problems related to iron losses, it is required to solve questions related to the maximum magnetic flux B_{max} value of the ferromagnetic material. In thin electrical steel of $h = 0.1-0.35$ mm, this value is 1.6-1.8 T [53]. If this limit is exceeded, its magnetic permeance decreases significantly, reaching approximately $B_{sat} = 2.1$ T, which becomes similar to the magnetic permeance of air [32]. Therefore, when planning the magnetic circuit of an electrical machine, reaching this level of penetrating magnetic flux should be avoided. Otherwise, major part of the magnetomotive force F_m of the magnets is spent on directing the magnetic flux with given B_{max} value through a saturated ferromagnetic substance, and thus the resulting magnetic flux decreases significantly [32]. Magnetic flux density higher than the operational point increases iron losses significantly.

Nowadays other alternatives are searched for electrical steels in use. In high-frequency applications, electrical steels can be replaced with amorphous materials, where the losses are considerably smaller. This is achieved due to the thin material structure with the thickness between 20-30 μm . Therefore, they can be well used for high frequency applications [52].

For the thin electrical steel (NO18), the saturation flux density B_{sat} is typically between 1.0-2.1 T [32], [54]. For example, B_{sat} value for the most effective material Metglas B_{sat} is only 1.56 T [55]. In case very high saturation flux density is needed, Permendur, an iron alloy with cobalt, can be used [52]. This material contains equal shares of iron and cobalt. Permendur 49 (Co49/Fe49/V2) has the highest saturation flux density $B_{sat} = 2.34$ T [56].

Fig. 2.10 shows magnetization waveforms of the abovementioned materials.

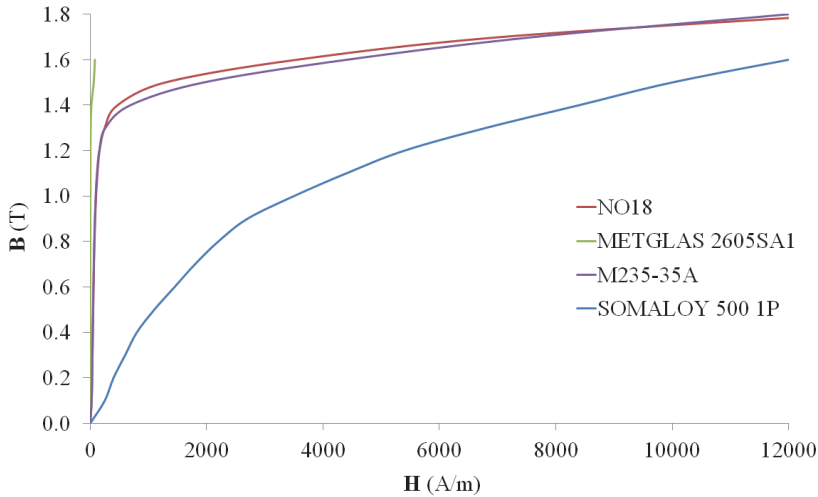


Fig. 2.10. Comparison of B - H curves of selected soft magnetic materials [54]-[57].

Additionally, specifications regarding losses of Permendur are almost as good as those of Metglas. In spite of its very good soft magnetic properties, high cost of Permendur as well as Metglas is a problem. For example, Permendur $V2$ costs approximately a hundred times more than low carbon iron [52]. Additionally, processing of such materials is rather complicated as both of the materials are very thin for making a stator sheet. Common punching and laser cutting are probably not suitable methods. Additionally, these materials are brittle. Another problem is forming packages of sheets as a necessary amount of sheets to be fixed is significantly larger as compared to usual electric steel laminates.

During the last decades, iron-based materials, e.g. Soft Magnetic Composites (SMC) or Somaloy covered with an ultra thin isolation layer, are increasingly used in electrical machines. To make magnetic parts for electrical machines (e.g. stator), the powder is placed into a mould where it is sintered using high temperature so that the powder material becomes monolithic [57]. SMC-materials allow 3-dimensional shaping of the components as the material has spatially isotropic magnetic and thermal properties [52]. At frequencies below a few hundred Hertz, the losses in SMC-materials are typically higher than in laminated structures. Fig. 2.11 shows that at frequencies up to 900 Hz, iron losses of the rest of the materials are lower than in Somaloy 500.

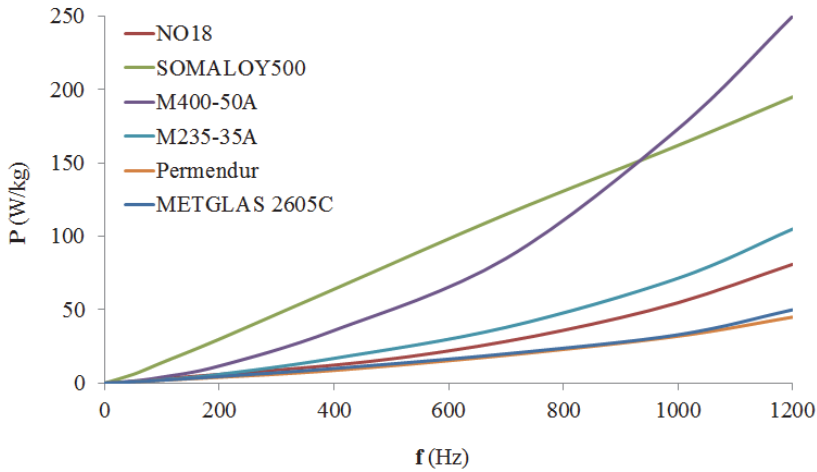


Fig. 2.11. Power loss comparison of some soft magnetic materials $B = 1.5 \text{ T}$ [54]-[57].

At 50 Hz frequency, the power loss P_{loss} in SMC-materials is typically 15 W/kg at the magnetic flux density of 1.5 T whereas in M600-50A electrical steel, it is 5.2 W/kg and in M1000-100A material, it is about 8.9 W/kg [52], [54]. Reducing iron losses is one of the main purposes in electrical machines like HPSMG and FESM that have multiple pole pairs and thus operate at high frequencies. Higher losses in the stator yoke or the rotor yoke cause a significant decrease in the efficiency of such machines. As a large part of energy spreads out as heat and current densities of both machines are significantly higher, more problems occur with cooling of these machines. Regarding Somaloy, the situation is more critical because of twice lower heat conduction compared to the typical values of non-grain-oriented electrical steels [52].

2.6.1 Analysis of HPSMG stator material

Based on the analysis in Section 2.6, an optimal material for constructing stators for HPSMG and FESM is electrical steel with the cross-sectional area as thin as possible. Calculation of the thickness of the stator sheet was limited by complicated mechanical processing and possibilities, also availability and cost of the material. Considering dimensions and electromagnetic parameters, the HPSMG stator was constructed of non-grain-oriented electrical steel sheets NO18 with a thickness of 0.18 mm. As the number of HPSMG pole pairs is $p = 10$ and the main rotational speed is in the range of $n = 3000\text{-}4000$ rpm, up to 5000 rpm at takeoff, high remagnetizing frequencies $f = 500\text{-}833.33$ Hz were obtained from these values.

Comparison of NO18 power losses to those of other materials presented in Fig. 2.11 reveals that only ultra thin amorphous materials Permendur and Metglas are superior to NO18 by their properties starting from frequencies $f = 400$ Hz. Thus, usage of material NO18 was justified.

In no-load situation, magnetic circuit is formed only because of the magnetic flux Φ_m coming from the pole of the electrical machine. This is divided into two in the stator yoke after passing through the layer of teeth. Preliminary simplified calculations for estimating the density of the magnetic flux in the HPSMG stator yoke and tooth layer were performed based on this pattern. Theoretical value for the air gap $B_g = 0.85$ T was used as a reference to find these values (Section 2.5) [46]. Density of the magnetic flux in the stator yoke B_{sy} was calculated using an empirical equation (2.15) [42]:

$$B_{sy} = B_g \cdot \frac{Z_e(w_{th2} + 2l_g)}{4h_{sy} \cdot p}, \quad (2.15)$$

where Z_e is the number of elementary slots.

Preliminary result was $B_{sy} = 1.5$ T. Using a similar simplified method, apparent maximum value of the magnetic flux in the tooth $B_{th} = 2.3$ T (Eq. (2.16)) was calculated:

$$B_{th} = B_g \cdot \frac{Z_e(w_{th2} + 2l_g)}{2w_{th1} \cdot p}. \quad (2.16)$$

Values obtained with Eqs. (2.15) and (2.16) are approximate and allow preliminary estimation of possible densities of the magnetic flux. To obtain real results, more detailed analysis of the magnetic circuit should be performed. This is described in Chapter 3.

In everyday practice, calculated B_{sy} values conform to the limits adjusted to the stators of PMSM machines [46]. A tendency for saturation is noticeable in the calculated results of B_{th} . Yet the result does not exceed significantly the maximum value of the magnetic flux density level for DC-machines [46]. In real operating situation where the temperature of permanent magnets is significantly higher, magnetic flux density decreases also in the stator and teeth layer. If the machine is loaded, the secondary field of stator windings causes armature reaction, which in turn, induces demagnetizing and decrease of the resulting magnetic flux.

Mean density of the magnetic flux $B_{sy} = 1.8$ T was found by interpolating B_{sy} and B_{th} values; this allowed evaluating presumed mass-based iron losses in the HPSMG stator at maximum and minimum operating frequencies $f = 500$ and 833.33 Hz, depending on the material's specific losses P_{loss} .

Fig. 2.12 shows NO18 P_{loss} at the minimum and maximum value of the frequency range mentioned above, specific loss of the material was found to be $P_{loss} = 55$ W/kg ($f = 500$ Hz) and $P_{loss} = 106$ W/kg ($f = 833.33$ Hz).

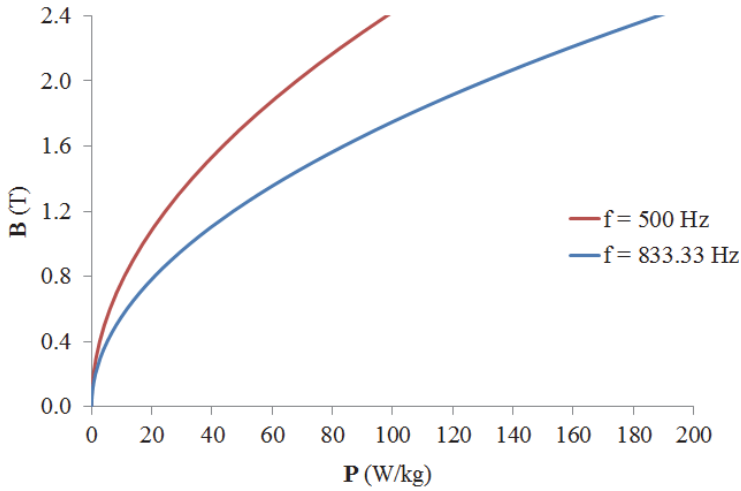


Fig. 2.12. NO18 power losses at $f = 500$ and 833.33 Hz [54], [58].

Volume of the HPSMG stator was found to be $V_{sy} = 18764 \text{ mm}^3$, which allowed finding calculated mass of its stator core $m_{sy} = 0.145$ kg. Based on the material density $\rho = 7650 \text{ g/mm}^3$ given by the manufacturer of the material [54], approximate iron losses of the stator were estimated at $P_{Fe} = 8.0$ W ($f = 500$ Hz) and $P_{Fe} = 15.0$ W ($f = 833.33$ Hz), which form respectively 0.9% and 1.7%, compared to the HPSMG electrical nominal power $P_l = 0.9$ kW (Table 2.2).

Fig. 2.13 shows specifications of sheet steel NO18 B - H at the frequencies of $f = 400$, 1000 and 2500 Hz [54], which was used as the HPSMG stator material.

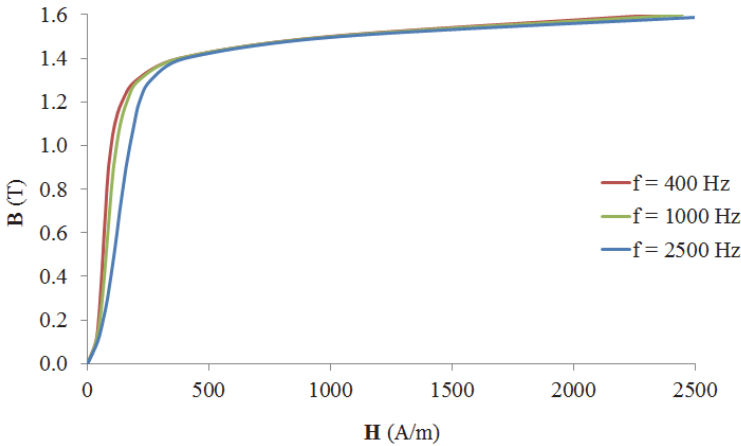


Fig. 2.13. NO18 B - H curve with $f = 400$ and 1000 Hz [54].

The figure shows that differences between the three magnetization curves at different frequencies are minimal. This is important in HPSMG, which operates at a frequency higher than usual.

2.6.2 Analysis of FESM stator material

Parameters of the FESM stator material were evaluated by the same methods as for HPSMG. In similar way the following material parameters were considered as most important: thickness, availability, price, work consumption and cost, and ease of processing (Section 2.6). According to these requirements, electrical sheet steel NO20 was selected. Compared to NO18, specific losses P_{loss} were slightly higher at frequencies over 500 Hz (Fig. 2.14).

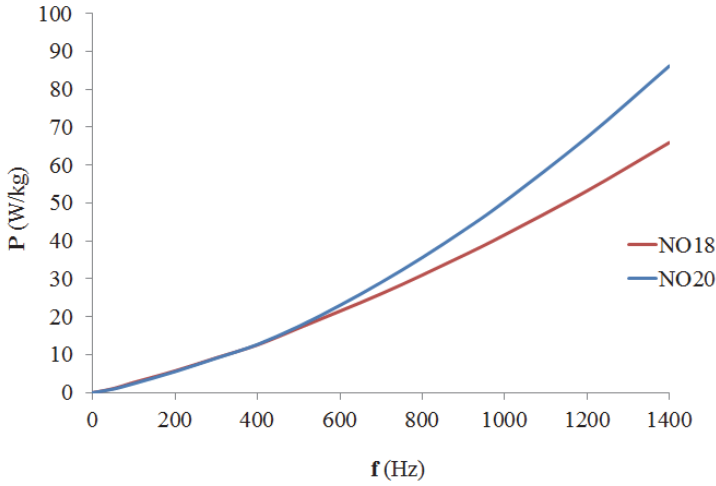


Fig. 2.14. Power loss comparison of NO18 and NO20 electrical steels [53], [54], [58].

FESM has been designed to operate at rotational speeds in the range of $n = 2000$ - 3000 rpm. Fig. 2.15 shows P_{loss} of NO20 material according to the frequencies corresponding to the rotational speeds mentioned above, i.e. $f = 700$ and 1050 Hz.

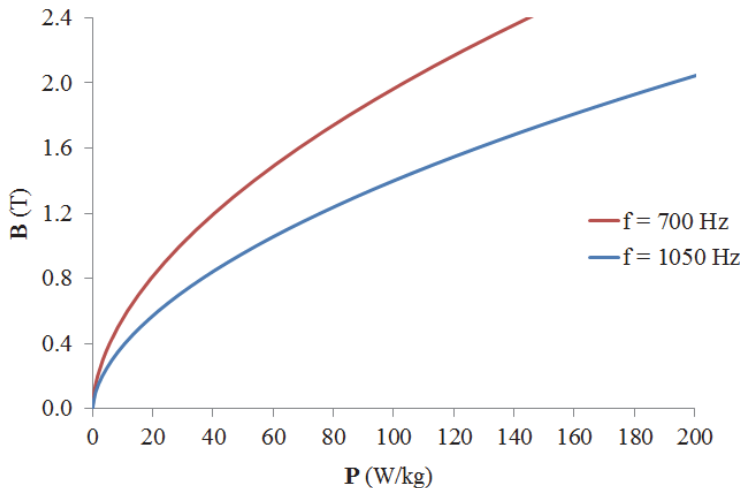


Fig. 2.15. NO20 power losses at $f = 700$ and 1050 Hz [53], [58].

In preliminary calculations of magnetic flux densities of the FESM stator yoke and the tooth layer, the same empirical and simplified methods were used as in HPSMG [42]. The results were $B_{sy} = 0.8$ T and $B_{th} = 1.7$ T (Eqs. (2.15) and (2.16)), on interpolating, an average magnetic flux density of $B_s = 1.3$ T was obtained. Accordingly, presumed iron losses of the FESM stator by mass were evaluated at minimum and maximum operating frequency $f = 700$ and 1050 Hz of FESM.

Fig. 2.15 shows P_{loss} of NO20 at the minimum and maximum value of the frequency range described above, from which, depending on the materials' frequencies, specific losses $P_{loss} = 47$ W/kg ($f = 700$ Hz) and $P_{loss} = 87$ W/kg ($f = 1050$ Hz) were calculated [53], [58].

Volume of the FESM stator was calculated at $V_{sy} = 235870$ mm³, and the calculated mass of its stator core $m_{sy} = 1.804$ kg was found. Based on the material density $\rho = 7650$ g/mm³ given by the manufacturer of the material [53], approximate iron losses of the stator were estimated at $P_{Fe} = 85$ W ($f = 700$ Hz) and $P_{Fe} = 157.0$ W ($f = 1050$ Hz), which form respectively 0.7% and 1.2%, compared to the FESM electrical nominal power $P_l = 13.0$ kW (Table 3.3). The values were compared to those of HPSMG, iron losses in the FESM stator proved to be proportionally smaller regardless of a thicker material.

Fig. 2.16 shows specifications of sheet NO20 B - H at frequencies of $f = 400$, 1000 and 2500 Hz, which was used as the FESM stator material.

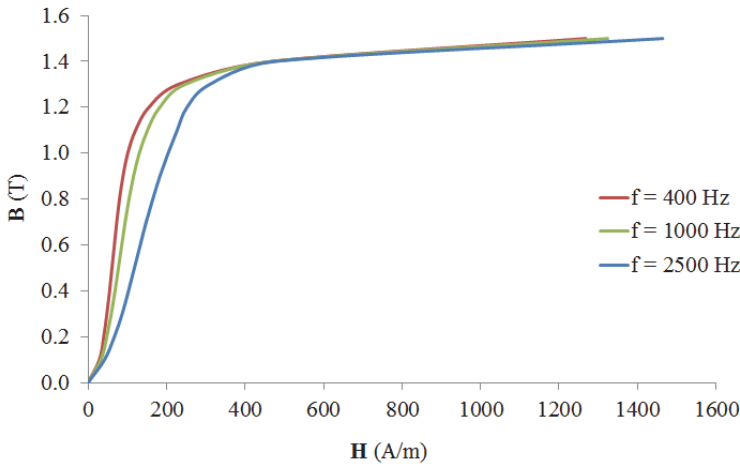


Fig. 2.16. NO20 B - H curve with $f = 400$, 1000 and 2500 Hz [53].

In FESM, the most important operating frequency is $f = 1000$ Hz. Comparing its parameters to those obtained at significantly lower frequency ($f = 400$ Hz), the differences appear to be marginal.

2.7 Permanent Magnets

Good magnetic properties of lodestone or magnetite Fe_3O_4 were known already around 3000 BC [52]. Some references suggest that good permanent-magnet steel was available from China as early as 500 A.D. Permanent-magnet steels progressed to alloyed cobalt steels with carbon content by 1920 [59].

An important milestone in the research field of magnetism was set in 1600 when William Gilbert published his book "*De Magnete*", which was the first systematic study related to the phenomenon of magnetism. The artificial permanent magnets discussed in "*De Magnete*" were made of sword steel and were used to lift iron parts. According to the present standards, the carbon steel used those days was an extremely poor permanent magnet material, offering a low coercivity, $H_c < 4$ kA/m, and a low energy product, $BH_{max} < 2$ kJ/m³. This remained the quality level of artificial permanent magnets until about 1880 when a systematic study on alloy properties started. The addition of tungsten and chromium was shown to raise H_c to some degree. An important discovery was the use of cobalt as an additional material and in 1917, K. Honda achieved the ultimate properties of steel magnets by adding 35% of cobalt to the alloy. The maximum energy product of this steel magnet was 8 kJ/m³ and its coercivity was 20 kA/m [52].

In 1931, T. Mishima patented the first hard magnetic alloy based on aluminum, nickel and iron. This was the start of the development of the permanent magnet family known as AlNiCo. Due to the remarkably improved magnet properties, the AlNiCo magnets were then made useful for many electrical engineering applications. Supported by a better understanding of material physics, further development of the artificial permanent magnet materials has been rapid since the 1940s. In the 1950s, another permanent magnet family, known as ferrites, became commercially available. Because of their better material properties and much lower material costs, the ferrites became extremely popular for DC electric motor applications used in automobiles, hand tools, etc. [52].

The development of rare earth permanent magnet materials started in the 1960s with the Samarium-Cobalt alloys. The material properties of SmCo_5 and $\text{Sm}_2\text{Co}_{17}$ make these permanent magnet materials very suitable for use in electrical motors and generators, but they are expensive due to the rare raw material Cobalt. An important addition to permanent magnet materials was made in 1983, when the high performance Neodymium-Iron-Boron (Nd-Fe-B) permanent magnet material was introduced. Nd-Fe-B magnets contain Neodymium approximately 31% of their mass [60]. Compared to Sm-Co permanent magnets, Nd-Fe-B magnets offer compatible material properties but are essentially cheaper [52]. Developmental stages of permanent magnets are shown in Fig. 2.17.

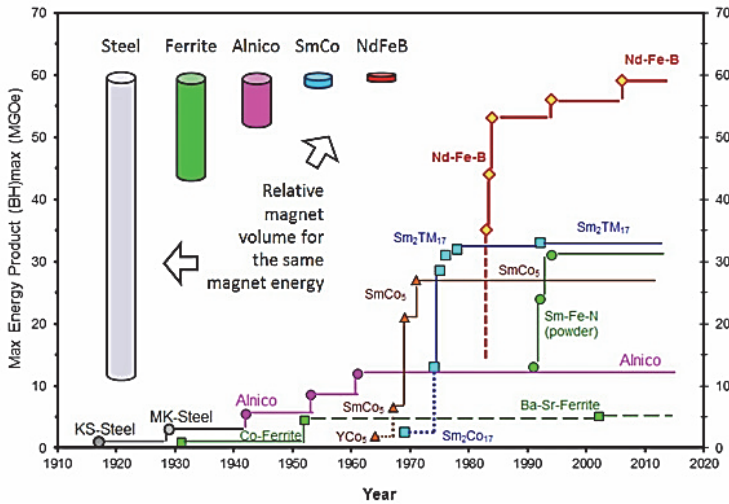


Fig. 2.17. History of permanent magnet materials [61].

In spite of very good magnetic properties of Nd-Fe-B magnets, they have certain weaknesses. First, they have low temperature tolerance and low operating temperature of 150 °C. This is caused by strong dependence of the magnetic properties on their temperature, and if the temperature rises, residual magnetic flux density B_r and intrinsic coercivity H_{ci} are sharply reduced. Temperature tolerance can be increased, substituting neodymium partly with dysprosium and iron with cobalt, but these materials also have anti-ferromagnetic coupling, which weakens the magnetic properties [52]. Table 2.3 compares the temperature of Nd-Fe-B magnets to that of other common types of permanent magnets.

Table 2.3. Temperature ranges of mainly used permanent magnet materials [61]

Properties	PM magnet type				
	AlNiCo ₅	Ferrite	Nd-Fe-B	SmCo ₅	Sm ₂ Co ₁₇
Max. service temp. (°C)	540	300	150	300	300-550
Curie temp. (°C)	850	460	310	700	820-950

The table shows that the temperature values of Nd-Fe-B are significantly lower than those of other materials.

Secondly, an important weakness of neodymium magnets is susceptibility to corrosion, which significantly lowers the value of H_{ci} and weakens magnetic properties due to the changes on the surface of the magnet. Additionally, in a moist environment, hydrogen reacts with neodymium and thus, initial structure of the material is reduced; it becomes porous and magnetic properties disappear. To avoid this, Nd-Fe-B magnets are covered with an ultra thin protective layer with a thickness of 15-80 μm . Usually nickel, chromium, aluminum, zinc, tin, silver, gold, also multi-components, such as Ni-Cr or Ni-Cu, are used [62].

Thirdly, Nd-Fe-B material is brittle, especially in the process where the stator and the rotor are interconnected. The easiest solution to the problem is usage of jigs. Additionally, combined magnets are used where the powder of Nd-Fe-B is mixed with a resin or a polymer and then press molding in a vertical or in a lateral magnetic field is performed, followed by sintering at high temperature [63]. In Nd-Fe-B magnets, B_r is usually twice as low ($B_r = 0.5-0.7$ T) and maximum energy density approximately four to five times lower ($BH_{\max} = 40-90$ kJ/m³) than in non-combined neodymium magnets [52]. However, their level of energy density remains significantly higher than in the types of permanent magnets. In addition to temperature ranges, Fig. 2.18 compares energy densities of main permanent magnet materials.

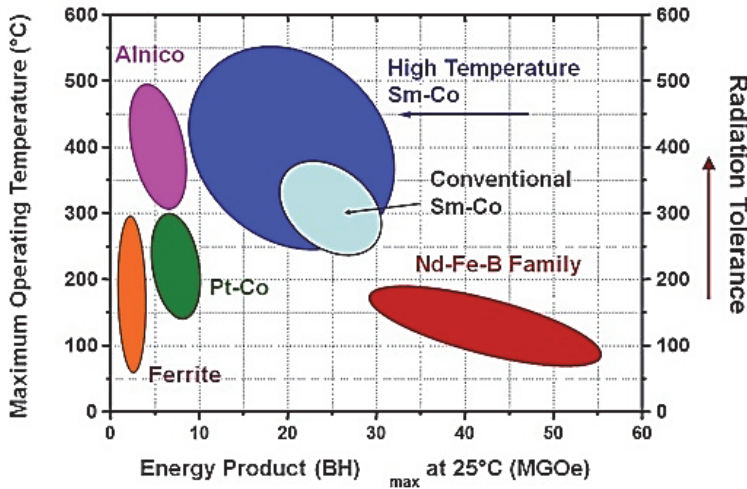


Fig. 2.18. Operating temperatures of different permanent magnets [61].

The figure shows that the level of energy density of Nd-Fe-B magnets is twice as high as that of SmCo magnets.

2.7.1 HPSMG and FESM permanent magnets

As high power density and torque density are essential in HPSMG and FESM, considering their small volume and mass, it was extremely important to achieve high energy density of permanent magnets. This is supported by the results in practice, which show that at the same volume, almost twice as high power can be reached, and almost 20% smaller volume can be reached at the same power with neodymium magnets compared to ferrite magnets [63]. Considering many advantages and weaknesses, Nd-Fe-B magnets were designed to be used in both of the machines.

In both machines, length of magnets l_m based on the axial diameters of the rotor and the stator L_{stk} , L_{sy} , radial widths w_m were also calculated (Sections 2.4 and 2.5). Magnet height h_m was found based on the following rule used in practice: height of the magnet is at least $h_m = 5 \cdot l_g$ [42]. As a result, preliminary

result of h_m in HPSMG was 2.5 mm and in FESM the value was 3.0 mm. Final measurements defined available magnets, the parameters of which in HPSMG were $l_m = 20$ mm, $w_m = 5.4$ mm, $h_m = 2.2$ mm and the parameters in FESM were $l_m = 40$ mm, $w_m = 10$ mm, $h_m = 4$ mm.

High energy density causes more intense heating processes in machines. Thus, the magnets were chosen to have as high operating temperature as possible, which was 180 °C in HPSMG and 150 °C in FESM. In Figs. 2.19 and 2.20, B-H characteristics of both machines at different temperatures are shown.

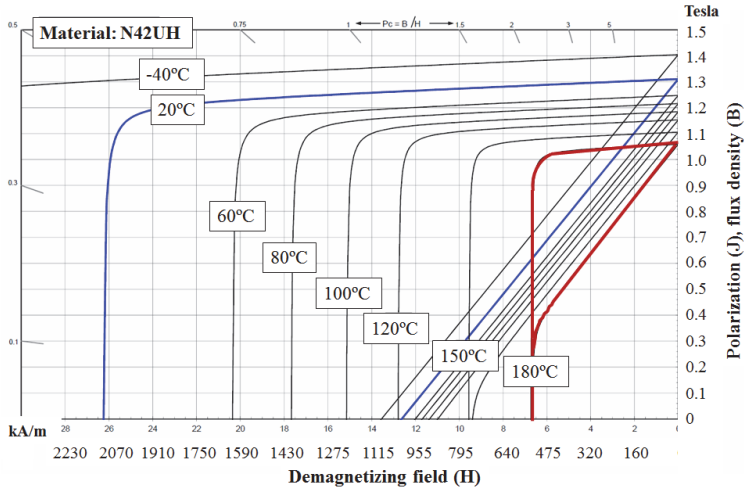


Fig. 2.19. B-H characteristics of permanent magnets used in HPSMG [64].

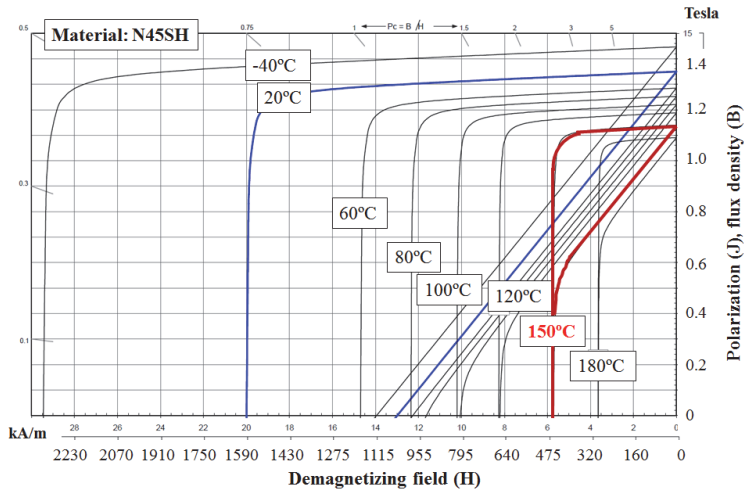


Fig. 2.20. B-H characteristics of permanent magnets used in FESM [64].

2.8 Windings

Electromagnetic and thermal values of toroidal winding or Gramme's winding of HPSMG were compared to more common windings. In this case, HPSMG was compared to FESM where a concentrated winding is used. HPSMG version with the concentrated winding has been modelled with the same winding geometry as FESM.

All windings are similar in one aspect: the end-windings are connected in delta connection in the motor mode.

As a main difference with FESM, HPSMG operates also as a generator in a hybrid propulsion system, therefore, the end-windings in this mode are connected in star connection.

2.8.1 HPSMG Gramme or toroidal winding

In a HPSMG winding, the coils are placed in the inner and outer slots. The advantage is that it has very short end connections as compared to the overlap winding of conventional machines. One of the main reasons to implement it was the better filling factor to mount more active conductors into a single slot as compared to the common winding style, which winds the conductors around the stator teeth.

Such winding also weakens the armature reaction and provides a slightly stiffer load characteristic of HPSMG in a generator mode. Table 2.4 shows the calculated parameters on the basis of the applied winding scheme.

Table 2.4. HPSMG winding parameters [23]

No.	Name	Values
1	Slots per pole and phase (q)	0.4
2	Winding pitch (τ_u)	1.2
3	Electrical offset angle (α)	150
4	Winding conductors per slot (N)	66
5	Stacking factor (k_{stk})	0.95

Based on these results, the vector diagram of phase electromotive forces (EMF) and the winding scheme were compiled (Figs. 2.21 and 2.22).

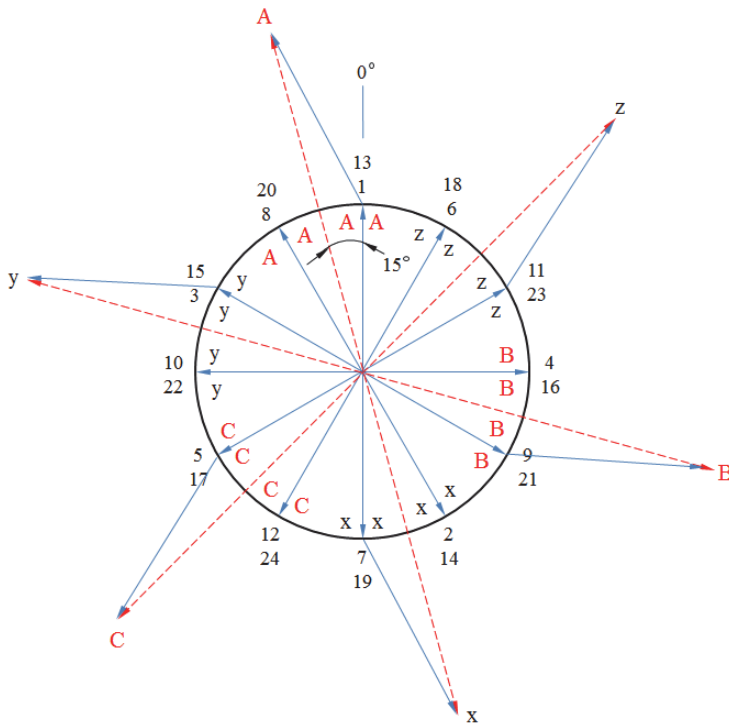


Fig. 2.21. HPSMG EMF vector diagram [23].

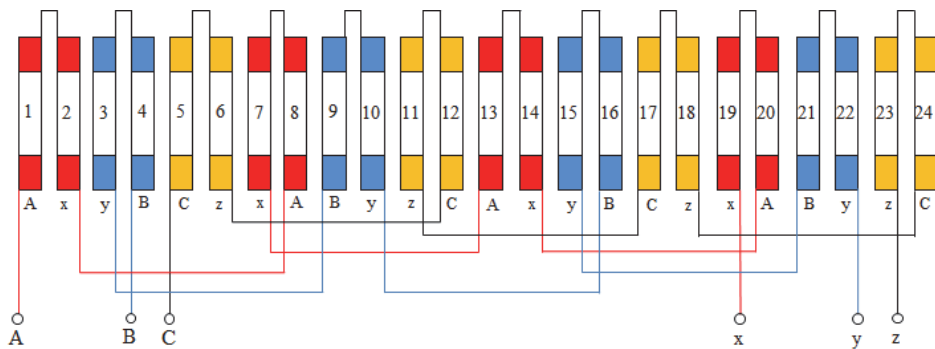


Fig. 2.22. Scheme of HPSMGs Gramme's winding [23].

Each phase winding consists of 8 coils connected in series. For example, the phase A winding has coils 1, 2, 8, 7, 13, 14, 20, 19 connected to each other. The same principle has been established with the rest of phase windings. Endings of the phase windings were connected to a star, in order to eliminate the EMF third harmonic.

A double-insulated winding wire with the temperature index of 212 °C and cross-sectional area of 0.1 mm² and resistance $R_{\text{con}} = 173 \Omega/\text{km}$ was used for the winding [65]. Coils were wound with the 12-wire stranded conductor, which

provided the total cross-sectional area of 1.2 mm². The following step was to find the maximum allowable current density to this cross-sectional area, taking into account that HPSMG operates in intensive cooling conditions.

Conventional electric machines operating in a continuous duty cycle are permitted to use current densities in the range of 4...6 A/mm². In practice, if the current density is higher than 15 A/mm², it should be cooled down with intense forced convection rather than natural cooling. This may be done, for example, with an impeller, a liquid, a gel or any other means of cooling. For HPSMG, mechanically machined rotor plate openings are used for cooling the coils and the magnets. The openings are operating as an impeller ensuring the intensive cooling during the rotation of the machine, at the same time being a simple and reliable solution.

Table 2.5 shows the interdependencies between the temperature classes of the wire insulation and the corresponding values of current densities.

Table 2.5. Copper wire insulation rating and corresponding current densities [66]

No.	Insulation Rating (°C)	Current Density (A/mm ²)
1	240	25.1
2	200	24.1
3	180	23.7
4	155	23.1
5	130	22.5
6	105	21.9

According to data in Table 2.5, the cross section of the winding wire can be loaded with the current nearly by 27 A. Taking into account the effect of demagnetization of permanent magnets at the high temperature, and considering the intensive cooling provided by the airplane propeller, the minimum current density value 21.9 A/mm² was taken. With the cross-section of 1.188 mm², the total current is 26.01 A.

The magnetic flux density in the air gap had the measured average value of 0.45 T. The estimated RMS value of the phase EMF at the nominal speed of 5500 rpm was 15.39 V. This result coincides with the HPSMG experimental value 15.46 V obtained during the open-circuit test (Section 5.3.1).

Taking into account the measured value of EMF and the rated current density 26.01 A, the estimated nominal electrical power of HPSMG was calculated 1.2 kVA.

2.8.2 FESM concentrated winding

In FESM, the usual two-layered concentrated winding was used. Fig. 2.23 shows the corresponding winding scheme.

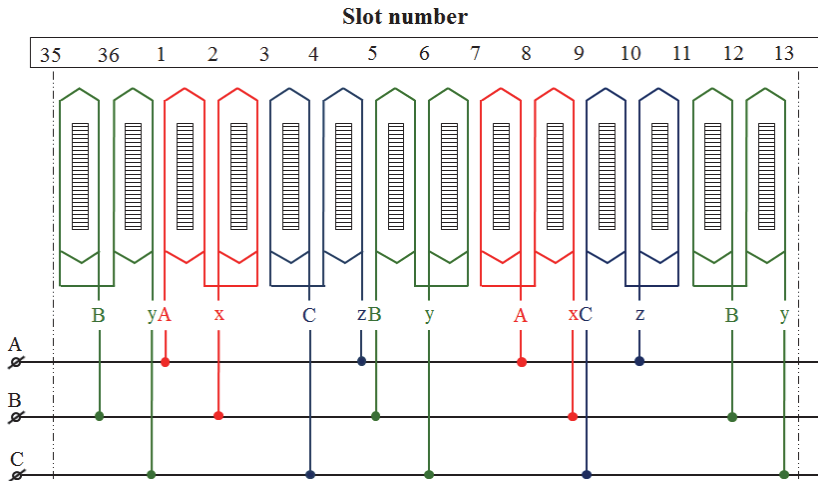


Fig. 2.23. Scheme of FESM concentrated winding [49].

Used electrical offset angle α between the two slots is 210 electrical degrees ($> 180^\circ$), which shows use of extended pitch in the winding. In Fig. 2.24, vector diagram of the EMF of FESM is shown.

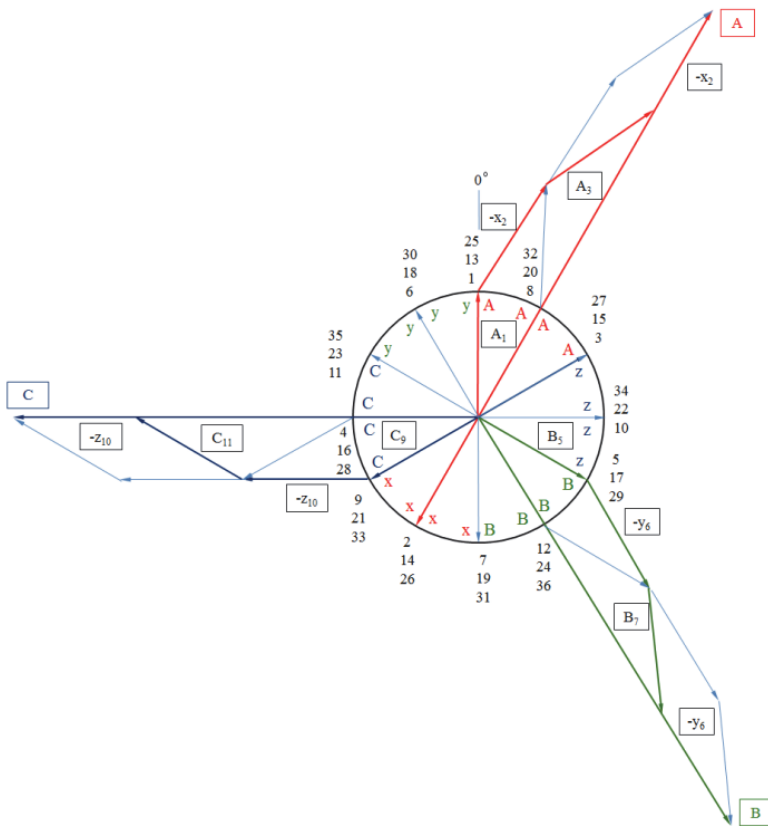


Fig. 2.24. FESM EMF vector diagram [49].

Overlap of electromotive forces of phases is visible in the vector diagram. Thus, the winding is also an overlapped winding.

With 36 slots and 3 phases, a typical arrangement would be 12 coils per phase, a total of 36 coils, i.e., 72 coil sides, which is termed a 2-layer winding. The throw or span of each coil is 1 slot-pitch, i.e., each coil is wound over one tooth. Even greater flux linkage can be achieved with a greater throw, but then the bulk of the end-windings would be greater, which would produce losses but no torque.

Number of slots for a pole and a phase can be calculated as follows:

$$Q_s = \frac{Z_e}{2pm}, \quad (2.17)$$

where Z_e is the number of elementary slots, $2p$ is the number of poles and m is the number of phases in the winding.

In the FESM winding, the result is $Q_s = 2/7$, i.e. two winding sections for seven phase zones. This means that the winding is a solenoidal or a concentrated fractional slot winding. Windings of each phase are isolated from each other and concentrated around individual teeth or salient poles.

The winding pitch per pole is found as follows:

$$\tau_u = mq \quad (2.18)$$

The result is 6/7.

Coil groups in the FESM winding are in parallel connection and the end-windings are in delta connection to reduce current values in windings (Fig. 2.25).

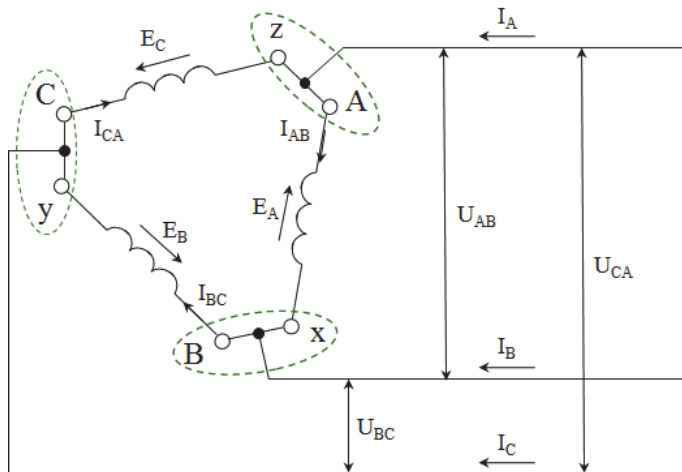


Figure 2.25. Scheme of FESM winding connected in delta connection.

Most BLDC machines used in industry are wye-connected because of their higher energy-power efficiency compared to delta-connected machines. However, the delta-connected type is more often used on small UAVs, allowing higher top speeds [67]. A weakness of delta connection is the generation of the third harmonics of EMF, which would be eliminated in star connection. This problem is of importance mostly in generators connected to a grid. However, this is not decisive in a motor with an autonomous power source.

The basic flux per pole Φ_m was calculated:

$$\begin{aligned}\Phi_1 &= B_r d A_m, \\ S_m &= \beta_m \cdot L_{stk},\end{aligned}\tag{2.19}$$

where B_r is the remanent flux density of the magnets, which is 1.32 T and A_m the area of a magnet on a rotor side [42].

The calculation results were $\Phi_1 = 0.70$ mWb, which allows determination of the electromotive force of one phase of a motor in delta connection:

$$E_1 = 4.44 f_1 \Phi_1 N_1 k_1,\tag{2.20}$$

where f_1 is maximum operating frequency 1050 Hz and k_1 is the winding factor, the maximum value of which is 0.933 by calculation, N_1 is the preliminary number of coils in series connection per two coils, i.e. 14 turns altogether.

As phase voltage is equal to line voltage in delta connection, the line EMF is also $U_l = 42.6$ V_{AC}.

The number of coils was defined based on the nominal voltage of the provided 14 cell lithium-ion polymer battery, which in total is $U_{sup} = 51.8$ V_{DC}. To obtain this voltage value, it is required to increase the turn per coil pair N_{cp} :

$$N_{cp} = \frac{N_1 \cdot U_{sup}}{E_1}\tag{2.21}$$

As a result, the number of turns was $N_{cp} = 17$ or 8.5 per coil. In practice, 8 turns are wound on one coil pair and 9 on the other.

To estimate the wire size, the slot area was calculated $A_{sl} = 106.34$ mm² (Section 2.5).

In total, each slot contains 18 conductors. Based on practical knowledge, it can be assumed that copper occupies not more than 40% of the slot area in each slot [42]. Thus, the slot fill factor k_{sl} can be considered 0.4. The copper cross-sectional area of one conductor is:

$$A_{con} = \frac{k_{sl} \cdot A_{sl}}{N_{cp}}\tag{2.22}$$

The result is $A_{con} = 2.5$ mm², i.e., the maximum diameter of one conductor is $D_{con} = 1.78$ mm.

According to the basic parameters, the electrical input power of the propulsion system is estimated at $P_l = 12.95$ kW. Taking into account the efficiency of the inverter $\eta = 0.95$, the supply active power of the motor can be calculated $P_{el} = 12.3$ kW. As the power factor of the inverter is $\cos \varphi = 0.95$, the calculated apparent power in the inverter output is $S = 12.95$ kVA. The apparent power of the phase S_{ph} then is 4.32 kVA. From this value, an estimated current value in the phase winding can be derived; $i_{ph} = 83.34$ A if voltage is 51.8 V. The number of slots of the machine studied was chosen to be 36. Thus, according to winding scheme 6, the parallel-connected groups of coils used consist of two series-connected windings. By the number of coil groups, estimated current can be determined in each coil group as the value of I_{ph} is distributed between them at parallel connection. Higher number of coil groups results in lower values of phase current and therefore, lower current densities per one coil group. This enables calculation of the current amplitude value per coil pair and the winding conductor:

$$i_{con} = \frac{i_{ph}}{m \cdot n_{cp}}, \quad (2.23)$$

where m is the number of winding phases and n_{cp} is the number of coil pairs.

The resulting value $i_{con} = 13.9$ A is an amplitude value, thus with a 120° square waveform of the rms current I_{rms} is:

$$I_{rms} = \sqrt{\frac{2}{3}} \cdot i_{con}, \quad (2.24)$$

the result of which is $I_{rms} = 11.3$ A.

Conventional fan-cooled electric machines operating in a continuous duty cycle are permitted to use current densities in the range of $J = 5.0\text{-}10.0$ A/mm² [32].

In this case, an increasing number of slots is an option, such that the desired current density does not exceed the abovementioned range. Increasing the number of coil pairs up to, e.g. 7, the result in the same winding scheme is 42 slots. Thus, the value of I_{rms} would decrease to 9.72 A and the filling factor of slots would improve. Increasing the number of slots, on the contrary, would decrease slot areas at the same diameter of the stator, which, in turn, would make the winding more complicated.

In the studied motor, the propeller and mechanically machined openings in the rotor plate are used to provide intensive cooling. The openings are operating as an impeller, at the same time, providing a simple and reliable solution.

Considering intensive cooling during the flight, the temperature class of the winding wire insulation and the effect of demagnetization of permanent magnets at high temperatures, the maximum current density $J = 10.0$ A/mm² was determined.

At a given J , the cross-sectional area of the conductor is $A_{con} = 1.0$ mm²,

which gives the conductor diameter of 1.13 mm. To construct a winding, the diameter of the conductor was increased to 1.2 mm, which is still flexible by its mechanical properties and allows obtaining the expected value of current density $J = 10.0 \text{ A/mm}^2$ at the winding conductor current of 11.3 A.

2.9 Conclusion

Chapter 2 provided an overview of the designing process of HPSMG and FESM. First, rotor topology of the machines was determined. According to the results of the analysis based on secondary data, the configuration of the exterior rotor proved to be optimal. As compared to the interior rotor, higher mechanical torque can be achieved.

In the next step, stator geometry was designed, using similar basic principles and calculation methods for both of the machines. However, as toroidal winding or Gramme's winding is used in HPSMG, vertical halving of the slot is required, bringing the stator yoke in the central part of it.

This chapter also presents an overview and theoretical analysis of the properties of soft and hard ferromagnetic materials. Materials for the stator and permanent magnets used in the machines were chosen based on this analysis. First, thin non-grain-oriented electrotechnical steels NO18 and NO20 were found as optimal solutions according to their electromagnetic properties, availability, processability and cost. As a result, iron losses were significantly lower at high operating frequencies characteristic of both machines.

Out of permanent magnet materials, NdFeB magnets of the highest energy density were chosen, while maximum operating temperature values were at least $150 \text{ }^\circ\text{C}$ (even $180 \text{ }^\circ\text{C}$ in HPSMG).

In the last part of the chapter, focus is on designing the winding geometry and calculations based on electrical parameters. Similarly, the configuration of series-connected double winding coils was used in concentrated phase windings of both machines. Pole pairs were series-connected in HPSMG, but parallel-connected in FESM. Both windings were connected in delta connections in a motor mode.

HPSMG and FESM windings differ by their physical location of winding coils on the stator. In FESM, a usual two-layered winding was used where coils are located around the tooth layer. In HPSMG, however, the winding coils were turned by 90° and placed around the stator yoke, forming an inversed concentrated winding or Gramme's winding.

A reason for such configuration in HPSMG was a narrower geometry of the stator from the front view, also a higher possible number of turns in horizontal winding coils and higher slot filling factor in a one-layered winding.

3 ELECTROMAGNETIC DESIGN

3.1 Possibilities of PM Machine Description and Analysis

Technical specifications and operational characteristics of a permanent rotor PM synchronous machine are mostly defined by the magnetic flux in the air gap between the rotor and the stator and its distribution in different parts of the magnetic circuit of the machine. Value and shape of the electromotive force induced in the stator winding are defined by the value and distribution and change of the magnetic flux density of the rotating rotor PM excitation field in the air gap. The magnetic field generated by the stator winding, in turn, causes distortions of the resulting magnetic field in the air gap and this affects also permanent magnets. These effects are present in the PM electrical machine in the motor mode as well as in the generator mode.

Distribution of the electromagnetic field of the PM synchronous machine is mathematically characterized by Maxwell equations, generally in 3D presentation. Dependence of the vector of the magnetic field strength H on the current density J of the stator winding is described by Maxwell's total current law [68]:

$$\nabla \times H = J \quad (3.1)$$

Maxwell's II law or electromagnetic induction law presents the dependence of the intensity of electric field E on the changing speed of magnetic flux density vector B as follows:

$$\nabla \times E = -\frac{\partial B}{\partial t} \quad (3.2)$$

- principle of continuity of magnetic flux:

$$\nabla \cdot B = 0, \quad (3.3)$$

- principle of continuity of electrical current:

$$\nabla \cdot J = 0 \quad (3.4)$$

- mathematical expressions uniting field values:

$$B = \mu_a \cdot H = \mu_r \mu_0 H \quad (3.5)$$

and

$$J = \sigma \cdot E, \quad (3.6)$$

where the following environmental properties affect distribution of the electromagnetic field:

μ_0 - magnetic permeance of the environment in vacuum,

μ_r - relative magnetic permeance of the environment compared to vacuum,
 σ - specific electric conductance of the environment.

To characterize the magnetic field of electrical machines, magnetic vector potential $A(r, \alpha, z)$ is used, through which the value of magnetic flux density can mathematically be expressed:

$$B(r, \alpha, z) = \nabla \times A(r, \alpha, z) \quad (3.7)$$

Laplace or Poisson equation describes the distribution of the magnetic vector potential according to the presence or absence of areas of different magnetic flux densities.

In a special case, if the magnetic flux is observed, e.g. in the area of an air gap where currents are absent, to characterize the distribution of the magnetic scalar potential of the magnetic field in a cylindrical or cross-coordinate system $U_m(r, \alpha, z)$ or $U_{ms}(x, y, z)$ can be used for the determination of the expression of which Laplace's differential equation can be used.

Magnetic scalar potential $U_m(r, \alpha, z)$ can be expressed as a solution of a differential equation, considering the geometrical shape, size and boundary conditions of the air gap of the PM electric machine observed. Then, using the magnetic scalar potential $U_m(r, \alpha, z)$, magnetic field strength H or distribution of the magnetic flux density B in the air gap can be determined:

$$B_r(r, \alpha, z) = -\mu_0 \text{grad } U_m(r, \alpha, z), \quad (3.8)$$

because

$$H = -\text{grad } U_m \quad (3.9)$$

and

$$B = \mu_0 H \quad (3.10)$$

To study and analyze the magnetic field of electrical machines, the vector potential $A(r, \alpha, z)$ method is commonly used. Analytical solution of the respective Laplace or Poisson differential equation is usually very complicated, mostly because of complex geometry, non-linearity and indefinite boundary conditions of the area observed. Thus, numerical methods of mathematical modelling in computers are used to solve differential equations based on Maxwell equations. Software packages have been developed based on the finite elements method. This method fails to give general solutions for the distribution of the field of the electrical machine observed, but can provide a special solution for the case under study.

Properties and technical specifications of all electric machines, including PM synchronous machines, are mostly defined by the permeance of the air gap. Thus, to characterize an electrical machine in general terms, it is sufficient to

determine the value of the magnetic flux of the air gap and its distribution between the different parts of the magnetic circuit. Equivalent circuit method of a unified magnetic circuit is frequently used for this primary approximate analysis. Equivalent circuits of magnetic circuit are compiled and analyzed similar to equivalent circuits of united parameters, using also similar solution methods with electrical circuits. In some cases, to obtain higher precision, analytical methods of non-linear circuits should be used to calculate non-linear magnetic permeance of ferromagnetic parts of the magnetic circuit.

In BLDC machines, like in other permanent magnet machines, primary magnetic flux Φ_m is obtained using permanent magnets of the rotor. Electromagnetic torque T_{em} arising in the stator changes proportionally to Φ_m and armature current i_a resulting from the load (Eq. (3.11)) [32].

$$T_{em} = \frac{E_a \cdot I_a}{\omega_m} = C_M \Phi_m \cdot I_a, \quad (3.11)$$

where E_a is electromotive force and I_a armature current, ω_m angular speed and C_M mechanical constant.

Although BLDC machines are synchronous by their nature, in many aspects, they are similar to DC machines. For example, on starting, they act like DC series motors but in their speed characteristics, they resemble shunt motors [26]. Thus, the rotor's rotational speed n in no-load conditions is proportional to E_a , but inversely proportional to Φ_m value (Eq. (3.12)) [3].

$$n = \frac{E_a}{C_E \Phi_m}, \quad (3.12)$$

where C_E is the constant of the electromotive force.

Based on Eqs. (3.13) and (3.14), in BLDC magnetic circuit design, first, the main magnetic flux Φ_m of the machine is calculated. It is also important to find optimal balance between the densities of the magnetic flux of chosen magnets and saturation levels of rotor's steel cores. The next step is to find the distribution of the primary magnetic flux in the air gap, as this also determines the shape of fundamental components of the electromotive force. Section 3.2 describes the structure of the magnetic circuit of HPSMG and FESM and the calculation methods.

Secondary magnetic field generated by the stator windings distorts the resulting distribution of the magnetic flux in the air gap and thus also sinusoidal shape of the electromotive force, decreasing the torque of the motor and the electromotive force of the generator. Thus, analysis of the effect of the armature reaction is important in the magnetic circuit design.

Secondary magnetic flux is generated by electromagnets or winding coils located on the stator, which altogether form a phase winding. Geometry of this determines also the properties of the secondary field. In BLDC motors, pairs of phase windings are switched periodically by using power electronics, by which

an inverse magnetic field independent of the main circuit is generated, which links to the primary magnetic flux generated by permanent magnets. The result is the magnetic field, which enables synchronous operation of the rotor. As constant magnetic excitation takes place in BLDC, it is possible to change the values of the resulting magnetic flux and thus also the speed and torque only by changing the voltage and current in the stator windings. Therefore, intense attention was paid to designing the structure of HPSMG and FESM windings and calculating electromagnetic parameters discussed in Section 2.8.

3.2 Analysis of the Primary Magnetic Field

Magnetomotive force F_m resulting from the magnetic poles of BLDC machine generates the magnetic flux Φ_m , which closes through different parts of the machine, forming a symmetrical magnetic circuit. Its parts are permanent magnets, the air gap between the magnetic poles and stator teeth, stator core with the teeth and rotor yoke, which altogether form the calculating part of the machine. All the components of the above calculating part are characterized by the magnetic resistance r , which is proportional to the length of the observed part of the circuit l and inversely proportional to its cross-sectional area A and the absolute magnetic permeability μ_a of the material. Calculation of the magnetic circuit of the machine is based on finding the components mentioned above and using them to find magnetic flux density of different parts of the magnetic circuit.

Magnetic circuit calculations in electrical machines fall into three main classes [42]:

- magnetic equivalent-circuit methods;
- analytical solutions of Laplace/Poisson equations;
- finite element method.

The first two are related to the classical magnetic circuit theory. Calculation results are approximate, at the same time, the results are precise enough to evaluate primary parameters.

Distribution and parameters of the primary magnetic field of HPSMG and FESM were analyzed by a simple analytical method and the finite element method. Modelling software tools *SPEED PC-BDC* and *FEMM 4.2* were used.

3.2.1 Magnetic circuit of HPSMG

HPSMG magnetic circuit is a circuit where tooth layers are located in the outer as well as in the inner part of the stator. Thus, the magnetic circuit can be divided into five paths which include the following:

- main path: the rotor yoke, the air gap, the outer layer of stator teeth and its core;
- the pole pair between the two magnets, excluding the air gap;
- only one magnetic pole;
- two teeth of the outer layer, excluding the stator's yoke;

- two teeth of the inner layer, excluding the stator's yoke.
- Fig. 3.1 shows the HPSMG magnetic circuit for one pole pair.

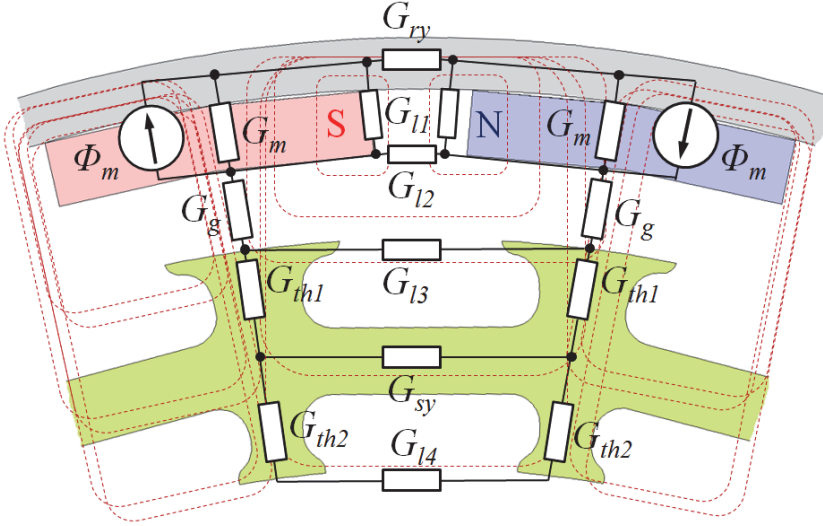


Fig. 3.1. The magnetic circuit of HPSMG's single pole pair.

Norton's equivalent circuit was used to describe the paths where the source of the magnetic flux is parallel to its internal conductance. Also, the other parts of magnetic circuits are expressed through their magnetic conductances G [32]. Generally, magnetic conductance G is found by using the following equation:

$$G = \frac{1}{R_{\Sigma}} = \frac{\mu_a A_x}{l_x} = \mu_a \int (A_x) dx \quad (3.13)$$

where R_{Σ} is the sum of the magnetic reluctance of the magnetic circuit.

The magnetic circuit is calculated in no-load condition of the machine. As the loop of the calculation part is symmetrical, it is sufficient to calculate the components of one side G_{ry} , G_m , G_g , G_{th1} , G_{sy} , G_{th2} and leakage values G_{l1} , G_{l2} , G_{l3} and G_{l4} . To calculate these values, the length of path elements in every calculation part l_x and its cross-sectional area A_x should be found using Eq. (3.13).

According to Eq. (3.14), permanent magnetic conductance G_m can be calculated as follows [47]:

$$G_m = \mu_a \frac{l_m w_m}{h_m} \quad (3.14)$$

Similarly, magnetic conductance G_g of the air gap can be calculated without taking into account the fringing effect of the magnetic field [43]:

$$G_g = \mu_0 \frac{l_m W_m}{l_g \cdot k_c}, \quad (3.15)$$

where $\mu_0 = 4\pi \cdot 10^{-7}$ H/m is absolute magnetic permeance of vacuum, and k_c is Carter's coefficient.

As the air in the gap has the same permeability as the air surrounding the air gap, there are some flux fringes or leaks into the surrounding air (Fig. 3.2).

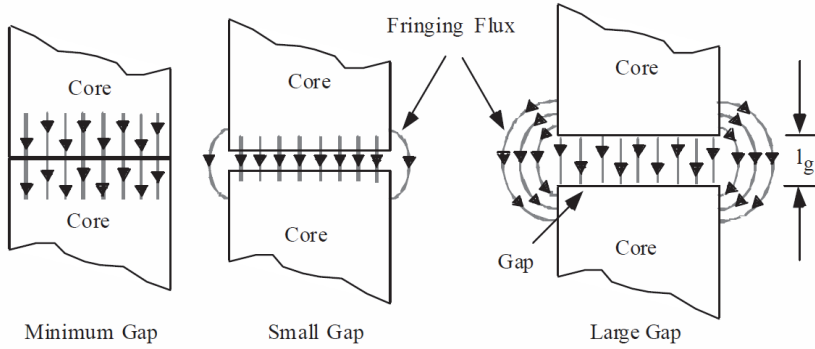


Fig. 3.2. The basic principle of a fringing flux [69].

The figure shows that the higher the l_g , the larger is the perimeter of the flux fringe. In case of small air gaps, the result is precise enough if l_g values are added to the core width. The fringing flux is assumed to follow a circular arc from one side of the block and then travel in a straight line across the air gap and again follow a circular arc to the other block. Although the model is simplified, it is precise enough for analytical calculations [43].

Fig. 3.3 shows a theoretical air gap permeance model of HPSMG based on the data mentioned above.

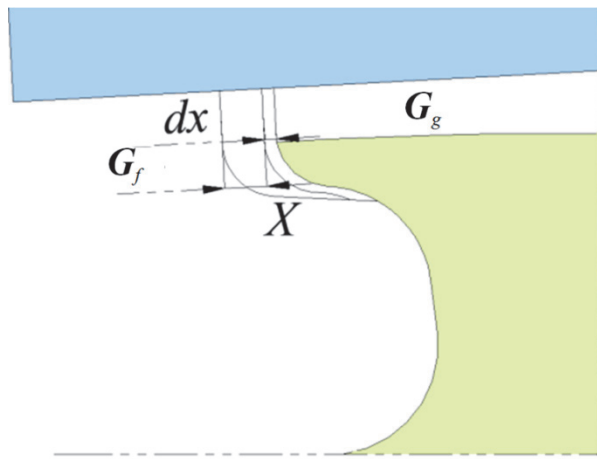


Fig. 3.3. The theoretical air gap magnetic conductance model of HPSMG.

As shown in the figure, fringing conductance G_f comprises the sum of differentials, the width of each being $l_g + \pi x$. Thus, G_f can be expressed as follows [43]:

$$G_f = \sum \frac{\mu_0 dA_x}{l_x} = \sum \frac{\mu_0 l_m dx}{l_x} = \int_0^x \frac{\mu_0 l_m}{l_g + \pi x} dx = \frac{\mu_0 l_m}{\pi} \ln \left(1 + \frac{\pi x}{l_g} \right), \quad (3.16)$$

where $dA = l_m dx$ is the cross-sectional area of each differential conductance.

Fig. 3.4 shows the semiprofile of a tooth from the outer layer of the teeth of HPSMG.

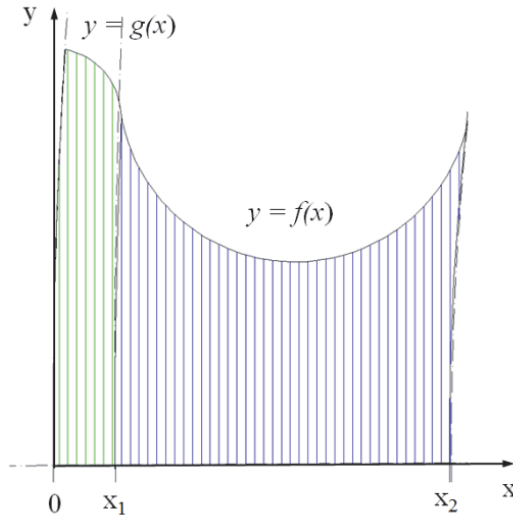


Fig. 3.4. The half profile of HPSMG single tooth.

To find a half of cross-sectional area $A_{1/2th}$, it was divided into two parts limited with two curved trapezes $y = x^2 + y^2 = r^2$ and straight lines $x = \{0; x_1\}$ and $\{x_1; x_2\}$. The area $A_{1/2th}$ is expressed as follows:

$$A = \int_a^b f(x) dx = F(b) - F(a) \quad (3.17)$$

In the case of the region $\{x_0; x_1\}$:

$$r_2 = (x + y)^2 = r^2 \Rightarrow y_2 = \sqrt{(r - x)^2} \quad (3.18)$$

In the case of the region $\{x_1; x_2\}$:

$$r_1 = \sqrt{(x - a)^2 + (y - b)^2} \Rightarrow y_1 = \sqrt{r^2 - (x - a)^2} + b \quad (3.19)$$

Thus, a half of the cross-sectional area of the tooth $A_{1/2th}$ is:

$$A_{1/2th} = \int_0^{x_1} g(x)dx + \int_{x_1}^{x_2} f(x)dx = \int_0^{x_1} \sqrt{(r-x)^2} dx + \int_{x_1}^{x_2} \sqrt{r^2 - (x-a)^2} + b \quad (3.20)$$

where r is radius of arc sectors.

Similar to the previous calculation, the area of the tooth of the inner layer can be calculated.

To simplify further calculations, the widths of the teeth were reduced to a mean width using the areas previously calculated, which is in the teeth of the outer layer $w_{tha1} = 3.72$ mm and in the teeth of the inner layer $w_{tha2} = 2.24$ mm. According to the same principle, mean widths of the outer and inner layer slots were calculated, which are $w_{sla1} = 7.24$ mm and $w_{sla2} = 7.66$ mm, respectively.

Then, while knowing the length of magnets l_m , cross-sectional areas of all steel parts of the magnetic circuit and the air gap can be calculated.

Through these, conductances of the outer and inner layer of teeth G_{th1} and G_{th2} can be expressed:

$$G_{th} = \frac{\mu\mu_0 A_{th}}{l_{th}} \quad (3.21)$$

where l_{th} is the length of the tooth loop.

Similar to Eq. (3.21), magnetic conductances G_{ry} and G_{sy} of the rotor yoke and the stator yoke were calculated

Mean width of teeth and slot openings w_{tha} and w_{sla} can be used to find the mean value of the magnetic conductance of the air gap G_{ga} :

$$G_{ga} = 2G_f + G_g = \mu_0 l_m \left[\frac{w_{tha}}{l_g \cdot k_c} + \frac{4}{\pi} \ln \left(1 + \frac{\pi w_{sla}}{4l_g \cdot k_c} \right) \right] \quad (3.22)$$

Carter coefficient delivered on the correction of G_{ga} is expressed as follows:

$$k_c = \left[1 - \frac{w_{sl}}{\tau_{sl}} + \frac{4l_g}{\pi\tau_{sla}} \ln \left(1 + \frac{\pi w_{sla}}{4l_g} \right) \right]^{-1}, \quad (3.23)$$

where τ_{sla} is the mean slot pitch.

The k_c value of 2.06 mm obtained refers to a high ratio of w_{sl} and τ_{sl} of HPSMG.

Magnetic conductance G_{l1} of the contour surrounding only one magnetic pole is expressed as follows [43], [47]:

$$G_{l1} = \frac{\mu_0 l_m}{\pi} \int_0^{\frac{w_m}{2}} \frac{dx}{x + \frac{h_m}{\pi}} = \frac{\mu_0 l_m}{\pi} \cdot \ln \left(1 + \frac{\pi w_m}{2h_m} \right) \quad (3.24)$$

Conductivity of the flux leakage G_{l2} between the two magnetic poles not passing the air gap can be expressed as follows [43], [47]:

$$G_{l2} = \frac{\mu_0 l_m}{\pi} \int_0^{l_g} \frac{dx}{x + \frac{w_{rsl}}{\pi}} = \frac{\mu_0 l_m}{\pi} \cdot \ln \left(1 + \frac{\pi l_g}{w_{rsl}} \right), \quad (3.25)$$

where w_{rsl} is the distance between the two magnetic poles.

Leakage conductances G_{l3} and G_{l4} can be expressed similarly:

$$G_{l3} = \frac{\mu_0 l_{sy}}{\pi} \int_{h_m}^{l_g} \frac{dx}{x + \frac{w_{sla1}}{\pi}} = \frac{\mu_0 l_{sy}}{\pi} \cdot \ln \left(1 + \frac{\pi l_g + h_{sl1}}{w_{sla1}} \right), \quad (3.26)$$

$$G_{l4} = \frac{\mu_0 l_{sy}}{\pi} \int_{h_s}^{h_s} \frac{dx}{x + \frac{w_{sla2}}{\pi}} = \frac{\mu_0 l_{sy}}{\pi} \cdot \ln \left(1 + \frac{\pi h_s}{w_{sla2}} \right) \quad (3.27)$$

Solving the scheme in Fig. 3.1, maximum calculated density in the air gap $B_g = 0.89$ T was obtained [42], [46]:

$$B_g = \frac{c_\varphi k_l P_m}{k_r P_\Sigma} B_r, \quad (3.28)$$

where $c_\varphi = A_m / A_g$ on the flux concentration factor ideally 1.0, k_l is the leakage factor, typically between 0.9-1.0, k_r is the reluctance factor in the range of 1.0-1.2, P_Σ is the summarized permeance, and B_r the remanent magnetic flux of the magnets.

In case the geometry is complex, the finite element method is the most accurate. In Fig. 3.5, the distribution of the HPSMG main magnetic flux in the magnetic circuit is shown.

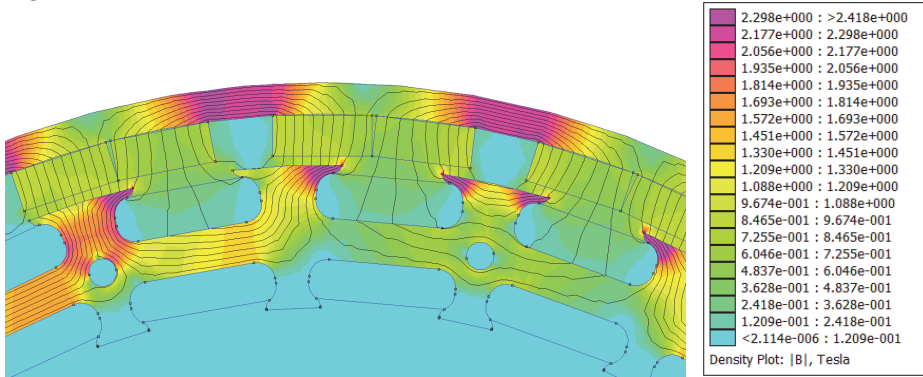


Fig. 3.5. Distribution of HPSMG primary magnetic flux.

The result of modelling shows that the contour of the main magnetic flux comprises only yoke and the outer layer of teeth in the stator. Regarding the inner teeth circle, the magnetic circuit between the two teeth can close only through an opening of a slot of low conductance ($G_{I4} = 5.23 \cdot 10^{-5}$ H), increase of the density of the magnetic flux in it is only marginal. Thus, in the modelling of the HPSMG main magnetic flux, the inner teeth layer can be excluded. Fig. 3.6 shows the distribution of the primary magnetic field modelled with FEMM software, excluding the inner tooth layer.

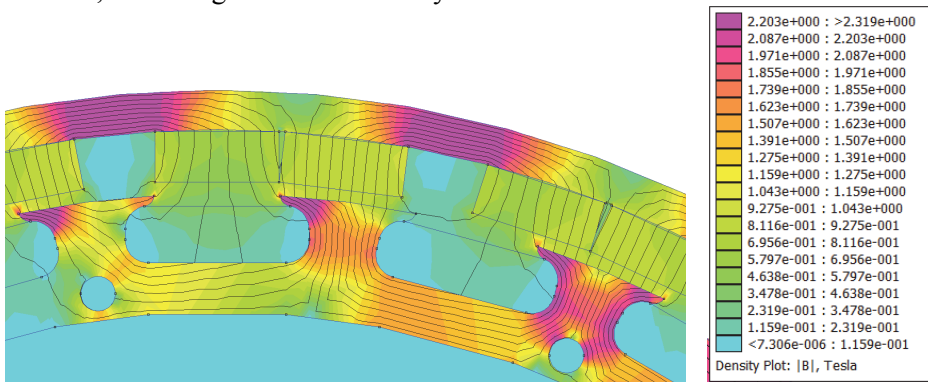


Fig. 3.6. Distribution of the HPSMGs primary magnetic flux without inner tooth layer.

The distribution of the main magnetic field is almost unchanged after excluding the inner layer of teeth.

Fig. 3.7 shows the modelled distribution of the HPSMG magnetic flux density starting from the longitudinal axis d up to the transversal axis q in the middle of the permanent magnet.

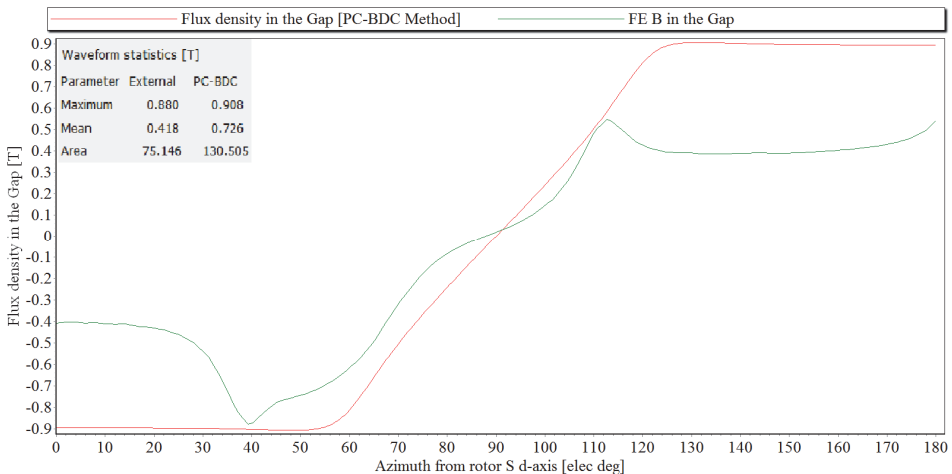


Fig. 3.7. Distribution of the HPSMGs primary flux density in the air gap.

In modelling, the analytical BLV-method (marked as red) [32] and the numerical method FEA based on finite elements (marked as green) were used for comparison.

Significant differences can be seen in both distributions of B_g . Maximum value of the magnetic flux density $B_g \approx 0.9$ T in the air gap matches, which is close to the distribution of the main magnetic field obtained in Figs. 3.5 and 3.6. The calculation results (Eq. (3.28)) and the value of B_g 0.85 T were found in Section 2.5. Overlap of graphs is the largest between 40-110 electrical degrees. The largest difference is in B_g values in the ranges where the magnetic pole is aligned with the slot. Slotting causes difficulties with the BLV method, as it modulates the air gap flux distribution [32]. The BLV method presumes a slotless stator where the conductors are filaments on the diameter [32]. This causes distinctions in the median values of magnetic flux density in the air gap obtained by modelling, the value of which is $B_{ga} \approx 0.73$ T using the analytical BLV method, but $B_{ga} = 0.42$ T using the FEA method. The FEA method should be considered more precise, as it matches the results in Figs. 3.5 and 3.6 and also the measuring results, which were $B_{ga} = 0.45$ T (Section 2.8.1) [23].

Either method gave different densities of the magnetic flux also in the layer of HPSMG teeth. Fig. 3.8 shows the graph of the results, which likewise can be caused by the limitations of the BLV method.

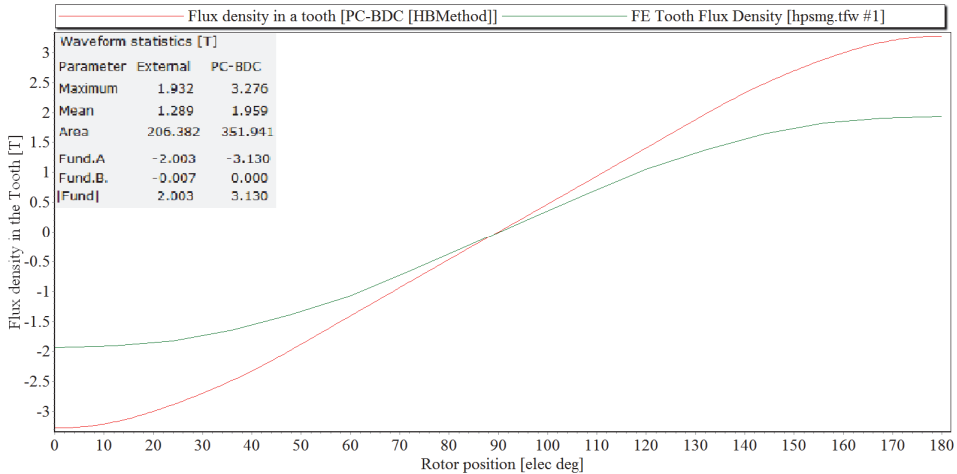


Fig. 3.8. Distribution of the HPSMG primary flux density in teeth.

The BLV method marked with red gives the mean value of the magnetic flux density $B_{tha} = 1.96$ T and the amplitude value $B_{gmax} = 3.28$ T. Comparison of these results with those in Figs. 3.5 and 3.6 shows that the maximum and the mean values of B_{th} are possibly overestimated.

Results obtained by the FEA method are also this time more close to the magnetic field image in Figs. 3.5 and 3.6, giving the value for $B_{tha} = 1.3$ T and amplitude value $B_{gmax} \approx 2.0$ T.

Fig. 3.9 presents the distribution of the magnetic flux in the stator yoke B_{sy} , modelled using the FEA method and including the value $B_y = 1.4$ T.

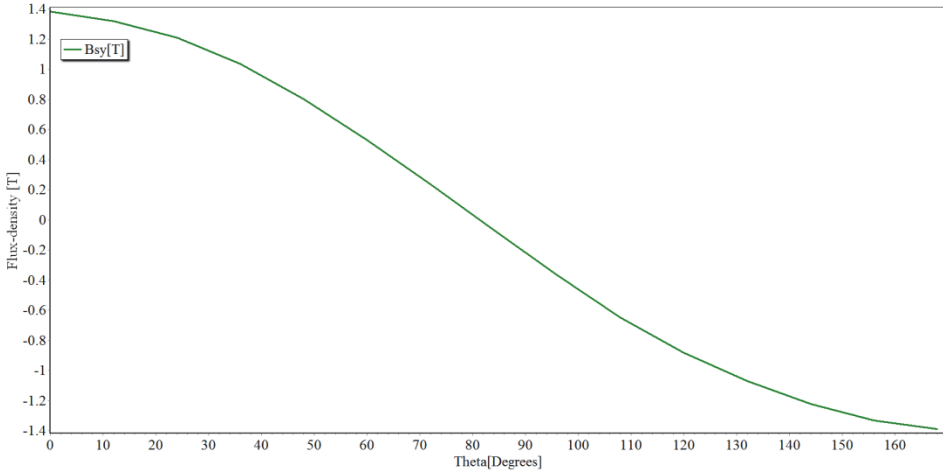


Figure 3.9. Distribution of the HPSMG primary flux density in the stator yoke using the FEA method.

3.2.2 Magnetic circuit of FESM

As the magnetic circuit of HPSMG was discussed only for the upper layer of teeth, the structure of the FESM magnetic circuit will be described similarly. Fig. 3.10 shows the magnetic circuit of the FESM single pole pair.

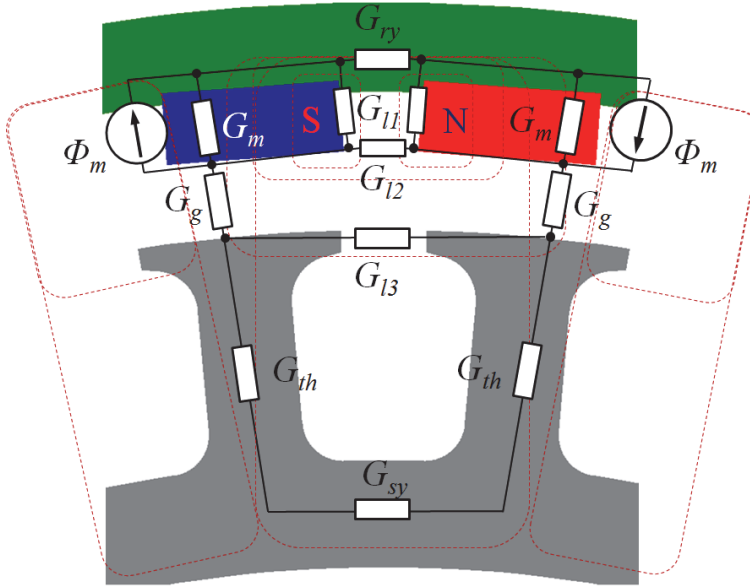


Fig. 3.10. Magnetic circuit of FESM single pole pair.

As the schemes are identical, the calculation methods for the parameters of each scheme (Eqs. (3.13) to (3.28)) are similar. Fig. 3.11 presents the modelling of the FESM main magnetic field.

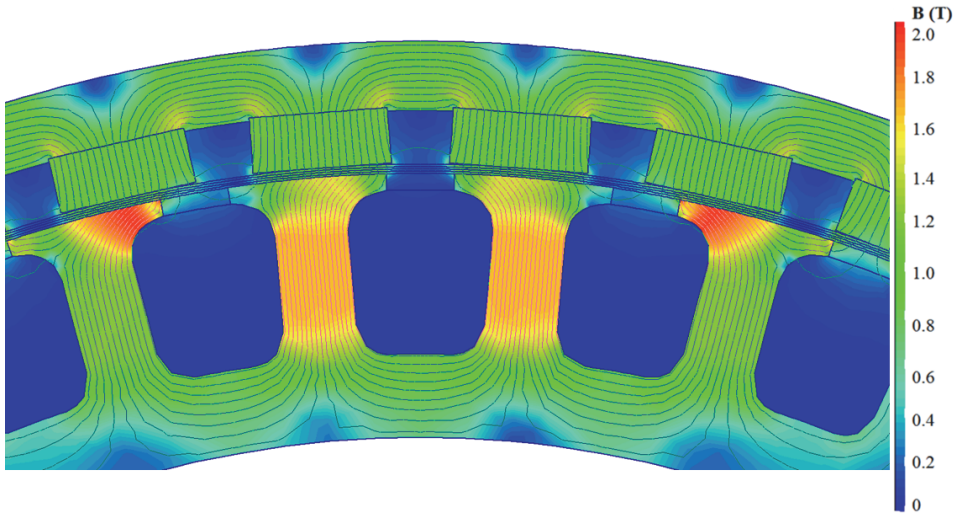


Fig. 3.11. FESM primary field distribution.

Similarly, the distribution of the magnetic flux of FESM was modelled using the BLV and the FEA method. The results of the magnetic flux density distribution in the air gap coincide significantly more than in the previous example, in the range of 45-150 electrical degrees. The shapes of the distribution curves of both methods are different in the same pattern in the sectors where the magnet is aligned with the slot (0-35 and 150-180 electrical degrees), which can be explained with the BLV method approach of slotless stator geometry.

The more precise FEA method (marked in green) gave the values of magnetic flux density in the air gap as $B_{ga} = 0.67$ T (mean value) and $B_{gmax} \approx 1.2$ T (maximum value), both being considerably higher than the corresponding HPSMG values. The difference arises mostly due to larger and more powerful magnets used with the air gap l_g equivalent to the air gaps of HPSMG.

Fig. 3.12 shows the modelled FESM magnetic flux density distribution in the air gap with the BLV and the FEA method, starting from the direct axis d to the quadrature axis q in the middle of the permanent magnet. In addition to main harmonics, both graphs also indicate the remarkable distorting effect of the third harmonics due to delta connection.

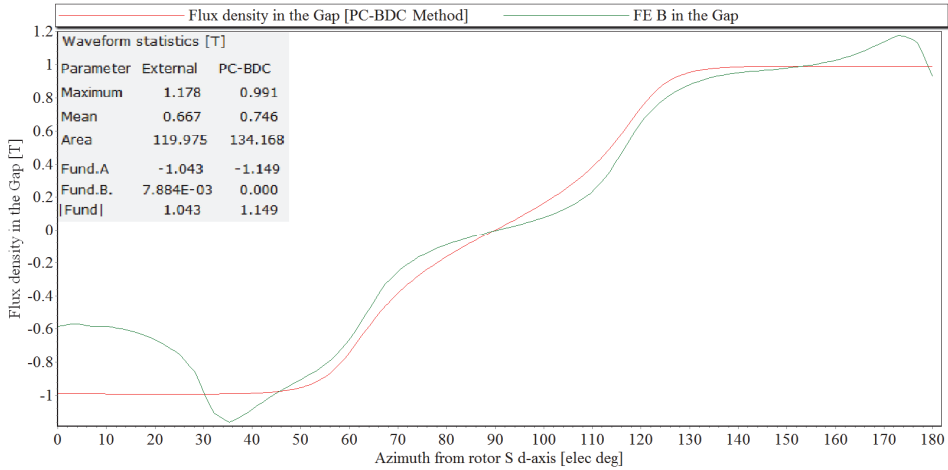


Fig. 3.12. Distribution of the FESM primary flux density in the air gap.

The magnetic flux density distribution was different with the BLV and the FEA method, similar with the HPSMG example. The mean value for the whole layer of teeth was obtained by the FEA method $B_{tha} \approx 1.1$ T, and the BLV method $B_{tha} \approx 1.2$ T, the maximum values being $B_{thmax} \approx 1.7$ T and 2.0 T, accordingly (Fig. 3.13).

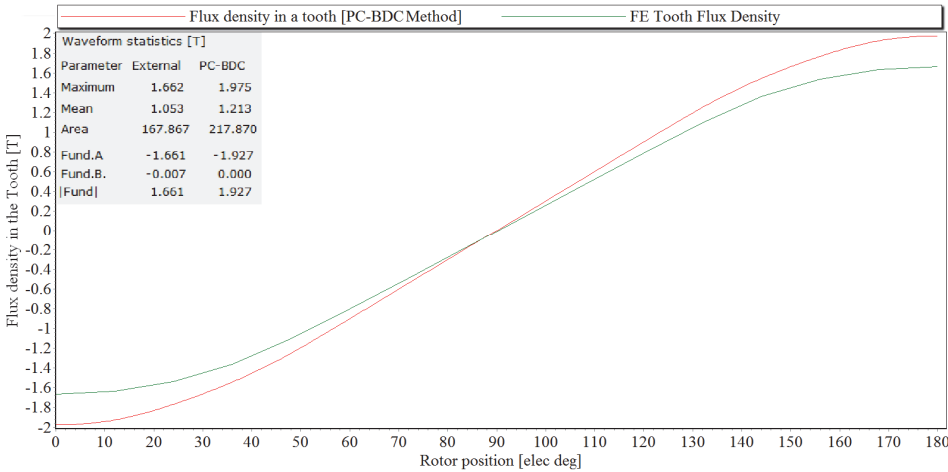


Fig. 3.13. Distribution of the FESM primary flux density in teeth.

Comparing Fig. 3.11 with the results above, it can be concluded that the teeth tips still indicate a higher level of saturation ($B_{thmax} \approx 2.0$ T) than the results by the FEA method that are the same as the BLV result. Therefore, the FEA result is slightly underestimated.

The modelled mean value of B_{sy} was obtained by the BLV method; $B_{sya} = 0.64$ T and the maximum value $B_{sy\max} = 0.9$ T. The FEA method gives $B_{sya} = 0.46$ and max $B_{sy\max} = 0.76$ T (Fig. 3.14).

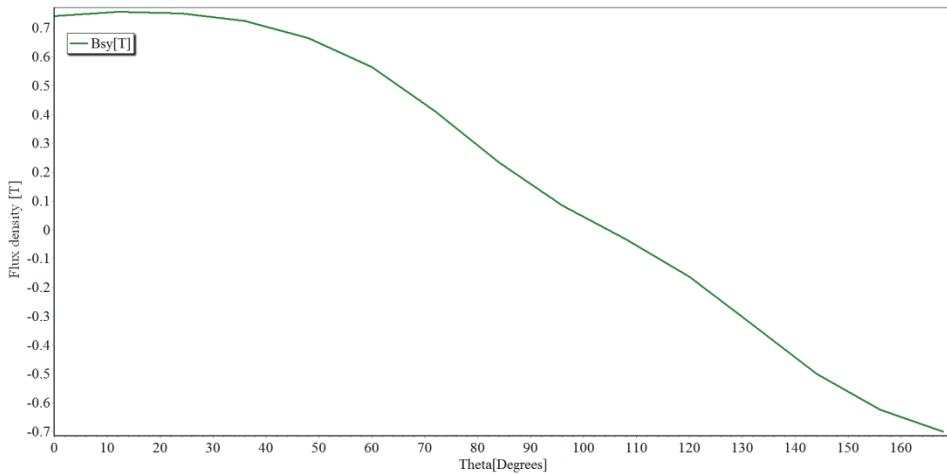


Fig. 3.14. Distribution of the FESM primary flux density in the stator yoke.

Compared to the magnetic field distribution (Fig. 3.11), the FEA method is closer.

The analysis of the primary field shows that the geometry of the magnetic circuit of both machines has been optimally designed and suitable materials were chosen. Certain saturation was detected in the contours of a smaller cross-section, mostly in the teeth tips under the magnet pole. But generally, the level of magnetic saturation corresponds to the magnetic characteristics of the material of the stator core.

The FEA method based on the final elements used for modelling can generally be considered more precise than the analytic BLV method. Nevertheless, further analysis will also consider the BLV method and the results, as it enables comparison and checking of the results obtained by both methods.

3.3 Armature Reaction and Demagnetization

When the armature winding is loaded with current, it creates its own magnetic field, called armature reaction [70]. In conventional DC machines, it is perpendicular to the main magnetic field, i.e. to the direction of the quadrature axis q . Unlike in conventional DC machines, quite remarkable armature reaction that strengthens or weakens the primary circuit is created in the BLDC machines and synchronous machines. The perpendicular field also induces excessive electromotive force in the armature winding [70].

HPSMG and FESM rotors have permanent magnets that are mounted to the interior surface and are separated from each other by air gaps. Thus, an asymmetric surface is created on the inner perimeter of the exterior rotor, which physically distorts the geometry of the air gap. With conventional salient pole synchronous machine inductors, the magnetic resistance to the magnetic circuit of the quadrature axis q is considerably higher than the resistance to the current

on the direct axis d direction. This can be explained with the large space between the poles of the salient pole rotors. That influences the amount of the magnetic flux on the d -axis. As the magnetic permeability of permanent magnets does not differ much from that of air, it means that PM machines are generally considered as non-salient machines [71]. In non-salient machines, the magnetic flux is the same on both d - and q -axis. But changes occur due to the asymmetry of rotors, i.e. permanent magnets on its surface can be seen as analogues to the winding coils that are only on the direct axis d , creating a magnetic flux of the same direction and a link also with the armature flux on the d -axis, causing electrical asymmetry [70].

Generally, the armature reaction of surface mounted permanent magnet machines affects less than 10% of the air gap magnetic flux density created by permanent magnets. It also applies to the stator teeth layer and yoke, where the influence of the secondary field is considerably smaller compared to the primary field. Without the saturation of ferromagnetic material, the distribution of permanent magnet and electromagnet magnetic field in the magnetic circuit would total by the superposition principle [43].

3.3.1 Special case of armature reaction – sudden short circuit

As the effect of the secondary magnetic field is quite small, then if the teeth and shoes are not highly saturated due to the permanent magnets alone, the armature reaction is generally not a problem. It will be a problem under fault conditions, when the machine currents exceed their normal range by a magnitude or more. In that case, the armature reaction can demagnetize the rotor magnets [43].

The following are the graphic time and current characteristics for instant simulated short circuit situations of HPSMG and FESM. The transient process for a 3-phase short circuit was studied.

Fig. 3.15 gives the Gramme's winding HPSMG short circuit characteristic that shows the short circuit current i_k maximum peak value up to 270 Amp, HPSMG rotational speed $n = 3000$ rpm, which exceeds the peak value of the nominal phase current more than ten times (Section 5.4.3) [72].

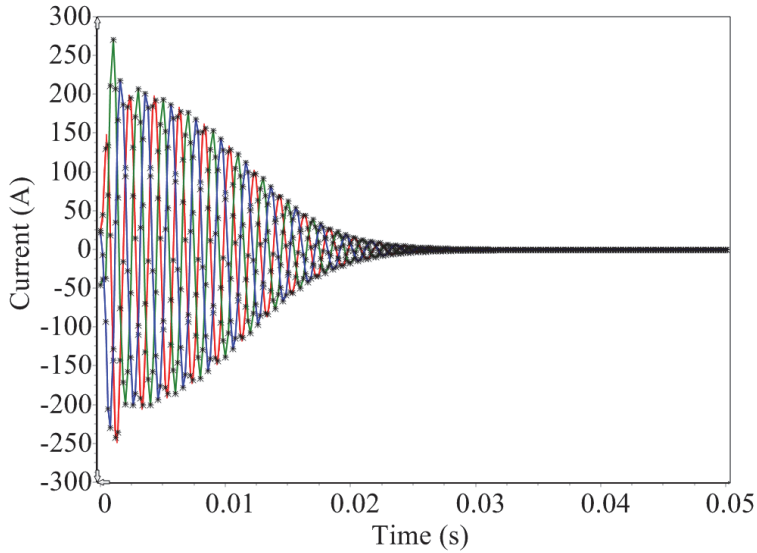


Fig. 3.15. Short circuit simulation of HPSMG with the Gramme's winding.

Fig. 3.16 gives the short circuit characteristic of the concentrated winding HPSMG, which is marginally shorter in its time interval (up to 0.025 s), also slightly smaller of its short circuit current total energy, as the i_k amplitude values fall more rapidly than in Fig. 3.15.

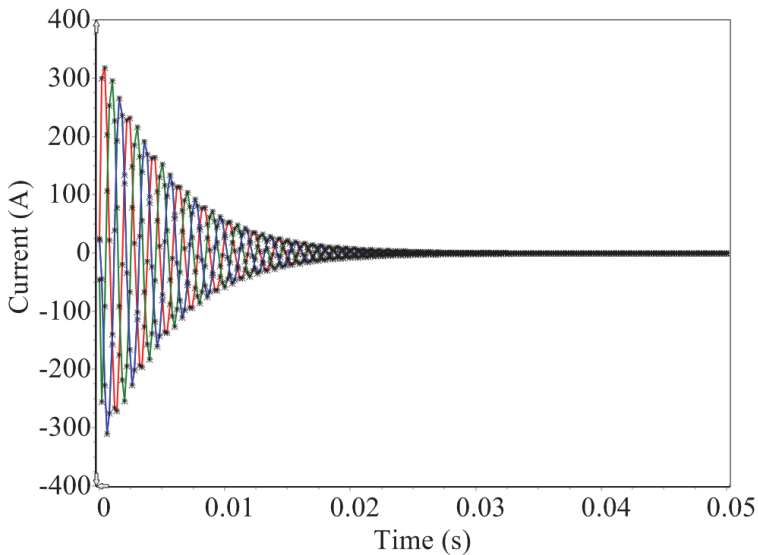


Fig. 3.16. Short circuit simulation of HPSMG with the concentrated winding.

In contrast, the maximum short circuit current amplitude value for the concentrated winding is almost 50 A higher, i.e. $i_k \approx 320$ A.

With inrush current of such values, there could be a real danger of non-reversible demagnetization of permanent magnets. Therefore, based on the i_k amplitude values, the most unfavorable conditions to the magnets, i.e. their maximum operating temperatures and the maximum inrush values i_{kl} , were analyzed.

The loaded machine is affected by the demagnetizing magnetomotive force F_{dem} , as in [42]:

$$F_{dem} = \frac{Q \cdot i_{kl}}{4p \cdot a}, \quad (3.29)$$

where Q is the number of slots, i_{kl} the amplitude value of inrush current, p the number of pole pairs, and a the number of parallel paths in the machine.

F_{dem} value is used to obtain the internal magnetizing force H_m [42]:

$$H_m = \frac{\pm F_{dem} - \frac{l_g \cdot k_c}{\mu_0}}{l_m + \mu_r \cdot l_g \cdot k_c}, \quad (3.30)$$

where l_g is thickness of air gap, k_c Carter's coefficient, l_m the magnet length and μ_r the relative permeability of magnets.

According to the calculations, both HPSMG winding types gave the value of H_m as 327 kA/m, which determines their operating point at various temperatures according to the characteristics of permanent magnets N42UH B-H given in Fig. 3.17. In the figure, 180 °C was chosen as the maximum operating temperature.

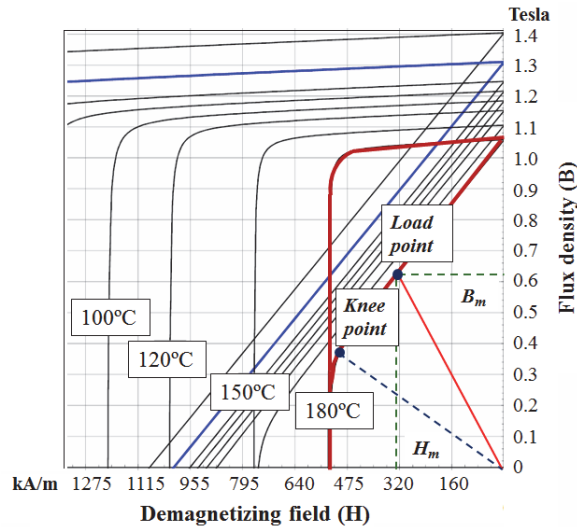


Fig. 3.17. Operating parameters of permanent magnets used in HPSMG [64].

According to the figure, the magnetic flux density of magnets B_m with the specific short circuit current i_k in the specific operating point is 0.63 T. Comparing the result with the knee point, which gives the minimum magnetic flux density before total demagnetization as $B_{min} \approx 0.4$ T, it can be concluded that even with the maximum temperature 180 °C and the inrush current $i_{kl} = 270$ A, the non-reversible demagnetization of both windings is avoided. Nevertheless, a possible hazard is posed by electro-dynamic forces (occurring with the short circuit) that can damage the windings. The hazard can be prevented with an effective short circuit protection device, which is generally installed in the inverter as well.

A similar simulated analysis was carried out with FESM to test the sudden short circuit probability at the rotational speed of $n = 2000$ rpm. Fig. 3.18 shows the characteristic of the 3-phase short circuit.

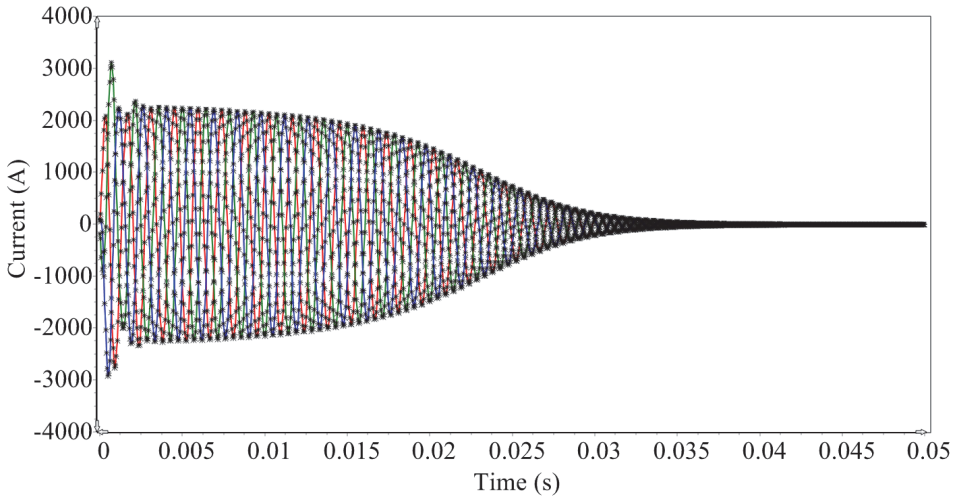


Fig. 3.18. Short circuit simulation of FESM with the concentrated winding.

The amplitude values of the short circuit current i_k with the FESM short circuit are considerably higher than with the previous examples. However, the inrush current amplitude value i_{kl} is up to 3100 A, which exceeds the phase current amplitude value $i_{phmax} = 144.3$ A by more than 20 times.

Fig. 3.19 gives the characteristic of the FESM rotor permanent magnets N45SH B-H, with the operating point or short circuit point of magnets in such short circuit conditions with the maximum operating temperature of the permanent magnets, accordingly. The location of the load point in the load line, even with such i_{kl} , will be high enough as compared to the critical part of the characteristic line or knee point ($B_m = 0.8$ T) where the minimum magnetic flux density is $B_{kp} = 0.58$ T.

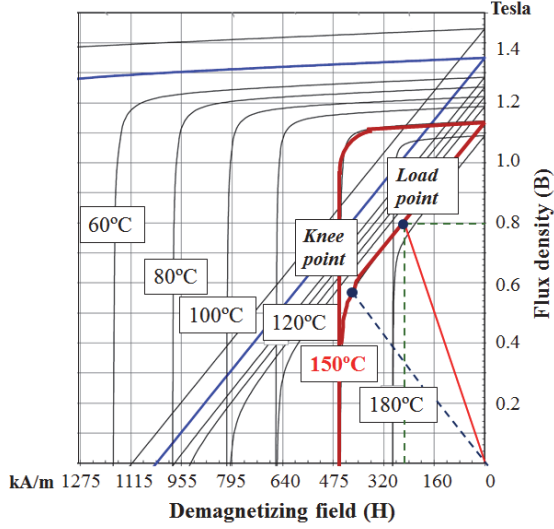


Fig. 3.19. Operating parameters of permanent magnets used in FESM [64].

Unlike the previous examples, the sudden short circuit of the FESM armature winding gives the current impulses of thousands of amperes, with powerful electromagnetic forces. Their value can generally be determined with the formula of electromagnetic force F_{em} per length unit that affects the winding conductors and is determined by multiplication of the magnetic flux density B and the conductor current i [3]:

$$F_{em} = Bi \quad (3.31)$$

When the current i increases, B also increases. Therefore, F_{em} increases in proportion to the square of the i . With a short circuit, F_{em} is as follows [3]:

$$F_{em} = B_{th} i_{f \max} \left(\frac{i_{kl}}{i_{f \max}} \right)^2, \quad (3.32)$$

where B_{th} is the magnetic flux density in teeth.

The result is $F_{em} = 26.6$ kNm with the inrush current of $i_{kl} = 3.1$ kA. That can cause mechanical damage to the machine. In this case, similar to HPSMG, the short circuit protection device in the inverter ensures safety.

3.4 Resultant Magnetic Field

When the primary and secondary magnetic fields join, a resultant magnetic field will occur in the magnetic circuit. Fig. 3.20 shows the distribution of the resultant magnetic field with the corresponding magnetic flux density of the toroidally wound HPSMG modelled in the final element method.

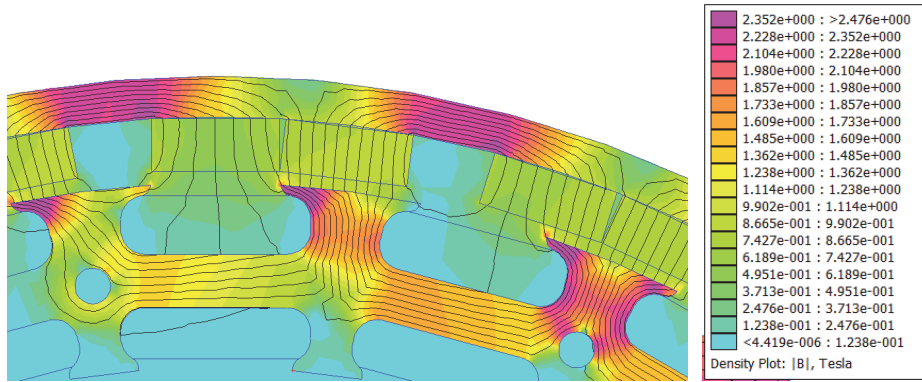


Fig. 3.20. The resultant magnetic field distribution of HPSMG.

The HPSMG characteristics of the resulting magnetic flux density in the air gap of the machine were modelled with the analytic BLV (in red) and the final elements with the FEA method (in green) (Fig. 3.21).

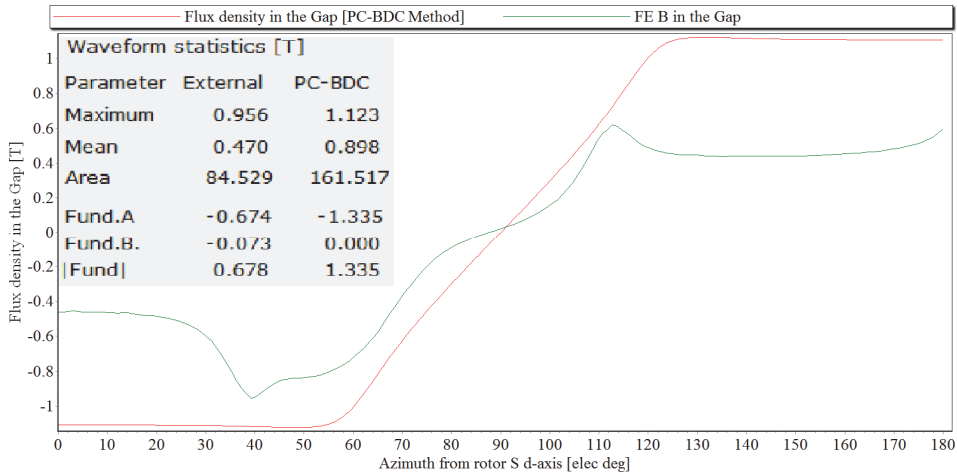


Fig. 3.21. Distribution of the HPSMG resultant flux density in the air gap.

From the comparison of previous data on the distribution of the primary and secondary magnetic fields and the numeric data of the magnetic flux density, it is revealed that the proportion of the secondary field created by the stator windings in the resulting magnetic field is quite low. With the air gap, the resulting magnetic flux density mean and maximum value $B_g \sim 0.1$ T is higher, which is very close to the corresponding arithmetic total B_{gmax} of both fields.

Similarly, the B_{th} values coincide, summarizing the magnetic flux density of the primary and secondary field and comparing them with the resulting B_{th} value (Fig. 3.22).

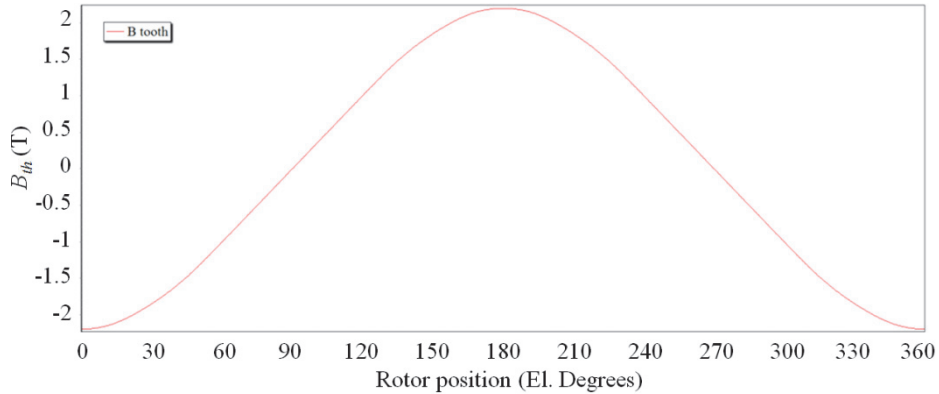


Fig. 3.22. Distribution of the HPSMG resultant flux density in teeth.

The maximum value of B_{th} is close to the modelled magnetic field distribution in Fig. 3.20, as well as to the analytical calculations of 2.3 T (Section 2.6, Eq. (2.16)).

In the case of the resulting magnetic field, like with the primary magnetic field, the magnetic flux density in the inner layer of teeth is only marginal, not higher than $B_{th} \approx 0.1$ T (Fig. 3.5, Section. 3.2.1). Therefore, the inner layer of teeth has no direct influence on the magnetic circuit. In this case, it helps to fix the windings mechanically.

Fig. 3.23 shows the distribution of the resulting magnetic flux density in the stator yoke of the toroidally wound HPSMG.

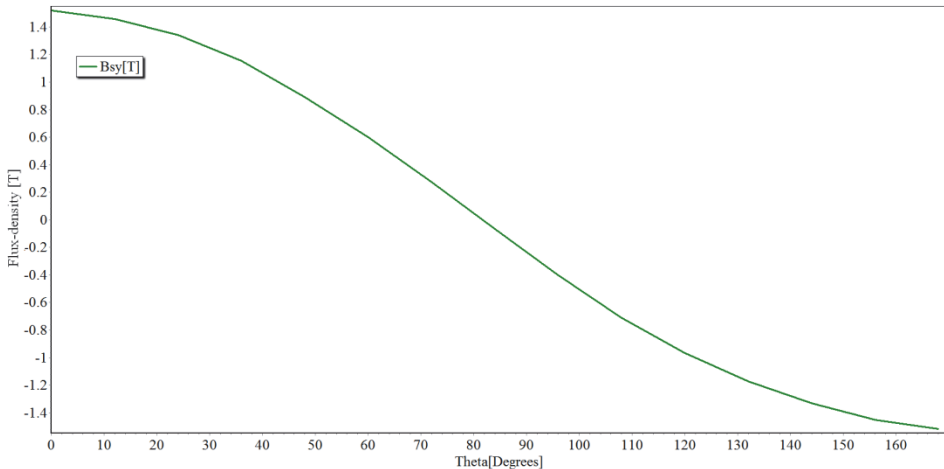


Fig. 3.23. Distribution of the HPSMG resultant flux density in the stator yoke.

The B_{sy} maximum value $B_{sy} \approx 1.6$ T on the characteristic matches with the result of the previous calculations $B_{sy} = 1.5$ T (Section 2.6, Eq. (2.15)). When the B_{sy} values of the primary and secondary fields are arithmetically summarized, it

is ~ 0.2 T larger, but the result ignores the reduction of magnetic flux density due to saturation.

Fig. 3.24 shows the FESM modelled resulting magnetic field distribution.

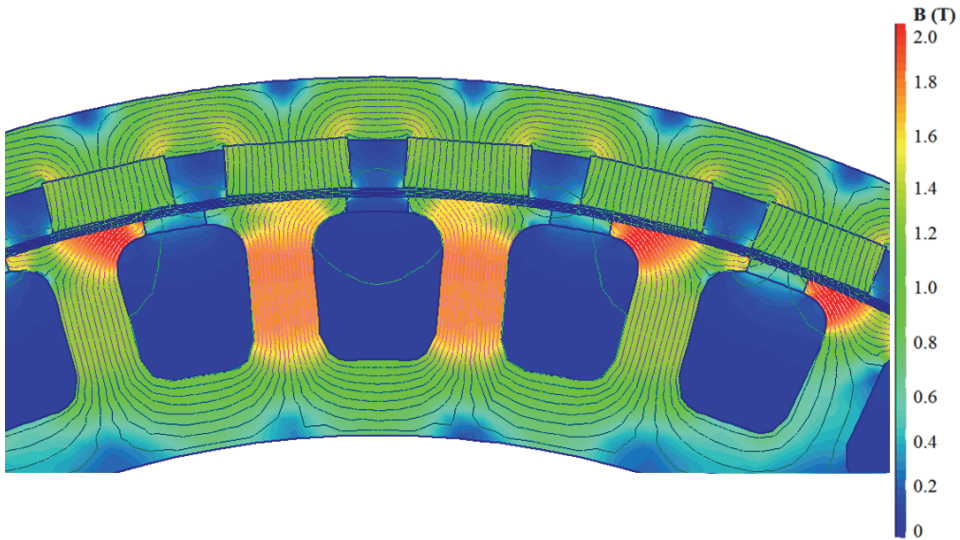


Fig. 3.24. The resultant magnetic field distribution of FESM.

In the comparison of the distribution of the magnetic flux density in the air gap, the previous example also shows matches between the resulting B_g value and the results of analytical calculations (Section 3.2.2). The FESM resulting magnetic flux distribution in the air gap is characterized by Fig. 3.25.

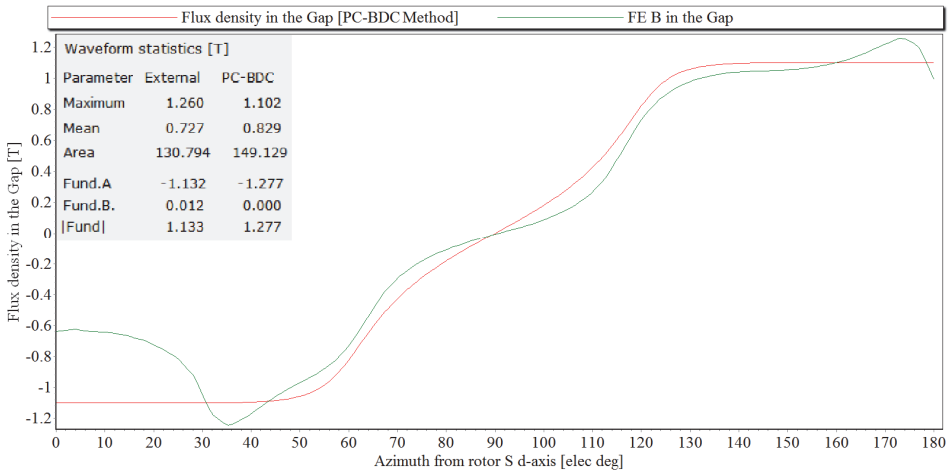


Fig. 3.25. Distribution of the FESM resultant flux density in the air gap.

With the resulting B_{th} values, the magnetic flux density has decreased similar to the HPSMG example, which can also be explained with teeth saturation. Theoretical calculations (Section 3.2.2) give the result as $B_{th} = 1.7$ T, which is approximately the same as the FEA method result to B_{th} in Fig. 3.26 (in green).

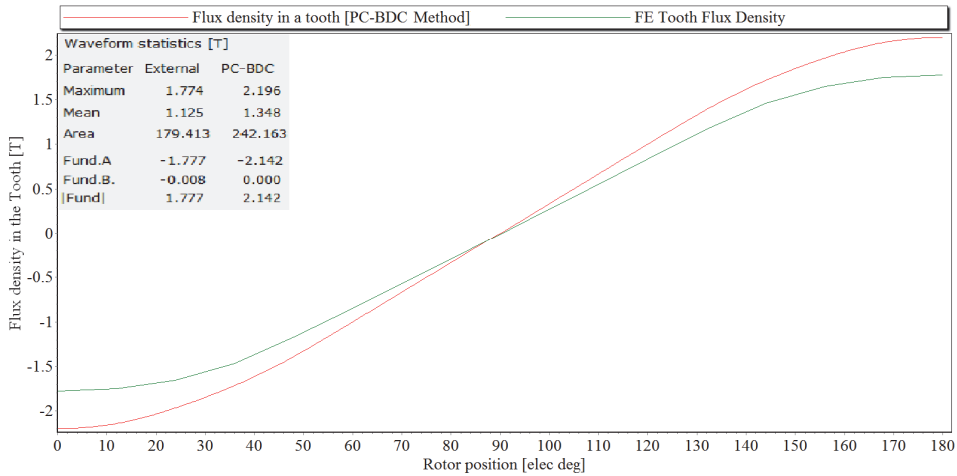


Fig. 3.26. Distribution of the FESM resultant flux density in teeth.

The result of the BLV method, however, coincides more with the arithmetic sum of the magnetic flux density of the primary and secondary magnetic fields. When comparing the results with the modelled resulting magnetic field distribution and its B_{th} values (Fig. 3.24), the results with the FEA method could be considered more correct.

Fig. 3.27 gives the magnetic flux density distribution in the stator yoke B_{sy} .

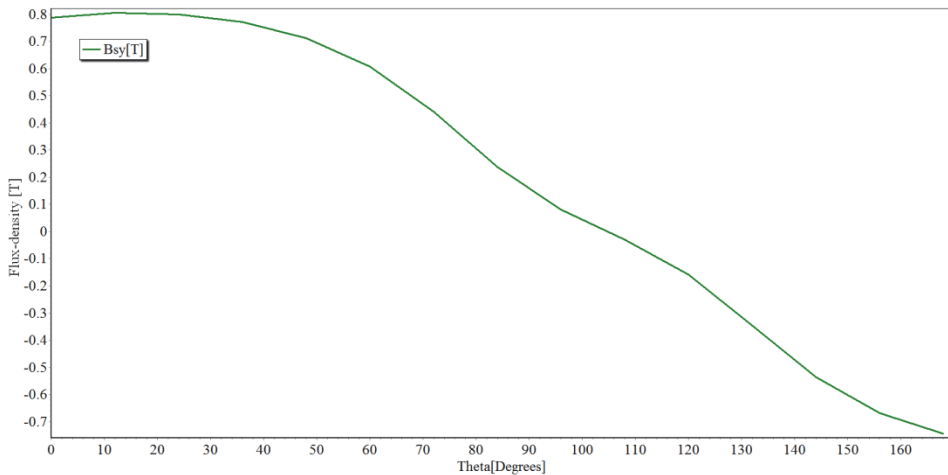


Fig. 3.27. Distribution of the FESM resultant flux density in the stator yoke.

Similarly, the B_{sy} value coincides with the B_{sy} values of both the modelled field distribution and the calculations ($B_{sy} = 0.8$ T). The arithmetically summarized value of the primary and secondary field is remarkably higher due to the saturation of the stator yoke in this case as well.

In conclusion, the resulting magnetic field distribution and the values of the magnetic flux density in the magnetic circuit were quite predictable, as the

analytical calculations of Sections 3.2.1 and 3.2.2 gave mostly the same results for both HPSMG and FESM. The modelling results showed that the mean and maximum values of magnetic flux density in the magnetic circuit were somewhat higher in some cases, but generally within the required limits. Thus, it can be concluded that the magnetic circuits of both machines have been used quite optimally.

3.5 Comparative Analysis of Gramme's and Concentrated Winding

The first part of the section dealt with the different windings of HPSMG and FESM. This subsection gives the comparative analyses, assessing the advantages and disadvantages of both types of windings. The aim of the comparison is first and foremost to test the hypothesis of the advantages of the toroidal winding located on the stator yoke as compared to the concentrated winding comprising only the teeth layer. To use a common starting point for an objective comparison, the geometry of the HPSMG stator was modified to make it similar to that used with the FESM. The rotor geometry, i.e. the number of magnetic poles and slots, stator inner and outer diameter, slot and teeth width, and therefore, the area and thickness of the yoke, is the same, but the yoke is relocated to the lower part of the stator. Winding coils are mounted in the slots surrounded by teeth (Fig. 3.28).

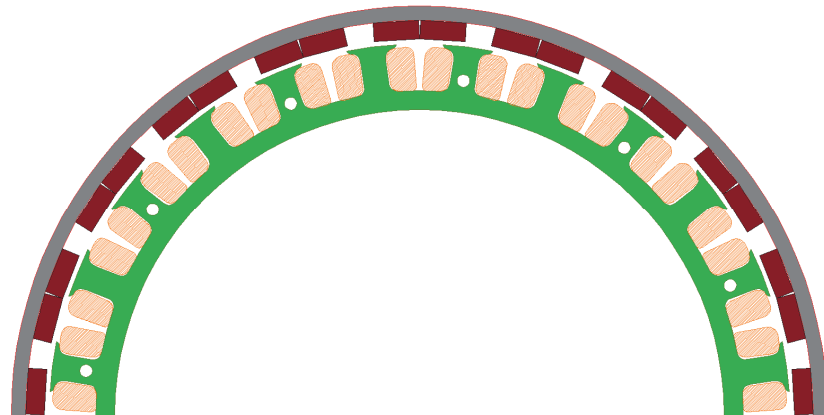
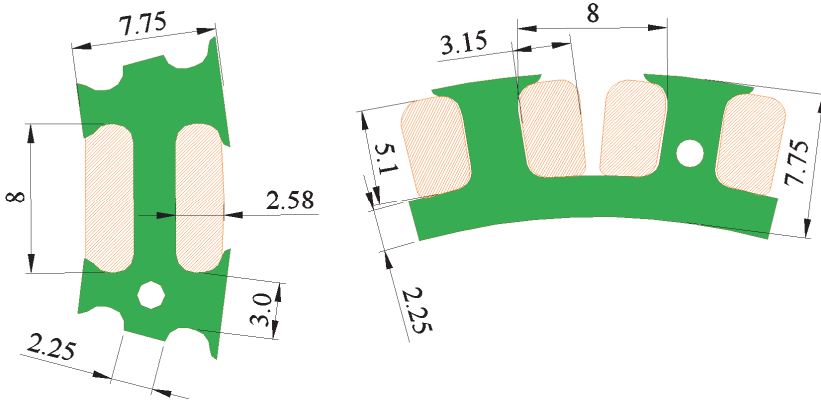


Fig. 3.28. HPSMG with the modified stator geometry.

The first comparison can be geometric, with the stator winding coils of both configurations compared in a vertical position. Fig. 3.29 shows that with the same stator height $h_s = 7.75$ mm, yoke thickness $h_{sy} = 2.25$ mm and conventional teeth geometry (a), the applicable height of the coil h_{coil} compared to toroidal winding (b) is almost 3.0 mm or 36% smaller. The ratio is the same when comparing the coil side areas of both windings, the width of the same winding coil being $w_{coil} = 2.58$ mm. If the $w_{coil(b)}$ value is increased to 18% (3.15 mm), the area will be $A_{coil(b)} = 15.26$ mm². Even then it is almost 21% smaller, compared to the toroidal winding (a) area, accordingly $A_{coil(a)} = 19.28$ mm². If a

conventional winding coil sides are widened radially, it causes an equal or 6% axial lengthening of end connections, which form 32% of the active part of the winding then. Although the calculated total winding volume of a toroidal winding is almost a fifth larger, the difference with end connections is only 2%.



a) Stator geometry of Gramme's winding b) Stator geometry of common winding

Fig. 3.29. Sectional views of two different stator geometries.

Due to the conditions specified above, the filling factor for a concentrated winding (b) will be $k_{sl(b)} = 0.76$, which is a very good result for the winding conductor with a diameter of $D_{con} = 0.61$ mm used (Fig. 3.30).

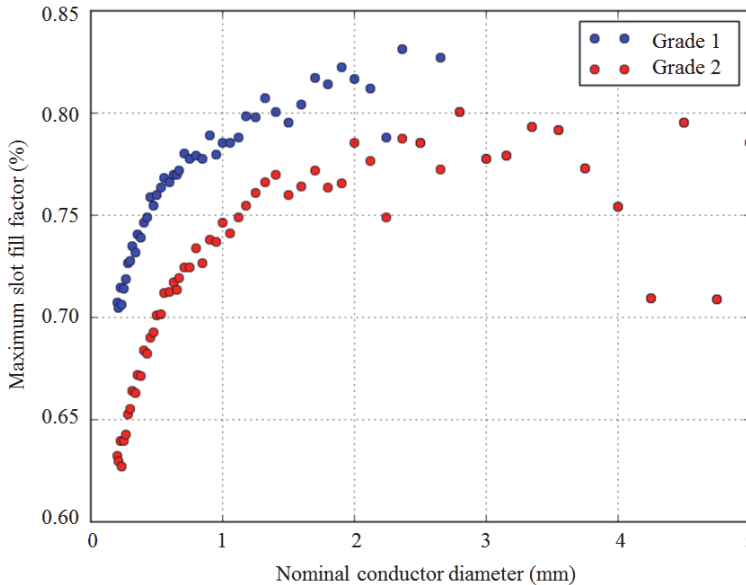


Fig. 3.30. Maximum slot fill factors according to IEC 60317-0-1 [73].

With a toroidal winding (a), the corresponding calculated filling factor for the winding for the whole slot is almost 20% higher ($k_{sl(b)} = 0.94$).

Based on the cross sectional area $A_{con} = 1.2 \text{ mm}^2$ (Section 2.8.1) of the winding conductor, the Gramme's winding would enable mounting almost 26% more or 3 extra winding turns per coil. Therefore, it can be concluded that applying such winding method, slot openings can be used with much higher efficiency and with a larger total area for winding conductors. To obtain comparable results with configuration (b), the length of teeth should be increased, which would increase the general length of the stator and the total weight of HPSMG, accordingly.

Another comparison can be made based on a conventional inductive coil. According to the total current law and Hopkinson's law for the magnetic circuits, it can be concluded:

$$\oint_c H_l dl = \int_s J_f dA = Ni = \sum_1^n I_i = F_m, \quad (3.33)$$

where H_l is the magnetic field strength within the coil (A/m) around the closed curve C , l - coil length (m), J_f - current density (A/m^2), A - contour cross-sectional area (m^2), N - the number of turns in a coil, I_i - total current in the winding conductor (A), and F_{em} - magnetomotive force in the magnetic circuit (A).

Accordingly, the magnetomotive force in the wound cores derives from the multiplication of the current through the winding and the number of turns. As the HPSMG coils in the phase winding are in series connection, the current through the windings is the same. Considering the rms value of the current in a coil $I_{rms} = 26.0 \text{ A}$ (Section 2.8.1) and assuming that the number of turns in the Gramme's winding (a) is 16 and in the concentrated winding (b) accordingly 3 turns less, i.e. 13 turns, the values of magnetomotive forces are $F_{m(a)} = 416 \text{ A}$ and $F_{m(b)} = 338 \text{ A}$. With the constant cross-sectional area of the magnetic circuit, the magnetic flux is calculated as follows:

$$\Phi = BA = \mu_a H_l A = \mu_a \frac{NI_i}{l} A = \mu_a \frac{F_m}{l} A, \quad (3.34)$$

According to the formula, considering the above mentioned F_m values as the basis for the coils (a) and (b), the value of Φ is influenced only by the height of the coil, or the height of the winding and the cross-sectional area A of the cores. With the same stator length L_{sy} , the HPSMG yoke height h_{sy} is considerably smaller than the width of a tooth w_{th} , therefore both of them are calculated as 1 in order to obtain a comparable result. In that case, the difference depends on the value of the coil length l , which is inversely proportional to the amount of the magnetic flux. As the toroidal winding coil (a) length l_a is considerably larger than the l_b of the winding coil (b), it causes the lower value of Φ , being almost 19% smaller than for the coil (b). This comparison brings out the advantages of the coil (b) that has a shorter core.

However, when we compare the electromagnetic torque T_{em}

$$T_{em} = \frac{1}{2\pi} \left(N \frac{I_i}{2a} \right) (2p \Phi_m) = k_m \Phi_m I_i, \quad (3.35)$$

we can see from the formula that T_{em} is proportional to the flux from all poles and with the total armature current in all conductors. As the cross-section area A of the coil (a) is larger, it enables use of conductors with larger cross-section with the same number of turns N of the coil (b) and the currents can be 26% larger with the same current density. Therefore, the winding method (a) enables a smaller Φ_m , but with a larger I_i value, the electromagnetic torque T_{em} will still be almost 2% higher than with the winding method (b).

Electromotive force E_i is created as an absolute value in the winding as follows:

$$E_i = N \frac{d\Phi_m}{dt} = \frac{d\Psi_m}{dt} = \frac{pN}{a} \Phi_m \omega = k_e \Phi_m \omega, \quad (3.36)$$

which shows that E_i is proportional to the main magnetic flux Φ_m and the angular speed ω . Comparing the electromotive forces of both winding methods depending on their geometry, the winding method (a) gave almost 2% larger calculated E_i value with the same cross-sectional area A of the core.

The magnetic flux lines not passing the air gap are generally considered to be flux leakage. They are distributed as follows [46]:

- slot leakage flux (Φ_{sl});
- tooth tip leakage flux (Φ_{th});
- end winding leakage flux (Φ_{ew});
- pole leakage flux (Φ_p).

Fig. 3.31 gives the principles of the main paths of the leakage fluxes, comprising both HPSMG winding types and the stator geometry.

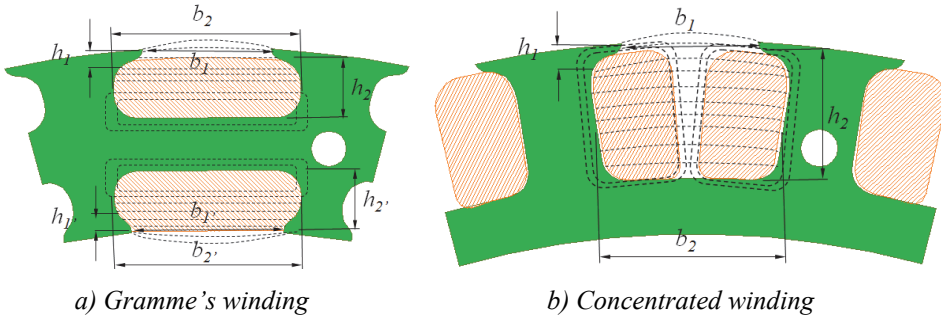


Fig. 3.31. Leakage flux distributions in both geometries.

With both the toroidal and the concentrated winding type, all the flux leakages mentioned above are present. The pole leakage flux (Φ_p) originating from the rotor magnetic poles of the machine has not been discussed.

Slot leakage inductance L_{sl} is created by Φ_{sl} and is calculated as follows:

$$L_{sl} = \mu_0 l_{con} \frac{Q}{m} \left(\frac{N_{con}}{a} \right)^2 \lambda_{sl}, \quad (3.37)$$

where l_{con} is the length of the active part of the winding conductor, N_{con} - the number of active conductors in the slot, Q - the number of stator slots, m - the number of phases, a - the number of parallel paths, λ_{sl} - the permeance factor of the whole slot.

The permeance factor of the whole slot λ_{sl} :

$$\lambda_{sl} = \lambda_1 + \lambda_2, \quad (3.38)$$

of which

$$\lambda_1 = \frac{h_2}{3b_2} \quad \text{and} \quad \lambda_2 = \frac{h_1}{b_1} \quad (3.39)$$

where λ_1 is the permeance factor of the wound part and λ_2 - the permeance factor of the slot opening.

Similarly, the number of slots L_{sl} on the inner perimeter of the toroidal winding (a) can be calculated.

The analytic calculations with the same l_{con} , N_{con} , Q , m and a values with the concentrated winding (b) gave the slot leakage inductance $L_{sl} = 15.6 \mu\text{H}$ and with the toroidal winding (a) $L_{sl} = 11.2 \mu\text{H}$, which is almost 28% lower. Thus, the L_{sl} caused slot leakage flux Φ_{sl} is also lower accordingly.

The tooth tip leakage inductance L_{th} is determined by the permeance factor λ_{th} [46]:

$$\lambda_{th} = k_2 \frac{5 \left(\frac{l'_g}{b_1} \right)}{5 + 4 \left(\frac{l'_g}{b_1} \right)}, \quad (3.40)$$

where the air gap factor k_2 :

$$k_2 = \frac{1 + l'_g}{2}, \quad (3.41)$$

where l'_g is the air gap thickness without magnets.

The tooth tip inductance:

$$L_{th} = \frac{4m}{Q} \mu_0 l_{con} \lambda_{th} N^2 \quad (3.42)$$

The winding type (b) gave $L_{th} = 0.23 \mu\text{H}$. As the number of teeth tips of the toroidal winding (a) is double, it gives almost 34% higher value of $L_{th} = 0.31 \mu\text{H}$ than type (b). Therefore, the proportion of leakage inductance in teeth tips with a

concentrated winding is approximately 1% of the L_{sl} value against the toroidal winding proportion of up to 3%, which also has a marginal effect for electromagnetic losses.

A more relevant difference in leakage inductance is attributed to the end connections. Fig. 3.29 gives the dimensions of the winding types for comparison. If the geometric dimensions are the same, but the yoke is relocated to the inside of the stator, the winding type (b) coil length around the tooth is reduced considerably, as compared to the toroidal winding (a) with the coil around the stator yoke. Therefore, to have the same amount of winding conductors in a slot of the same cross-section of the winding type (a), the winding type (b) requires about 47% increase in the coil side diametric dimensions. Accordingly, the end windings increase as well.

For end windings, it is sufficient to use the empirical calculus and the determined permeance factors λ_{lew} and λ_w . The end winding leakage induction can then be calculated [46]:

$$L_{ew} = \frac{4m}{Q} \mu_0 l_{ew} \lambda_{lew} q N^2, \quad (3.43)$$

where l_{ew} is the average length calculated as follows:

$$l_{ew} = 2b_{ew} + w_{ew}, \quad (3.44)$$

$$l_{ew} \lambda_w = 2b_{ew} \lambda_{lew} + w_{ew} \lambda_w, \quad (3.45)$$

where b_{ew} is the axial length and w_{ew} - the width of the end winding.

As the length of the end windings of the concentrated winding type (b) in both radial and axial direction exceeds the corresponding dimensions of the toroidal winding (a), it also shows in the leakage inductance value $L_{ew} = 30.0 \mu\text{H}$ due to the end windings, which is almost 27% higher than for the toroidal winding, i.e. $L_{ew} = 23.5 \mu\text{H}$.

Summarizing the results obtained with Eqs. (3.37)-(3.45), the leakage inductance caused by windings for the toroidal winding (a) was $L_{\Sigma l} = 35.0 \mu\text{H}$ and for the concentrated winding (b), it was $L_{\Sigma l} = 45.7 \mu\text{H}$, i.e., almost 31% higher.

Thus, it could be concluded that the main causes for flux leakage in the windings of both types are the end windings of considerable proportion. It is especially evident with the winding type (b), as its width of sides of the coil compared to the winding type (a) is remarkably larger due to the reduced length of the coil (b).

Substantially lower values of L_{sl} and L_{th} can be explained with the relatively low height of the teeth for both windings, compared to the large width of slots and the gap between teeth tips, which creates magnetic resistance R to flux leakages Φ_{sl} ja Φ_{th} as well.

The secondary magnetic field distribution of FESM would be a good example here to confirm that. As the gap between the FESM teeth tips and the

diameter of slot openings is considerably smaller compared to the length and diameter of the winding coil, the values of L_{sl} and L_{th} are also considerably higher. It is illustrated by Fig. 3.32, which shows the distribution of the FESM secondary field modelled with the FEM software.

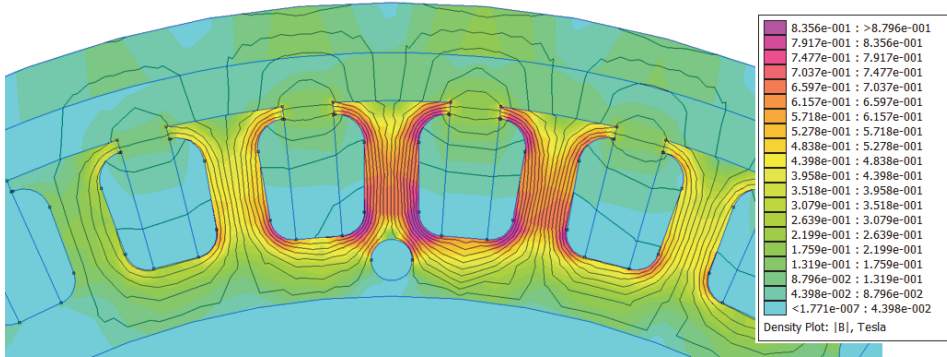


Fig. 3.32. Distribution of FESM secondary magnetic field.

The large relative diameter of slots and the gap between teeth tips also applies to the inner teeth and slot layer not influenced by the air gap of the HPSMG toroidal winding (a). As the distance between the teeth in the inner layer is even larger compared to the outer layer of teeth, the winding has also a massive air perimeter inside, the R value is still greater and the L_{sl} and L_{th} smaller accordingly, which was confirmed by the calculations. Therefore, it can be concluded that the magnetic flux created by the inner sides of the coils of the toroidal winding flows almost entirely along the stator yoke, joining the magnetic flux created by the outer sides of the coils.

The same is confirmed by Fig. 3.33, which shows the FEM software simulated toroidally wound HPSMGs secondary field distribution in the HPSMG magnetic circuit.

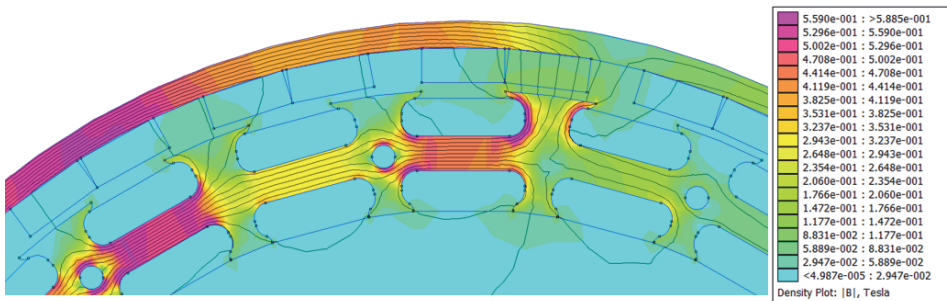


Fig. 3.33. Distribution of toroidally wound HPSMGs secondary magnetic field.

Due to the high magnetic resistance R , the field lines have been mainly formed in the stator yoke, crossing the air gap to some extent and are moving to the rotor yoke from there, reaching the magnetic flux density of up to $B = 0.45$ T. In the slots and between teeth tips of the inner perimeter of the

stator, however, the magnetic flux density is of marginal value, i.e. between $B = 0.02\text{-}0.04\text{ T}$. The magnetic flux density in the outer layer of teeth in-slot and between the teeth tips is of the same level. This also confirms the low leakage results of the calculations.

Comparison of the electromagnetic field distribution of toroidal windings to Motor-CAD EMag software modelled concentrated windings (Fig. 3.34) reveals that the values of magnetic flux density in the stator yoke, teeth, slots and teeth tips do not differ much, being just slightly higher with the toroidal windings.

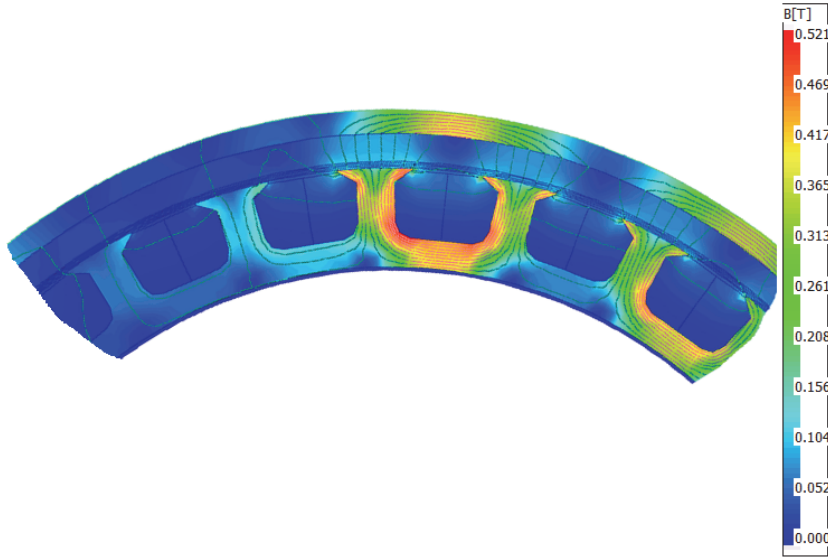


Fig. 3.34. Concentrically wound HPSMGs secondary magnetic field distribution.

Based on the analysis above, it can be concluded that the toroidal windings used with HPSMG and its stator geometry are justified when considering losses due to flux leakages that were smaller than in the more conventional concentrated windings. One of the advantages of toroidal windings is that when the stator height is the same, its windings are located more effectively and the slot filling factor is more effective, which enables more winding in the slots; at the same time, the stator core can be smaller and lighter in weight.

In spite of the good filling factor of slots in toroidal windings, the field intensity H and magnetic flux Φ accordingly, were lower than these in concentrated windings. The reason could be the relative length of the winding coils compared to the width. This drawback can be improved by modifying the geometry of teeth.

Regardless of the lower values of H and Φ of toroidal windings, it is possible to achieve the same or even higher electromagnetic torque T_{em} by mounting larger cross-sectional conductors, as the slot filling factor k_{sl} is higher. Therefore, the higher k_{sl} value and a larger amount of loops guaranteed the same or slightly higher value of the electromotive force.

3.6 EMF and Back-EMF

Fig. 3.35 presents the HPSMG and FESM 3-phase electrical scheme in delta connection.

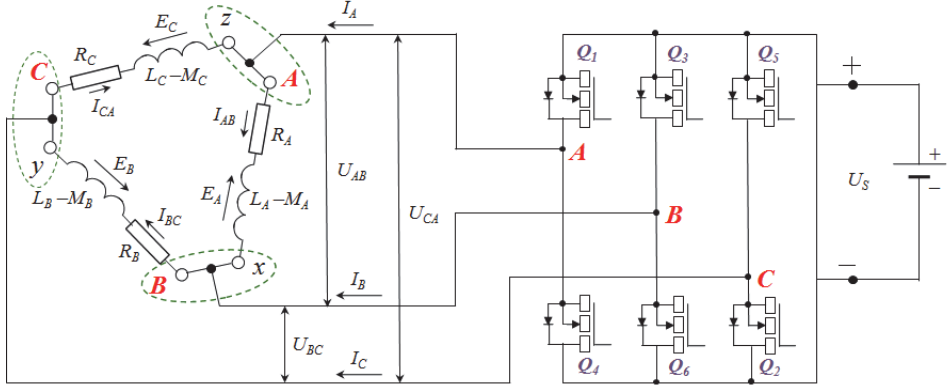


Fig. 3.35. The principal electrical scheme of HPSMG and FESM in delta connection.

As the line voltages in delta connections are equal to phase voltages, according to Fig. 3.35, the matrix of the phase voltages can be expressed:

$$\begin{bmatrix} u_{AB} \\ u_{BC} \\ u_{CA} \end{bmatrix} = \begin{bmatrix} R_A & 0 & 0 \\ 0 & R_B & 0 \\ 0 & 0 & R_C \end{bmatrix} \begin{bmatrix} i_{AB} \\ i_{BC} \\ i_{CA} \end{bmatrix} + \frac{d}{dt} \begin{bmatrix} L_A & M_B & M_C \\ M_A & L_B & M_C \\ M_A & M_B & L_C \end{bmatrix} \begin{bmatrix} i_{AB} \\ i_{BC} \\ i_{CA} \end{bmatrix} + \begin{bmatrix} e_A \\ e_B \\ e_C \end{bmatrix} \quad (3.46)$$

where L is self-induction and M is mutual induction.

Presuming that

$$\begin{aligned} L_A &= L_B = L_C = L, \\ M_A &= M_B = M_C = M, \end{aligned} \quad (3.47)$$

the active resistors and inductivity can be given as a matrix:

$$R_\Sigma = \begin{bmatrix} R_A & 0 & 0 \\ 0 & R_B & 0 \\ 0 & 0 & R_C \end{bmatrix} \quad \text{and} \quad L_\Sigma = \begin{bmatrix} L & M & M \\ M & L & M \\ M & M & L \end{bmatrix}, \quad (3.48)$$

as the instantaneous value of the phase voltage is:

$$u_{AB} = R_A i_{AB} + L_A \frac{di_{AB}}{dt} + M_B \frac{di_{AB}}{dt} + M_C \frac{di_{AB}}{dt} + e_A = R_\Sigma i_{AB} + L_\Sigma \frac{di_{AB}}{dt} + e_A, \quad (3.49)$$

with the instantaneous value of the electromotive force as:

$$e_A = N \frac{d\Phi_m}{dt} = \frac{d\Psi_m}{dt} = \frac{pN}{a} \Phi_m \omega = k_e \Phi_m \omega, \quad (3.50)$$

Methods for calculating the back-EMF waveform can be classified into analytical or numerical methods. The main analytical methods are [32]:

- Magnetic equivalent circuit or the lumped-parameter reluctance network;
- Conformal transformation;
- Analytical solution of Laplace's equation.

The main numerical methods are based on the following well-developed computer software:

- Finite-element method;
- Boundary-element method.

At present, analytical design calculations are still more productive and efficient as they are much faster, even though they may be less accurate. The finite element analysis is therefore used to check and refine designs, or analysis of problems, which are too difficult to solve analytically [32].

Therefore, this thesis has applied similar methods, using an analytic approach as the starting point for calculations of the counter electromotive force.

The simplest and most widely used method for such calculations is the BLV method based on the Faraday induction law, which describes the distribution of the magnetic flux as quasi-static, without distortions by slotting [32].

In another method, the back-EMF is calculated using the tooth flux method based on the fact that all coils in a motor can be described in terms of a sequence of the equivalent single tooth coils. The tooth flux is crucial in the determination of the motor performance [43].

The single-tooth EMF e_{th} is also based on the Faraday induction law according to Eq. (3.51):

$$e_{th} = \frac{d\psi_{th}}{dt} = \varpi_m w_{th} L_{stk} k_{stk} \frac{dB_{th}}{d\theta_e} \quad (3.51)$$

where ψ_{th} is the current linkage in a tooth, ω_m - the angular speed of the rotor, w_{th} - the mean width of the tooth, L_{stk} - stator length, B_{th} - the magnetic flux density in a tooth, and θ_e - the electric position angle of the rotor.

As the numerical value of the magnetic flux in teeth ϕ_{th} is considered to be constant, the difference of them in other teeth is determined merely by the electrical position angle of the rotor θ_e :

$$\begin{aligned} & \phi_{th}(\theta_{e1}), \\ \phi_{th} &= \phi_1(\theta_{e1} - \theta_{e2}), \\ \phi_{th} &= \phi_1(\theta_{e1} - 2\theta_{e2}) \end{aligned} \quad (3.52)$$

Thus, the instantaneous value of the single tooth EMF is [43]:

$$e_{th}(\theta_e) = \sum_{n=-\infty}^{n=\infty} E_{th} \exp(jn\theta_e), \quad (3.53)$$

of which

$$E_{th} = jnN\omega_e\phi_{th} \quad (3.54)$$

Therefore, the electromotive force in a single coil is:

$$e_{coil}(\theta_e) = e_{th}(\theta_{e1}) + e_{th}(\theta_{e1} - \theta_{e2}) + e_{th}(\theta_{e1} - 2\theta_{e2}) + \dots + e_{th}(\theta_{e1} - n\theta_{e2}) \quad (3.55)$$

The previous result enables the calculation of the EMF values of other coils that have the same amplitude and characteristic line, but shifted from each other by the electrical grade θ_e . Summarizing them according to the connections of winding coils in a phase winding, the single phase EMF value is obtained. With other phases, the phase shift is equal to the abovementioned electrical angle θ_e .

Based on the analyses, the back-EMF waveforms for the toroidally wound HPSMG were modelled (Fig. 3.36).

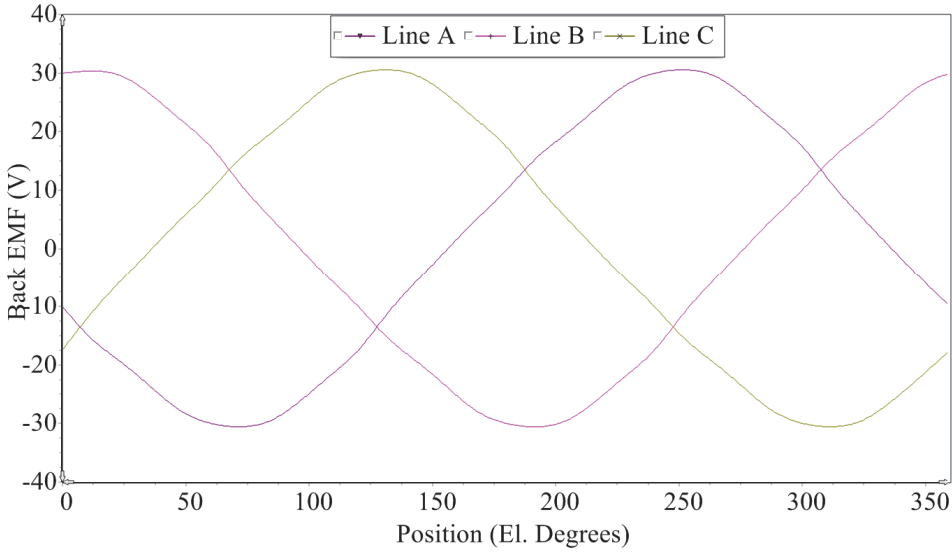


Fig. 3.36. The back-EMF waveform of toroidally wound HPSMG.

The waveforms show that the phase EMFs (e_{ph}) have a regular sinoidal shape without major distortions.

Fig. 3.37 also gives the e_{ph} higher harmonics distribution according to the number of the harmonics.

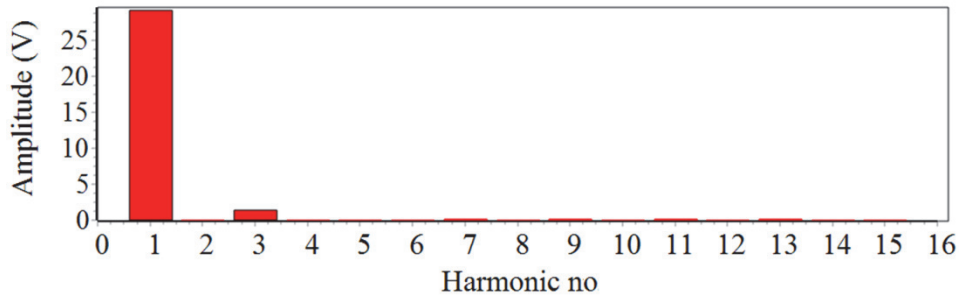


Fig. 3.37. Distribution of higher harmonics in toroidally wound HPSMG.

The graph shows that besides the first harmonic, the symmetrical back-EMF carries also odd harmonics to some extent. The largest of them is the third harmonic, depending on the HPSMG winding delta connection.

Fig. 3.38 gives the HPSMG concentrated winding e_{ph} characteristics.

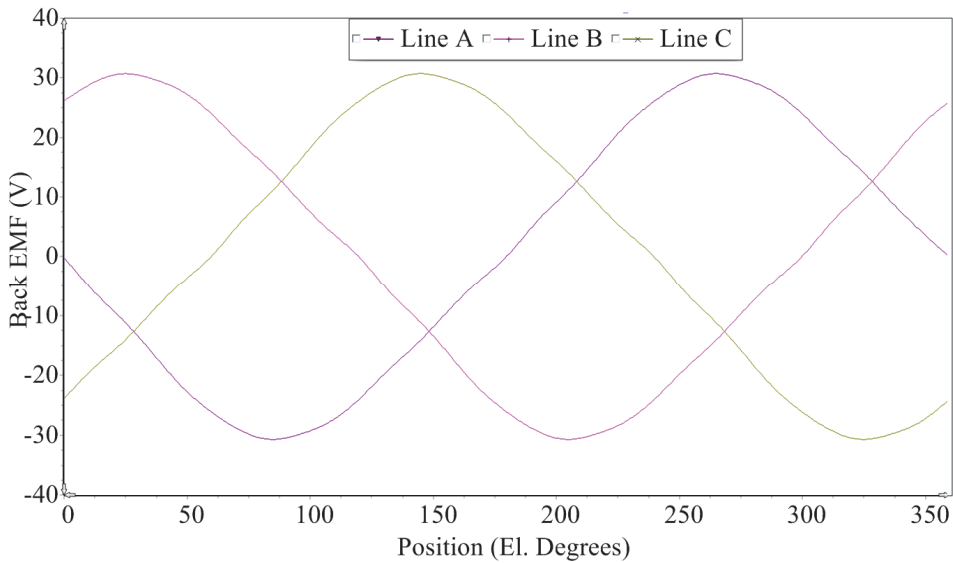


Fig. 3.38. The back-EMF waveform of concentrically wound HPSMG.

Comparison of Figs. 3.36 and 3.38 reveals that with both windings, the e_{ph} is similarly symmetrical and equal in the amplitude value e_{phmax} .

The toroidal and concentrated winding harmonics distribution is similar as well, with the first, third and to some extent, the eleventh harmonics standing out (Fig. 3.39).

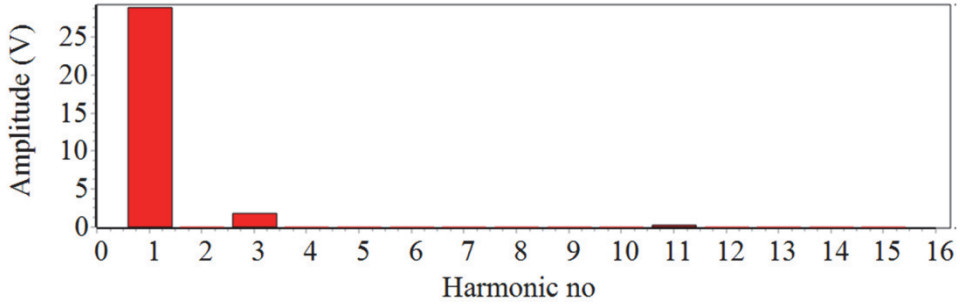


Fig. 3.39. Distribution of higher harmonics in concentrically wound HPSMG.

There are slight differences in the numerical values of harmonics, i.e. 29.2 V for the main harmonics with the toroidal winding and 28.9 V with the concentrated winding. The third harmonic on the concentrated winding was almost 0.35 V higher than on the toroidal winding.

That indicates higher efficiency of toroidal windings with higher main harmonics, but lower with the other distorting harmonics.

With FESM, some distortions can be identified in the sinusoidal shape of the simulated back-EMF, which refers to higher influence of harmonics (Fig. 3.40).

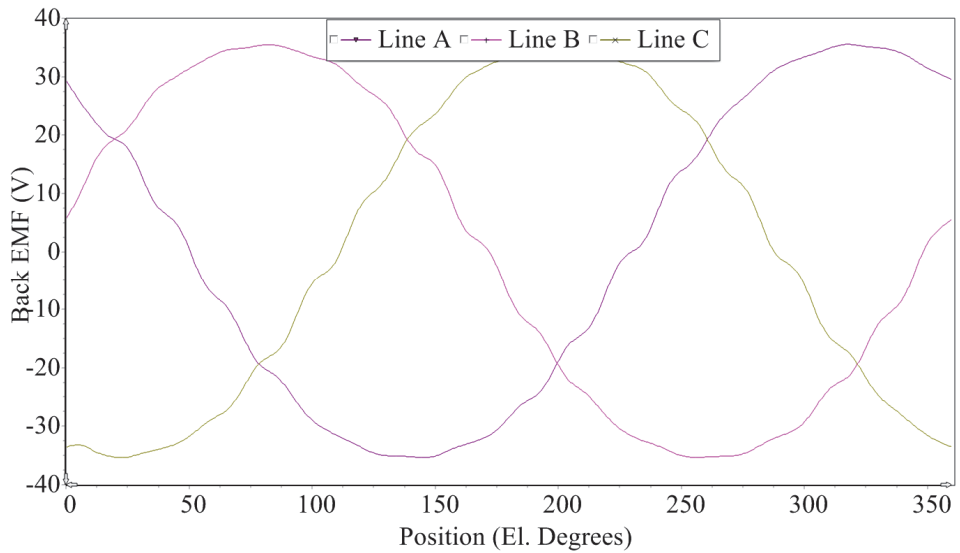


Fig. 3.40. The back-EMF waveform of concentrically wound FESM.

Fig. 3.41 shows the shape of the FESM higher harmonics. Based on the figure, it can be stated that in addition to the main harmonic, a third harmonic exists due to the delta connection of the odd numbered harmonics.

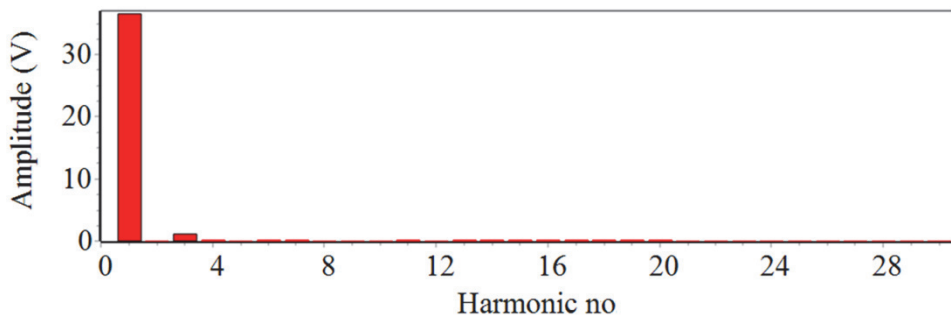


Fig. 3.41. Distribution of higher harmonics in concentrically wound FESM.

Table 3.1 shows the voltage and e_{ph} of the different winding types of HPSMG and FESM.

Table 3.1. Comparison of simulated voltage and back-EMF results in differently wound HPSMG and FESM

No.	Properties	Type of machine and winding			
		HPSMG (Toroidal)	HPSMG (concentrated)	FESM (concentrated)	Units
1	Supply voltage (U_{sup})	27.6	27.6	51.8	V _{DC}
2	Phase voltage (U_{ph})	19.5	19.5	36.6	V _{AC}
3	Total harmonic distortion of phase voltage (THD_u)	3.9	6.4	4.1	%
4	Peak back-EMF in phase (e_{phmax})	30.6	30.7	35.5	V
5	Back-EMF in phase (rms) (E_{ph})	20.7	20.5	25.8	V
6	Total harmonic distortion of back-EMF (THD_e)	5.1	6.3	3.8	%

The results show the lowest effect of the parasitic harmonics of the back-EMF with FESM, $THD_e = 3.8\%$. The proportion of harmonics is the highest with the concentrated winding of HPSMG, $THD_e = 6.3\%$. Comparison of the total harmonic distortion of the phase voltage (THD_u) shows that it is lowest with the toroidal winding and highest with the concentrated winding.

However, compared to the supply voltage U_{sup} , HPSMG is able to create considerably higher back-EMF with both winding types.

Based on the comparisons of three different types of winding geometry, in terms of the back-EMF, the toroidal winding of HPSMG can be regarded optimal.

3.7 Electromagnetic Force and Torque

It is required to apply force to make electromagnetic rotors rotate. It could be physical rotating force applied to the rotor in the generator operation, or the electromagnetic force F_{em} created by a magnetic field. In both cases, the body is rotated by a force that can be geometrically divided into two components. The first is the radial component and the second tangential component, which is relevant to rotating. A body is similarly affected by forces created by magnetism. According to Maxwell's stress theory, the intensity of the magnetizing field H between bodies creates a force in vacuum that can also be divided into the radial and tangential component [46]:

$$\sigma_{Fr} = \frac{1}{2} \mu_0 (H_r^2 - H_{\tan}^2), \quad (3.56)$$

$$\sigma_{F_{\tan}} = \mu_0 H_r H_{\tan} \quad (3.57)$$

$\sigma_{F_{\tan}}$ has been caused by uneven magnetic reluctance in different rotor positions. Because of this force, the rotor always tries to reach the position where the reluctance is smallest [47].

Even though the tangential component $\sigma_{F_{\tan}}$ is relevant, as it creates the rotating torque, the component σ_{Fr} also needs attention, because it could largely affect the dynamics of a power machine by causing more intensive wear and eccentricity to the bearing assembly in case of an asymmetric air gap [47].

Fig. 3.42 gives the HPSMG $\sigma_{F_{\tan}}$ and σ_{Fr} graphics in no-load conditions. The amplitude values of both components are between 12-15 kN/m², which confirms the applicability of the air gap shear stress $\sigma = 14$ kN/m² chosen for the design (Table 2.2).

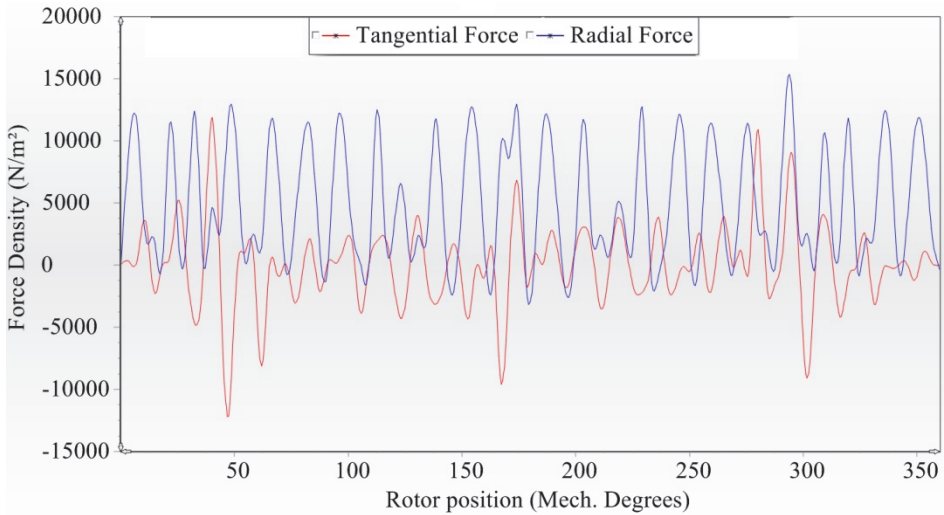


Fig. 3.42. The simulation of radial and tangential force components in HPSMG.

Fig. 3.43 presents analogous data for FESM.

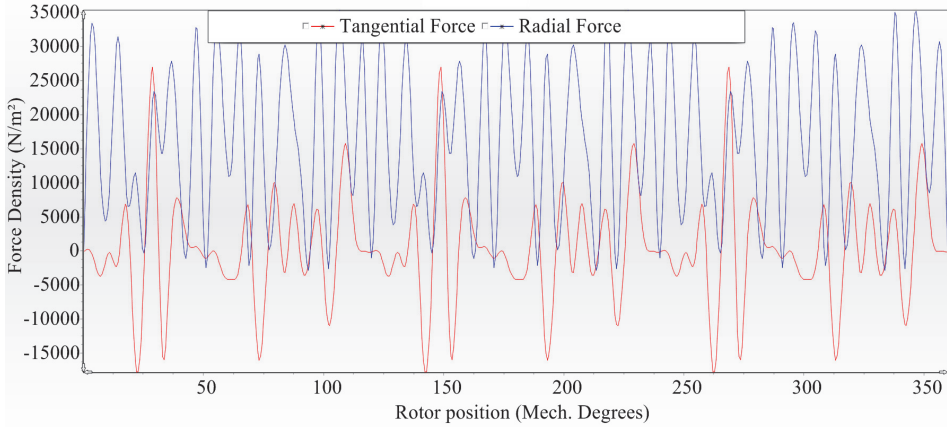


Fig. 3.43. The simulation of radial and tangential force components in FESM.

In this case, it should be noticed that the mean value of the FESM tangential component σ_{Ftan} does not differ significantly from that of the HPSMG, being within the limits of the initial numbers (Table 2.2). There are differences, however, in the peak values that are up to 25 kN/m². The differences are significant for the radial component σ_{Fr} , with the peak values up to 25 kN/m². It could be caused by the great number of poles and consequently, greater radial forces per stator surface unit.

Different theoretical methods are used to calculate the electromagnetic torque T_e . The main methods are Maxwell's stress tensor, the dq model and the magnetic co-energy method. Maxwell's stress tensor method is the simplest and most widely used. It considers the local flux density distribution along a defined contour around the air gap of the machine [46].

The virtual work method (VW) assumes that the electromagnetic torque equals the derivative of the magnetic co-energy with respect to the angular position at constant current.

The dq -model uses the fixed permeability method (FPM), which consists of inductances of dq -axes (single current excitation of the stator winding) and back-emf (single magnet excitation) [74].

Taking into account the asymmetry caused by rotor surface mounted permanent magnets, the electromagnetic torque T_{em} for the HPSMG and FESM can be calculated with the quadrature and direct axes dq -methodology. Accordingly, T_{em} would be [75]:

$$T_{em} = \frac{3}{2} p (\psi_{sd} \cdot i_{sq} - \psi_{sq} \cdot i_{sd}), \quad (3.58)$$

where p is the number of pole pairs, ψ_s - the flux linkage, and i_s - the current to the direct or quadrature axis in the stator.

With this methodology, the flux linkage ψ_s depends on both direct or quadrature component of the current:

$$\begin{aligned}\psi_{sd} &= \psi_{sd}(i_{sd}, i_{sq}), \\ \psi_{sq} &= \psi_{sq}(i_{sd}, i_{sq})\end{aligned}\quad (3.59)$$

If the motor is working on low load (low current), the flux linkage ψ_m on the direct axis from permanent magnets is added:

$$\begin{aligned}\psi_{sd} &= \psi_{sd} + \psi_{md} = L_{sd} \cdot i_{sq} + \psi_{md}, \\ \psi_{sq} &= L_{sq} \cdot i_{sd}\end{aligned}\quad (3.60)$$

If the machine is working on high load and torque, then saturation effects have to be considered. Therefore, the flux linkage is a function of both d - and q -axis current components. The complete model for a saturated motor [74]:

$$\begin{aligned}\psi_{sd}(i_{sd}, i_{sq}) &= L_{sd}(i_{sd}, i_{sq}) \cdot i_{sd} + \psi_{dm}(i_{sd}, i_{sq}), \\ \psi_{sq}(i_{sd}, i_{sq}) &= L_{sq}(i_{sd}, i_{sq}) \cdot i_{sq} + \psi_{qm}(i_{sd}, i_{sq})\end{aligned}\quad (3.61)$$

Adding up Eqs. (3.58) and (3.61), the electromagnetic torque T_{em} :

$$T_{em} = \frac{3}{2} p \left\{ [L_{sd}(i_{sd}, i_{sq}) - L_{sq}(i_{sd}, i_{sq})] \cdot i_{sd} \cdot i_{sq} + [\psi_{dm}(i_{sd}, i_{sq}) \cdot i_{sq} - \psi_{qm}(i_{sd}, i_{sq}) \cdot i_{sd}] \right\} \quad (3.62)$$

With modelling, the maximum value of HPSMG T_{em} by the dq -method was 3.06 Nm. For comparison, Fig. 3.44 gives the T_{em} characteristic in the virtual work method (VW) with a slightly lower result - 2.97 Nm.

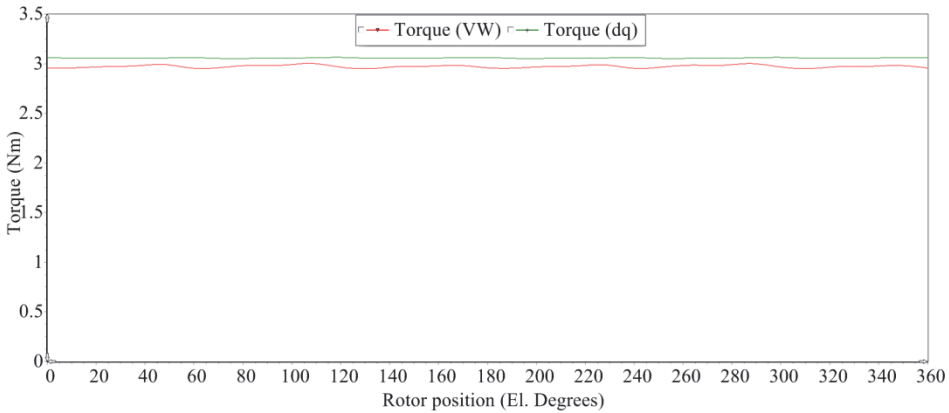


Fig. 3.44. HPSMG electromagnetic torque T_{em} simulation with the Gramme's winding in the VW method.

Fig. 3.45 shows the characteristic curve of the electromagnetic torque of the HPSMG concentrated winding modelled by the VW method, with an equivalent maximum result $T_{em} = 2.92$ Nm.

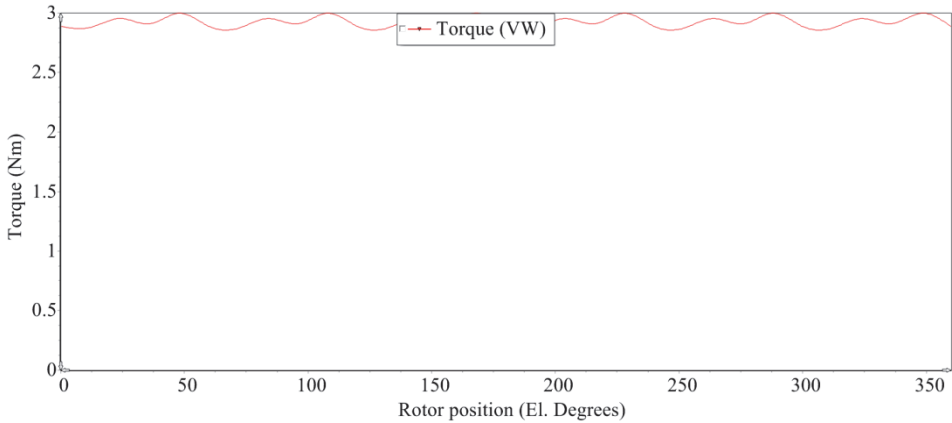


Fig. 3.45. HPSMG electromagnetic torque T_{em} simulation with the concentrated winding in the VW method.

However, comparison of the results in Figs. 3.44 and 3.45 shows that the characteristic line profile for the toroidal winding is much more even, which can be explained with the remarkably higher filling factor of the slots.

The T_{em} characteristic modelled by the FESM VW method presented in Fig. 3.46 is of similar pulsating character.

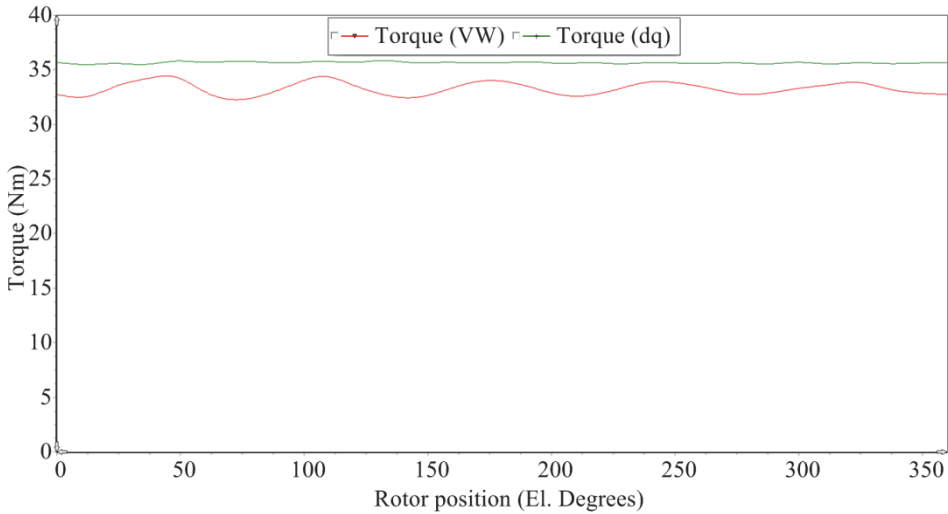


Fig. 3.46. FESM electromagnetic torque T_{em} simulation with the concentrated winding in the VW method.

As the FESM stator and winding geometry is similar to that of HPSMG concentrated windings, the shape of the T_{em} characteristic line can be attributed to the air gaps between the winding coils, which result in a lower filling factor of the slots as compared to toroidal windings.

The FESM moment maximum value by the dq -method was $T_{em} = 35.7$ Nm, which is close to the initial (Table 2.2) presumed value of the mechanical

moment $T_m = 36.0$ Nm. The modelled value for the last one was $T_m = 31.7$ Nm, which is slightly lower than the initial estimation.

3.8 Cogging Torque

Cogging torque describes the interaction between the rotor magnets and the stator teeth without any current. It is created by rotor magnets when they try to align to the smallest magnetic reluctance position to the stator, which generally are stator teeth. In reality, cogging torque has a very small part of the electromagnetic torque created by a motor [43].

There are several methods for calculating the cogging torque T_{cog} . The most widespread and easiest is the Maxwell's stress tensor surface integral method (TMSI) that only requires the flux density distribution around the air-gap [76].

$$T_{cog} = \frac{L_{stk}}{\mu_0} \int_0^{2\pi} r^2 B_r B_{tan} d\theta, \quad (3.63)$$

where L_{stk} is the length of the rotor, r - the closed surface radius surrounding the rotor, B_r and B_{tan} - radial and tangential components of the flux density. The result of integration can be multiplied by the number of pole pair p .

Another more widely spread method is the magnetic co-energy method (TCE). According to that, T_{cog} is proportional to the changes of the co-energy ΔW_c from the magnets and inversely proportional to the changes in the angle between the position of the rotor and the stator $\Delta\theta$ [74].

$$T_{cog} = \frac{\Delta W_c}{\Delta\theta} \quad (3.64)$$

This method can be considered more accurate than the previous one, as it helps to avoid the discretization noise which troubles the TMSI method [42]. Both of the methods above are applicable with the finite element analysis.

Analytically, T_{cog} can be calculated with an extended formula that takes into account the change of co-energy with the rotating magnet, also the number of pole pairs and the skewing effect [32]:

$$T_{cog} = \frac{\pi}{4} D L_{stk} \sum_n \frac{\sin(n\sigma \cdot L_{stk})}{n\sigma \cdot L_{stk}} \Lambda_n f_n \sin(n\theta), \quad (3.65)$$

where $n = k \cdot S$, $k = 1, 2, \dots, S$ is the lowest common multiple of the number of slots N_{slot} and poles $2p$, $\sin(n\sigma L_{stk})/n\sigma L_{stk}$ is the skewing effect, where σ is the skew angle, and Λ_n the n -th space harmonic of the permeance of the magnetic circuit.

For the HPSMG and FESM T_{cog} modelling, the SPEED PC-BDC and FEA software were used. The results were obtained with the finite elements method in the two ways described above.

Fig. 3.47 presents the corresponding HPSMG data for T_{cog} .

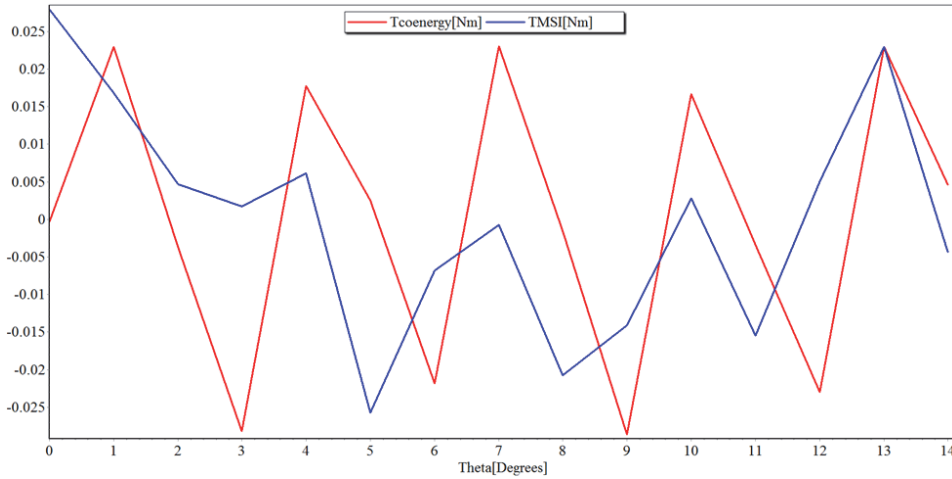


Fig. 3.47. HPSMG cogging torque simulation.

The graph shows that the amplitude values for T_{cog} vary with TMSI and TCE, being up to 0.03 Nm (the first case). With TCE, the maximum value is slightly lower, up to 0.023 Nm. In the middle section of the graph, a significant drop of T_{cog} can be noted with the TMSI. Maximum impulses left aside, the mean amplitude value of T_{cog} can be set as 0.02 Nm, which is almost 1% of the calculated mechanical torque T_m (Table 2.2). This result can be considered good, since the cogging and electromagnetic torque ripple in high-quality machines is 1-2% of the rated torque [32].

Similar modelling was used for the FESM T_{cog} parameters. Fig. 3.48 shows the results obtained.

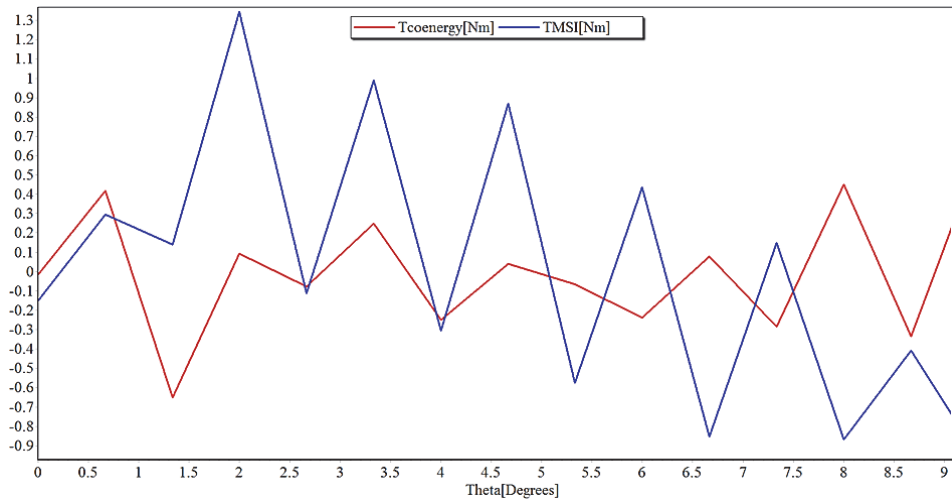


Fig. 3.48. FESM cogging torque simulation.

The graph once again shows TMSI impulses of large amplitude, reaching up to 1.4 Nm. With TCE, the maximum values of T_{cog} are almost up to 0.6 Nm, which is also the T_{cog} mean value of both graphs. That is almost 1.7% of the calculated T_m value (Table 2.2). Similar to the HPSMG results, the FESM T_{cog} level could be considered good according to the modelling results.

One of the reasons for these results for both machines is a large number of slots and poles. Also, fractional slot per pole, thicker tooth tips to avoid saturation, minimal slot openings and radius or chamfer of magnet poles and stator tooth tips [32] could be pointed out.

3.9 Output Power and Efficiency

For the HPSMG and FESM power output and efficiency data, the modelling software Motor-CAD E-Mag was used. To obtain the HPSMG output parameters, a concentrated winding was modelled in addition to the toroid winding. The basis for the analyses was the nominal supply voltage $U_{sup} = 18.5 \text{ V}_{DC}$ that had to guarantee the propeller rotational speed of at least $n = 3000 \text{ rpm}$, which was needed for stable flight of the light aircraft (Section 2.2) [72].

Table 3.2 gives the numeric values from modelling for the toroidally wound HPSMG on the nominal supply voltage.

Table 3.2. Modelled parameters of toroidally wound HPSMG ($U_{sup} = 18.5 \text{ V}_{DC}$)

No.	Symbol	Name	Values	Unit
1	n_{const}	Speed limit for constant torque	3340	rpm
2	n_0	Speed limit for zero torque	4380	rpm
3	P_1	Input power	616	W
4	P_2	Output power	558	W
5	P_{loss}	Total losses	57.7	W
6	η	Efficiency	90.6	%
7	T_m	Mechanical shaft torque	1.53	Nm

The table displays the parameters shaping and influencing the mechanical power P_2 , including P_{loss} and η . In addition, the created mechanical torque T_m directly dependent on P_2 and the rotational speed n is given. For rotational speeds n with the supply voltage U_{sup} , the highest no-load torque n_0 and minimal rotational speed n_{const} necessary for the T_m is presented. The results indicate that regardless of the low supply voltage, amounts of current in windings on the input power P_1 , the HPSMG total losses P_{loss} are comparatively small, resulting in the efficiency coefficient $\eta = 90.6\%$. As the BLDC machines have no official standard [26], the η value can be compared to a certain extent to the standards IEC 60034-30 and IEC 60034-31 for industrial electrical machines comprising motors of the supply frequency $f_1 = 50 \text{ Hz}$. According to these standards, the lowest limit for

useful output with Super Premium Efficiency IE4 is $\eta \approx 88\%$ (Fig. 2.1) [19]. As the HPSMG operating frequency in this case is ten times higher ($f_m = 500$ Hz, $n = 3000$ rpm) than the industrial machines, it also increases the iron losses P_{Fe} , in addition to copper losses P_{Cu} due to high level of current. Therefore, considering the previous, the efficiency of the toroidal winding HPSMG can be rated as very good.

Under normal conditions, motor speed is limited by the voltage supplied to the motor windings by the inverter. The voltage on the motor windings is usually synchronized with the rotor position, which produces the maximum torque per ampere from the motor. A phase advance is the demagnetizing armature reaction of the current \dot{I}_{res} relative to the main electromotive force \dot{E}_1 . This is exploited for flux-weakening, which permits the BLDC machines to operate at high speeds even when the back-EMF exceeds the supply voltage [42]. As the stator current \dot{I}_{res} is not up to the electromotive force \dot{E}_1 , the armature reaction on the direction of the d -axis is demagnetizing, which reduces \dot{E}_1 and the main magnetic flux Φ_m (Fig. 3.49).

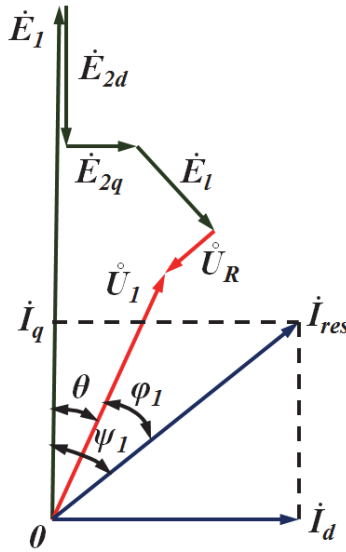


Fig. 3.49. Typical vector diagram to illustrate armature reaction in BLDC machines.

Speed characteristics of both HPSMG and BLDC machines are similar to shunt motors with brushes. Therefore, the rotational speed n and main magnetic flux Φ_m are inversely proportional (Section 3.1, Eq. (3.12)) [26]. However, this depends on the demagnetizing effect of the anchor field that strengthens or weakens the main magnetic flux. This extent of the effect is first and foremost determined by the value of the directional component \dot{I}_d and the phase advance θ_{ph} of the resulting load current \dot{I}_{res} . If the last one is changed, the rotational speed or torque of the BLDC machine can be changed, as they are inversely proportional.

Fig. 3.50 gives the characteristics of the toroidal winding HPSMG mechanical power P_2 depending on the nominal supply voltage U_{sup} , power used I_{sup} and rotational speed n at different phase advances between $\theta_{ph} = 0-90^\circ$.

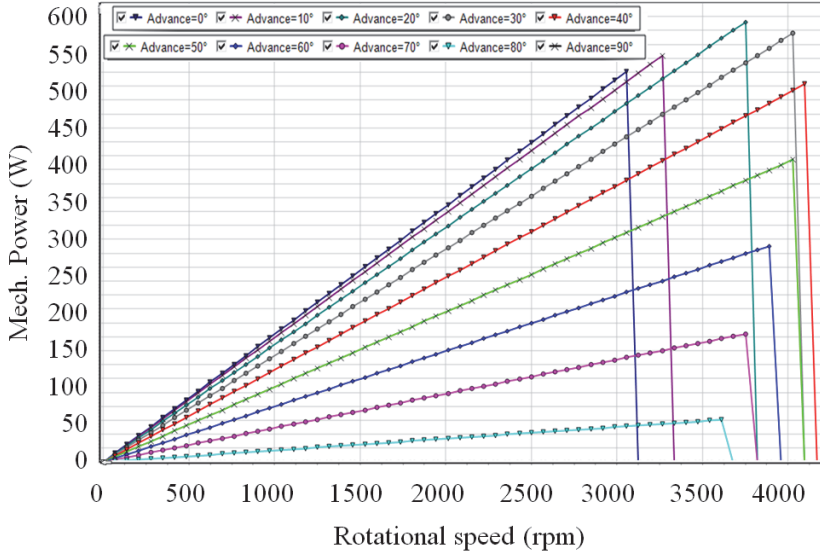


Fig. 3.50. Mechanical output power relation to the rotational speed of HPSMG with the toroidal winding $U_{sup} = 18.5 V_{DC}$ and $I_{sup} = 35 A$ corresponding to different phase shift angles.

Phase shift angles are at the step $\theta_{ph} = 10^\circ$. In that case, the highest rotational speed for the HPSMG will be $n = 4380$ rpm, phase shift $\theta_{ph} = 40^\circ$, but as the field weakening reduces the overall torque output available from the motor [77], the output power will also be reduced to the minimum level.

Table 3.3 presents the characteristics of the concentrated winding HPSMG.

Table 3.3. Modelled parameters of HPSMG with the concentrated winding ($U_{sup} = 18.5 V_{DC}$)

No.	Symbol	Name	Values	Unit
1	n_{const}	Speed limit for constant torque	3530	rpm
2	n_0	Speed limit for zero torque	3760	rpm
3	P_1	Input power	617	W
4	P_2	Output power	548	W
5	P_{loss}	Total losses	69.2	W
6	η	Efficiency	88.8	%
7	T_m	Shaft torque	1.50	Nm

The output parameters given in Tables 3.2 and 3.3 show that the toroidal winding HPSMG is able to hold the constant useful torque T_m up to the

rotational speed $n_{const} = 3341$ rpm, which is almost $n \approx 190$ rpm lower than with the concentrated winding. However, in the first case, the rotational speed on no-load is almost $n_0 = 620$ higher. That refers to a smaller demagnetizing effect of the armature reaction in the case of concentrated windings, which increases the torque T_m but reduces the rotational speed n_0 .

Even though certain reduction of the main magnetic flux and EMF can be observed with toroidal windings due to the demagnetizing effect of armature reaction, its T_m value exceeds the concentrated winding torque by 2% for useful torque. The result coincides with the percentage ratio of T_{em} of the electromagnetic torque calculated in the comparative study of the toroidal and concentrated windings (Section 3.5), which was also 2% (Eq. (3.35)).

Comparison of the rate of losses P_{loss} and consequently, the efficiency factor η shows that the first parameter is almost 12 W lower for the toroidal winding, which also results in the efficiency factor of $\sim 2\%$ and 10 W higher output power P_2 .

Table 3.4 gives the distribution of losses and the numerical data according to their type for HPSMG.

Table 3.4. HPSMG losses

HPSMG with the Gramme's winding

No.	Symbol	Name	Values	Unit
1	P_{Cu}	Copper loss in windings	43.8	W
2	P_{eddy}	Eddy current loss in the stator	1.9	W
3	P_{hys}	Hysteresis loss in the stator	5.7	W
4	P_{PM}	Magnet loss	6.4	W

HPSMG with the concentrated winding

No.	Symbol	Name	Values	Unit
1	P_{Cu}	Copper loss in windings	51.9	W
2	P_{eddy}	Eddy current loss in the stator	2.2	W
3	P_{hys}	Hysteresis loss in the stator	6.7	W
4	P_{PM}	Magnet loss	8.4	W

As the tables show, the losses with the concentrated windings geometry are larger in all sectors, which can be explained by more end connections than in toroidal windings (Section 3.5). As the concentrated winding has the winding coil around the stator tooth, which gives the cross-sectional area of 33% larger than the yoke with the toroidal winding coil, it results in about twice more iron loss in the tooth section ($P_{Fe} = 7.3$ W ja $P_{Fe} = 3.5$ W) due to the larger magnetic flux from the smaller, but with a larger cross-section magnetic core.

The situation is reversed with the stator yoke of a toroidal winding where $P_{Fe} = 4.1$ W and $P_{Fe} = 1.6$ W are about 2.6 times larger.

To sum up, with toroidal windings, the total iron losses are about 15% lower, $P_{Fe} = 7.6$ W; and with concentrated windings $P_{Fe} = 8.9$ W. In both cases, the

results coincide with the calculated results in Section 2.6.1, $P_{Fe} = 8.0$ W, which confirms the relevance of the calculations.

Next, the characteristics of FESM power and efficiency are described. The results obtained by modelling with the software Motor-CAD EMag are shown in Table 3.5.

Table 3.5. Modelled parameters of FESM with the concentrated winding ($U_{sup} = 51.8$ V_{DC})

No.	Symbol	Name	Values	Unit
1	n_{const}	Speed limit for constant torque	3630	rpm
2	n_0	Speed limit for zero torque	4100	rpm
3	P_1	Input power	10747	W
4	P_2	Output power	9970	W
5	P_{loss}	Total losses	776.4	W
6	η	Efficiency	92.8	%
7	T_m	Shaft torque	31.7	Nm

Fig. 3.51 gives the modelled characteristic for the output power P_2 of FESM that depends on the rotational speed n at different phase advances between $\theta_{ph} = 0-90^\circ$.

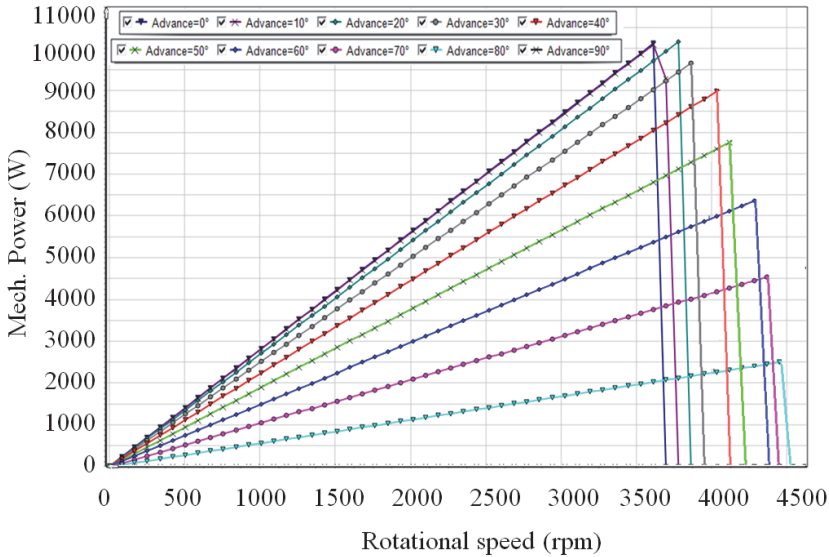


Fig. 3.51. Mechanical output power relation to the rotational speed of FESM $U_{sup} = 51.8$ V_{DC} and $I_{sup} = 250$ A.

The result indicates that the FESM input power P_1 is almost 17% lower than the initial estimated number (Table 2.2), which is directly the result of the technical data of the inverter used and could be taken into account for modelling

(more precise data compared to the initial input). Therefore, the output power ($P_2 \approx 10$ kW) on the nominal rotational speed $n_n = 3000$ rpm is also smaller. As the FESM efficiency factor is even higher than the efficiency factor for the HPSMG examples ($\eta \approx 93$ %), the difference of the initial estimated results and modelled results is only 9%. Due to that, the FESM mechanical moment T_m is also almost 12% smaller. To obtain the initial data for P_2 and T_m given in Table 3.3, a more powerful inverter should be used with the input DC for the supply voltage $U_{sup} = 51.8$ V_{DC} at least 30 A larger, i.e. $I_{sup} = 280$ A.

Table 3.5 shows that the value of T_m is ensured by FESM for the rotor rotational speed of up to $n = 3630$ rpm, which gives a sufficient margin for the value of the predefined nominal rotational speed $n_n = 3000$ rpm (Table 2.2). The FESM rotational speed at no-load n_0 is only 4100 rpm. As the machine has a significant number of magnetic poles ($2p = 42$), the remagnetization frequency in the magnetic circuit is very high ($f_n = 1050$ Hz, $n_n = 3000$ rpm). The remagnetization frequency for the previously given no-load rotational speed $n_0 = 4100$ rpm would be $f_0 = 1435$ Hz, which would increase the iron losses P_{Fe} almost 20% (Fig. 2.14, Section 2.6.2) as compared to the iron losses at nominal frequencies f_n . Therefore, the chosen nominal rotational speed n_n is reasonable for lower hysteresis losses.

Table 3.6 gives the numerical data of the FESM losses.

Table 3.6. FESM losses

No.	Symbol	Name	Values	Unit
1	P_{Cu}	Copper loss in windings	395.2	W
2	P_{eddy}	Eddy current loss in the stator	67.9	W
3	P_{hys}	Hysteresis loss in the stator	115.9	W
4	P_{PM}	Magnet loss	197.4	W

As the currents in the windings are large even in nominal conditions, it can be expected that the proportion of copper losses P_{Cu} is the largest 51% of the total loss P_{loss} , but the percentage is almost 25% smaller than the losses in either HPSMG winding.

Losses in permanent magnets P_{PM} are 25% of the total losses. It can be explained by the large number of poles in the FESM, i.e., 2.1 times more than for the HPSMG, where the percentage of magnetic loss is proportionally smaller, i.e., 10...11%, depending on the type of the winding. FESM also uses more powerful permanent magnets.

As FESM operates on high frequencies, it causes higher hysteresis losses P_{hys} that are 15% of the total losses. For HPSMG operating at lower remagnetizing frequencies, the result is 10%.

The eddy current losses P_{eddy} are also predictable, 9% of total losses (3% for both windings of HPSMG). The noticeable difference is mainly caused by the longer FESM stator length L_{stk} , marginally also by the slightly thicker stator material.

The highest iron losses $P_{Fe} = 150.2 \text{ W}$ are in the teeth layer of FESM, forming 19% of the total losses P_{loss} , mainly caused by hysteresis losses occurring at high frequencies f_n . The number is lowest, 6%, for the HPSMG toroidal winding and 11% for the HPSMG concentrated winding.

Depending on the location of the coils, the proportion of iron losses to total losses is the highest for the toroidal winding HPSMG, amounting to 7%. With FESM, the result was 4%, but with the HPSMG concentrated winding, only 2%.

Even though the loss percentages for FESM were higher for some characteristics than those for HPSMG, the efficiency factor η for FESM is still 2.2% higher than for the HPSMG toroidal winding and 4% higher than for the concentrated winding. One of the main reasons for that could be the thin material for the stator, i.e. the proportion for thickness to the stator length L_{stk} of one sheet is almost twice smaller than for HPSMG.

3.10 Conclusion

Chapter 3 covered the analysis and planning of the electromagnetic aspects of HPSMG and FESM. First, through a theoretical analysis, the magnetic circuit parameters of both machines were studied schematically and mathematically. Then, the characteristics of the secondary magnetic field were described and finally, the total impact of the resulting magnetic field was discussed.

The software FEMM 4.2, SPEED PC-BDC and Motor-CAD BPM-EMag was used for modelling the distribution of the magnetic field. The results were compared with analytic results that coincided to a considerable extent.

The armature reaction or short circuit was discussed in a subsection of the chapter. The modelled inrush current created in the process exceeded the nominal current of HPSMG for more than ten times and FESM for more than 20 times. In general, such current levels are quite regular for inrush currents. Short circuit due to armature reactions is a problem mainly for HPSMG and FESM in the generator operation, when both machines are mechanically rotated by ICE, which is not affected by a short circuit. However, in a motor operation, the protective device inside the inverter will be activated due to short circuit and the motor will stop. It applies both HPSMG and FESM.

Chapter 3 also presented a comparative analysis of the one-layer Gramme's and two-layer concentrated windings. For that purpose, electrical and magnetic parameters of a machine similar to HPSMG in its geometrical dimensions were modelled. The main difference was the configuration of the stator yoke, which was not inside the stator, as in a conventional HPSMG, but mounted on the inner perimeter to make it comparable to FESM. Such configuration enabled use of the two-layer concentrated winding and direct comparison with the toroidal winding.

The analyses showed that in the case of Gramme's winding, the losses due to flux leakages were somewhat smaller than those of the more conventional concentrated winding. Further, with the same stator height, a remarkably higher

slot filling factor was obtained, which enables more turns in a slot. Additionally, a stator core smaller in dimension and lighter in weight can be used.

Contrary to the lower calculated magnetic flux values, modelling gave the same or higher values for the electromagnetic torque for the toroidal winding in HPSMG (compared to the concentrated two-layer winding). In addition, the iron losses were about 15% lower. The lowest back-EMF extra harmonics effect was with FESM, the highest with the two-layer concentrated winding HPSMG. However, toroidal windings had the highest efficiency concerning the phase voltage distortions.

To conclude, the comparative study of the three different machines showed that the stator and winding geometry, parameters and mass, magnetic losses and consequently, the electromagnetic characteristics are optimal for the Gramme's windings and the stator configuration, accordingly.

4 THERMAL ANALYSIS

Working electrical machines generate heat which results from their electrical, magnetic and mechanical losses. Additionally, electrical machines produce losses which are difficult to take into account. These are, for example, eddy current losses, losses caused by uneven distribution of the magnetic flux in a stator core. These losses are called additional losses, which are estimated by $P_{add} \approx 0.5-2.5\%$ of useful output of the generator or of the power taken from the mains by the motor [46]. Extraction of the resulting thermal energy is of critical importance while maintaining useful life of an electrical machine. This is of particular importance for electrical machines of larger energy density and specific powers, which constitutes the main part of this thesis research.

As with electrical machines in general, distribution of temperature field in synchronous machines with permanent magnets is commonly described using field equations. The sources of the temperature field are dissipated power p_k in the construction elements of PMSM and volume densities $p_k(x,y,z)$ of those which generate the vector field of the heat flux density $q(x,y,z)$ defining the distribution of the temperature field. In the defined distribution of the temperature, the dissipated power P_v in volume V must be proportional to the summary leaving heat flow Q'_v , which passes through the area A , limiting the volume:

$$Q'_v = \int_A q \cdot dA = \int_V p_k \cdot dV = P_v \quad (4.1)$$

This expression can be shortly expressed as a differential through the divergence of the vector of heat flux density:

$$\text{div } q = \nabla \cdot q = p_k \quad (4.2)$$

By its essence, temperature field is a field of potential which is characterized by a scalar value temperature $\theta(x,y,z)$. Therewith spreading direction of the heat flux density vector q in an observable body or environment is defined by the direction of the fastest temperature decrease direction in a respective field point where the heat resistivity of the material or the environment is λ . Spreading of the vector q of heat conduction can be thus characterized by the following differential equation:

$$q = -\lambda \cdot \text{grad } \theta = -\lambda \nabla \theta \quad (4.3)$$

Distribution of the temperature field in this situation can be described by the second order Poisson differential equation, describing the dissipation of heat flux density factor in the field point through the temperature function gradient:

$$-\nabla \cdot (\lambda \nabla \theta) = p_k \quad (4.4)$$

In the heat transition process analysis, time-dependent characterizing component is added to this equation:

$$-\nabla \cdot (\lambda \nabla \theta) + \rho c_p \left(\frac{\partial \theta}{\partial t} \right) = P_k, \quad (4.5)$$

where ρ is density and c_p is the specific heat of air at constant pressure.

To solve such type of a field potential task in a stationary situation, in the first step, the distribution of the scalar temperature function $\theta(x,y,z)$ is defined by solving the Poisson equation. On this basis, the vector field of the heat flux density $q(x,y,z)$ as the distribution of the gradient function of the temperature field is determined.

Boundary conditions of the area observed should be defined to solve the Poisson equation and thus find the distribution of the temperature field. In some boundary sections where the predefined temperature value or the pattern of temperature distribution is known, Dirichlet boundary condition is applied:

$$\theta = \text{const} \quad \text{or} \quad \theta = \underline{\theta} = \theta_o(x,y,z).$$

Using the sum of the dissipation values of the heat flux and heat conduction from the surface, continuity of a normal component of the heat flux density vector as a second order boundary condition can be expressed for some boundary sections:

$$q_n = \underline{q} + \alpha_{con} \theta, \quad (4.6)$$

where α_{con} is the heat conduction coefficient (convective or irradiative heat conduction) on the boundary surface.

In electrical machines, such boundary surfaces usually are surfaces of windings, magnetic circuits, housing of the machine or endcaps being cooled with a gas (e.g. cooling air) or a liquid. This boundary condition can be expressed with another equation frequently used:

$$\lambda \left(\frac{\partial \theta}{\partial n} \right) = -\underline{q} - \alpha_{con} \theta \quad (4.7)$$

This mixed type boundary condition, called also Cauchy boundary condition, unites an effect of boundary surface temperature and heat flux density dissipating from the boundary surface. If the temperature field is present, the Neumann boundary condition known from the field theory can be calculated from the Cauchy boundary condition in case of no convective or irradiative heat conduction ($\alpha_{con} = 0$).

In case the temperature field is present, the Neumann boundary condition is applied directly when the heat flux passes through the boundary surface between the two construction elements made from two materials with different heat conduction coefficients.

Solution of these two field equations enables the exact distribution of temperatures in the PM electrical machine and the temperature of each

construction assembly should be theoretically found. However, this would mean using materials with homogeneous and isotropic properties, and exact defining of the geometry of boundary conditions of the temperature field.

In actual permanent magnet synchronous machines, several active and construction materials have inhomogeneous heat resistivity and some of them have anisotropic properties. For example, in the cross-sectional area of the armature winding, conductor copper, wire insulation and impregnation, also air bubbles are placed intermittently and irregularly. In armature magnetic field, heat conductivity along the electrotechnical steel sheet is 15...20 higher than conductivity in the transversal to the sheets. Additionally, technological air gaps are present between the construction elements of many electrical machines, decreasing heat transmission and deteriorating cooling conditions.

Boundary surfaces of the volume parts characterizing different zones of the temperature field are of a very complicated shape in PM machine and describing them by coordinates is mathematically difficult. Thus, setting limiting conditions is complicated while solving differential equations. Examples of boundary surfaces with a complicated shape are end-connections of an armature winding, also the boundary surface of the air gap in the zone between the armature teeth and slot openings and permanent magnets. But if their shape is simplified significantly, precision of the analysis results is lost.

Thus, a thermal equivalent circuit method is used in heat calculations of synchronous machines excited with permanent magnets. Thermal equivalent circuits of different complexity are used giving a certain number of measurable average temperatures of active nodes of an electrical machine. Precision of temperatures calculated with thermal equivalent circuits method is up to $\pm 3...5$ °C, which is sufficient in electromechanics. If necessary, after calculation of average node temperatures, additionally, more precise distribution of the temperature of the temperature field in an important or critical zone of an electrical machine is calculated using differential equations in this part of the zone.

Temperature field equations can also be solved by analytical modelling, using computed modelling methods (finite element method, finite-difference method, trace element method etc.). Several software packages have been developed for use in modelling in the temperature field, like MotorCAD, which was used in this thesis.

Heat resulting from losses breaks away into the surrounding environment by thermal conductivity, emission and convection.

In electrical machines, thermal conductivity occurs mainly in solid components like the winding and its isolation, magnet and rotor yoke, steel laminations of stator core etc. In this case, thermal conduction moves from a warmer object to a cooler one. Heat flow dissipated by the conduction Q'_{con} is expressed as follows [37]:

$$Q'_{con} = \frac{\alpha_{con} A}{l} (g_1 - g_2), \quad (4.8)$$

where A is the area and l is the length of the flow path, ϑ_1 is the temperature of the warmer object, and ϑ_2 is the temperature of the colder object.

The heat flow dissipated by radiation Q'_{rad} depends mostly on the temperature, color, and the texture of the surface. The resulting heat flow is manifested according to the Stefan-Boltzmann law [46], [78]:

$$Q'_{rad} = e_s q_{sb} A (T_{k1}^4 - T_{k2}^4) = \alpha_{rad} A (T_{k1}^4 - T_{k2}^4), \quad (4.9)$$

where q_{sb} is the Stefan-Boltzmann constant, $5.65 \cdot 10^{-8} \text{ W/m}^2\text{K}^4$, e_s is emissivity of the surface, $T_{k1} = (\vartheta_1 + 273)$ and $T_{k2} = (\vartheta_2 + 273)$, α_{rad} is the converted radiation coefficient.

While the electrical machine is warming up, as a result of losses, convection takes place, which means contact of its hot solid parts with gas or liquid, resulting in a rotating process where hotter gas or liquid rises upwards as its density and mass are lower, giving its place to particles not yet warmed up. Regarding gases and liquids, in electrical machines, they are usually cooling components. The two types of convection are natural and artificial dissipation of heat. As for the latter, forced ventilation of exterior and interior parts of the machine with increased air velocity is used to intensify heat dissipation. Ventilators of different configurations or impellers are used there similar to HPSMG and FESM.

The heat flow Q'_{cv} resulting from natural convection is found by the following equation [70]:

$$Q'_{cv} = \alpha_{cv} A (\vartheta_1 - \vartheta_2), \quad (4.10)$$

where α_{cv} is the heat transfer coefficient of convection.

To calculate heat flow from the ventilated surface resulting from forced cooling, an approximate empirical heat transition coefficient α_f is applied [37]:

$$\alpha_f = \alpha_{cv} (1 + C_{cv} \sqrt{v}), \quad (4.11)$$

where C_{cv} is the empirical coefficient depending on the uniformity of the surface ventilated, v is the motional velocity of the cooling medium (gas, liquid etc.) related to the cooled surface.

Total heat flow Q'_T resulting from thermal dissipation into ambient environment is the sum of thermal conduction, thermal emission and thermal convection:

$$Q'_T = Q'_{con} + Q'_{rad} + Q'_{cv} = (\alpha_{con} + \alpha_{rad} + \alpha_{cv}) (T_{k1}^4 - T_{k2}^4) \cdot A = \alpha_T A (T_{k1}^4 - T_{k2}^4) \quad (4.12)$$

If the total heat flow Q'_T and the temperature rise of the machine are known, it is possible to calculate the amount of cooling medium [78]. The cooling element for HPSMG and FESM is air, thus the amount of air Q necessary for heat dissipation is calculated. Similarly, the rated power of the ventilator and in

the context of HPSMG and FESM, rated power of the impeller and also rated power of the propeller necessary for generating such an amount of air are calculated. The amount of air Q is calculated as follows [78]:

$$Q = \frac{Q_T}{c_p \Delta T_k} V \frac{(\vartheta_{in} + 273)}{273} \cdot \frac{760}{H_g} \cdot 10^3, \quad (4.13)$$

where c_p is the specific heat of air at constant pressure, V is the volume of 1 kg air in m^3 , ϑ_{in} is the temperature of the air incoming into the machine, and H_g is the barometric pressure.

In case the amount of air Q should be generated by the ventilator (impeller and/or propeller) that has efficiency η and defined air pressure p_{air} , the necessary rated power of ventilator P_{vent} is expressed as follows [78]:

$$P_{vent} = \frac{p_{air} Q}{\eta \cdot 10^3} \quad (4.14)$$

HPSMG and FESM have similar internal axial self-cooling properties by using impellers mounted on their outer rotors (Figs. 4.1 and 4.2).

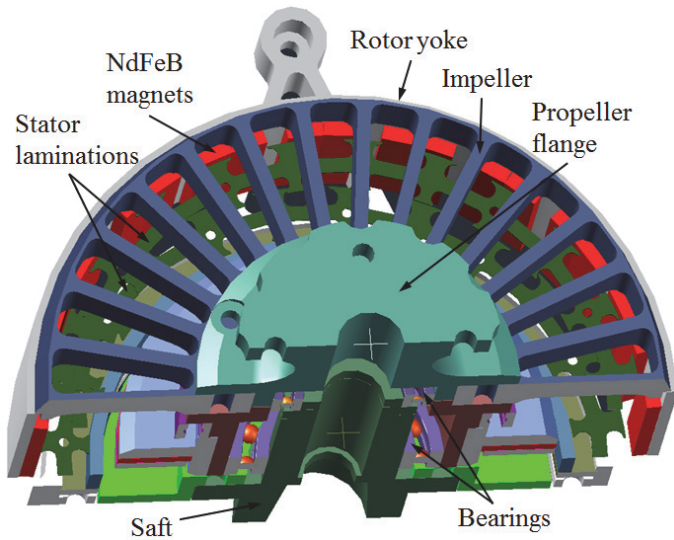


Fig. 4.1. Axial cooling system of HPSMG.

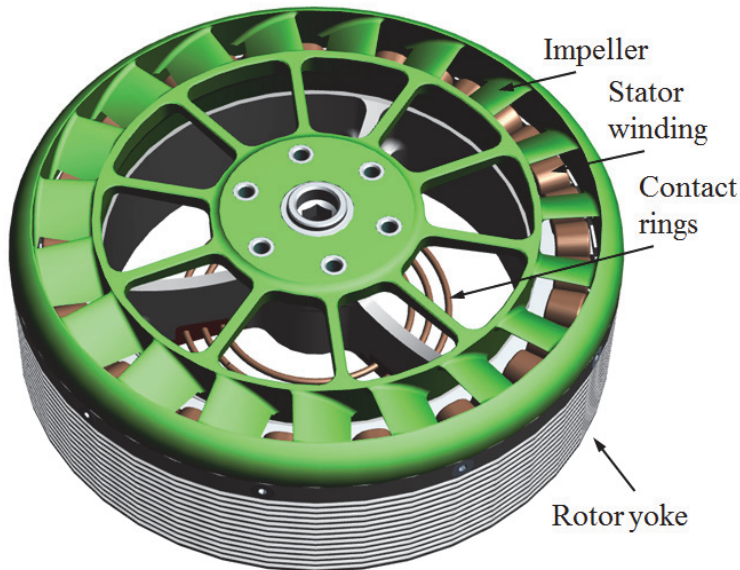


Fig. 4.2. Axial cooling system of FESM.

In both machines, pusher propellers situated at the back side of UAV and the paraglider are used. Thus, impellers are located in the rear of the ventilation system of the machines (regarding the direction of aerial vehicle motion). Based on the above, an impeller has been designed, which ensures sucking ventilation where the air suctioned from the frontal ambient environment goes through the interior of the machine and then returns to the environment.

In case of axial ventilation, the air flow moves across the exterior surfaces of the stator and magnets, crossing the air gap. Moving alongside the parts to be cooled, the air warms up; thus, heating of the machine in the axial direction is inhomogeneous. Usually, axial cooling is applied in machines in which the active part of the rotor does not exceed $L_{stk} = 200-250$ mm [70]. As respective lengths of HPSMG and FESM do not exceed 40 mm, this type of cooling is justified and in this case also more effective than radial cooling. In trough ventilation, one of the main dangers is dust in the suctioned ambient air, which deteriorates cooling properties while the air passes through the machine and in the worst case, may cause overheating or mechanic failures. As HPSMG and FESM are both of open design, this improves air passage inside them. Also, the front side of the machines is attached to the fuselage of the aerial vehicle where it is more shielded. Additionally, the environment is clean, as most of the time the machines function high above the ground.

4.1 Thermal Modelling

This section discusses HPSMG and FESM cooling. To receive relevant results, cooling a machine was modelled using special software Motor-CAD

Thermal. In HPSMG, Gramme's winding and a concentrated winding were compared. Thermal modelling is based on the principal concept of the selected cooling type and nominal parameters of the machines, including supply voltages U_{sup} , supply currents I_{sup} , and nominal rotating speeds n_n (Table 2.2).

4.1.1 HPSMG with the toroidal winding

Based on our modelling results, temperature characteristics of different parts of HPSMG were obtained (Fig. 4.3).

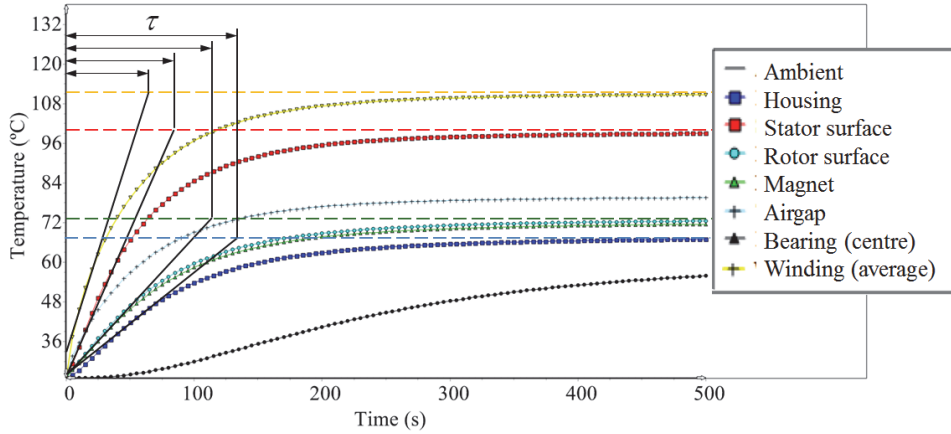


Fig. 4.3. Heat transient graphs of HPSMG with Gramme's winding.

The hottest part of the machine is the winding, the maximum value of mean temperature of which exceeds $\vartheta_{2win} = 110$ °C. The winding with the stator attains consistent working temperature slightly faster than permanent magnets and the rotor. Therefore, their temperature constant average is $\tau \approx 70$ s in the first case and $\tau \approx 120$ s in the second case. In conclusion, the final temperature is reached within four times of the time constant values. A thermal time constant τ can also be found analytically [37]:

$$\vartheta_{(t)} = \vartheta_0 + (\vartheta_p - \vartheta_0) \left(1 - e^{-\frac{t}{\tau}} \right), \quad (4.15)$$

where ϑ_0 is the initial temperature (°C) and t is time (s).

Regarding temperatures, the surface covered by the stator winding is the next, the maximum temperature of which is approximately $\vartheta_{2s} = 98$ °C and which develops in about 350 s. Temperature in the air gap reaches up to 80 °C and up to 72 °C in magnets. In Figs. 4.4 and 4.5, radial and axial distribution of the temperatures of HPSMG with Gramme's winding is shown.

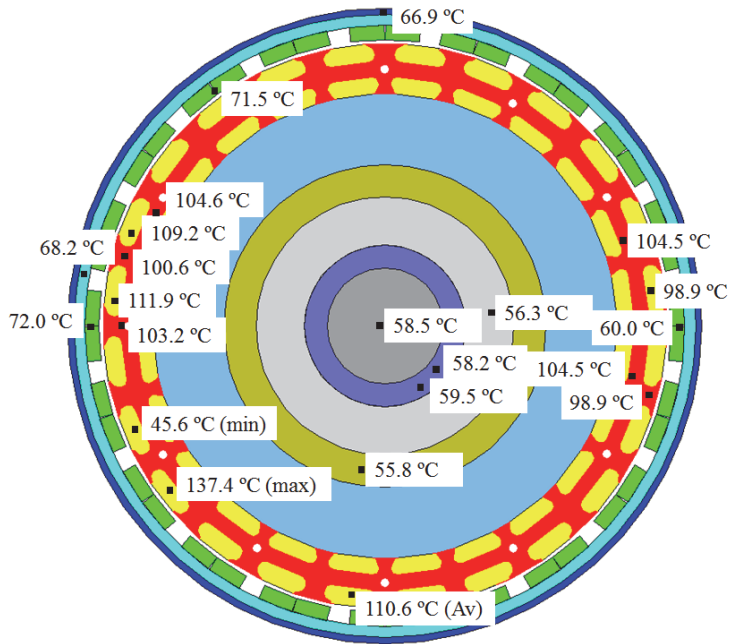


Fig. 4.4. Radial temperature distribution of HPSMG with the toroidal winding.

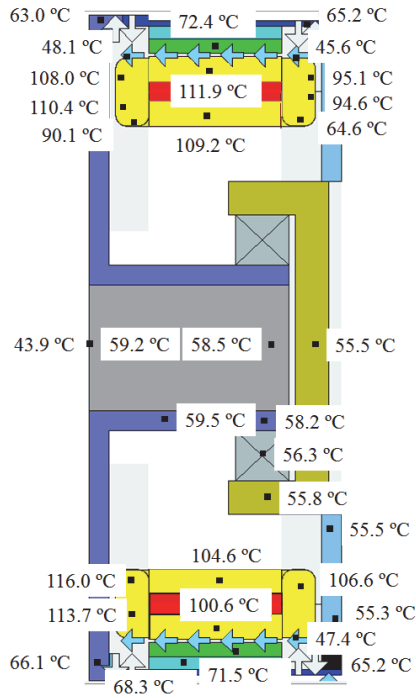


Fig. 4.5. Axial temperature distribution of HPSMG with the toroidal winding.

Temperature distributions show that inside the winding the mean temperatures are $\vartheta_{2win} = 110\text{ }^{\circ}\text{C}$. But the maximum values are up to $\vartheta_{2max} = 137\text{ }^{\circ}\text{C}$ (Fig. 4.4), which is to be taken into account when finding the temperature class of the winding conductor. For HPSMG, it has been chosen with the temperature index of $212\text{ }^{\circ}\text{C}$. (Section 2.8.1). In other important parameters, including permanent magnets, temperatures do not exceed maximum permitted values (Section 2.7.1, Fig. 2.19).

Appendix 2 shows an equivalent scheme of temperatures in different parts of HPSMG with the Gramme's toroidal winding.

4.1.2 HPSMG with the concentrated winding

Temperature characteristics of HPSMG with the concentrated winding to be compared are shown in Fig. 4.6.

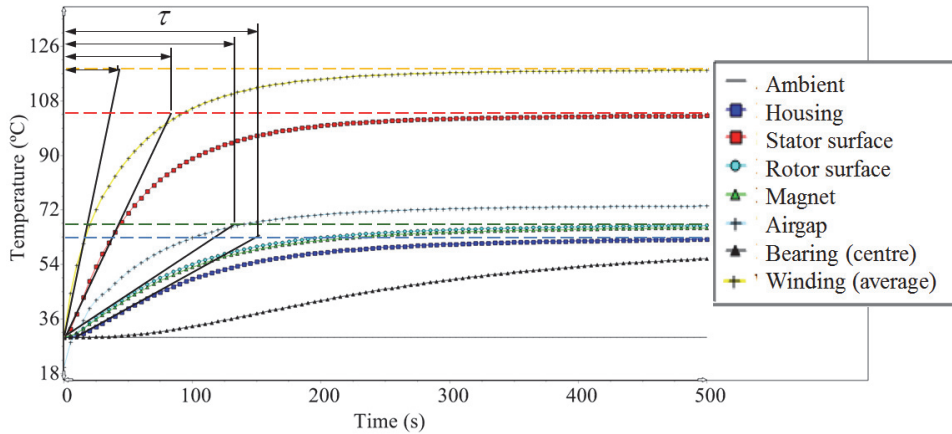


Fig. 4.6. Heat transient graphs with the concentrated winding.

Maximum permanent value of the mean temperature of the winding is higher than $\vartheta_{2win} = 117\text{ }^{\circ}\text{C}$, i.e. approximately by $7\text{ }^{\circ}\text{C}$ higher than in the toroidal winding. Constant temperature of active parts is attained similar to the abovementioned winding approximately within 400 s, as a result, giving the temperature constant similarly $\tau = 100\text{ s}$. In Figs. 4.7 and 4.8, the radial and axial distribution of temperatures in different parts of the machine is shown.

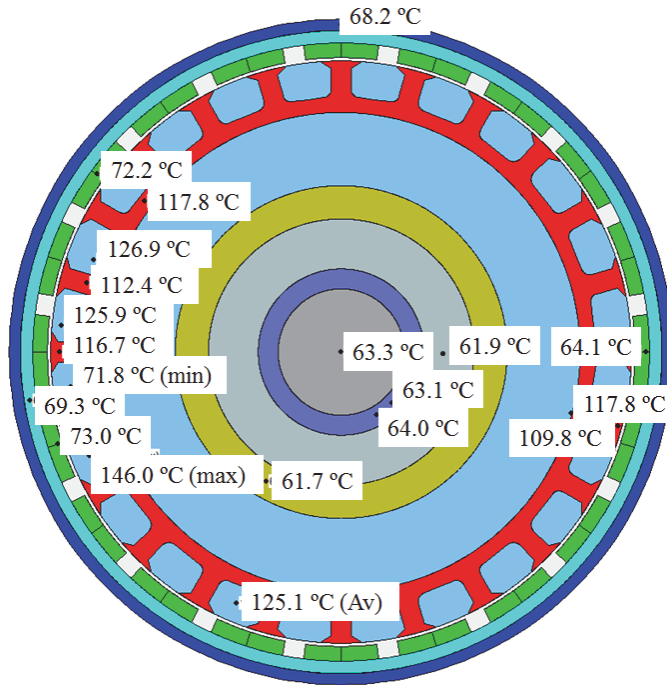


Fig. 4.7. Radial temperature distribution of HPSMG with the concentrated winding.

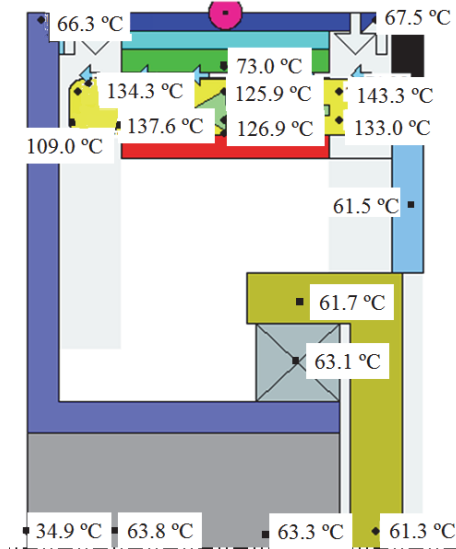


Fig. 4.8. Axial temperature distribution of HPSMG with the concentrated winding.

Appendix 3 shows an equivalent scheme of temperatures in different parts of HPSMG with the concentrated winding.

In the concentrated winding, the presence of higher temperatures can be measured in almost all of its parts in radial and axial views. Temperature

differences in permanent magnets are quite small compared to the toroidal winding. Differences in the temperatures of the windings are the largest: mean temperature of the concentrated winding is $\vartheta_{2win} = 125.1\text{ }^{\circ}\text{C}$ and maximum temperature is $\vartheta_{2max} = 146.0\text{ }^{\circ}\text{C}$. This is approximately $9\text{ }^{\circ}\text{C}$, i.e. 6% more than in the toroidal winding. However, maximum permitted temperature for the isolation of a winding conductor has not been exceeded by given temperatures.

Differences in temperatures obtained as a result of modelling lie in the geometry of the winding of the machine, as the rotor configuration, its dimensions, cooling type (impeller) and number of slots and poles are identical. The dimensions of both stators are similar as well. The only difference is in the locations of yokes: in the inner part of the stator of the concentrated winding and in the central part of the stator of the toroidal winding. Thus, lower temperature measured in a similar impeller of the toroidal winding is related to its size of the winding surface open to the axial movement of air, which is approximately 25% larger than that of the concentrated winding (Section 3.5, Fig. 3.29).

Fig. 4.9 shows the distribution of the temperature fields in the slots of both winding types and in the winding conductors located in it. Modelling was performed according to the finite element method, using Motor-CAD software module FEA.

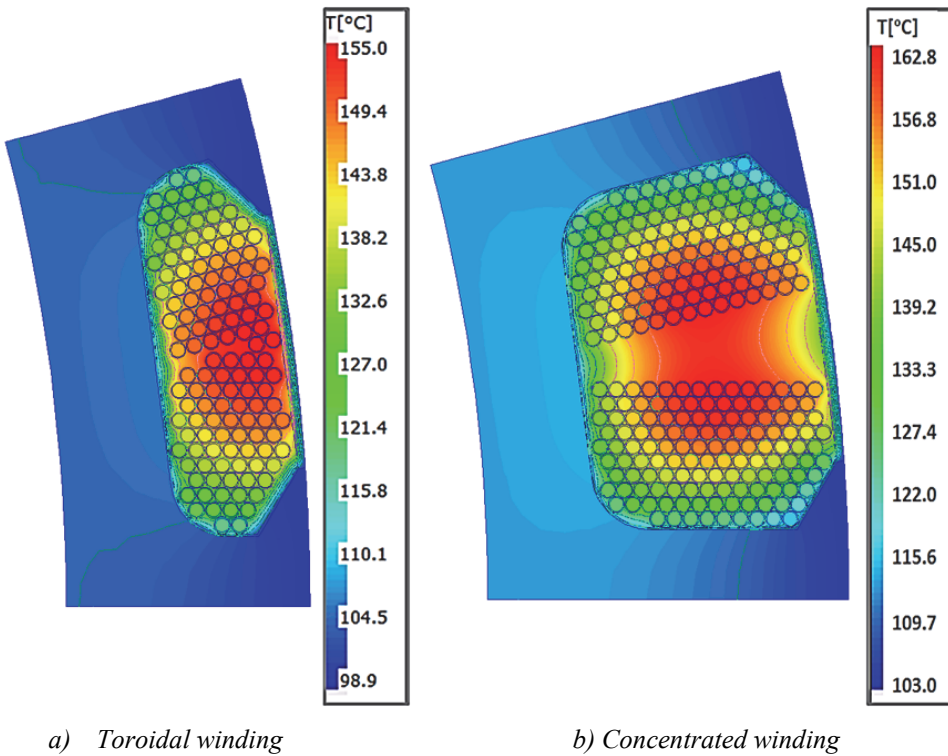


Fig. 4.9. Distribution of temperatures in slots and winding conductors of HPSMG with two different stator geometries.

Cross-sections of the modelled slots show the presence of temperature fields of almost 12% higher maximum values in the winding conductors (Figs. 4.3-4.8). Higher temperature fields there are accumulated into central parts of the winding coil where the cooling conditions of the winding conductors are the worst. Maximum temperatures of the winding conductors are almost 163 °C in the concentrated windings and almost 155 °C in the toroidal windings. However, even at these temperatures, maximum permitted temperature for the winding conductor is not exceeded.

The effect of high-temperature heat fields emerging in the stator windings should be taken into account when using permanent magnets.

Fig. 4.10 shows the analysis of the rotor yoke of HPSMG with both stator geometries and the temperature field of one magnetic pole.

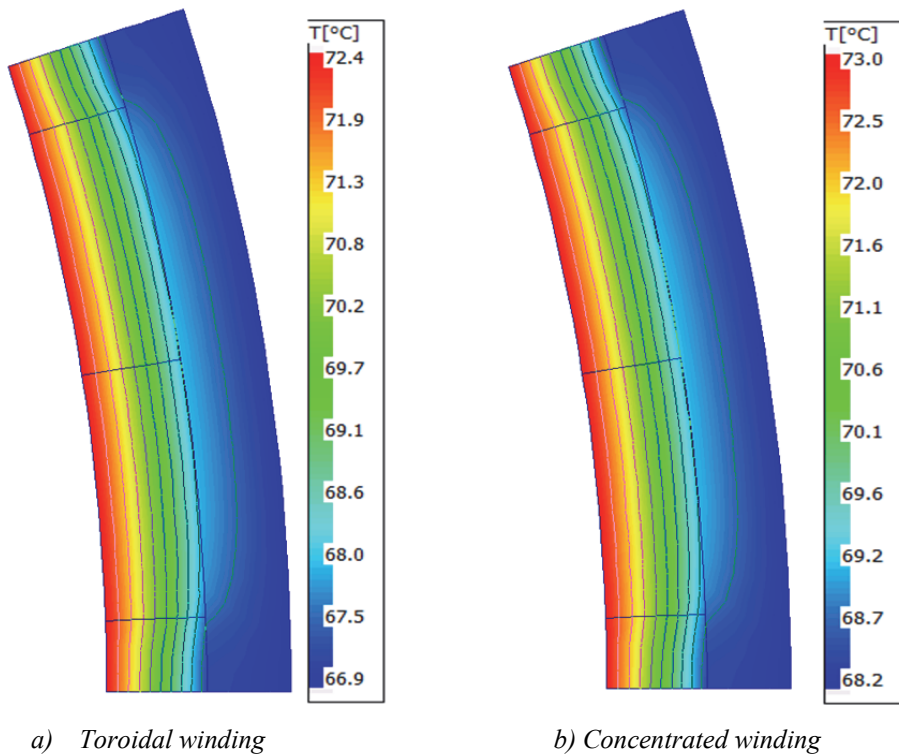


Fig. 4.10. Distribution of temperatures in the rotor yokes of HPSMG with two different stator geometries.

The modelling results show temperatures of permanent magnets and rotor yoke, which are similar to Figs. 4.3-4.8 and are low enough not to worsen magnetic properties of permanent magnets.

4.1.3 Analysis of FESM temperature fields

The following section describes the output parameters of FESM during the heating process. Similar to HSPMG, modelling software Motor-CAD Thermal

was used. Also, modelling was based on the cooling concept described in Section 3.4 and nominal parameters of the machine (Table 2.2).

Cooling methods in FESM and HPSMG are similar: an impeller located at the end of the ventilation system was used. Its purpose is to generate vacuum where the cooling air is suctioned through different parts of the machine and then channeled into the ambient environment. As the impellers of both machines are similar by operation, comparison of their temperature parameters is possible.

Fig. 4.11 shows FESM's modelled temperature characteristics at their nominal conditions, i.e. at supply voltage $U_{sup} = 51.8 \text{ V}_{DC}$, at supply current $I_{sup} = 250 \text{ A}$, and at rotational speed $n_n = 3000 \text{ rpm}$.

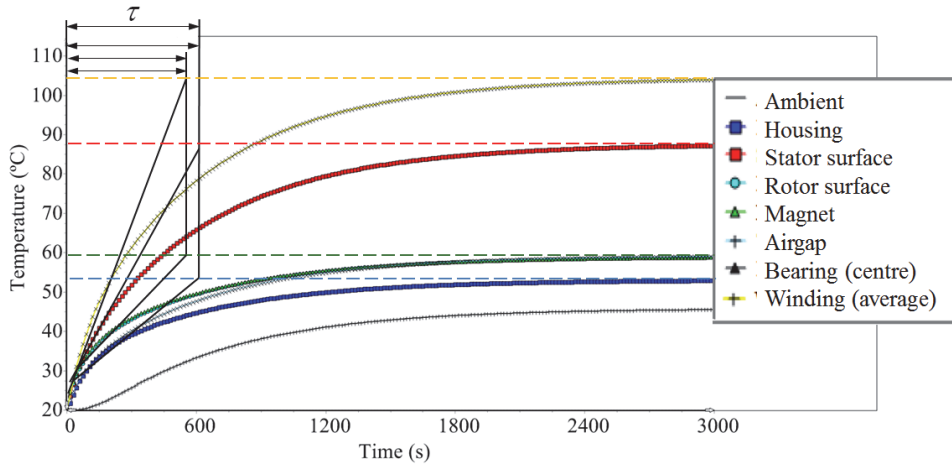


Fig. 4.11. Heat transient graphs of FESM.

In this case, mean temperature of the winding is obtained already at 105 °C. Also, in other parts of FESM, the temperatures are significantly lower than in HPSMG. As FESM is larger by dimensions and amount of materials, it heats up to constant temperature slower, i.e. 2500 s on average ($\tau \approx 600 \text{ s}$).

In Figs. 4.12 and 4.13, temperatures of different parts of FESM are shown.

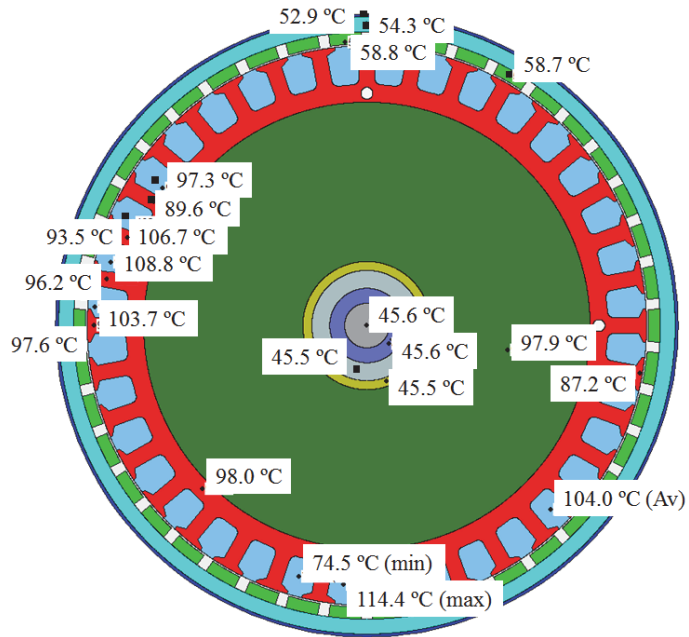


Fig. 4.12. Radial distribution of temperatures in FESM.

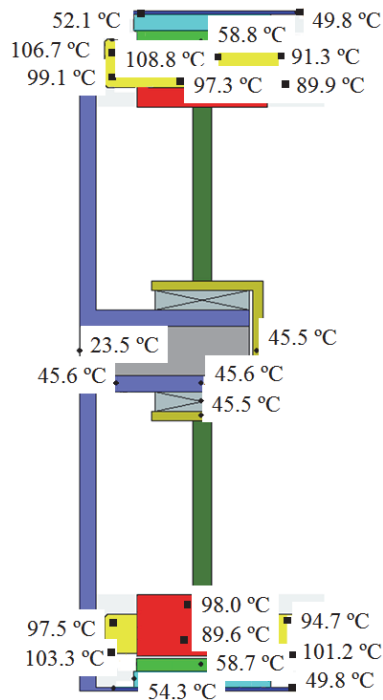


Fig. 4.13. Axial distribution of temperatures in FESM.

The figure shows that the mean temperature of the winding is $\vartheta_{2win} = 104\text{ }^{\circ}\text{C}$ and the maximum temperature is $\vartheta_{2max} = 114.4\text{ }^{\circ}\text{C}$, which is $23\text{ }^{\circ}\text{C}$, i.e. almost 17% lower than in HPSMG with the toroidal winding and $31.6\text{ }^{\circ}\text{C}$, i.e. almost 22% lower than in HPSMG with the concentrated winding.

Such difference in temperatures can be explained with the the rotor of FESM, which is larger in diameter and more powerful and capable of generating larger amounts of air Q directed through different parts of the machine. Additionally, FESM's impeller on the perimeter of windings and magnets is designed with nineteen aerodynamic blades to raise the intensity of the air flow (Fig. 4.2). By the blades, new cooling air is suctioned into the machine and heated air is removed from the magnets and windings at the same time.

Fig. 4.14 shows precise distribution of the heat fields of FESM, modelled using the finite element method in one stator slot with winding conductors located in it and across of one of the rotor's poles.

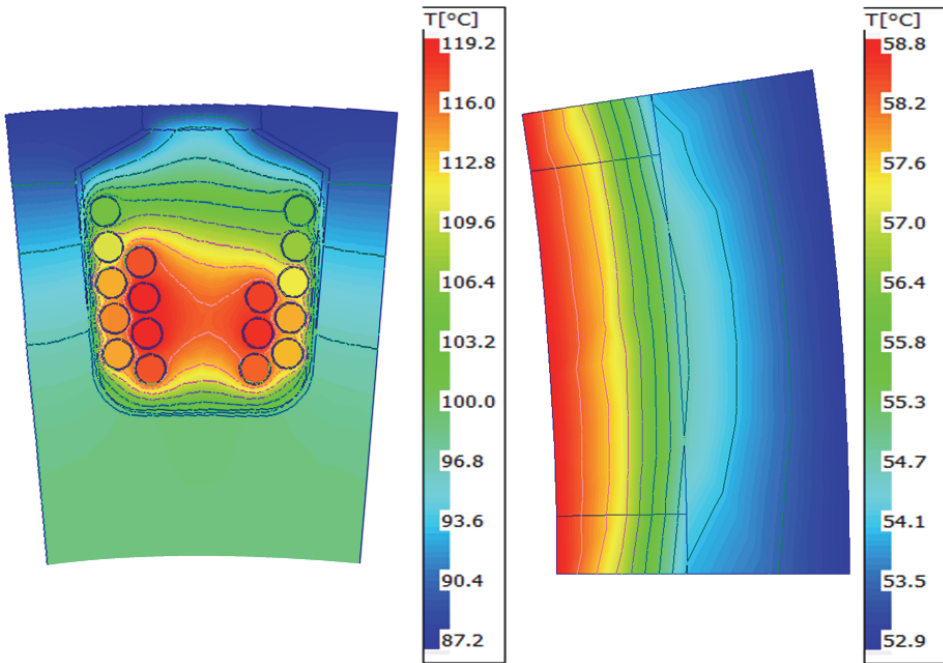


Fig. 4.14. Distribution of temperatures in the slot of the FESM stator; its winding conductors and rotor yoke.

Results of modelling show that similar to the HPSMG examples, the maximum temperature of winding conductors located in the central part of the FESM slot is higher ($\vartheta_{2max} = 119.2\text{ }^{\circ}\text{C}$) than that shown in Fig. 4.12 ($\vartheta_{2max} = 114.4\text{ }^{\circ}\text{C}$), although the difference is smaller. As the FESM winding conductor uses a single strand copper wire, the temperature limit of which is $200\text{ }^{\circ}\text{C}$, the temperature values above leave enough space to avoid isolation damage caused by overheating.

Regarding rotors and magnets, the results obtained are similar to those shown in Figs. 4.12 and 4.13.

Appendix 4 shows an equivalent scheme of temperatures in different parts of FESM.

4.2 Conclusion

In this section, HPSMG and FESM temperature field modelling was described. Regarding HPSMG, temperature values were compared based on its geometry with the toroidal and the concentrated winding. Modelling software was used to visualize transient processes of heating in different parts of the machines. Then the temperature constants were expressed, which were similar in both HPSMG windings to the mean values of exponential heating of different parts.

Regarding temperatures in HPSMG, the mean and maximum values of the two-layered concentrated winding were higher. In this winding, it can be explained by the larger difference of the diameters of coils and with the presence of environment with lower heat conductivity. In the toroidal winding, three sides of much thinner sides of the winding coil located in slots are surrounded by the stator material of good heat conductivity. Additionally, the winding is cooled through the air gap. The surface of the winding sides facing towards the impeller, which is almost 25% larger in the toroidal winding than in the HPSMG concentrated winding, is also important. Temperature differences of the HPSMG rotor and permanent magnets were marginal.

Compared to HPSMG, the heat values of FESM were significantly lower. Lower temperature values of FESM are derived from the larger surface of windings open to the air flow, larger diameter and higher power of its impeller with axial cooling, which enable sucking larger amounts of air through the winding. The current density in the winding conductor, which is twice as large in HPSMG, is also of essential importance.

The analysis showed that the designed impeller with axial cooling ensures sufficient cooling in both cases, taking into account the high current densities. Even at the highest load described in this section, maximum temperatures are at values which do not exceed temperature limitations for the isolation material of the winding conductors and permanent magnets.

In the concentrated windings, especially in the simulated HPSMG with a wide slot, it is possible to optimize winding temperatures to a certain extent. An option is also to design narrow ventilation holes between the compounded winding conductors through which the air can move. The other option is to change the stator geometry and design of teeth between the coils which do not bear the winding [7]. In this solution, ferromagnetic material located close to the winding coils improves the overall heat conductivity of the winding. Also, additional teeth affect, decreasing the loss caused by the leakage flux and obviously it also increases the electromagnetic torque.

5 EXPERIMENTAL VERIFICATION

This chapter describes practical tests and the results of HPSMG, the main study object of this doctoral thesis. Output parameters and first test results of FESM available are also compared.

5.1 Overview of Laboratory Test Benches

A test bench shown in Fig. 5.1 was constructed to measure electrical and mechanical output parameters of HPSMG.

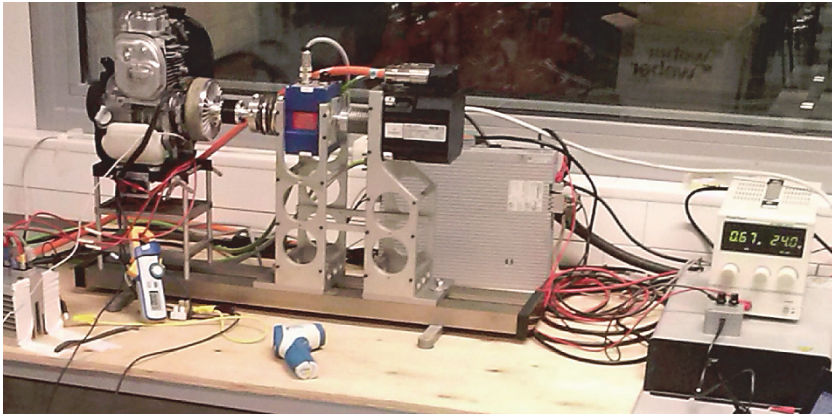


Fig. 5.1. The test bench for HPSMG testing.

As HPSMG is a part of a hybrid drive designed for a small UAV, an ICE functioning with it was also installed on the bench. Shafts of both machines are coupled with each other by a dry clutch, the operations of which are controlled by a lever system and a small servo drive.

The torque sensor was provided to measure the mechanical torque and power. Before setting a precise rotational speed during the tests in the HPSMG generator mode, a servo drive was implemented. The same servo drive was used also as a motor while testing HPSMG where its purpose was to create different loads. Additionally, the operating software of the servo drive enabled recording of different output parameters and output characteristics of HPSMG and simulated loads of different types, mostly the load of ventilator resembling propeller parameters used.

The bench that was initially designed only for HPSMG, was also used for generator no-load and motor tests of the first prototype of FESM (Fig. 5.2).

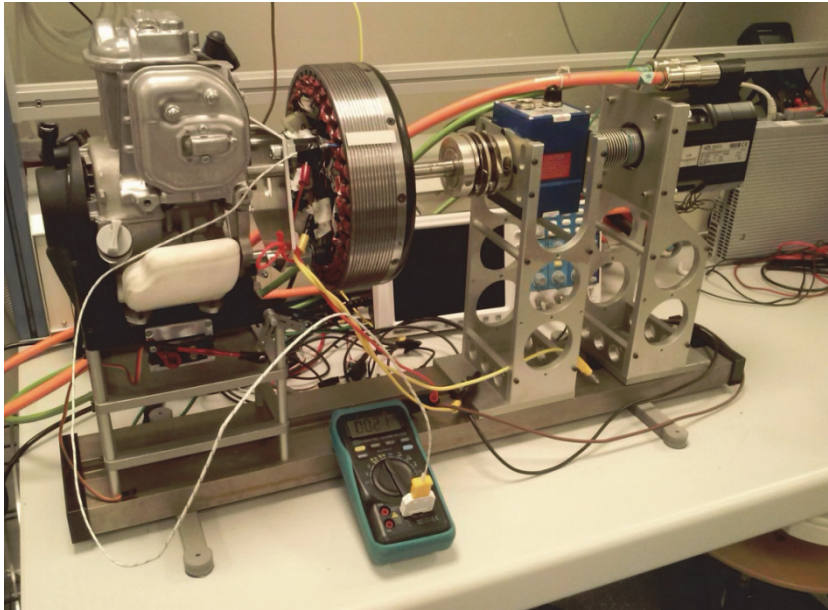


Fig. 5.2. The test bench for testing the first FESM prototype.

Adjustable DC power supply unit with the following output parameters was used for the power supply of both HPSMG and FESM: $U = 0-72 \text{ V}_{\text{DC}}$ as $I = 0-64 \text{ A}$ [79].

5.2 Distribution of the Magnetic Field in the Air Gap

Distribution of primary magnetic flux density in HPSMG with Gramme's winding and FESM was measured during practical testing across one magnetic pole τ in the air gap. A teslameter/gaussmeter Koshava 5 and a compatible open top transverse probe specially adjusted for usage on air gaps of small air gap length were used. Density of the magnetic flux was measured in both machines in no-load condition radially over one magnetic pole. The results obtained were recorded in a tabular form. The data from the table were used to construct the distribution of the magnetic flux in the HPSMG and FESM air gap. This enabled comparison of the results obtained by modelling the primary field and practical testing, and evaluation of general validity obtained analytically and virtually in the preparation phase.

Fig. 5.3 shows the distribution of magnetic flux density in the air gap in the length of one magnetic pole, which was modelled based on the measuring results of HPSMG with Gramme's winding. Each of the magnet poles of HPSMG consists of magnet pairs of the same polarity installed beside each other.

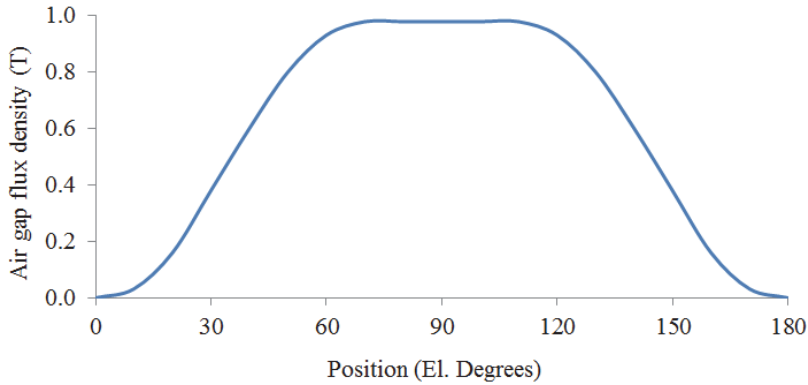


Fig. 5.3. Measured primary magnetic flux over one pole of HPSMG.

The measured maximum value of magnetic flux density of the primary field was $B_g = 0.96$ T, which is on average only 0.06 T higher than that from modelling the primary field of HPSMG (Fig. 3.7, Section 3.2.1) and only 0.07 T higher than the result obtained via analytical calculations (Eq. (3.28), Section 3.2.1), which confirms that initial data and results of the preparation phase were correct.

Fig. 5.4 shows the distribution of the magnetic flux density of FESM in its air gap for one pole pitch measured as above.

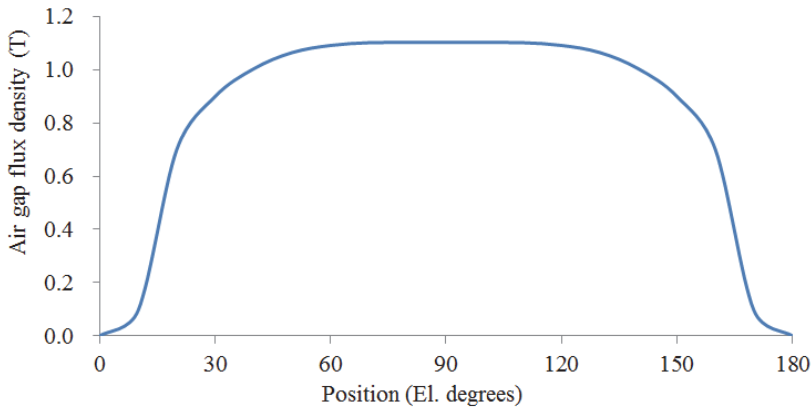


Fig. 5.4. Measured primary magnetic flux over one pole of FESM.

The maximum value of the magnetic flux density of FESM in the air gap was $B_g = 1.1$ T. The result complies with that obtained using the FEA method, which was by 0.08 T lower (Fig. 3.12, Section 3.2.2). Thus, the results obtained using modelling were confirmed also in this case.

5.3 Generator Mode

HPSMG operates also as a generator in a hybrid drive to charge battery devices on board of UAV during flight. For this, in generator tests, the HPSMG windings were connected in star connection, which ensured correct sinusoidal output voltage.

No-load tests for a generator were performed also with FESM, the main function of which is to operate only as a motor where the delta connection of windings is used. Thus, also FESM generator tests were performed with the same scheme of windings.

5.3.1 Open-circuit test

HPSMG and FESM were tested under no-load conditions. Measurements as a generator were performed in both cases on the star connection of the windings. The phase voltages and line voltages (U_{ph} and U_l), also rectified voltage U_{DC} after passing the inverter of both machines were recorded.

No-load characteristics of HPSMG are shown in Fig. 5.5.

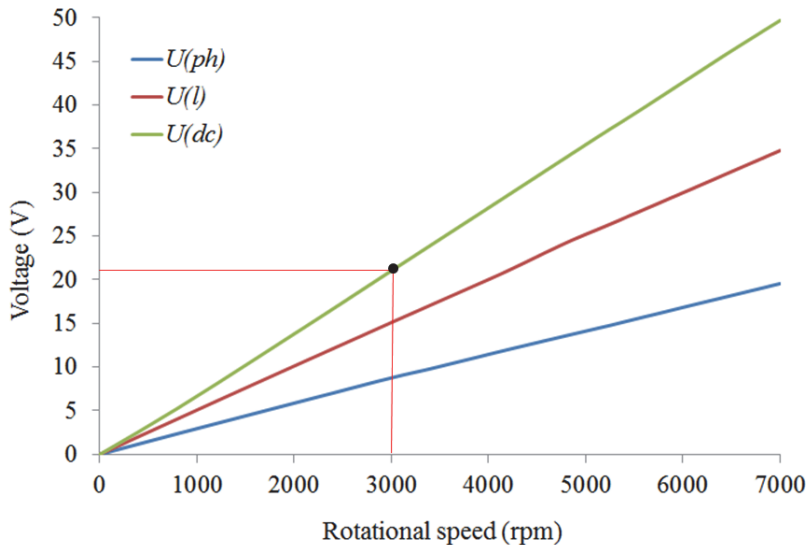


Fig. 5.5. HPSMG open-circuit test results.

The diagrams show that at the rotational speed $n = 3000$ rpm, the rectified output voltage value was $U_{DC} = 21.0$ V. In previous sections, the rotational speed mentioned above was used as a minimal rotational speed of the used propeller at which the flight mode of the aerial vehicle is still stable. Additionally, an effective battery charge should be ensured at this rotational speed $U_{DC} = 18.5$ V. Thus, the voltage level from the inverter output of HPSMG meets the requirements for charging the batteries.

Fig. 5.6 shows the no-load characteristics of FESM.

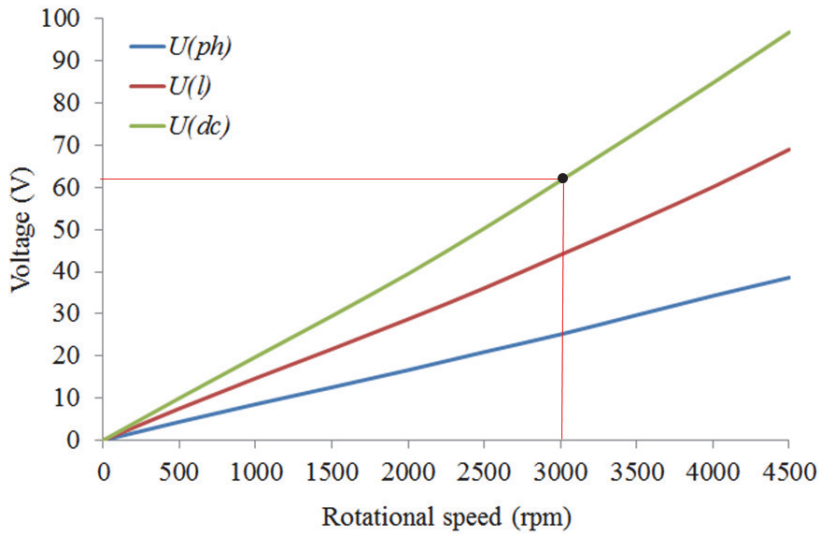


Fig. 5.6. FESM open circuit test results.

In FESM, the level of output voltage $U_{DC} \approx 61.6$ V generated after the inverter is almost three times higher than the same level in HPSMG.

The ratio of the rotational speed n and the output voltage U_{DC} allows finding the speed constant k_v of both machines. Based on the HPSMG values, the result is $k_v = 142.72$ (rpm/V), but based on the FESM values, the result is $k_v = 48.7$ (rpm/V). This comparison shows advantages of HPSMG as a motor rather than as a generator. The reason is that as compared to FESM, in this function, three times higher rotational speed for one volt can be attained. In the generator mode, on the contrary, several times higher rotational speed should be applied to obtain higher output voltage than in FESM, as the k_v value is higher in HPSMG. The main cause is the lower number of turns of HPSMG winding coils at the ratio $\Delta N = 2.32$.

To describe the quality of output voltages of both machines operating as generators, their line voltages U_l and phase voltages U_{ph} depending on time on no-load at different rotational speeds were oscillated.

Fig. 5.7 shows the correct sinusoidal shape of the HPSMGs line voltage U_l at the rotational speed of $n = 3000$ rpm.

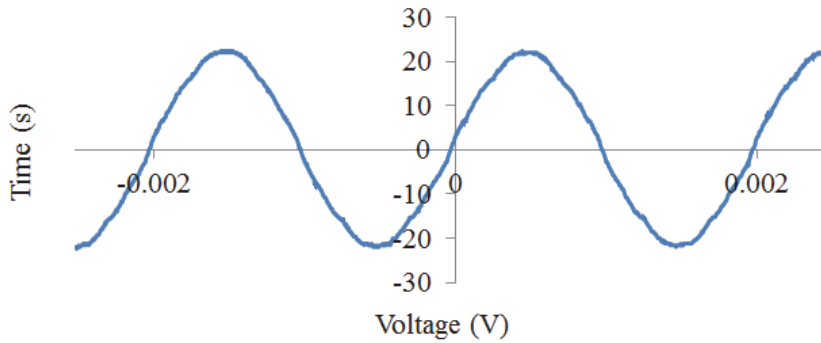


Fig. 5.7. Waveform of the HPSMG line voltage U_l at $n = 3000$ rpm.

Similarly, Fig. 5.8 shows the phase voltage U_{ph} of FESM as a waveform from a screenshot of an oscilloscope at the rotational speed of $n = 1500$ rpm.



Fig. 5.8. Waveform of the FESM phase voltage U_{ph} at $n = 1500$ rpm.

Clearly, the shape of the phase voltage waveform is correct again.

5.3.2 Load test

As devices for testing more powerful prototype of FESM with loads were not available at the time of writing this doctoral thesis, only load tests of HPSMG generator with the toroidal winding are discussed in this research.

In the generator mode, HPSMG has to provide sufficient power for equipment on board of the UAV. As those devices are active power consumers,

our load tests were also performed with active loads and a cascade of rheostats was used.

Fig. 5.9 shows the load characteristics at the rotational speeds of 3000, 4000 and 5500 rpm [24].

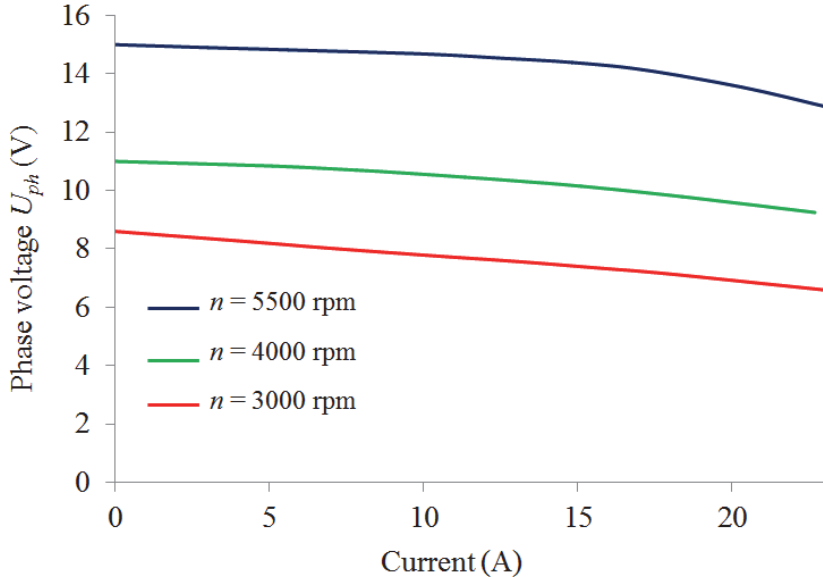


Fig. 5.9. Load characteristics at 3000, 4000 and 5500 rpm.

Comparison of load characteristics reveals higher linearity at lower rotational speeds 3000 and 4000 rpm.

At the rotational speed $n = 5500$ rpm and phase current $I_{ph} = 23.0$ A, the U_{ph} deviation was $\Delta U = 2.57$ V ($U_{ph(max)} = 15.46$ V, $U_{ph(min)} = 12.89$ V), which gives the voltage increase rate nearly by 20%. This figure is a normal result on the basis of permanent magnet synchronous generators in use today [70].

As a HPSMG in the HDS is designed to work with a passive rectifier, a full-period 3-phase rectifier bridge B6U was used also for load tests. During the tests, HPSMG was loaded with an active load. The increase of the active voltage drop and the armature reaction across the stator caused a continuous decrease of the terminal voltage.

Voltage drop in HPSMG was also influenced by the value of the rectifier's power factor $\cos \varphi$, which varied depending on the load in the range from 0.95 to 0.98. Due to the diode bridge, the rectifier causes also negative feedback effect in the output circuit of HPSMG. These distortions of voltage waveforms are caused by diodes during load switching, which induce voltage peaks (Fig. 5.10).

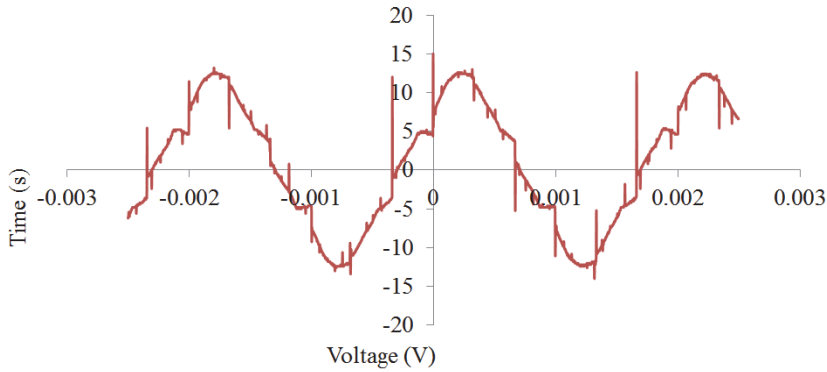


Fig. 5.10. The distorted waveform of the phase voltage U_{ph} at 3000 rpm.

5.3.3 Short circuit test

In the absence of the load in a short circuit situation, the resistance of the stator circuit is determined only by the active resistance of the conductors. For HPSMG, the winding resistance was measured $R_{win} = 0.07 \Omega$ at 48°C .

In general, short-circuit parameters can be neglected due to their small values and it is generally considered that the total resistance of the stator winding has an inductive nature [46]. During a short-circuit, the armature reaction has a strong demagnetizing influence, which at higher short-circuit currents can damage the rotor magnets by changing their magnetic parameters.

Fig. 5.11 shows the short-circuit characteristic of HPSMG. The nominal phase current $I_{ph} = 23.0 \text{ A}$ was achieved at $n = 750 \text{ rpm}$.

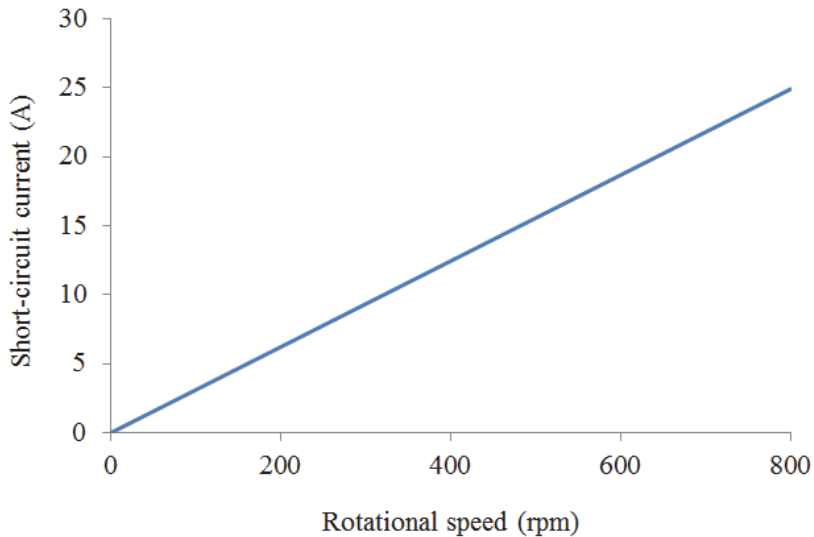


Fig. 5.11. Short circuit characteristic of HPSMG.

5.3.4 Temperature measurements

HPSMG in the generator mode was tested up to the current of $I_{ph} = 23.0$ A. At that current, the winding temperature stabilized at $\vartheta_2 = 106$ °C (Fig. 5.12).

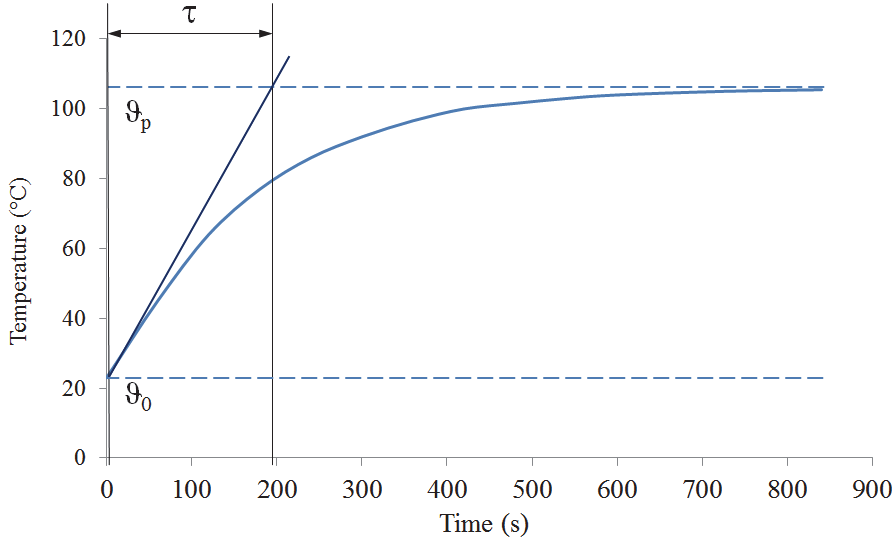


Fig. 5.12. HPSMG temperature characteristic with the thermal constant τ .

HPSMG's time constant was $\tau = 200$ s and the heat transfer process lasted in total of approximately $t = 13$ min.

The winding insulation and also the parameters of the permanent magnets would probably tolerate even a higher load current, since HPSMG's impeller can create sufficiently intense cooling. The limiting factor in our further testing was the mechanical design feature of HPSMG, which prohibited proceeding with higher currents, as these were causing too strong electromagnetic forces for the construction. Thus, the nominal phase current was considered $I_{ph} = 23.0$ A.

In FESM, the first prototype of the stator was made of electrotechnical steel laminations M600-50A with a thickness of 0.5 mm, which was received as a support for a project from ABB Motors and Generators Factory. This allowed optimization of costs related to the construction of FESM and performing the first tests before a new stator is constructed from a more expensive material NO20, which was initially planned in the modelling process.

Temperature tests were performed with a stator constructed of the material named above, the purpose of the tests was to map the thermal values. In this case, FESM was constructed with permanent magnets but without stator windings. The test was performed as no-load test on the CNC bench, which allowed rotating the rotor at several rotational speeds. It was possible to evaluate heating of the core based on the result.

Fig. 5.13 shows the diagram with results at the temperature constant τ .

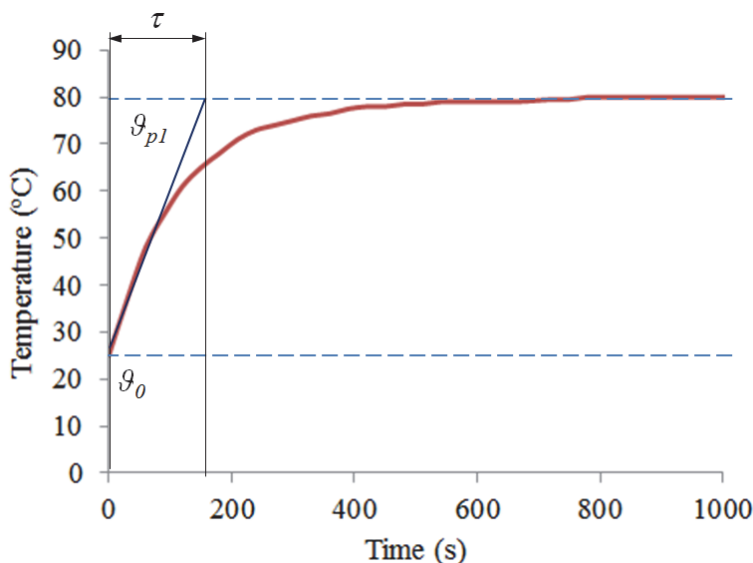


Fig. 5.13. FESM temperature characteristic with the thermal constant τ .

With this stator material, constant temperature was obtained for approximately 600 s, which gives the temperature constant a value of $\tau \approx 170$ s. Compared to the results obtained on modelling ($\tau \approx 600$ s) (Fig. 4.11, Section 4.1.3), heating takes place almost four times as fast in the stator core because of using sheet material M600-50A, which is 2.5 times thicker.

5.3.5 Losses

In HPSMG and FESM, copper and iron losses were evaluated experimentally. First, pre-test temperatures ϑ_1 , short-circuit currents I_k and short-circuit power P_k of phase windings of both machines after heating up were measured. Resistance r_k of the phase winding was expressed through the data obtained:

$$r_k = \frac{P_k}{3I_k^2}, \quad (5.1)$$

which was reduced to the resistance of the working temperature r_{kt° , chosen to be $\vartheta_2 = 106$ °C in HPSMG and $\vartheta_2 = 95$ °C in FESM:

$$r_{kt^\circ} = r_k \frac{235 + \vartheta_2}{235 + \vartheta_1} \quad (5.2)$$

The resulting value r_{kt° was used to calculate copper losses P_{Cu} in the phase windings [63]:

$$P_{Cu} = \frac{b_0 l^{h_0}}{\sigma_c} \int_0^{h_0} J^2 dh = r_c I^2, \quad (5.3)$$

where b_0 is conductor strand width, h is strand thickness, l is length, σ_c is conductivity, and J is current density.

Copper loss in HPSMG at the nominal current $I_{ph} = 23.0$ A and according to the measured temperature $\vartheta_2 = 106$ °C (Section 5.3.4) was $P_{Cu} = 44$ W. This result coincides with the modelling results (Table 3.4, Section 3.9).

Fig. 5.14 shows the diagram of copper losses P_{cu} at different temperatures and the working temperature $\vartheta_2 = 106$ °C based on the measurement values.

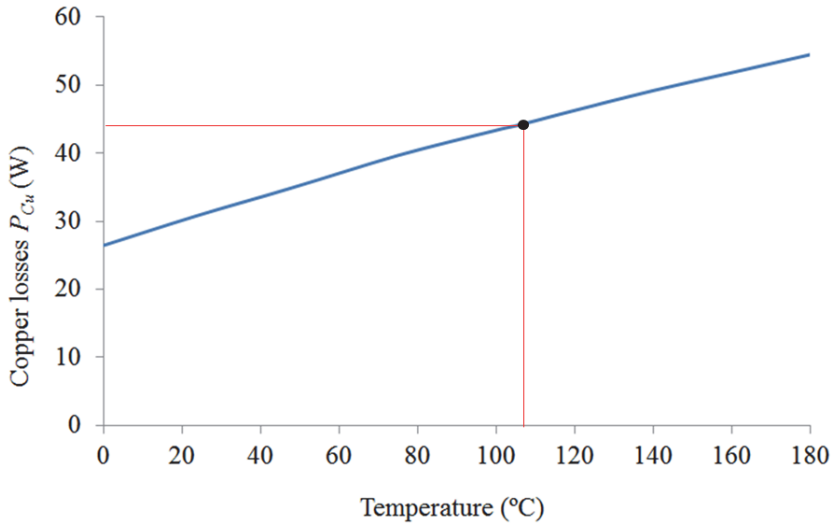


Fig. 5.14. HPSMG resistive losses at different temperatures.

Similarly, the diagram of copper losses of FESM is given in Fig 5.15.

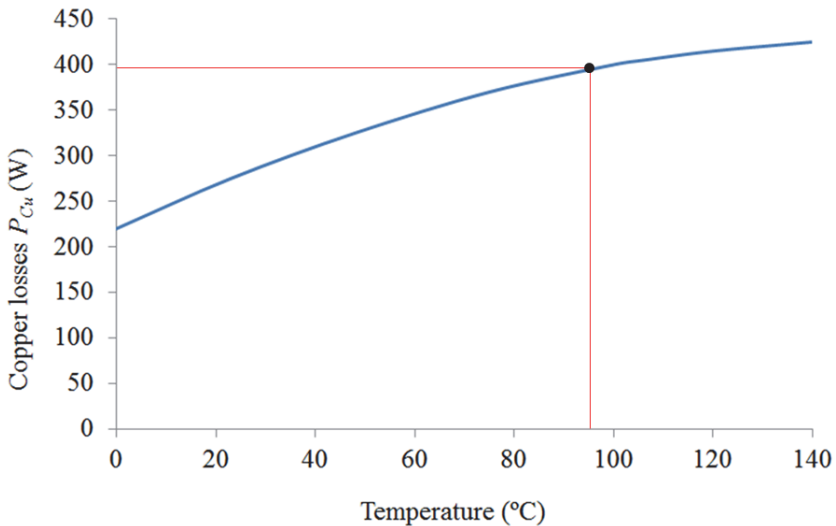


Fig. 5.15. FESM resistive losses at different temperatures.

Based on the working temperature of phase windings $\vartheta_2 = 95 \text{ }^\circ\text{C}$ expressed before, the value of copper losses is $P_{Cu} \approx 395 \text{ W}$, which complies to the respective value in Table 3.6 (Section 3.9).

The operating frequencies of HPSMG were compared to the respective power loss values of the electrical steel related to the same frequency rate throughout the stator volume, which formed the total iron loss P_{Fe} . Stator's P_{Fe} at the rotational speed of $n = 3000 \text{ rpm}$ ($f = 500.0 \text{ Hz}$) was $P_{Fe} = 7.2 \text{ W}$, which is of the same magnitude as the values obtained in modelling, presented in Table 3.4 (Section 3.9).

The dynamics of the stator iron losses is shown in Fig. 5.16.

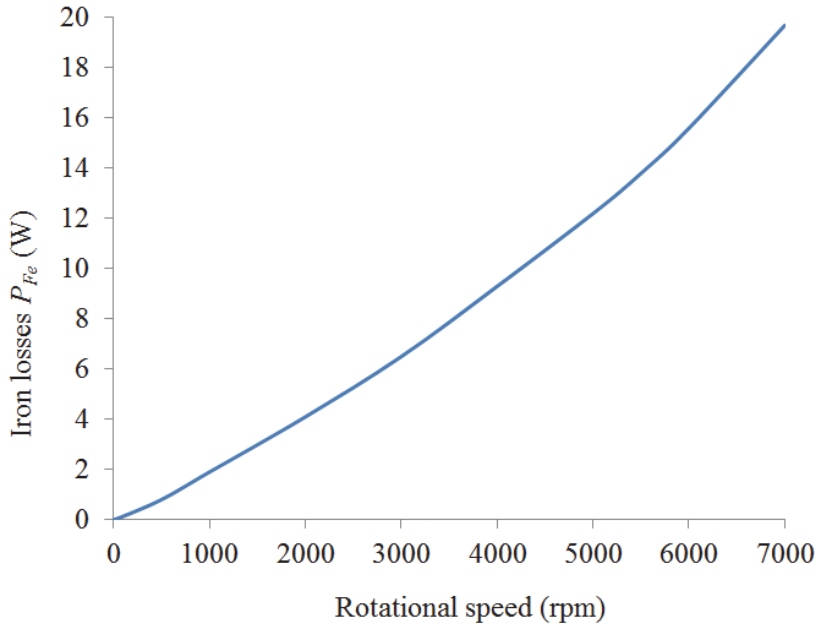


Fig. 5.16. HPSMG stator iron losses at different rotational speeds.

Another method was used to evaluate iron losses of FESM. In this case, the machine was constructed with permanent magnets and without windings, like in the temperature tests performed before (Section 5.3.4). A programmable CNC bench was used again as a test device to allow rotating of FESM rotor at given speeds and measure mechanical power at the same time. Based on the results, losses of FESM were evaluated, including magnetic losses and excluding copper losses.

Fig. 5.17 shows the abovementioned test device.



Fig. 5.17. FESM open circuit test in the CNC bench.

To optimize measurement errors, the power values of the CNC bench were recorded on no-load operation.

Fig. 5.18 shows the diagram based on the measurements above.

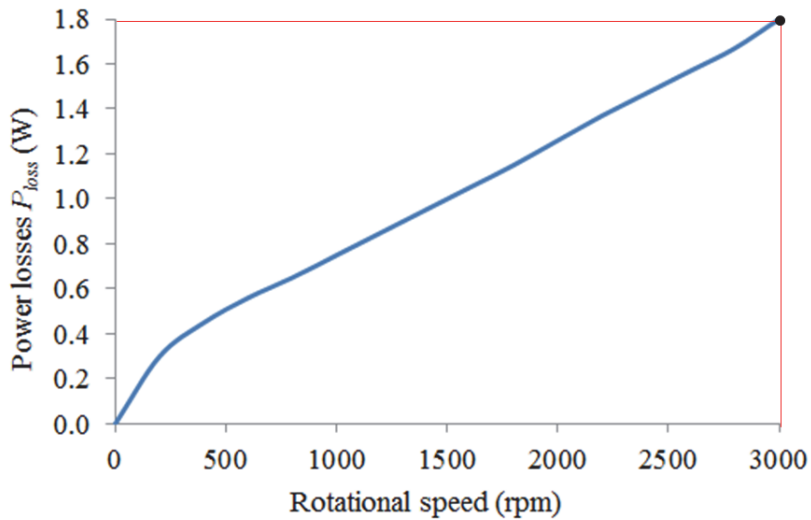


Fig. 5.18. FESM stator iron losses at different rotational speeds.

The diagram shows that the losses in magnets and core at the nominal rotational speed $n_n = 3000$ rpm can be up to $P_{loss} = 1800$ W. For an independent comparison of the results, the parameters of the stator's material were adjusted to

the values of M600-50A in the modelling software. Results obtained are shown in Table 5.1.

Table 5.1. Power losses in FESM

No.	Symbol	Name	Values	Unit
2	P_{eddy}	Eddy current loss in the stator	973	W
3	P_{hvs}	Hysteresis loss in the stator	399	W
4	P_{PM}	Magnet loss	307	W
3	P_{loss}	Total loss (open circuit)	1678	W

The total loss value P_{loss} is very close to the results obtained during the tests. Excluding magnetic losses P_{PM} , the result of the tests for iron losses are $P_{Fe} = 1493$ W. The result obtained in modelling is $P_{Fe} = 1371$ W. In this case, additional losses from the rotor yoke have not been included, thus the no-load test with FESM can be considered precise enough, which can certainly be used for evaluating losses.

5.4 Motor Mode

In this section, test results describing the function of HPSMG as a motor are discussed. As with FESM, the windings of HPSMG are connected in delta connection (Section 2.8).

Results of FESM no-load tests in the motor mode are also described in this section.

5.4.1 Batteries

One of the first problems with HPSMG as a multifunctional machine was to ensure that the voltage level in a generator mode for on board battery charging would be sufficient also for HPSMG operation in the motor mode and at the same rotational speed. This voltage is dependent on the predefined minimal rotational speed $n_{min} = 3000$ rpm. Thus, the value of HPMG's no-load DC voltage $U_{DC} = 21.02$ V at the rotational speed $n_{min} = 3000$ rpm was used as a reference to find the output voltage of the battery. Battery type 5 S intended for this voltage was used, the resulting nominal working voltage was $U_{DC} = 18.5$ V and charging voltage maximum $U_{DC} = 21.0$ V. Internal resistance of the chosen battery for an element was $R_{in} = 1.2$ m Ω [80]. Thus, the total internal resistance is $R_{\theta} = 0.006$ Ω . As the outer resistance R_{out} of the supply circuit consists of mostly the active resistance of connecting wires, the charging voltage of batteries is basically equal to no-load voltage in the HPSMG generator mode.

At the selected working voltage in the function as a motor, it was required that HPSMG would ensure rotational speed between $n = 3000$ -4000 rpm. To obtain the condition, the windings of HPSMG in the motor mode were switched from star connection to delta connection. This connection increases line currents and thus places a higher load on the controller and it demands also batteries of higher capacity, at the same time, allowing the motor to function at a lower

voltage, which was also the purpose of this task.

Test results show that to achieve minimal rotational speed $n_{min} = 3000$ rpm in delta connections of the windings with a propeller, the supply voltage $U_{DC} = 14.77$ V and the supply current $I_{DC} = 28.7$ A are required. After the inverter, the values of phase currents and also line voltages were significantly lower ($U_L = 10.3$ V_{AC} and $I_{ph} = 13.3$ A) (Table 5.2).

Table 5.2. Measurement results in HPSMG delta connection

n (rpm)	U_{DC} (V)	I_{DC} (A)	U_l (V _{AC})	I_{ph} (A)	S (VA)	P_{DC} (W)
3014	14.8	28.7	10.3	13.3	412	424
4002	20.9	46.2	14.6	21.1	922	966
4874	27.6	65.7	19.2	29.6	1703	1812

At the same rotational speed in star connection (Table 5.3), the input DC power P_{sup} is in the same magnitude, but the input voltage is significantly higher ($U_{DC} = 25.7$ V).

Table 5.3. Measurement results in HPSMG star connection

n (rpm)	U_{DC} (V)	I_{DC} (A)	U_{ph} (V _{AC})	I_{ph} (A)	S (VA)	P_{DC} (W)
3040	25.7	16.0	10.2	12.7	388	412
4042	36.4	26.2	14.5	20.5	888	953

To generate voltage of that magnitude, HPSMG's rotational speed on no-load should be minimally $n = 3600$ rpm. To obtain rotational speeds $n = 4000$ rpm in star connection, HPSMG would need a supply voltage $U_{DC} = 36.4$ V. But this means a rotational speed of HPSMG as a generator in constant mode already at the value $n = 5200$ rpm, which would obviously be an overload and also ICE, as the charging voltage of batteries can drop only to a certain limit. Thus, the most feasible solution in this case would be a star-delta-connection.

Nominal output voltage of the batteries $U_{DC} = 18.5$ V_{DC} is the mean value of the working voltages, the voltage of an element of 5S battery is $U_{DC} = 3.7$ V, which is $U_{DC} = 4.2$ V when fully charged.

Thus, operating voltage of batteries is initially up to $U_{DC} = 21.0$ V, which ensures the speed of rotation of HPSMG with a propeller up to $n = 4000$ rpm (Table 5.2). Reaching a minimum level of voltage where the voltage of an element is $U_{DC} = 2.75$ V and the total voltage is $U_{DC} = 13.75$ V, the value of the rotational speed is $n = 2800$ rpm, which is only by 200 rpm less than the minimal level of rotational speed $n_{min} = 3000$ rpm and allows landing of the plane.

The batteries used also have Over Discharge Protection (ODP), which applies and disrupts the supply line if the voltage of any of the cells becomes lower than $U_{DC} = 2.30 \pm 0.05$ V [80].

According to the goal set, UAV has to be able to fly at least 15 min in the

HPSMG motor mode. Thus, it is required to consider this in the calculations of capacity. The calculations show that it is sufficient to have a lithium polymer battery with a capacity of 8000 mAh the discharge coefficient of which on a constant load is 25 C. The battery of suitable parameters was chosen to be Turnigy nano-tech 8000mAh 5S 25~50 C Lipo Pack, the specifications of which allow approximately 16.7 min of flight time at the supply current of $I_{DC} = 28.7$ A from the batteries (Table 5.2) [31].

If the supply voltage is elevated up to the mean output voltage of batteries ($U_{DC} = 18.5$ V_{DC}), the rotational speed of $n = 3500$ rpm is reached. Thus, the consumption of current increases ($I_{DC} = 35$ A). In this case, the flight time is shorter, i.e. 13.7 min.

5.4.2 Open-circuit test

Below, the results obtained in the no-load test of HPSMG and FESM with toroidal windings compared to the results obtained in modelling are discussed.

Fig. 5.19 shows the dependence of HPSMG of the supply voltage U_{DC} in star and delta connections.

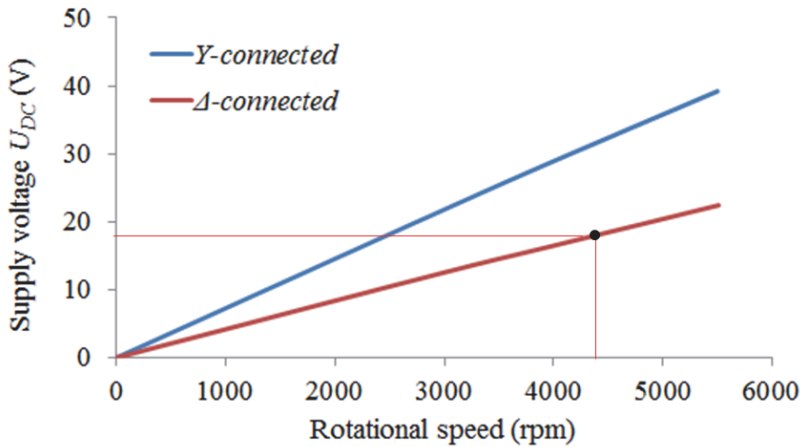


Fig. 5.19. Dependence of HPSMG supply voltage U_{DC} on the connection type and the rotational speed in an open circuit condition in the motor mode.

The diagram illustrates U_{DC} , which in delta connections is significantly or square root of three times lower than in star connections to make different rotational speeds reachable. At the nominal supply voltage $U_{DC} = 18.5$ V, the maximum no-load rotational speed of HPSMG measured was $n_0 = 4450$ rpm in the case of delta connection. Comparison of this result to that obtained in modelling ($n_0 = 4377$ rpm), the difference of rotational speeds appeared to be marginal $\Delta n = 70$ rpm. This confirms reliability of the results obtained in modelling.

The value of n_0 obtained in the measurement results in the speed constant, i.e. the square root of three times higher or $k_v = 240.5$ (rpm/V) in HPSMG delta connection, as was expected (Section 5.3.1).

To obtain the same n_0 value in star connection, $U_{DC} \approx 32.0$ V supply voltage is necessary, which would require significantly higher nominal rotational speed of HPSMG as a generator $n = 4500$ rpm (Fig. 5.5, Section 5.3.1).

Similar no-load tests in the motor mode were performed also with FESM. At the beginning, the rotational speeds in delta connection were recorded up to the nominal value of the supply voltage $U_{DC} = 51.8$ V from the inverter. Maximum reached no-load rotational speed was $n_0 = 3990$ rpm, which was lower by $\Delta n = 110$ rpm than the result obtained in modelling ($n_0 = 4100$ rpm) (Table 3.5, Section 3.9). This result may be considered precise enough.

Nominal supply voltage $U_{DC} = 51.8$ V in the application of star connection measured on the no-load test was at only $n_0 \approx 2400$ rpm. To reach the abovementioned rotational speed $n_0 \approx 3990$ rpm, the supply voltage required would be already $U_{DC} \approx 91.0$ V; however, it is impossible because of technical specifications of the inverter used.

Similar to HPSMG, the speed constant of FESM in delta connection is the square root of three times higher than in star connection or $k_v = 77.0$ (rpm/V) (Section 5.3.1).

Fig. 5.20 shows the dependence of the no-load rotational speed n_0 of FESM obtained in the test results on the value of U_{DC} in both star connection and delta connection.

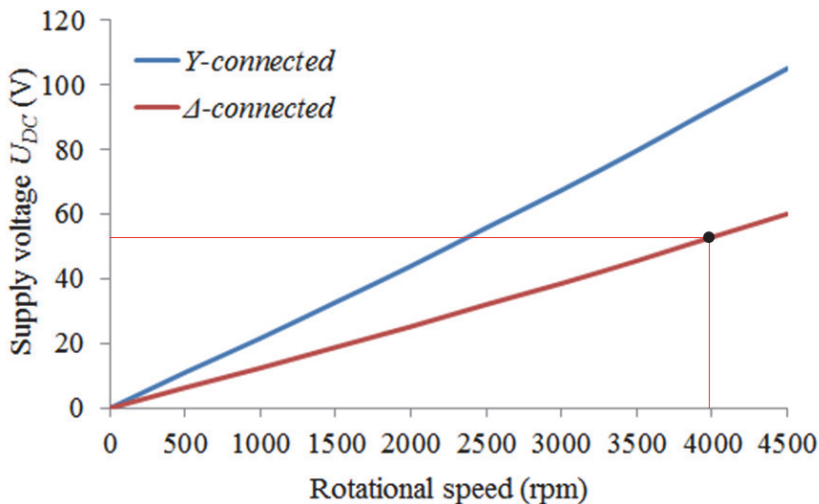


Fig. 5.20. Dependence of the FESM supply voltage U_{DC} on the connection type and the rotational speed in an open-circuit condition in the motor mode.

HPSMG and FESM are designed to work at quite high rotational speeds but at low supply voltages in the motor mode. This is possible by using delta connection. Although, to reach the same rated power, it causes higher current

levels in delta connection compared to star connection. This pattern applies also to no-load situation.

Fig. 5.21 shows the relations of measured no-load phase currents in HPSMG in star connection and delta connection.

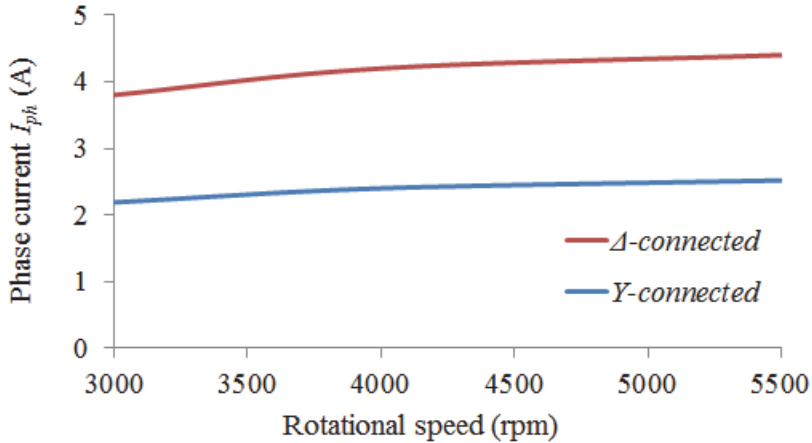


Fig. 5.21. HPSMG open-circuit test results in the motor mode.

The diagrams show that an effective value of the no-load phase current at the rotational speed $n = 3000$ rpm in delta connection is $I_{ph} = 3.8$ A, but in star connection, it appeared to be $I_{ph} = 2.2$ A, which makes only 9.6 % of the effective value of the nominal phase current $I_n = 23.0$ A measured in HPSMG functioning as a generator (Section 5.3.2).

To draw a parallel, dependence of the no-load phase currents I_{ph} of FESM on the rotational speed n is shown (Fig. 5.22).

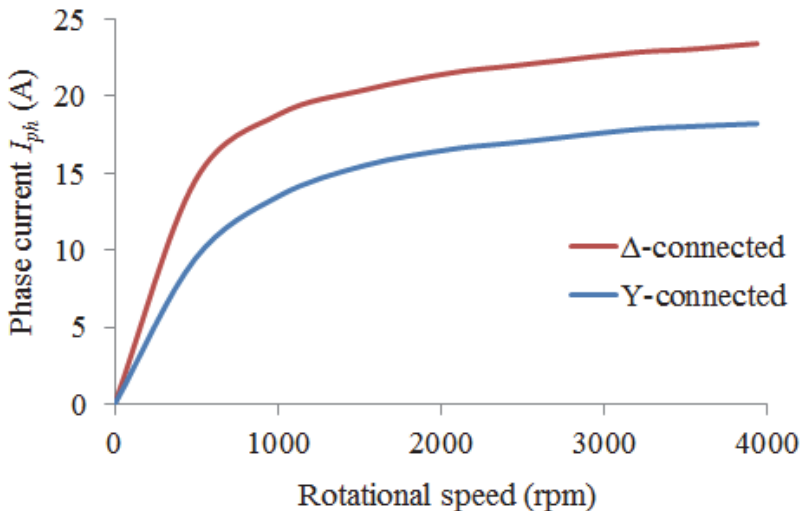


Fig. 5.22. FESM open-circuit test results in the motor mode.

To evaluate the rotational speed $n = 3000$ rpm of FESM, the no-load phase current in delta connection is $I_{ph} = 23.0$ A; at the same time, it is approximately $I_{ph} \approx 16.0$ A or 19% in star connection. The major percentage difference in the no-load currents i_0 of HPSMG and FESM results from thicker sheet material used in the test prototype of the FESM stator, i.e. approximately 14 times higher eddy current losses P_{eddy} (Table 3.6, Section 3.9 and Table 5.1, Section 4.3.5). In the stator material NO20 taken into account in the modelling, the no-load current value in delta connection would be $i_0 \approx 13$ A and that in star connection $i_0 \approx 8$ A, which in percentage resembles the respective values of HPSMG, 14.4 and 9.6% of the phase nominal current I_n .

5.4.3 Load test

In the experiments, HPSMG mechanical characteristics were documented with the help of a specific test bench with a servo drive for loading HPSMG (Fig. 5.1), enabling torque and rotational speed measurements.

During the load tests of HPSMG in the motor mode, the actual wooden propeller of UAV with the diameter of 508 mm and pitch of 355.6 mm was used as a load [72].

Fig. 5.23 shows the dependence of the counter torque of the propeller T_{pr} characteristics on the rotational speeds.

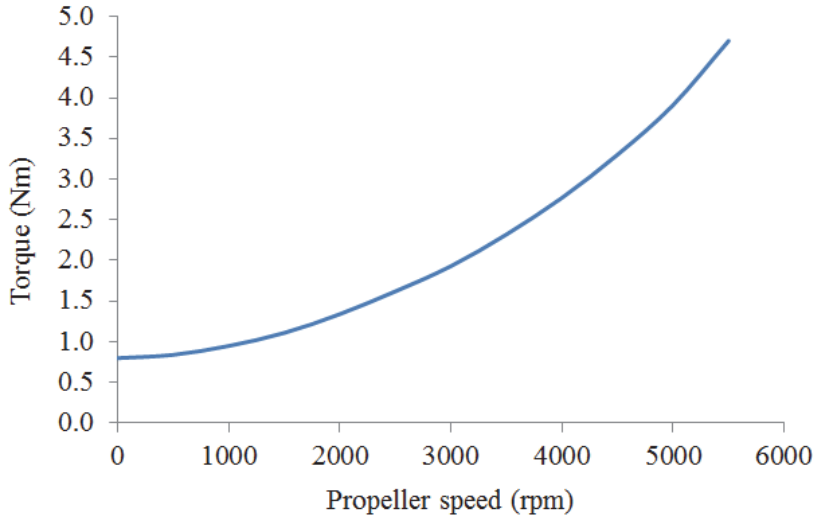


Fig. 5.23. Measured torque characteristic of the propeller.

HPSMG load tests in the motor regime were conducted in delta configuration to achieve higher power at lower rotational speeds. Three primary supply voltages were used, $U_{DC} = 14.8, 18.5$ and 20.9 V; $U_{DC} = 14.8$ V, being the minimal voltage at which the specified propeller rotational speed $n = 3000$ rpm was guaranteed. Voltage $U_{DC} = 18.5$ V was chosen by the nominal voltage of 5 S-type batteries, which was achieved at the abovementioned rotational speed

in the HPSMG generator mode in star connection [24]. The chosen voltage level of $U_{DC} = 20.9$ V is equivalent to the voltage output of the battery at fully charged state, at which the rotational speed $n = 4000$ rpm was reachable.

While loading HPSMG with a propeller, using the nominal battery voltage $U_{DC} = 18.5$ V, the rotational speed of nearly $n = 3500$ rpm was reached. Due to a rapid rise from $n = 2500$ rpm, the counter torque of the propeller was increasing with the supply current from the batteries. At $n = 3500$ rpm, the measured supply current was $I_{DC} = 35$ A at the torque level of $T_{pr} = 1.46$ Nm.

The measured phase current values in the machine after rectification were considerably smaller than the supply currents. As noted previously, the supply voltage from the batteries was $I_{DC} = 35.0$ A. In this case, the measured phase current in the machine was $I_{I3} = 16.4$ A and the phase voltage too was only $U_I = 12.2$ V_{AC}.

Fig. 5.24 presents the dependency of phase and supply voltages and phase and supply currents at different rotational speeds.

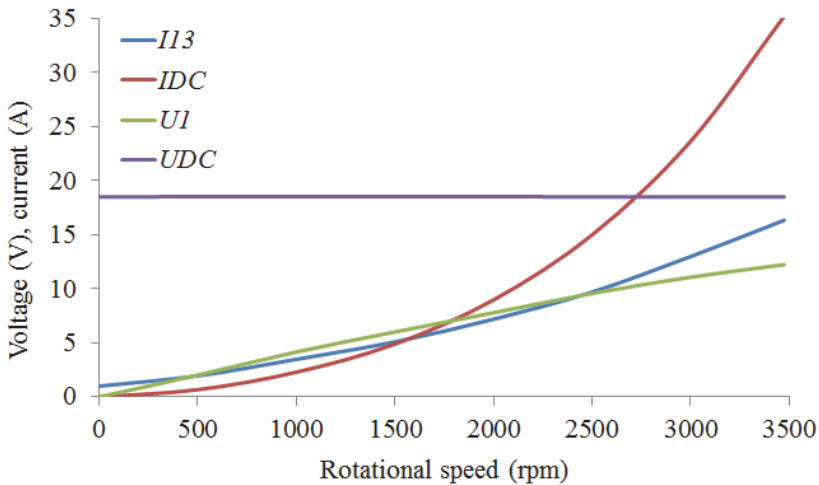


Fig. 5.24. Current and voltage dependencies on the rotational speed with a propeller as the load.

The ratios between the incoming power to the inverter P_{DC} and the mechanical power P_2 measured by a torque sensor connected to the HPSMGs rotor are characterized in Fig. 5.25.

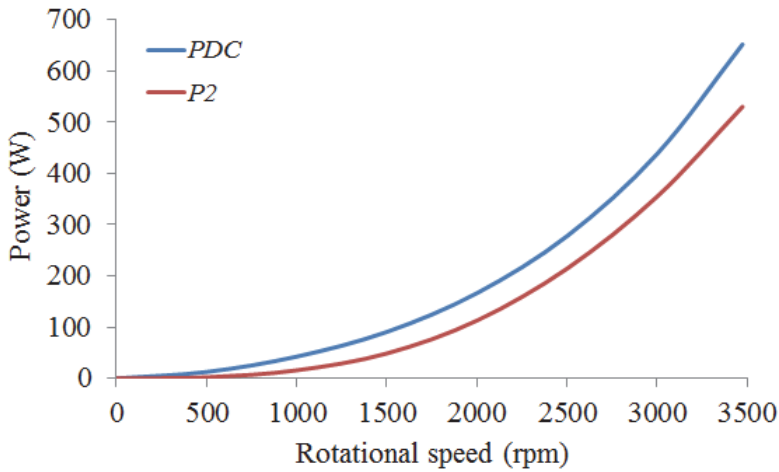


Fig. 5.25. The relations between the input P_{DC} and the output power P_2 in the dependence on the rotational speed.

The difference between P_{DC} and P_2 is an expression of the total exponential rise in the power loss P_{loss} of the machine while consisting of magnetic, mechanical and residual losses. Losses in the semiconductors of rectifying circuits are also contained in those losses. The most significant portion, though, is formed by the HPSMG copper losses P_{Cu} , which constitute 55% of the total loss in the example conditions where $n = 3500$ rpm, $U_{DC} = 18.5$ V_{DC}, $I_{DC} = 35.0$ A. Almost 30% of the P_{loss} value resulted from the higher harmonics by the inverter during switching. Other losses are composed of iron losses $P_{Fe} = 8.0$ W, which were determined previously [24], mechanical losses P_{mech} , induced by friction in bearings and aerodynamic losses, generated by aerodynamic drag dependant on the rotational speed of the rotor.

During the load tests, servo drive was configured to be equivalent to the torque characteristics of the propeller.

Based on the propeller, in Fig. 5.26, the values of the dependence of the mechanical torque T_m values on rotational speeds are given. Additionally, the maximum torque value of 2.2 Nm at the supply voltage of $U_{DC} = 18.5$ V can be observed.

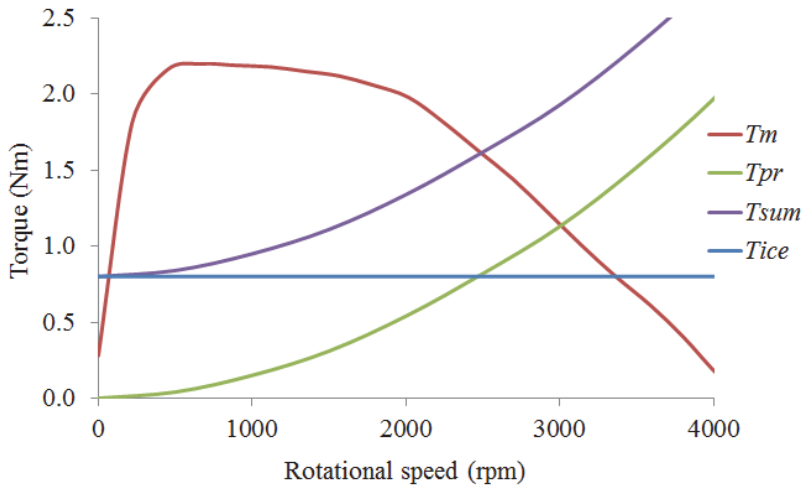


Fig. 5.26. Measured mechanical torque-speed characteristics at $U_{DC} = 18.5$ V.

At the rotational speed of $n = 3000$ rpm, the counter torque of the propeller was $T_{pr} = 1.13$ Nm. On the graph, the crossing point of T_m and T_{pr} can be seen. Correspondingly, the mechanical torque T_m is sufficient for maintaining a stable flight regime of the UAV.

The motor operation of HPSMG also consists of functioning as a starter, during which the torque level and the rotational speed must be achieved that should be sufficient for starting an ICE connected with the propeller.

According to previous measurements, the starting torque of ICE can be specified as $T_{ICE} = 0.8$ Nm [30], [81]. In addition to the starting torque, the propeller counter torque $T_{pr} = 1.13$ Nm at the rotational speed of $n = 3000$ rpm must be taken into account. Therefore, the optimal starting torque is the sum of T_{pr} and T_{ICE} and gives a result of $T_{sum} = 1.9$ Nm. At this starting torque, at the nominal battery voltage of $U_{DC} = 18.5$ V, the reduction in the rotational speed at the starting moment was expected.

According to Fig. 5.26, crossing of T_m and T_{sum} curves can be observed on the rotational speed of $n = 2500$ rpm. Nevertheless, because the starting interval does not exceed 3 s, loss in the flight speed caused by the loss of rotational speed can be interpreted as marginal.

In addition, in the case of fully charged batteries, it would be possible to exploit voltages higher than the nominal U_{DC} for starting.

Fig. 5.27 shows the torque characteristic at $U_{DC} = 20.9$ V, at the rotational speed of $n = 4000$ rpm.

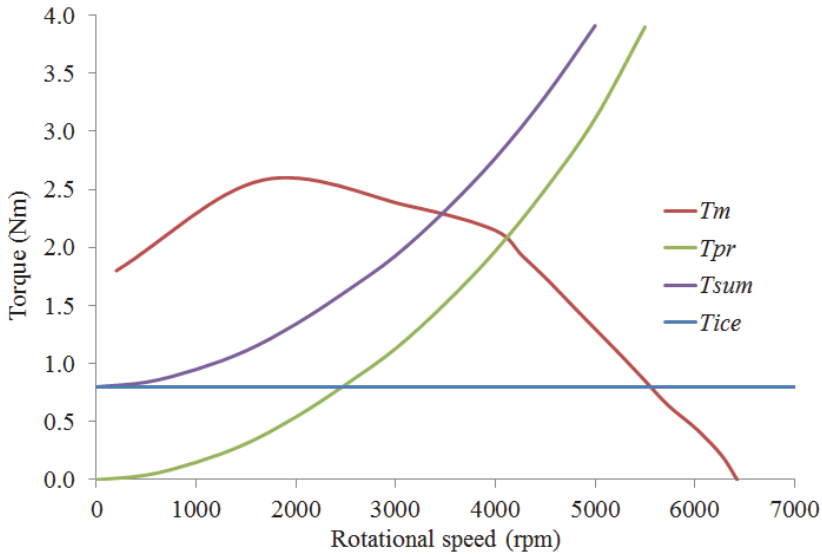


Fig. 5.27. Measured mechanical torque-speed characteristics at $U_{DC} = 20.9 V$.

The rise in phase voltages ($U_I = 14.6 V_{AC}$), phase currents ($I_{I3} = 25.0 A$) and rotational speed ($n = 4000 \text{ rpm}$) induces the rise in the HPSMG mechanical torque up to $T_m = 2.6 \text{ Nm}$.

Fig. 5.27 depicts also the rise of the counter torque of the propeller ($T_{pr} = 1.97 \text{ Nm}$) at this rotational speed. Therefore, the torque required to start ICE increases to $T_{sum} = 2.77 \text{ Nm}$, which exceeds the maximum mechanical torque T_m .

At the given conditions, the crossing of $T_{sum} = T_{pr} + T_{ICE}$ with T_m can be marked at the rotational speed of $n = 3500 \text{ rpm}$, which exceeds the minimal rotational speed of the propeller, required for a stable flight by 500 rpm. Therefore, the necessary flight speed is ensured even during the ICE starting period.

At HPSMG operation as a motor, it is also used for take-offs of the UAV. Ensuring the required rate of increase in the flight height, the flight speed of 80 km/h at normal atmospheric pressure must be achieved. Therefore, sufficient thrust must be generated by the propeller, i.e. the rotational speed $n = 3800 \text{ rpm}$ must be reached, without considering the aerodynamic drag of the UAV.

At the take-off, ICE and HPSMG work in parallel, being mechanically coupled. Fig. 5.28 shows the summation of the output torques T_m and T_c of both machines at various rotational speeds, based on HPSMG maximal supply voltage $U_{DC} = 20.9 V$, and using the counter torque of the propeller T_{pr} as a contrast, the total output torque of HDS $T_{sum} = 2.95 \text{ Nm}$ and the maximal rotational speed of $n = 4860 \text{ rpm}$ at given conditions.

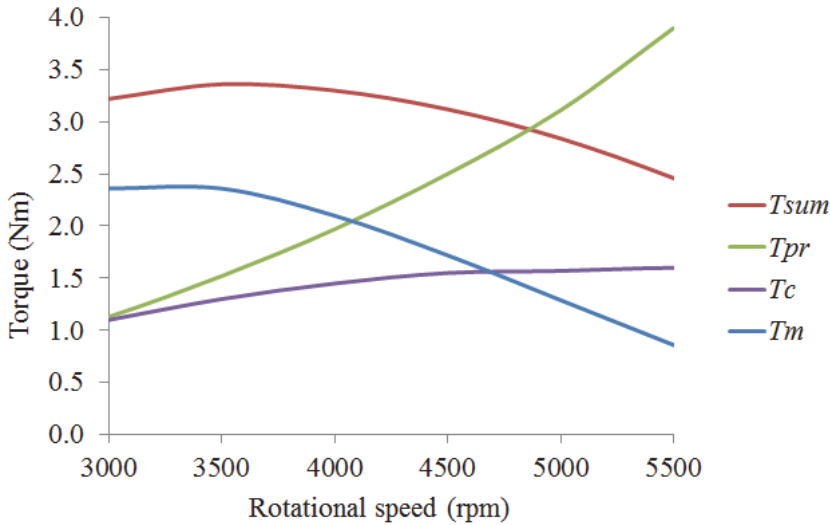


Fig. 5.28. Torque-speed characteristics during the take-off.

At such rotational speed, theoretical flight speed in relation to earth of 103 km/h could be reached. Still, taking into account the increasing aerodynamic drag of the UAV, the real flight speed would be lower, but still exceeding minimal take-off speed.

To increase the reliability of load tests, tests were performed also with a propeller with the shorter pitch, i.e. 304.8 mm (12 inches) (Type 2). Fig. 5.29 shows counter torque characteristics of each propeller depending on the rotational speed.

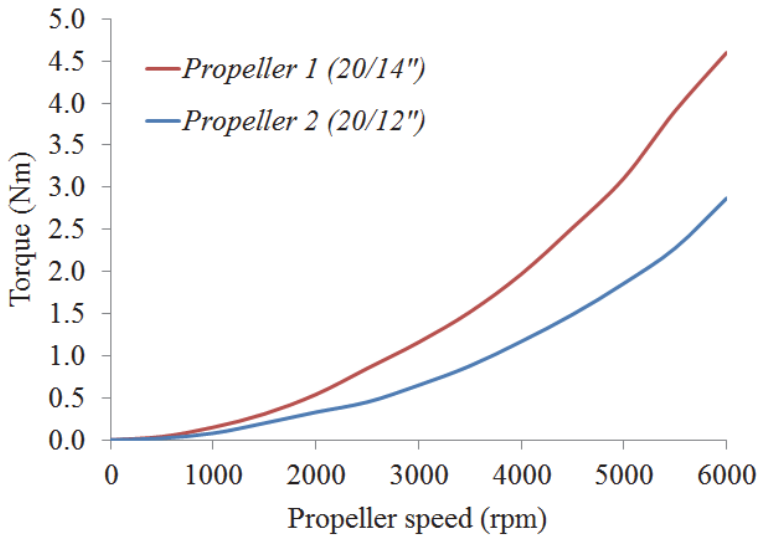


Fig. 5.29. Comparative counter torque characteristics of two tested propellers.

Fig. 5.30 shows the characteristics measured at $U_{DC} = 18.5$ V.

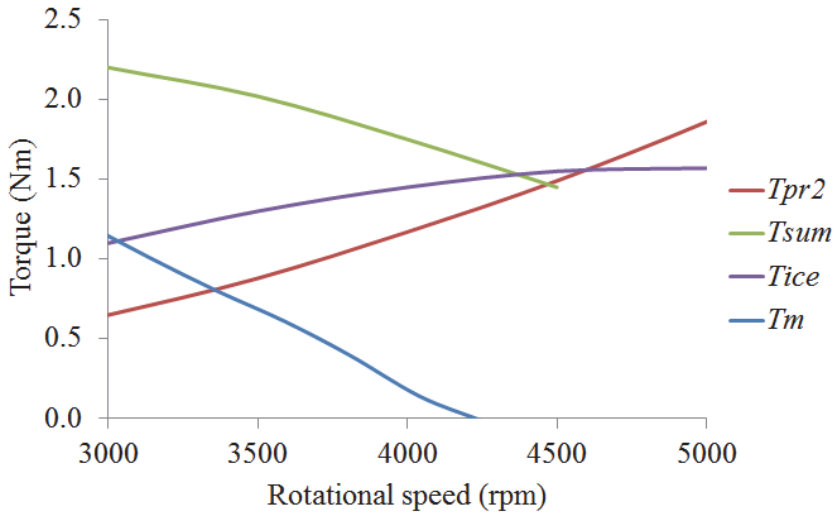


Fig. 5.30. Propeller 2 torque-speed characteristics during the take-off at $U_{DC} = 18.5$ V.

The characteristics show that at this supply voltage, only in the HPMG mode, the rotational speed $n = 3300$ rpm is obtained, which is almost 300 rpm higher than that of propeller 1 (Fig. 5.26). Only in ICE, the rotational speed is significantly higher, i.e. almost 4600 rpm. The validity of the latter is confirmed also by the practical experience of the airplane manufacturer ELI Airborne Solutions Ltd. who uses this propeller type in their products.

Parallel operation of HPSMG and ICE shows that the highest rotational speed is even decreased by 200 rpm, compared to the situation where only ICE is operating. Therefore, if the rotational speed is higher than that mentioned above, HPSMG is switched to the generator mode, as this is an additional load to ICE. But in parallel operation, at the rotational speed less than 4300 rpm, the summary moment T_{sum} is obtained, the values of which exceed the counter-torque of propeller 2 notably.

At the supply voltage $U_{DC} = 20.9$ V, HPMG with propeller 2 obtains the rotational speed of almost $n = 4600$ rpm. An equivalent rotational speed is obtained also in the ICE mode. Choice of propeller 2 is justified when comparing the result with that obtained with propeller 1 where operating only in the ICE mode, the rotational speed obtained was even less than the minimal required rotational speed of 3000 rpm (Fig. 5.28).

A better result was obtained also in the parallel operation of HPSMG and ICE where the rotational speed obtained at the supply voltage $U_{DC} = 20.9$ V was almost 700 rpm higher than that obtained in propeller 1, i.e. $n = 5560$ rpm.

Fig. 5.31 shows the characteristics of the torques modelled based on the results measured at the supply voltage of $U_{DC} = 20.9$ V depending on the rotational speed.

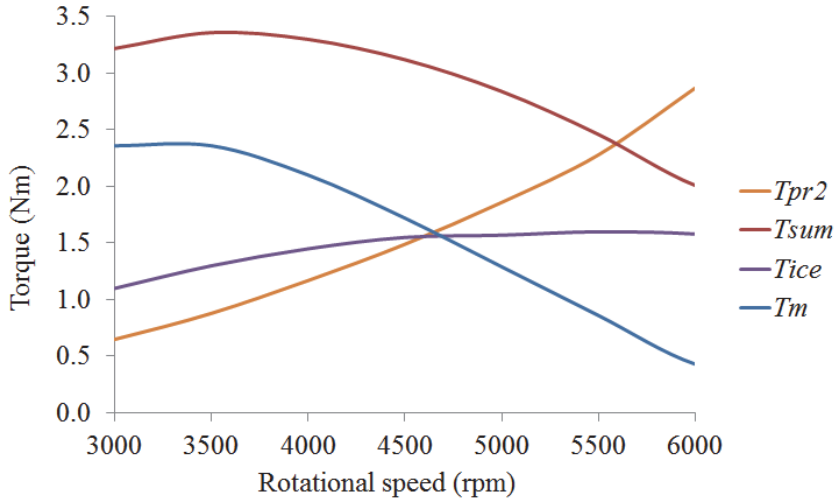


Fig. 5.31. Torque-speed characteristics of propeller 2 during the take-off at $U_{DC} = 20.9$ V.

As the pitch of type 2 propeller is smaller, its counter torque is also smaller. This, in turn, causes lower current and power consumption by HPSMG and allows usage of battery units with lower capacity and thus a decrease of their total weight.

Tables 5.4 and 5.5 show electrical specifications measured on using type 1 and type 2 propellers at the supply voltage of $U_{DC} = 18.5$ V and at fully charged battery units on the voltage of $U_{DC} = 20.9$ V.

Table 5.4. Measurement results with type 2 propeller in HPSMG delta connection

U_{DC} (V)	I_{DC} (A)	U_l (V _{AC})	I_{ph} (A)	S (VA)	P_{DC} (W)
18.5	28.4	13.1	12.8	503	527
20.9	33.8	14.8	15.1	670	708

Table 5.5. Measurement results with type 1 propeller in HPSMG delta connection

U_{DC} (V)	I_{DC} (A)	U_l (V _{AC})	I_{ph} (A)	S (VA)	P_{DC} (W)
18.5	35.2	12.2	16.4	600	652
20.9	46.2	14.6	21.1	922	966

Comparison of tables shows that the current and power values consumed by type 2 propeller are 20-25% lower than in type 1 propeller.

An important element in the evaluation of the efficacy of propellers is the linear velocity obtained with them at a certain rotational speed. To ensure sufficient efficacy on take-off, UAV linear velocity of 80 km/h must be obtained. In propeller 1, this was obtained at a rotational speed of $n = 3800$ rpm. In propeller 2, which has a shorter pitch, significantly higher rotational speed

$n = 4400$ rpm must be obtained. This is attainable only with fully charged batteries in the HPSMG mode, also with the help of ICE and in the parallel operation of both of the motors. However, at the nominal voltage of $U_{DC} = 18.5$ V and less, rotational speed, power and torque of HPSMG are insufficient. In case higher rotational speeds are used, changing batteries to level 6S could be helpful, allowing nominal supply voltage of $U_{DC} = 22.2$ V.

Based on the calculations, maximum theoretical linear velocity with type 2 propeller attainable at the parallel operation of HPSMG and ICE at the voltage of $U_{DC} = 20.9$ V would be similar, i.e. 103 km/h with type 1 propeller.

In conclusion, type 2 propeller is apparently a better choice for an ICE, allowing usage of a higher torque area of the internal combustion engine. Nominal value of the supply voltage of battery devices should have been increased in HPSMG. In this doctoral thesis, analysis is based on the parameters of type 1 propeller.

5.4.4 Temperature measurements

The aim of the thermal experiments was to determine the maximal temperature of HPSMG active parts on a steady load. Type 1 propeller was used as a load and as a cooling element. Assuming intensive cooling by the propeller, HPSMG could handle supply currents substantially higher than expected. The first load experiment was made at the rotational speed of 4000 rpm ($U_{DC} = 20.9$ V) that was near to 5 S batteries voltage of $U_{DC} = 21$ V at their fully charged state. The current during the experiment reached $I_{DC} = 46.17$ A, while the line voltage was measured at $U_l = 14.6$ V_{AC} and the phase current $I_{ph} = 20.39$ A. Based on that, the resulting HPSMG apparent power $S = 890$ VA.

At set parameters, the constant temperature of windings was stabilized after 8 min, i.e. 480 s to the temperature of $\vartheta_{p1} = 64$ °C, resulting as the time constant of $\tau \approx 120$ s. The characteristics in Fig. 5.32 indicate the thermal time constant τ .

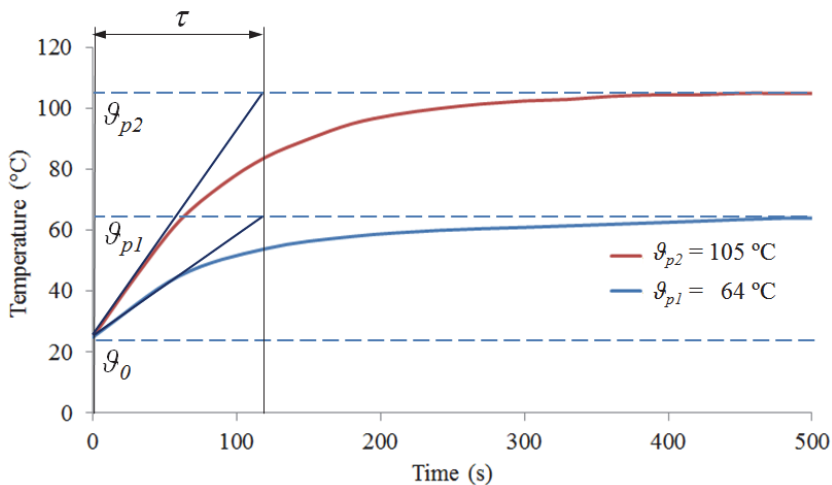


Fig. 5.32. Temperature characteristics with the thermal constant τ .

As the maximum temperature of the chosen magnets and winding insulations was substantially higher [64], [65], the additional experiment was made at the rotational speed of $n = 5610$ rpm, supply voltage of $U_{DC} = 35.0$ V and current of $I_{DC} = 118.0$ A. At given parameters, the line voltage $U_l = 22.6$ V_{AC} and the phase current $I_{ph} = 52.5$ A were measured, resulting in the apparent power $S = 3560$ VA.

Although at higher power, the constant temperature of $\vartheta_{p2} = 105$ °C was measured with the temperature probe, similar to the previous experiment, the winding temperature rose to the constant value during 480 s and gave the same time constant $\tau \approx 120$ s. The measured temperature in the windings is always higher than the temperatures of other components in the machine, which ensures that in previous load conditions, the allowed maximum temperatures are not exceeded in permanent magnets.

A thermal camera was also used to capture temperatures of various parts in the machine, enabling comparison with the results collected by use of a temperature probe.

In Fig. 5.33, the maximum temperature in windings registered on scale was $\vartheta_{p2} = 104$ °C, i.e. close to the results achieved with the temperature probe.

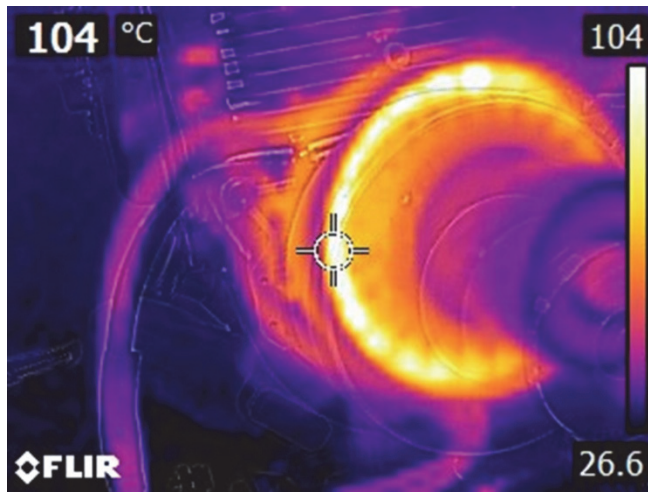


Fig. 5.33. The thermal image of the rotating HPSMG resulting from the heating process.

Comparison of the measured temperature values with those obtained in modelling (Fig. 4.3, Section 4.1.1) revealed approximately 70% slower heating of HPSMG windings on the propeller use. Practical tests performed during functioning as a generator showed that reaching constant temperature takes place 60% faster. In this case, it is caused by using twice as high load current I_{ph} in the phase winding (Fig. 5.9, Section 5.3.2).

As the temperature was measured on the external surface of the winding, significantly higher heating of winding conductors inside the winding coil can be presumed. The same is discussed in Section 4.1.1 (Figs. 4.4, 4.5, and 4.9), which

describes the division of the modelled temperature across the slots where the temperatures may rise from average (110.6 °C) to 40% higher or up to 147 °C in this case, which neither endangers insulation of the winding, nor allows a significant increase in the load if the same propeller and cooling type are used. Increasing the input power by estimably $\Delta P_1 = 300$ W, the temperature of winding conductors would rise approximately by $\Delta \theta_{p2} = 50$ °C, which is the maximum temperature limit of their insulation material.

5.5 Power and Torque Density

One of the goals of this thesis research was to analyze output parameters of HPSMG in the context of specific power and torque density.

Table 5.6 summarizes the specifications of these values.

Table 5.6. HPSMG output parameters in terms of power and torque density

No.	Symbol	Type	HPSMG	Unit
1	T_m	Torque	4.7	Nm
2	P_2	Output power	2.9	kW
3	L_{stk}	Axial length	22.0	mm
4	D	Diameter	96.5	mm
5	W	Weight (mass)	0.7	kg
6	$P\text{-to-}W$	Power-to-weight ratio	4.1	kW/kg
7	$P\text{-to-}V$	Power-to-volume ratio	19.8	MW/m ³
8	$T\text{-to-}V$	Torque density	32.1	kNm/m ³

The specifications of HPSMG shown in the table are results of experimental measurements while HPSMG was loaded with a propeller. In this stage of research, load-tests were not performed with FESM. The output parameters of HPSMG are based on the usage of propeller 1 both as a load and a cooling element.

The table shows that the ratio of maximum continuous power and mass of HPSMG is $P\text{-to-}W = 4.1$ kW/kg at the rotational speed of $n = 5600$ rpm.

Table 5.7 shows some examples of the machines designed for light aviation from world known manufacturers. In the presented machines the high specific power and torque density are important parameters.

The data collected in this table can provide only general estimation about the ratios of $P\text{-to-}W$, $P\text{-to-}V$ and $T\text{-to-}V$ and do not give the exact comparance between machine parameters, as the power is proportional to rotational speed and torque with mass. However, it is possible to get some indication in which level are those ratios comparing to HPSMG.

Table 5.7. Comparison of power and torque densities with different products and producers

Manufacturer		YASA Motors Ltd.	Geiger Engineering GmbH	ENSTROJ d.o.o.	Turnigy	Siemens AG	Rotex Electric	Unit
Country	Symbol	United Kingdom	Germany	Slovenia	United States	Germany	Czech Republic	
Type		YASA-400	HPD-12	EMRAX 348 AC	G160	LUFO IV	REX30	
Cooling		Oil	Air	Air	Air	Liquid	Air	
Torque		T_m	250	35.2	500	2.3	1000	73.7
Power	P_2	70	11.4	70	2.2	261	18.5	kW
Axial length	L_{stk}	75	71	107	66	300	74	mm
Diameter	D	280	218	348	64	418	216	mm
Weight (mass)	W	24	3.8	39	0.6	50	5.2	kg
Power-to-weight ratio	$P-to-W$	2.9	3.0	1.8	3.4	5.2	3.6	kW/kg
Power-to-volume ratio	$P-to-V$	15.2	4.3	6.9	10.5	6.3	6.8	MW/m ³
Torque density	$T-to-V$	54.1	13.3	49.1	10.9	24.3	27.2	kNm/m ³

The table includes machine types with air cooling and liquid cooling, the first type of which has direct cooling of housing and the second type has indirect cooling of the radiator with the propeller.

Comparison of the specifications of HPSMG to the values in table reveals that the ratio of $P-to-W$ is better only in the electrical motor prototype LUFO IV manufactured by Siemens AG and designed for light aviation (Fig. 1.6, Section 1.3) [20]. Still, the given specification is superior to that of all the other specifications, including machine types with oil cooling and liquid cooling. The levels of $P-to-W$ in FESM are average.

The $P-to-V$ value in HPSMG is well superior comparing to other products, even with the respective value of LUFO IV [20]. The smallest difference in this value is that of YASA-400 [82].

Torque density $T-to-V$ value of HPSMG can be considered better than average, but it remains lower of the respective values of YASA-400 and EMRAX 348 AC manufactured in Slovenia [83].

Based on the comparison is possible to estimate that the specifications of the specific power and torque density of HPSMG is competitive in the area of light aviation. In some aspects, respective specifications of HPSMG can be considered very good.

These specifications have been improved in several experimental electrical machines. Section 1.3 (Fig. 1.3) describes a PM synchronous machine developed by PEMC Group (Power Electronics, Machines and Control Group) of the University of Nottingham, which achieved a specific power of 16 kW/kg [18]. To achieve such a high specific power, very high rotating speed of the rotor $n = 32000$ rpm is necessary [18]. In comparance the maximum rotational speed of HPSMG is only in between $n = 4000-5600$ rpm.

The other machine developed by PEMC Group (Fig. 1.4, Section 1.3) has high torque density measured to be $T-to-V = 270$ kNm/m³. To obtain high torque for this machine, PEMC Group recommends the following [18]:

- Outer-rotor configuration;

- High pole number with a single layer concentrated winding;
- Unequal wound and unwound tooth widths;
- Halbach magnet arrangement;
- High grade soft magnetic material;
- Open slot design;
- Special thermal paths to enhance heat transfer;
- High saturation flux density material;
- Advanced thermal management to minimize temperature rise.

5.6 Conclusion

Practical tests of HPSMG as a generator and a motor were described in this section. To compare and to add weight to arguments, the preliminary test results of the final phase of FESM construction in no-load operation as a motor and a generator were outlined.

The measured nominal current of $I_{ph} = 23.0$ A during the generator load test is close to 26.0 A, which was originally estimated [23]. The last higher current value is theoretically possible, taking into account the parameters of the winding insulation and permanent magnets. This, however, requires mechanical improvements of the stator and bearing fixation construction in order to achieve longer endurance, particularly during high loads, which generate significant electromagnetic forces.

The performed generator tests with HPSMG were made with the maximal phase current of $I_{ph} = 23.0$ A at the rotational speed of $n = 5500$ rpm. Therefore, the current density in the winding conductor reached up to $J = 19.3$ A/mm². The rise in the temperature during the experiment stabilized at 106 °C. From the perspective of current density and temperature, the given values are notably high. In the current case though, copper wire with the insulation rating of 212 °C (Section 2.8.1) was used, which has the maximum allowable current density of 23.7 A/mm² [66], resulting in even higher allowable rate. According to the experiment results, the apparent power of the generator was $S = 890$ VA [24]. During the generator tests, the cooling was only provided by the impeller on the HPSMG's external rotor. Taking into account the dimensions of the machine and the weight of active materials (742 g), the specific power of HPSMG is 1.2 VA/g, which is a very good result.

In conclusion, it can be stated that HPSMG fulfils its requirements as a generator.

During the load experiments in a HPSMG motor mode, the forced cooling by using a propeller allowed even higher phase currents I_{ph} , resulting in the very high current density of $J = 44.2$ A/mm² while the winding temperature was still stabilized at $\vartheta_{p2} = 105$ °C. The effect of high currents gave an apparent power of the value $S = 3.56$ kVA and active power of $P_2 = 2.9$ kW.

Hence, the performed thermal experiments indicated significantly higher

power and current density handling capabilities of HPSMG with forced cooling provided by the propeller while keeping other machine active parts at notably lower constant temperatures.

In conclusion, based on the experimental work, HPSMG fulfils the initial requirements set as a primary propulsion element in a motor mode, either working in parallel with ICE or in the starter mode in stable flying or in take-off regimes of UAV at the provided propeller pitch. Experimental work was performed in the laboratory conditions at normal atmospheric pressure. Therefore, air mass dynamics in open air, which has an impact on UAV flight speed, were not considered.

6 FUTURE RESEARCH

Focus in this doctoral thesis is on the development of two exterior-rotor permanent magnet synchronous machines, i.e. HPSMG and FESM. This expertise can be used in further research. The purpose is to continue studies of electrical machines of high specific power, the target group of which is mostly electrical means of transport. In addition to light airplanes, this area includes also surface vehicles, e.g. cars and motorcycles.

Thus, in the next stage, permanent magnet synchronous machine design with liquid cooling for an electrical motorcycle will be studied; the maximum output power of the motorcycle is 150 kW, rotational speed $n = 9000$ rpm, DC/AC controller with the supply voltage of $U_{sup} = 650$ V_{DC}, the supply current of $I_{sup} = 250$ A. It is planned to use the exterior-rotor topology similar to that of HPSMG and FESM. Outer measurements of the machine housing are approximately $D_r = 250$ mm and $L_{stk} = 250$ mm. As the machine is designed to be closed, a stator open internal perimeter is used for liquid cooling whereas a cooling jacket is located inside the stator.

The development process is divided into several stages similar to those described in this doctoral thesis, incorporating analytical calculations to determine preliminary dimensions. Materials selection is an essential part of the study. In this solution, NdFeB-based high-temperature magnets and winding conductors with respective specifications are used.

Highly thin ferromagnetic materials are planned as stator materials. Outer housing of the machine will be designed from fusible alloys or composite materials.

A two-year time period is planned for the whole development process comprised of preliminary calculations, electromagnetic and thermal modelling, materials acquisition, assembling, and testing of the prototype.

REFERENCES

- [1] C. Mi, M. A. Masrur, and D. W. Gao, "*Hybrid Electric Vehicles: Principles and Applications with Practical Perspectives*," 1st ed. Publication: John Wiley & Sons, Ed. United Kingdom: John Wiley & Sons, Ltd. 2011, p. 448.
- [2] N. A. Owen, O. R. Inderwildi, and D. A. King, "The status of conventional world oil reserves—Hype or cause for concern?" *Energy Policy*, vol. 38, no. 8, pp. 4743–4749, Aug. 2010.
- [3] M. Katsman, "*Elektrimasinad ja transformaatorid*," 1st ed. Publication: Valgus, Tallinn, Estonia, 1971, p. 396.
- [4] Toyota Global Site, "Environmental Technology," [Online]. Available: http://www.toyota-global.com/innovation/environmental_technology/. [Accessed: 01-Feb-2016].
- [5] M. Hepperle, "Electric Flight - Potential and Limitations," *AVT-209 Work. Lisbon*, no. October, pp. 1–30, 2012.
- [6] C. Friedrich and P. A. Robertson, "Hybrid-Electric Propulsion for Aircraft," *J. Aircr.*, vol. 52, no. 1, pp. 176–189, Jan. 2015.
- [7] "Le Ballon dirigeable LA FRANCE de Renard et Krebs - 1884" [Online]. Available: http://rbmn.free.fr/Dirigeable_LA_FRANCE_1884.HTML. [Accessed: 01-Feb-2016].
- [8] N. Tesla, "*My Inventions - The Autobiography Of Nikola Tesla*," 2nd ed. Publication: SoHo Books, USA, 2011.
- [9] A. B. Cryer, "Electric aircraft explained," [Online]. Available: http://everything.explained.today/Electric_aircraft/. [Accessed: 01-Feb-2016].
- [10] R. J. Boucher and A. F. Inc., "History of Solar Flight," *AIAA/SAE/ASME 20th Jt. Propuls. Conf.*, vol. c, no. July, pp. 1–22, 1984.
- [11] L. A. Costello, "State of the art of piloted electric airplanes, NASA's centennial challenge data and fundamental design implications" Master's Thesis, Embry-Riddle Aeronautical University, Daytona Beach, USA, 2011.
- [12] Solar Impulse SA, "Solar Impulse - Around the World to Promote Clean Technologies," [Online]. Available: <http://www.solarimpulse.com/adventure#route>. [Accessed: 01-Feb-2016].
- [13] T. A. Rotramel, "Optimization of Hybrid-Electric Propulsion Systems for Small Remotely-Piloted Aircraft" Master's Thesis, Air Force Institute of Technology, Ohio, USA, 2011.

- [14] Toyota (GB) PLC, "History of the Toyota Prius," [Online]. Available: <http://blog.toyota.co.uk/history-toyota-prius>. [Accessed: 01-Feb-2016].
- [15] Flight Design GmbH, "Flight Design Presents New Propulsion System; Green Power Proof of Concept to Debut at Aero," [Online]. Available: <http://flightdesign.com/wordpress/?p=2561>. [Accessed: 01-Feb-2016].
- [16] R. R. Glassock, "*Design, modelling and measurement of hybrid powerplant for unmanned aerial vehicles (UAVs)*" Master's Thesis, Queensland University of Technology, Brisbane, Australia, 2012.
- [17] S. Rogers and S. Boyd, "Overview of the DOE Advanced Power Electronics and Electric Motor R & D Program APEEM R & D Program Vehicle," 2014.
- [18] C. Gerada, "Future Powertrain Conference 2014 High Performance Electrical Machines for Electrical Propulsion electrical machines in electrical propulsion," 2014.
- [19] The Institute for Industrial Productivity, "Industrial Efficiency Technology and Measures," [Online]. Available: <http://ietd.iipnetwork.org/content/motor-systems#benchmarks>. [Accessed: 01-Feb-2016].
- [20] K. Petermaier, "Electric propulsion components with high power densities for aviation," 2015. [Online]. Available: <http://nari.arc.nasa.gov/sites/default/files/attachments/Korbinian-TVFW-Aug2015.pdf>. [Accessed: 01-Feb-2016].
- [21] F. Harmon, R. Hiserote, M. Rippl, and J. Ausserer, "Parallel Hybrid-Electric Propulsion Systems for Unmanned Aircraft," 16-Aug-2012.
- [22] N. Eshel, "Hybrid-Electric Propulsion For Rotax," 2015. [Online]. Available: <http://aviationweek.com/paris-air-show-2015/hybrid-electric-propulsion-rotax>. [Accessed: 01-Feb-2016].
- [23] R. Nukki, A. Kilk, A. Kallaste, T. Vaimann, and K. T. Sr, "Exterior-rotor permanent magnet synchronous machine with toroidal windings for unmanned aerial vehicles," in *2014 Electric Power Quality and Supply Reliability Conference (PQ)*, 2014, pp. 215–220.
- [24] R. Nukki, A. Kilk, A. Kallaste, T. Vaimann, and K. T. Sr, "Generator mode analysis of exterior-rotor PM synchronous machine with Gramme's winding," in *2015 IEEE 5th International Conference on Power Engineering, Energy and Electrical Drives (POWERENG)*, 2015, pp. 347–352.
- [25] Horizon Hobby LLC, "Sky Surfer RTF," [Online]. Available: <http://www.horizonhobby.com/product/airplanes/airplane-accessories/all-airframe-parts/sky-surfer-rtf-hbz7800>. [Accessed: 01-Feb-2016].

- [26] C.-L. Xia, "*Permanent Magnet Brushless DC Motor Drives and Controls*," 1st ed. Publication: John Wiley & Sons, Ed. Singapore: John Wiley & Sons Pte, Ltd. 2012, p. 282.
- [27] J. C. Gamazo-Real, E. Vázquez-Sánchez, and J. Gómez-Gil, "Position and Speed Control of Brushless DC Motors Using Sensorless Techniques and Application Trends," *Sensors*, vol. 10, no. 7, pp. 6901–6947, 2010.
- [28] ABB, *Low voltage motors Motor guide*, no. February. 2014.
- [29] G. G. Antony, "IEC defined 60034-1 S1...S10 Duty Types and their applicability to mechanical devices."
- [30] Honda Motor Co., Inc., "GX35 Mini 4-Stroke Engine," [Online]. Available: <http://engines.honda.com/models/model-detail/gx35>. [Accessed: 02-Feb-2016].
- [31] Hobbyking, "Turnigy dlux 250A HV 14s 60v ESC," [Online]. Available: http://www.hobbyking.com/hobbyking/store/_25202_Turnigy_dlux_250A_HV_14s_60v_ESC.html. [Accessed: 02-Feb-2016].
- [32] J. R. Miller and T. J. E. Hendershot, "*Design of Brushless Permanent-Magnet Machines*," 2nd ed., Ohio: Magna Physics Publishing, New York: Oxford University Press 2011, pp. 1.1–5.1.
- [33] Minebea Co., Ltd. "The BLDC Motor – Introduction to Brushless DC Motors - NMB," [Online]. Available: http://www.nmbtc.com/brushless-dc-motors/engineering/brushless_dc_motors_engineering/. [Accessed: 05-Apr-2016].
- [34] D. L. Gabriel, J. Meyer, and F. Du Plessis, "Brushless DC motor characterisation and selection for a fixed wing UAV," *IEEE AFRICON Conf.*, no. September, pp. 13–15, 2011.
- [35] H. Vu Xuan, "*Modeling of exterior rotor permanent magnet machines with concentrated windings*," Ph.D. Dissertation, Delft University of Technology, Delft, Netherlands, 2012.
- [36] P. Pillay and R. Krishnan, "Application characteristics of permanent magnet synchronous and brushless DC motors for servo drives," *IEEE Trans. Ind. Appl.*, vol. 27, no. 5, pp. 986–996, 1991.
- [37] J. F. Gieras, R.-J. Wang, and M. J. Kamper, "*Axial Flux Permanent Magnet Brushless Machines*," 2nd ed. Publication: Springer Science & Business Media, 2008, p. 362.
- [38] M. Aydin, S. Huang, and T. A. Lipo, "Axial Flux Permanent Magnet Disc Machines," Research Report, University of Wisconsin-Madison, Madison, USA, 2004.
- [39] F. Sahin, "*Design and Development of a High-Speed Axial-Flux*

- Permanent-Magnet Machine,*” Ph.D. Dissertation, Eindhoven University of Technology, Eindhoven, Netherlands, 2001.
- [40] R. Q. R. Qu and T. a. Lipo, “Dual-rotor, radial-flux, toroidally wound, permanent-magnet machines,” *IEEE Trans. Ind. Appl.*, vol. 39, no. 6, pp. 1665–1673, 2003.
- [41] Y. Li, J. Zhao, Z. Chen, and X. Liu, “Investigation of a Five-Phase Dual-Rotor Permanent Magnet Synchronous Motor Used for Electric Vehicles,” *Energies*, vol. 7, no. 6, pp. 3955–3984, Jun. 2014.
- [42] T. J. E. Miller, “SPEED ’ s Electric Machines,” 2014.
- [43] D. Hanselman, *Brushless Motors: Magnetic Design, Performance, and Control of Brushless DC and Permanent Magnet Synchronous Motors*, 1st ed. Publication: E-Man Press LLC, US. 2012, p. 640.
- [44] J. F. Gieras and I. A. Gieras, “Recent developments in electrical motors and drives,” *East Hartford, CT United Technol. Res. Center, R. Oak, MI Beaumont Serv. Co.*, pp. 1–8, 2001.
- [45] N. Veignat, “How to Optimize Performance and Minimize Size in High Speed Applications,” 2012.
- [46] J. Pyrhönen, T. Jokinen, and V. Hrabovcová, *Design of Rotating Electrical Machines*, 1st ed. Publication: John Wiley & Sons, Ed. United Kingdom: John Wiley & Sons Pte, Ltd. 2008, p. 514.
- [47] A. Kallaste, "*Low Speed Permanent Magnet Slotless Generator Development and Implementation for Windmills*" Ph.D. Dissertation, Tallinn University of Technology, Tallinn, Estonia, 2013.
- [48] HKCM Engineering e.K., “Magnets from stock.” [Online]. Available: <https://www.hkcm.de/tesla/?permanent%20magnets%20from%20stock%20and%20on%20demand>. [Accessed: 02-Feb-2016].
- [49] R. Nukki, T. Lehtla, A. Kilk, and T. Kangru, “Design of the exterior-rotor PM synchronous motor for an electric powered paraglider,” in *2015 56th International Scientific Conference on Power and Electrical Engineering of Riga Technical University (RTUCON)*, 2015, pp. 1–4.
- [50] MAGSY, s.r.o. “Magnet NdFeB 20x5,4x2,2,” [Online]. Available: <http://eshop.magsy.cz/en/product/79031.magnet-ndfeb-20x5-4x2-2-p/>. [Accessed: 02-Feb-2016].
- [51] O. Kudrjavnsev and A. Kilk, “Cogging torque reduction methods,” in *2014 Electric Power Quality and Supply Reliability Conference (PQ)*, 2014, pp. 251–254.
- [52] A. Parviainen, "*Design of Axial-Flux Permanent-Magnet Low-Speed Machines and Performance Comparison between Radial-Flux and Axial-*

- Flux Machines*" Ph.D. Dissertation, Lappeenranta University of Technology, Lappeenranta, Finland, 2005.
- [53] Surahammars Bruks AB, "Non-Oriented Electrical Steel | Products | Cogent Power," [Online]. Available: <http://cogent-power.com/products/non-oriented-electrical-steel>. [Accessed: 02-Feb-2016].
- [54] Surahammars Bruks AB, "Sura ® no18," 2010," Available: http://cogent-power.com/cms-data/downloads/Hi-Lite_NO18.pdf [Accessed: 02-Feb-2016].
- [55] Metglas Inc., "Metglas Magnetic Materials Overview," [Online]. Available: http://www.metglas.com/products/magnetic_materials/. [Accessed: 02-Feb-2016].
- [56] Goodfellow Cambridge Ltd.: "Permendur 49." [Online]. Available: <http://www.goodfellow.com/catalogue/>. [Accessed: 02-Feb-2016].
- [57] SG Technologies Ltd., "Soft Magnetic Composite, SMC," [Online]. Available: <http://www.sgtec.com/materials/soft-magnetic-components-smc>. [Accessed: 02-Feb-2016].
- [58] Emetor Aktiebolag, "Materials library," [Online]. Available: <https://www.emetor.com/edit/materials/sura-no18/?cat=6&co=10>. [Accessed: 02-Feb-2016].
- [59] W. H. Yeadon and A. W. Yeadon, "*Handbook of small electric motors*," 1st ed. Publication: McGraw-Hill Education, New York, USA, 2001, p. 1184.
- [60] U.S. Department of Energy, "Critical materials strategy," pp. 1–196, 2011.
- [61] Magnet Energy Corp., "PM history," [Online]. Available: <http://www.magnetnrg.com/pm-history.html>. [Accessed: 02-Feb-2016].
- [62] M. Drak and L. a Dobrzański, "Corrosion of Nd-Fe-B permanent magnets," *J. Achiev. Mater. Manuf. Eng.*, vol. 20, no. 1–2, pp. 239–242, 2007.
- [63] Y. Liu, "High efficiency Electrical Machines," Chalmers, Sweden, 2015.
- [64] Arnold Magnetic Technologies, "Neodymium Magnets," 2016. [Online]. Available: <http://www.arnoldmagnetics.com/en-us/Products/Neodymium-Magnets>. [Accessed: 02-Feb-2016].
- [65] Brocott UK, "Enamelled Copper Magnet Wire," 2016. [Online]. Available: <http://www.brocott.co.uk/>. [Accessed: 02-Feb-2016].
- [66] W. H. Yeadon and B. M. Frustaglio, "Current Density," SMMA Fall Conference 2010 Presented by Yeadon Energy Systems , Inc., 2010.

- [67] H. L. Chan and K. T. Woo, "Closed Loop Speed Control of Miniature Brushless DC Motors," *J. Autom. Control Eng.*, vol. 3, no. 4, pp. 329–335, 2015.
- [68] A. Kilk, "Multipole Permanent-Magnet Synchronous Generator for Wind Power Applications" Ph.D. Dissertation, Tallinn University of Technology, Tallinn, Estonia, 2008.
- [69] C. W. T. McLyman, "Fringing Flux and Its Side Effects," pp. 1–8.
- [70] A. Voldek, "*Elektrimasinad I–II*," Publication: Valgus, Tallinn, Estonia, 1972, p. 340–480.
- [71] J. L. Kirtley Jr, "*Introduction to Power Systems–Permanent Magnet Brushless DC Motors*," Massachusetts Institute of Technology, Department of Electrical Engineering and Computer Science, 2003.
- [72] R. Nukki, A. Kilk, S. Saarts, and K. Tiimus, "Motor Mode Analysis of Exterior-Rotor PM Machine with Gramme's Winding," *Elektron. IR, Elektrotehnika*, 2016.
- [73] Emeter AB, "Maximum possible slot fill factor using round conductors," 2016. [Online]. Available: <https://www.emeter.com/blog/post/how-big-maximum-possible-slot-fill-factor-using-round-conductors/>. [Accessed: 02-Feb-2016].
- [74] D. Gerling, "Comparison of Different FE Calculation Methods for the Electromagnetic Torque of PM Machines," *NAFEMS Semin. Numer. Simul. Electromechanical Syst.*, pp. 1–8, 2005.
- [75] M. Alaküla, "High efficiency electrical machines." Chalmers University of Technology, Chalmers, Sweden, pp. 4–46, 2015.
- [76] M. Popescu, "Prediction of the electromagnetic torque in synchronous machines through Maxwell stress harmonic filter (HFT) method," *Electr. Eng.*, vol. 89, no. 2, pp. 117–125, 2006.
- [77] J. Zambada, "Sinusoidal control of PMSM motors with dsPIC30F DSC," *Appl. note AN1017, Microchip Technol. Inc*, no. 1017, pp. 1–18, 2005.
- [78] K. G. Upadhyay, *Design of electrical machines*, 2nd ed. Publication: New Age International Publishers, Delhi, India, 2013.
- [79] Powernet Oy, "*Power Supplies and Battery Chargers 800W-3000W*," 2016. [Online]. Available: <http://www.powernet.fi/standard-products/acdc-dcdc/>. [Accessed: 04-Feb-2016].
- [80] Portable Power Corp, "Approve sheet for Lithium ion polymer rechargeable battery." Richmond, CA, USA, p. 14, 2008.
- [81] I. H. Mengistu, "*A Small internal combustion engine testing for a hybrid-electric remotely-piloted aircraft*" Master's Thesis, Air Force Institute of

- Technology, Ohio, USA, 2011.
- [82] YASA Motors Ltd., "*YASA-400 Advanced Axial Flux Electric Motor*," 2016. [Online]. Available: <http://www.yasamotors.com/products/yasa-400/>. [Accessed: 04-Feb-2016].
- [83] ENSTROJ d.o.o, "EMRAX 348 prototype is made," 2016. [Online]. Available: <http://www.enstroj.si/News/emrax-348-prototype.html>. [Accessed: 04-Feb-2016].

ABSTRACT

Research and Development of Exterior-Rotor Permanent Magnet Synchronous Machines for Light Aerial Vehicles

Electrical machines in electrical transport are of increasing importance. This, in turn, has contributed to higher capacity of electrochemical energy storage units, including lithium polymer battery units mostly used in electrical light aircraft. Intensive research of battery units has promoted development of novel autonomous electrical drives mostly applied in the car industry, but also in electrical light aircraft, which is the area covered in this thesis research. Thus, hybrid and fully electrical solutions of propulsion systems used in light aircraft are briefly described.

The main purpose of the research was to develop a novel stator geometry for unmanned light aircraft with toroidal winding and exterior-rotor permanent machine HPSMG. In our solution, this electrical machine is a part of the hybrid propulsion system of a small unmanned aircraft, which allows operation both as a motor and a generator. Parallel operation with an internal combustion engine included also its function as a starter and as an additional power source.

In addition, a permanent magnet synchronous machine FESM with a two-layered concentrated winding of a similar exterior-rotor topology was developed to support the solution.

In the prototype development,, analytical calculations were made to obtain geometrical and electromagnetic base parameters. Distribution of the magnetic fields of the machines was modelled using appropriate software.

As non-conventionally high current densities were present in HPSMG and FESM, it was required to address cooling of both machines, including modelling their temperature fields.

To confirm the results, prototypes of HPSMG and FESM and a test bench were constructed for practical testing.

Development of two machines with a similar structure allowed a comparative analysis of electromagnetic and thermal values of a stator with one-layer Gramme's winding and a stator with two-layered concentrated winding. Additionally, a machine with a similar rotor topology and measurements of the stator but with different yoke placement and windings or HPSMG with concentrated windings were modelled using Motor-Cad software.

It is concluded from the comparative analysis of the machines with two different windings that the strength of the electromagnetic field generated in the coil core rather than the number of active conductors crossing the main magnetic field is of prime importance. It passes through the air gap from the teeth and counteracts with permanent magnets of the rotor, which attracts or repels permanent magnets and by which electromagnetic torque is obtained. Strength of the electromagnetic field is defined by the number of coils around the conductor core, by the current value passing through it and by geometrical and magnetic

values of the core. Thus, windings around the stator yoke in toroidal winding are as efficient in their electromagnetic values in the HPSMG motor mode as the winding usually wound around the teeth used in FESM. This conclusion is supported by analytical calculations performed in this research, the results from modelling and comparative analysis between toroidal and concentrated winding, also tests performed with the real prototype.

It is obvious that only active conductors located in the outer layer of stator slots where electromotive force is induced at the same magnitude with the counter-electromotive force are in contact with the main magnetic field of HPSMG. This is not in conflict with the electromagnetic induction law. However, in this context, the function of non-active sides of winding coils cannot be considered insignificant. This is supported by Faraday's law of induction, which states that the magnitude of the electromotive force induced in the coil is equal to the rate of the change of flux that is linked to the coil. The flux linkage of the coil is the product of the number of turns in the coil and the flux associated with the coil. Thus, all parts of the turn are of equal importance, i.e. classification of coil sides to active connections and end windings is rather conditional.

Various ratios were also used for comparison between the machines. The most important of them were specific power $P\text{-to-}W$ and torque density $T\text{-to-}V$, which could be compared to the same values of similar machines constructed by different manufacturers. The load tests results in the motor mode indicate that HPSMG (apparently FESM as well) are competitive by their output parameters in the area of light aviation. In HPSMG, the ratios mentioned above are very good. However, in the perspective obtained parameters can probably be further improved with the more comprehensive optimization.

In conclusion, it can be clearly stated that the main research objective of the thesis has been achieved.

KOKKUVÕTE

Välisrootoriga püsomagnet-sünkroonmasinate uurimine ja väljatöötamine kergetele õhusõidukitele

Elektrimasinate tähtsus elektertranspordis on tõusuteel. Suure tõuke selleks on andnud peamiselt viimasel kümnendil toimunud elektrokeemiliste energiasalvestite, sh kergetes elektrilistes õhusõidukites enim kasutatavate liitiumpolümeerakude energiamahukuse kasv. Intensiivne arendustöö akuseadmete valdkonnas on hoogustanud ka uudsete autonoomsete elektriagamite väljatöötamist, mille suurimaks rakenduseks on autotööstus, kuid ka elektrilised kerglennukid, mis on ka käesoleva doktoritöö valdkonnaks. Sellega seoses anti töö esimeses osas lühiülevaade kergetel õhusõidukitel kasutatavatest hübriid- ja täiselektrilistest ajamilahendustest.

Eeltoodust lähtuvalt püstitati ka uurimistöö peamine eesmärk, mis nägi ette välja töötada uudset tüüpi staatorigeomeetria, toroidmähise ja välisrootoriga püsomagnet-sünkroonmasin HPSMG mehitamata kerglennukile. Elektrimasin oli antud lahenduses üks osa väikese mehitamata lennuki hübriidajamist ning võimaldas opereerimist nii mootori kui ka generaatorina. Paralleeltalitus sisevälisrootoriga hõlmas lisaks veel starteri ja täiendava jõuallika funktsiooni.

Põhieesmärgi saavutamist toetas lisaks sarnase välisrootori topoloogiaga kahekihiline kontsentreeritud mähisega püsomagnet-sünkroonmasina FESM kavandamine, mille rakenduseks oli täiselektriline paraplaan.

Kummagi prototüübi väljatöötamine sisaldas esmalt analüütilist arvutamist geomeetriliste ja elektromagnetiliste lähteparameetrite saamiseks. Eeltoodule kinnituse leidmiseks modelleeriti masinate magnetväljade jaotumine lisaks vastava tarkvara abil.

Kuna nii HPSMG kui FESM puhul oli tegemist ebatraditsiooniliselt kõrgete voolutihedustega, siis pöörati uurimistöös tähelepanu kummagi masina jahutuse teemaatikale, mis hõlmas ka nende temperatuuriväljade modelleerimise.

Eeltoodud tulemustele praktilise kinnituse saamiseks valmistati HPSMG ja FESM prototüübid ning vastav stend nende praktiliseks katsetamiseks.

Kahe sarnase struktuuriga masina väljatöötamine võimaldas läbi viia võrdlusanalüüsi ühekihilise Gramme'i ja kahekihilise kontsentreeritud mähisega staatori elektromagnetiliste ja soojuslike parameetrite suhtes. Sel puhul modelleeriti Motor-CAD tarkvara abil täiendavalt analoogse rootori topoloogia ja staatori mõõtmega, kuid erineva staatori ikke asetuse ja mähistega masin ehk kontsentreeritud mähistega HPSMG.

Kummagi eri mähisega masina võrdlusanalüüsi kokkuvõtteks saab välja tuua, et mootoritalitluses ei oma esmast tähtsust põhimagnetvälja jõujooni lõikavate aktiivsete juhtide arv, vaid pooli südamikus tekkiva ja hambast läbi õhupilu kulgeva ning rootori püsomagnetitega vastasmõjus oleva elektromagnetvälja tugevus, mis püsimateid tõmbab või tõukab ning millega saavutatakse

elektromagnetiline moment. Elektromagnetvälja tugevuse määrab ära südamikku ümbritseva juhi keerdude arv, seda läbiva voolu suurus ning südamiku geomeetrised ja magnetilised näitajad. Seega võib järeldada, et toroidmähise puhul ümber staatori ikke keerutatud poolid ei ole HPSMG mootoritalitluses oma elektromagnetilistelt näitajatelt vähem tõhusad võrrelduna tavapärase ümber hamba mähitud mähistega, millist on kasutatud FESM puhul. Tehtud järeldust toetavad ka töös läbi viidud analüütilised arvutused, modelleerimisel saadud tulemused ja võrdlusanalüüs toroid- ja kontsentreeritud mähise vahel ning läbiviidud katsed realselt töötava prototüübiga.

Antud juhul on ilmne, et generaatoritalitluses omavad kokkupuudet HPSMG põhimagnetväljaga ehk lõikuvad sellega vaid staatori välises uurdekihis asetsevad aktiivsed juhid, milles indutseeritakse elektromotoorjõud, mis on samas suurusjärgus ka tekkiva vastuelektromotoorjõuga. Seega ei minda siin vastuollu elektromagnetilise induktsiooni seadusega. Siiski ei saa ka antud kontekstis lugeda mähispoolide mitteaktiivsete külgede funktsiooni täiesti tähtsusetuks. Seda toetab ka eeltoodud elektromagnetilise induktsiooni seadus, mille kohaselt on juhtmekeerus indutseeritud elektromotoorjõud võrdne keeruga aheldatud magnetvoo muutumise kiirusega. Seetõttu on keeru kõik osad samaväärselt tähtsusega ehk pooli külgede liigитamine aktiivseteks ja laupühendusteks on tinglik.

Väljatöötatud masinate väljundparameetrite hindamisel rakendati mitmeid suhteid, millest peamised olid erivõimsus $P\text{-}to\text{-}W$ ja momenditihedus $T\text{-}to\text{-}V$, mida andis kõrvutada teiste tootjate samasse valdkonda kuuluvate masinate näitajatega. Käesoleva doktoritöö käigus läbiviidud koormuskatsed mootorina näitavad, et HPSMG (ja ilmselt ka FESM) on oma väljundparameetrite lõikes kerglennukite valdkonnas igati konkurentsivõimeline. HPSMG puhul võib katsetulemusi lugeda isegi väga headeks. Siiski annab neid parameetreid põhjalikumal optimeerimisel perspektiivis ilmselt veelgi parandada.

Kokkuvõttena võib aga kindlalt järeldada, et doktoritöös püstitatud peamine eesmärk sai täidetud.

ELULOOKIRJELDUS

1. Isikuandmed

Ees- ja perekonnanimi: René Nukki

Sünniaeg ja -koht: 01.03.1974, Pärnu maakond, Audru vald

Kodakondsus: Eesti

E-posti aadress: renenukki@gmail.com

2. Hariduskäik

Õppeasutus (nimetus lõpetamise ajal)	Lõpetamise aeg	Haridus (eriala/kraad)
Tallinna Tehnikaülikool	2012	Ärikorralduse magister
Tallinna Tehnikaülikool	2005	Tehnikateaduste bakalaureus
Eesti Mereakadeemia	1998	Rakenduslik kõrgharidus
Pärnu I Keskkool	1992	keskharidus

3. Keelteoskus (alg-, kesk- või kõrgtase)

Keel	Tase
Eesti	Emakeel
Inglise	Kõrgtase
Vene	Keskase

4. Teenistuskäik

Töötamise aeg	Ülikooli, teadusasutuse või muu organisatsiooni nimetus	Ametikoht
2012 - ...	Tallinna Tehnikakõrgkool	Elektritehnika õppetooli hoidja
2007 - ...	Rovanet OÜ	Juhatuse liige
2008 - 2009	Vallin Baltic AS	Tegevdirektor
2005 - 2008	Schneider Electric Eesti AS	Osakonnajuhataja
2001 - 2004	ABB AS	Madalpingekompo- nentide tootejuht
1999 - 2001	Elin AS	Elektripaigaldiste projekteerija

5. Teadustöö põhisuunad

Suure erivõimsuse ja -energiaga püsिमagnetmasinate uurimine, väljatöötamine ja rakendamine transpordivahendites

6. Jooksvad projektid

- Elektrilise paraplaani mootori optimeerimine
- Püsिमagnet-sünkroonmootori väljatöötamine mootorrattale

CURRICULUM VITAE

1. Personal information

Name: René Nukki

Date and place of birth: 01.03.1974, Pärnu county, Audru

Citizenship: Estonian

E-mail: renenukki@gmail.com

2. Education

Institution	Graduation year	Education
Tallinn University of Technology	2012	Master of Business Administration
Tallinn University of Technology	2005	Bachelor of Science
Estonian Maritime Academy	1998	Applied higher education
Pärnu Secondary School No 1	1992	Secondary education

3. Languages

Language	Level
Estonian	Native
English	Fluent
Russian	Intermediate

4. Professional Employment

Date	Organization	Position
2012 - ...	Tallinn University of Applied Sciences	Holder of the Chair of Electrical Engineering
2007 - ...	Rovanet OÜ	Member of the Board
2008 - 2009	Vallin Baltic AS	Managing director
2005 - 2008	Schneider Electric Eesti AS	Department Manager
2001 - 2004	ABB AS	Product Manager
1999 - 2001	Elin AS	Electrical Designer

5. Main areas of scientific work

Research and development of PM synchronous machines with high specific power and energy for electric vehicles

6. Current projects

- Optimization of the motor of the electric paraplane
- Development of the PM synchronous machine for the motorcycle

APPENDIX

Appendix 1. Dimensional data of HPSMG and FESM

Appendix 2. Temperature equivalent scheme of HPSMG with the Gramme's winding

Appendix 3. Temperature equivalent scheme of HPSMG with the concentrated winding

Appendix 4. Temperature equivalent scheme of FESM with the concentrated winding

Appendix 1. Dimensional data of HPSMG and FESM

No.	Symbol	Description	HPSMG	FESM	Unit
1	D_{rin}	Internal diameter of rotor	93	197	mm
2	D_s	External diameter of stator	87.5	188	mm
3	D_{sin}	Internal diameter of stator	72	150	mm
4	h_m	Magnet height	2.2	4	mm
5	h_{ry}	Height of rotor yoke	2.55	5	mm
6	h_s	Total height of stator	7.75	19	mm
7	h_{sy}	Height of stator yoke	2.25	6	mm
8	k_m	Coverage factor	0.74	0.68	
9	l_g	Air gap length	0.5	0.6	mm
10	l_m	Length of magnets	20	40	mm
11	L_{stk}	Machine axial length	22	42	mm
12	L_{sy}	Axial length of stator	20	40	mm
13	p	Number of polepairs	10	21	pcs.
14	Q_s	Number of stator slots	24	36	pcs.
15	w_m	Width of magnet	10.8	10	mm
16	w_{sl1}	Width of slot between outer teeth	5.5	5	mm
17	w_{sl2}	Width of slot opening	8	10	mm
18	w_{sl3}	Width of slot between inner teeth	8	-	mm
19	w_{th1}	Width of tooth	3	5.5	mm
20	w_{th2}	Width of tooth head	6	11.5	mm
21	τ_u	Winding pitch	11.45	16.4	mm

AUTHOR'S PUBLICATIONS

The present doctoral thesis is based on the following publications that are referred to in the text by Roman numbers.

- [PAPER-I] **Nukki, R.**; Kilk, A.; Kallaste, A.; Vaimann, T.; Tiimus, K. (2014). Exterior-rotor permanent magnet synchronous machine with toroidal windings for unmanned aerial vehicles. Electric Power Quality and Supply Reliability Conference PQ 2014, Rakvere, Estonia, June 11-13, 2014. IEEE, pp. 215 - 220.
- [PAPER-II] **Nukki, R.**; Kilk, A.; Kallaste, A.; Vaimann, T.; Tiimus, K. (2015). Generator Mode Analysis of Exterior-Rotor PM Synchronous Machine with Gramme's Winding. IEEE 5th International Conference on Power Engineering, Energy and Electrical Drives (POWERENG). IEEE, pp. 347 - 352.
- [PAPER-III] **Nukki, R.**; Lehtla, T.; Kilk, A.; Kangru, T. (2015). Design of the Exterior-Rotor PM Synchronous Motor for an Electric Powered Paraglider. 56th International Scientific Conference on Power and Electrical Engineering, RTUCON 2015, Riga Technical University, 14.10.2015. IEEE, pp. 1 - 4.
- [PAPER-IV] **Nukki, R.**; Kilk, A.; Saarts, S.; Tiimus, K. (2016). Motor Mode Analysis of Exterior-Rotor PM with the Gramme's Winding. 20th International Conference, Electronics 2016, Kaunas University of Technology in collaboration with Vilnius Gediminas Technical University. IEEE (*Accepted 24.04.2016*).

[PAPER-I] **Nukki, R.**; Kilk, A.; Kallaste, A.; Vaimann, T.; Tiimus, K. (2014). Exterior-rotor permanent magnet synchronous machine with toroidal windings for unmanned aerial vehicles. Electric Power Quality and Supply Reliability Conference PQ 2014, Rakvere, Estonia, June 11-13, 2014. IEEE, pp. 215 - 220.

Exterior-Rotor Permanent Magnet Synchronous Machine with Toroidal Windings for Unmanned Aerial Vehicles

René Nukki, Aleksander Kilk, Ants Kallaste, Toomas Vaimann and Kristjan Tiimus Sr

Abstract—This paper represents the study of the multimode permanent magnet synchronous machine constructed for a small-sized unmanned aircraft. An overview of commonly used electrical machine types for unmanned aircrafts is also given within this paper. The main objective of the research was to create an electrical machine that could be used in addition to the combustion engine as a motor-generator. Based on the specifics of the area and the goal of the research the most suitable and optimal solution of the machine topology is considered. The paper gives an overview of the design of the permanent magnet electrical machine and its mechanical and electrical parameters. The test bench for experimental study of the prototype permanent magnet machine was also designed and built. Using the test bench the no-load test was carried out and corresponding characteristics were charted in a generator mode of the machine.

Index Terms—AC-DC power converters, AC machines, conductors, generators, impellers, permanent magnet machines, prototypes, rotors, stators, topology, unmanned aerial vehicles.

I. INTRODUCTION

An Unmanned aerial vehicle (UAV) is an aircraft without an on-board human pilot. The aircraft is usually piloted remotely or having an autopilot system. UAVs are meant to fulfil roles that are too dangerous or too long in duration for manned flight. Their applications are for example wildlife tracking, traffic monitoring, border patrols, environmental research, geographical mapping, numerous military applications etc. [1].

Nowadays the UAV market has grown into a multi-billion dollar industry. Substantial increase has been in the use of electric propulsion in this field [1]. The main benefit of an electric UAV is lower noise comparing to an internal combustion engine and missing of exhaust gas emissions.

During the last decades there is a new generation of smaller, more flexible UAV-s available, based mainly on electrical propulsion systems [1].

The main objective of this research was to design and study a permanent magnet (PM) electrical machine for the described type of small UAV. As a novelty of this solution, the designed toroidally wound electrical machine is

mechanically coupled to the internal combustion engine (ICE) of the aircraft. In this configuration both machines work together as a hybrid system. The electric machine in this system will operate in two modes – as a motor and as a generator. Generator is responsible for ensuring an adequate charging voltage and current for energy storage devices of the UAV. The principle scheme of the hybrid system with the energy storage elements is shown in Fig. 1.

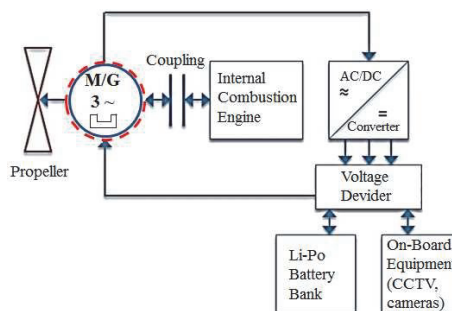


Fig. 1. Principal scheme of the UAV hybrid engine and energy storage system.

All electrical devices on board of the UAV are DC operating and supplied by the battery bank and a generator. In this solution an exterior-rotor permanent magnet synchronous machine (ERPMSM) is used as a generator or a motor according to the used mode. ERPMSM is connected with the AC/DC converter. The machines with such configuration are often called brushless DC machines (BLDC) with the exterior-rotor, but they are still synchronous AC machines as they consume and generate the alternating current. Hereinafter the studied electric machine in this paper is considered as a permanent magnet synchronous machine (PMSM).

II. SELECTION OF THE ELECTRIC MACHINE TOPOLOGY

The choice of the ERPMSM topology was determined by some basic requirements, such as simple construction, low cost, high power-to-weight and power-to-volume ratio, smallest possible size, good control options and high torque at low speed.

There are various types of electrical machines used today in electric-powered small UAV-s. The most commonly used are PMSM with external AC/DC converters. Mainly used types of these machines are with interior, exterior and axial rotor [2]. Their topologies are shown in Fig. 2.

This work was supported by the TTK University of Applied Sciences, Helicam Service Ltd and ELI Airborne Solutions.

R. Nukki, A. Kilk, A. Kallaste and T. Vaimann are with the Department of Electrical Engineering, Tallinn University of Technology, Ehitajate tee 5, 19086 Tallinn, Estonia (e-mail: renenukki@gmail.com, aleksander.kilk@ttu.ee, ants.kallaste@ttu.ee, toomas.vaimann@ttu.ee).

K. Tiimus Sr is with Helicam Service Ltd (e-mail: helicam@helicam.ee).

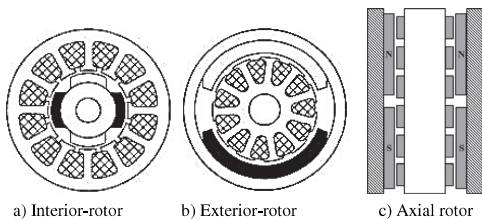


Fig. 2. Three basic machine configurations used in small UAV-s [2].

The exterior-rotor has some advantages over the interior-rotor. One of these is the option to mount the components into the internal opening of the stator, thus obtaining more compact solutions. In this case the clutch which mechanically connects and disconnects ICE from ERPMSM is mounted into the opened inner part of the stator core. This solution would be technologically quite sophisticated with an interior-rotor.

As another advantage of an exterior-rotor the centrifugal force due to the rotation compresses magnets to the inner surface of the rotor yoke. Thus, there is no need to use any bandages to fix the magnets. This increases the structural strength, performance and reliability of the machine.

In addition there are other design advantages of an exterior-rotor comparing to the interior-rotor:

- exterior-rotor allows to use lower energy magnet materials [1],
- exterior-rotor machine can have a larger diameter of the air gap by the same power and volume, which allows higher torque density [3],
- the bigger rotor diameter gives bigger inertial torque [2] necessary to overcome the air resistance caused aerodynamically by a rotating propeller,
- reduced copper losses and production costs [1].

Comparing the axial rotor with the radial flux exterior-rotor, both types have the same performance in terms of torque density, torque per mass, and efficiency [3]. A common structure of an axial rotor machine has two stators or two rotors to get the necessary balance. As a result the length of the air gap of an axial rotor machine is twice the size of the radial rotor machine. Also the axial rotor machine requires more magnet mass and larger ball bearings, which creates bigger losses. Therefore the manufacturing costs of a radial rotor machine are lower compared to the axial rotor machine [3]. Also the production methods of radial rotor machines are well-established for a significantly longer period of time.

The next step of the topology selection was to assess the differences between the slotted and slotless machines. The armature winding of PM machines is usually mounted in slots. A slotless winding has a reducing effect of the cogging torque, higher efficiency at high speeds, lower torque ripple and lower acoustic noise. However, the advantages of the slotted winding are higher efficiency at lower speeds, higher torque density, lower armature current, less PM material and lower material costs [4]. Several tests have proven that for the same produced torque a slotless machine needs higher magnetomotive force compared to a slotted machine. A slotless machine heats up very fast with high currents and therefore it needs special heat sinks for dissipating the heat. A slotted machine has also better

cooling conditions because of the axial air gap comparing to axial rotor machines having the radial air gap [5].

The aforementioned analysis was the basis on the selection of the machine topology with the aim to design and construct an exterior-rotor PM synchronous machine with slotted windings and external AC/DC converter.

III. BASIC DESIGN

Before the machine design begins, there are several important points that must be considered. A general procedure of the design is as following [2]:

- determination of application and requirements,
- choice of the rotor type,
- selection of number of phases, poles and stator slots,
- magnet grade selection,
- rough sizing estimation,
- selection of air gap length and determination of magnetic loading,
- rotor design and flux per pole determination,
- stator lamination lay out,
- calculation of number of conductors and turns per coil,
- wire size, resistance and inductance per phase calculations,
- performance calculation,
- checking of the temperature rise, current and flux densities and demagnetization of magnets,
- design modification until the objectives are met.

Some of the key points of machine designing procedures are observed in the following sections.

A. Determination of Application and Requirements

The first step in designing of a new electric machine is to determine the basic parameters such as the nominal and maximum speed, power and torque, nominal voltage, nominal current etc. In addition to the basic data the requirements for cooling, start-up, control and for the operating environment of the machine are needed to be defined.

As ERPMSM is working in conjunction with ICE, its basic parameters were related with ICE technical parameters, which had the nominal rotational speed of 5500 rpm and the maximum torque of 1.6 Nm.

The average rotational speed of the UAV propeller in the operating mode in the air is 4000 rpm. This is an important parameter that was considered during the design of the studied machine. At this rotational speed and in the motor mode ERPMSM had to ensure the required torque for the propeller, but in the generator mode at the same speed it had to generate the necessary voltage level to charge the battery bank and on-board devices.

To determine ERPMSM nominal revolutions, the respective figure of ICE was taken. Based on that figure, the nominal rotational speed of 5500 rpm of ERPMSM was also considered. The condition was that at this rotational speed the torque of ERPMSM had to be at least equivalent to the mechanical torque of ICE that means not less than 1.6 Nm.

B. Choice of the Rotor Type

The next step in the design procedure is to decide between the rotor types. If fairly low, slightly variable speed, zero cogging and smooth operation is required, the axial rotor machine is a wise solution. If high-torque and low speed is required, an interior-rotor design is appropriate.

If a higher speed is required which is constant or slightly varying, then the most suitable are exterior-rotor machines which are relatively easy and cost-effective to manufacture [2]. Exterior-rotor PM machines are also widespread in the small aircraft industry. On this basis the exterior-rotor design was decided.

C. Selection of Number of Phases, Poles and Stator Slots

The next basic step is the determination of number of phases. PMSM or BLDC are usually three phase machines. They have the possibility of wye-, delta-connected or unipolar windings and can operate with only three connecting leads with no loss of control flexibility. They have good starting characteristics, smooth rotation in both directions and low torque ripple. Those machines have similarities with the windings of AC induction and brushed DC machines. The configurations allow the use of a very large variety of magnets and winding configurations. Also they can be operated with either square- or sinewave controller, and are easily adapted with sensorless control, as it is with the machine in this study [2]. Table 1 shows the dependence between the number of phases, the conductor utilization, the number of commutation switches and torque ripple.

TABLE I. COMPARISON OF PMSM WITH DIFFERENT PHASE NUMBERS [2]

No. of phases	Reference Parameters		
	Conductor utilization (%)	No. of power switches	Torque ripple
1	50	2	100
2	50	4 or 8	30
3	67	3 or 6	15
4	75	8	10
6	83	12	7
12	92	24	3

The conductor utilization is the percentage of active conductors that carry current from the total number of conductors [3]. For ERPMSM the 3-phase solution was considered as the most common type.

The choice of the number of poles of the PM machine depends on several parameters as [2]:

- type and class of magnetic materials,
- rotor type (internal, external or axial rotor),
- physical layout of the magnets,
- required speed and inertial torque of a machine.

ERPMSM is designed for high-speed applications. To get higher speed at constant frequency it would be feasible to reduce the number of pole-pairs that minimizes excessive switching losses of transistors and iron losses in the stator. A good result in this case would have been a 2-pole machine, but on the other hand the diameter of this kind of machine would have been relatively large [2].

Considering the final implementation of ERPMSM it is important to get also a small diameter and low weight. Each time the number of poles is doubled, the rotor yoke or back-iron inside the magnets is reduced by half. According to the same principle higher number of poles reduces the thickness of the stator. Thus, in order to achieve small dimensions for a given machine and taking into account the dimensions of available magnets, the number of poles was increased to 20. To reduce cogging the number of the slots was chosen 24, which gave the slot per pole ratio of 1.2.

D. Selection of Air Gap Length

Maximum resistance to demagnetization requires a small air gap length. On medium size machines it is around 0.4–0.5 mm [2]. In ERPMSM the air gap length after the mechanical treatment was obtained to 0.56 mm, which is slightly more than in the above-mentioned range.

IV. PERMANENT MAGNETS

The most popular magnet materials of PM machines are the ferrites, bonded and/or sintered neodymium-iron-boron (NdFeB) and samarium cobalt (SmCo) [6]. The invention of high energy density rare earth magnets made a revolution in construction of high efficiency and high power density permanent magnet machines. The best sintered NdFeB magnets have the magnetic flux density (B) until 1.45 T and magnetic field strength (H) until 1100 kA/m [12]. The operating temperature of some NdFeB magnets is already over 250 °C.

The usage of PMs for field excitation gives several benefits [4]:

- no electrical energy is absorbed and therefore no excitation losses which means substantial increase in the efficiency,
- higher torque or output power per volume than when using electromagnetic excitation,
- better dynamic performance comparing to machines with electromagnetic excitation (higher magnetic flux density in the air gap),
- simplification of construction and maintenance,
- lower price for some types of machines.

In ERPMSM it was also decided to use sintered NdFeB rare-earth magnets. N42H NdFeB magnets were chosen, as these magnets gave the optimal ratio in respect of their technical parameters (high energy density, coercive force, maximum operating temperature 150 °C), quality and price.

The typical demagnetization characteristics of chosen magnets are represented in Fig. 4.

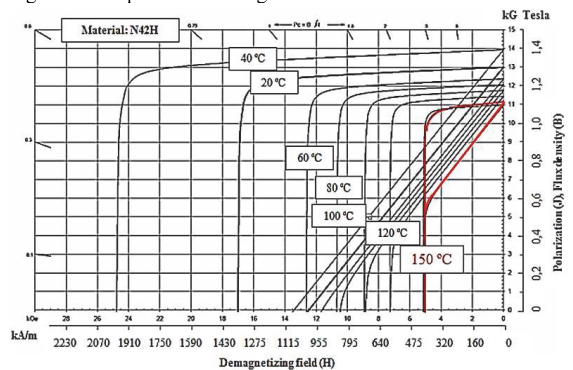


Fig. 3. Demagnetization curves of sintered NdFeB N42H magnets [7].

V. STATOR

The precondition of the design of ERPMSM was low weight and small external dimensions, which rated also the outer diameter of the stator. The stator inner diameter was determined by the clutch mechanism installed into the machine. In these conditions the stator was constructed with an internal diameter of 72 mm and with an outer diameter of 88 mm (Fig. 4).

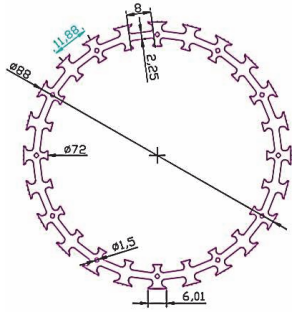


Fig. 4. The stator layout with dimensions.

The stator core was made of laminated electrical steel sheets with the length of 0.18 mm (type NO18) with slots on inner and outer surface. As the magnetic field in the stator is radial and circumferential, the core has to be laminated axially. Laminations between steel sheets are aimed to lessen eddy current losses. 110 pieces of sheets were glued together with epoxy adhesive to obtain necessary length of the stator (22 mm). The technical parameters of the used material are shown in Fig. 5.

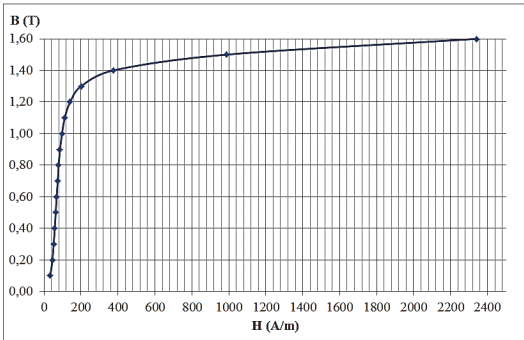


Fig. 5. The B-H characteristic of the stator core material NO18 steel [8].

VI. ROTOR

To get the required air gap length the rotor yoke of ERPMSM has been made of ferromagnetic stainless steel cylinder with the external diameter 98 mm, length 24 mm and thickness 4 mm. Its magnetic properties are not as good as those of soft magnetic alloys, but it is more cost-effective. This is important especially in these conditions, where the machine has to withstand for corrosive environments. Ferromagnetic stainless steel has relatively high electrical resistivity, which gives small eddy current losses in the rotor yoke. These types of stainless steels have properties of soft magnetic materials, such as high magnetic permeability, low coercive force, and low residual flux density. Its coercivity will rise in a cold environment, but permeability will reduce [3].

On the inner side of the rotor there are 40 NdFeB magnets glued pairwise with a special metal adhesive. The permanent magnets on rotor cylinder are polarized radially in the opposite directions. This makes the magnetic field in the core oriented as shown in Fig 6.

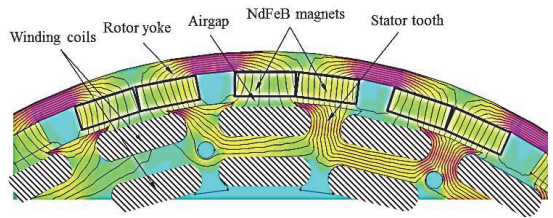


Fig. 6. ERPMSMs geometry and computed distribution of magnetic flux densities.

As ERPMSM is provided with rare-earth NdFeB magnets, it is not common to use an overhang because of the high remanence which cannot carry the extra flux on stator teeth [2]. Therefore the length of the magnet (20 mm) is almost equal to the thickness of the stator stack (22 mm).

VII. WINDINGS

One aspect of ERPMSM that slightly differs from the normal practice is that the toroidal winding known as the Gramme's winding is used, where the coils are placed in the inner and outer slots. The advantage of the Gramme's winding is that it has very short end connections comparing to overlap winding of conventional machines [5].

One of the main reasons for the use of the Gramme's winding was that this kind of winding gave a better filling factor of slots allowing the mounting of more conductors into a single slot comparing to common winding layout which winds the conductors around the stator teeth.

Such a way of winding also leads to weakening of the armature reaction and provides a slightly stiffer load characteristic of ERPMSM in a generator mode. Table 2 shows the calculated parameters on the basis of the applied winding scheme.

TABLE II. ERPMSM WINDING PARAMETERS

No.	Winding Parameters		
	Symbol	Parameter	Value
1	q	Slots per pole and phase	0.4
2	τ	Winding pitch	1.2
3	α	Electrical offset angle	150°
4	N	Number of turns per slot	6

Based on these results the vector diagram of phase electromotive forces (EMF) and the winding scheme were compiled (Fig. 7 and Fig. 8).

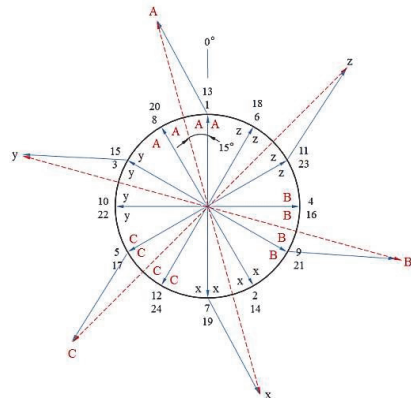


Fig. 7. EMF vector diagram.

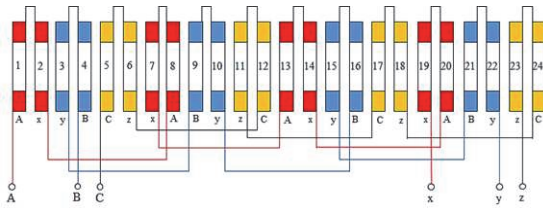


Fig. 8. Scheme of Gramme's winding.

Each phase winding consist 8 coils connected in series. For example, the phase A winding has coils 1, 2, 8, 7, 13, 14, 20, 19 connected to each other. The same principle has been established with the rest of phase windings. Endings of the phase windings were connected to star, in order to eliminate the EMF third harmonic.

H-class double-insulated wire was used for the winding with the cross-sectional area of 0.99 mm^2 and resistance of $172.7 \text{ } \Omega/\text{km}$ [9]. Coils were wound with the 12-wire stranded conductor which provided the total cross-section area of 1.19 mm^2 . The following step was to find the maximum allowable current density for this cross-section area, taking into account that ERPMMSM operates at intensive cooling conditions.

Conventional electric machines operating in a continuous duty cycle are permitted to use current densities in the range of $4.0\text{-}6.0 \text{ A/mm}^2$. In practice if the current density is more than 15.0 A/mm^2 , it should be cooled down with intense forced convection rather than natural cooling. This may be done for example with an impeller, liquid, gel or any other means of cooling [10].

In ERPMMSM the propeller of the UAV and mechanically machined openings in the rotor plate are used to provide the intensive cooling. The openings are operating as an impeller, and at the same time being a simple and reliable solution.

In intensively cooled high speed PM machines, the applied current densities are significantly higher. For example copper wire 23 AWG with the insulation rating of $180 \text{ }^\circ\text{C}$ (class H) has the maximum allowable current density of 23.7 A/mm^2 [10]. Considering the intensive cooling of ERPMMSM during the flight, the temperature class of the winding wire insulation and the effect of demagnetization of permanent magnets at high temperature, the rated current density 22.0 A/mm^2 was determined. It is slightly lower compared to the maximal value of the allowed current density, but takes into account a certain reserve. According to this the total current for the cross-section of 1.19 mm^2 is 26.14 A .

The magnetic flux density in the air gap had the maximum value of 0.415 T . The estimated rms value of phase EMF at nominal speed of 5500 rpm was 15.39 V . Taking into account the measured value of EMF and the calculated current the nominal electrical power of ERPMMSM was calculated to be 1.2 kVA .

VIII. GENERATOR NO-LOAD TEST

Experimental measurements have been made to verify the parameters of the prototype and to map the machine no-load characteristics in a generator mode. The ERPMMSM was tested in a test bench using a high speed servo drive (Fig. 9).

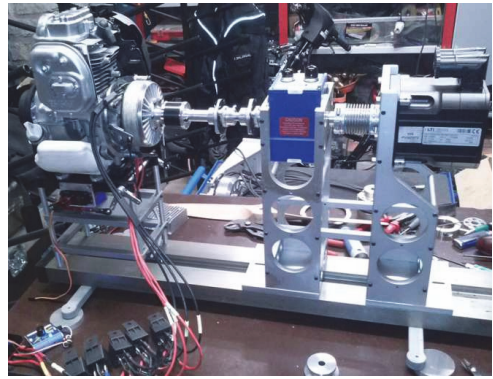


Fig. 9. The test bench with ERPMMSM prototype.

The no-load characteristics of the phase voltage U_{IF} and line voltage U_{IL} in dependence of the rotational speed and frequency were linear (Fig. 10). The experimental result of U_{IF} at the nominal speed of 5500 rpm was 15.46 V and differs only 0.45% from the calculated EMF rms value of 15.39 V .

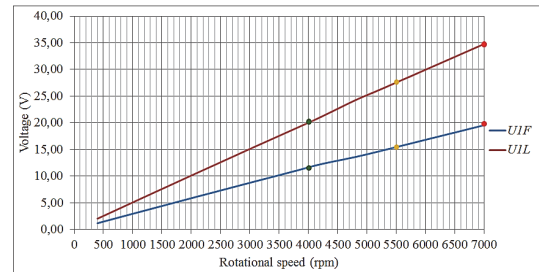


Fig. 10. No-load test results of U_{IF} and U_{IL} .

The EMF as the phase voltage has a correct sinusoidal waveform (Fig. 11).

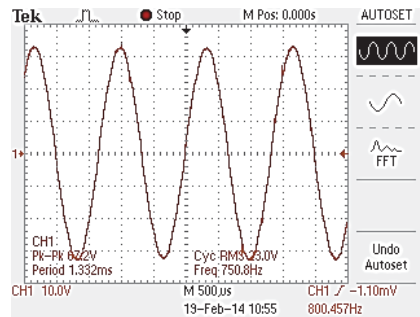


Fig. 11. The waveform of the phase voltage U_{IF} at 4500 rpm .

IX. CONCLUSION AND FUTURE WORK

As a result the topology and basic design of the working prototype of ERPMMSM was studied. No-load parameters were experimentally measured in a test bench. There were only small differences between the measured and calculated values of the induced voltage. Both phase and line voltages in generator mode of the machine were evenly sinusoidal. Based on test results the estimated electrical parameters of ERPMMSM were determined. Those parameters should be

verified with load tests. Initial test results confirm that ERPMSM design and electrical parameters are sufficient to fulfil the requirements in a generator mode.

The next step of the study is to carry out load tests of ERPMSM in a generator and in a motor mode. This includes tests as speed vs. torque, currents vs. torque, torque linearity to determine the effect of the armature reaction, and torque ripple test in a very low speed. Based on these results it is possible to map the mechanical and electrical losses and to prepare necessary characteristics.

In this paper studied ERPMSM has a toroidal winding on its stator surrounded by external rotor with permanent magnets. The next step will be the study of the dual-rotor machine having an external and an internal rotor and the Gramme's winding. Basically this type of machine has two rotors with the same armature current. Due to this the dual-rotor radial-flux toroidally wound permanent-magnet machine could have more efficiency and torque density [11]. As the result the dual-rotor machine could make a reference to ERPMSM covered in this paper.

REFERENCES

- [1] D. L. Gabriel, J. Meyer, F. du Plessis, "Brushless DC motor characterisation and selection for a fixed wing UAV" IEEE Africon. The Falls Resort and Conference Centre, Livingstone, Zambia, 13–15 September 2011.
- [2] J. R. Hendershot Jr and T. J. E. Miller, "Design of brushless permanent-magnet motors," 2nd ed., Ohio: Magna Physics Publishing, New York: Oxford University Press 2011, pp. 1.1–5.1.
- [3] V. X. Hüng, "Modeling of exterior rotor permanent magnet machines with concentrated windings," Ph.D. Dissertation, Delft University of Technology, the Netherlands, 2012, pp. 26–40.
- [4] J. F. Gieras and I. A. Gieras, "Recent developments in electrical motors and drives," East Hartford, CT: United Technologies Research Center, Royal Oak, MI: Beaumont Services Company, 2001.
- [5] R. K. Pratapa, "Modeling and analysis of radial flux toroidally wound twin rotor permanent magnet motor," MSc. Thesis, Louisiana State University, Agricultural and Mechanical College, 2010, pp. 3–8.
- [6] A. Kallaste, "Low speed permanent magnet slotless generator development and implementation for windmills," Ph.D. Dissertation, Tallinn University of Technology, Department of Electrical Engineering, Tallinn, 2013, pp. 22–23.
- [7] http://www.arnoldmagnetics.com/Neodymium_Literature.aspx
- [8] [http://www.sura.se/Sura/hp_products.nsf/vOpenocument/97F569BF197A21FDC1256A3B002FC03C/\\$FILE/NO18.pdf?OpenElement](http://www.sura.se/Sura/hp_products.nsf/vOpenocument/97F569BF197A21FDC1256A3B002FC03C/$FILE/NO18.pdf?OpenElement)
- [9] <http://www.brocott.co.uk/enamelled-magnet-wire/1kg-spools/0-355mm-enamelled-copper-winding-wire-1kg-ww0355-1000.html>
- [10] W. H. Yeadon and B. M. Frustaglio, "Current density," Yeadon Energy Systems, Inc., SMMA Fall Conference, 2010.
- [11] R. Qu and Thomas A. Lipo, "Dual-rotor, radial-flux, toroidally wound, permanent-magnet machines," IEEE Trans. Industry Application, vol. 39, no. 6, Nov.-Dec. 2003.
- [12] T. Vaimann, A. Kallaste, A. Belahcen, and A. Kilk, "Magnetic properties of reduced Dy NdFeB permanent magnets and their usage in electrical machines," Proceedings of IEEE AFRICON 2013 Conference, 2013, pp. 1124–1128.

BIOGRAPHIES

René Nukki was born in Pärnu, Estonia, in 1974. He received BSc and MBA degrees from Tallinn University of technology in 2005 and 2012 respectively. His research covers high power-to-weight PM synchronous machines for a small electric aircraft applications.

He has worked in an electrical industry for 16 years, including such companies as ABB and Schneider Electric. Currently he works as a lecturer and the holder of the chair of Electrical Engineering at Faculty of Mechanics at TTK University of Applied Sciences.



Aleksander Kilk was born in Viljandi district, Estonia, in 1946. He received Dipl.Eng, MSci and PhD from Tallinn University of Technology in 1969, 1992 and 2008, respectively, all in electrical engineering.

He has held academic posts of assistant professor, lecturer and associate professor at Tallinn University of Technology in electrical engineering and machines, where he currently works as associate professor of the Department of Electrotechnical Engineering. His research activities cover some different aspects of both electrical PM machines and induction MHD devices.



Ants Kallaste was born in Pärnu, Estonia in 1980 and received his BSc, MSc and PhD degrees in electrical engineering from Tallinn University of Technology, Estonia, in 2004, 2006 and 2013 respectively. He has been an IEEE member since 2013.

He has been working in several companies as an electrical engineer. Presently he is working at the Tallinn University of Technology Department of Electrical Engineering on researcher position and is the Head of Chair of Electrical Machines.

His main research interest includes PM machine design and wind generators.



Toomas Vaimann was born in Pärnu, Estonia, in 1984 and received his BSc and MSc degrees in electrical engineering from Tallinn University of Technology, Estonia, in 2007 and 2009 respectively. He is currently a PhD student in the same institution. He has been an IEEE student member since 2011.

He has been working in several companies as an electrical engineer. Presently he is working at the Tallinn University of Technology Department of Electrical Engineering on engineer's and assistant's position.

His main research interest includes diagnostics of electrical machines.



Kristjan Tiimus Sr was born in Tallinn, Estonia, in 1953. His educational background is related to the practical physics and electrical engineering, specialized mainly to electrical machines.

He has been working in several companies as a mechanical and electrical engineer. Presently he is working at Helicam Est OÜ on engineer's position.

His main research includes permanent magnet electric generators and motors for lightweight aircrafts.

- [PAPER-II] **Nukki, R.**; Kilk, A.; Kallaste, A.; Vaimann, T.; Tiimus, K. (2015). Generator Mode Analysis of Exterior-Rotor PM Synchronous Machine with Gramme's Winding. IEEE 5th International Conference on Power Engineering, Energy and Electrical Drives (POWERENG). IEEE, pp. 347 - 352.

Generator Mode Analysis of Exterior-Rotor PM Synchronous Machine with Gramme's Winding

René Nukki, Aleksander Kilk, Ants Kallaste, Toomas Vaimann and Kristjan Tiimus Sr

Abstract— The paper represents the study of electric output parameters of a multi-pole exterior-rotor permanent magnet (PM) synchronous machine, which is a part of a hybrid drive for a small unmanned aircraft. The PM synchronous machine's constructional feature is a toroidal or Gramme's type of stator winding. The studied machine is designed to operate as a generator and motor within the aircraft's hybrid drive. The main study is the PM synchronous machine's behaviour with different load values in generator mode. The motor mode shall not be covered in this paper. Active load was implemented during the load tests. This was due to the characteristics of electrical consumers, such as on board batteries in case of the real aircraft. Based on load tests' results the corresponding load and short-circuit characteristics were compiled. In addition, the machine's analytical values of iron and copper losses were determined.

Index Terms—AC-DC power converters, AC machines, conductors, generators, impellers, permanent magnet machines, prototypes, rotors, stators, topology, unmanned aerial vehicles.

I. INTRODUCTION

IN modern small unmanned aerial vehicles (UAV) electric machines (EM) are used in various applications. UAV's that implement an internal combustion engine (ICE) as their main source of power, use EM's mainly as generators. The EM's geometries that are more common in this field are interior-rotor, exterior-rotor, less axial-rotor generators. Similar trend can be observed also in the field of full-electric UAV's, which tend to use EM's with interior- and exterior-rotor configurations [1].

The studied multi-pole exterior-rotor PM synchronous machine (ERPMSM) is designed for a small UAV as part of the hybrid drive system (HDS).

A HDS is generally an integrated single system, which uses two or more different power sources to move the vehicle. ICE's have certain strengths and weaknesses. So do electric motors. A HDS combines the strengths of both motors [2].

Nowadays HDS's are becoming more and more widespread. At present this concerns mainly the land and the maritime transport, but the trend is already reaching to the air. In this study the hybrid concept will be implemented

to a small UAV, where the ERPMSM performs two types of functions.

In generator mode the ERPMSM has to ensure a sufficient charging voltage and current for the battery bank of the main power supply for the ERPMSM's motor mode, and for the batteries of other on-board systems, including video and photo cameras. The supply voltage and current with right parameters is ensured with the voltage stabilizer connected via three-phase rectifier. In motor mode the ERPMSM is fed by the battery bank through an adjustable frequency converter on board the UAV. The principle schematic of the hybrid machine is shown in Fig. 1 [3].

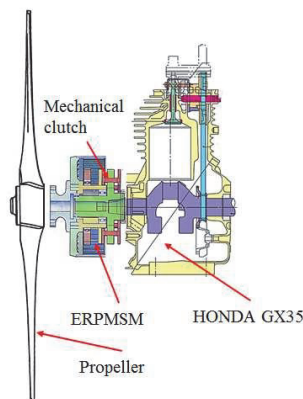


Fig. 1. Principal scheme of the UAV hybrid engine.

II. CONSTRUCTION

In an EM's right topology selection process the important factor was that the ERPMSM's rotor is rigidly connected through its bearing assembly with an ICE's crankshaft. In the EM's motor mode the ERPMSM should be detached from ICE to reduce excessive mechanical losses.

In this requirement can be met by using a mechanical clutch mechanism. One problem in this case was to solve the ergonomic placement of the clutch. The best way was to install it into the internal part of the EM. With interior-rotor designs this objective was difficult to achieve. With axial-rotor topology the solution would have been possible, but mechanically rather complex. With exterior-rotor the fulfilment of the given condition was most easily achieved by installing the clutch into the ERPMSM's stator inner area.

The exterior-rotor geometry was also supported by the following advantages:

- high torque density [4],

This work was supported by the TTK University of Applied Sciences, Helicam Service Ltd and ELI Airborne Solutions.

R. Nukki, A. Kilk, A. Kallaste and T. Vaimann are with the Department of Electrical Engineering, Tallinn University of Technology, Ehitajate tee 5, 19086 Tallinn, Estonia (e-mail: renenukki@gmail.com, aleksander.kilk@ttu.ee, ants.kallaste@ttu.ee, toomas.vaimann@ttu.ee).

K. Tiimus Sr is with Helicam Service Ltd (e-mail: helicam@helicam.ee).

- bigger rotor diameter gives bigger inertial torque [5],
- reduced copper losses and production costs [1].

Another relevant argument in choosing the right rotor geometry was related to the proper fixing of the permanent magnets. The exterior-rotor has a beneficial advantage by the centrifugal force that presses the rotor magnets against the inner surface of the rotor [3].

Choosing the stator geometry the important issue was to determine whether to design the slotted or slotless stator. The slotless core has a smaller inductance and enables higher rotational speed compared to the slotted core. As there are no teeth in the lamination stack, the cogging torque is also lower, which is a good property also for lower speeds [6].

The slotted winding have higher efficiency at lower speeds, higher torque density, lower armature current, less PM material and lower material costs [7].

The advantage of the slotted design is also that the coils are mechanically fixed more firmly in the slots and won't move off due to the electromagnetic forces in the EM.

One of the main disadvantages of the slotless EM is that it heats up faster than the of slotted EM and therefore needs a more efficient cooling [7]. As the ERPMSM has a high specific power (1.2 VA/g), there is a high current density also in windings. Therefore it is very important to maintain the proper operating temperature and prevent overheating. Thus, it was more efficient to design a slotted configuration.

The ERPMSM has 24 stator slots and 20 rotor poles formed from 40 paired neodymium magnets (Fig. 2).

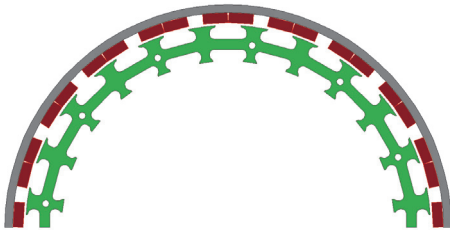


Fig. 2. Topological design of the ERPMSM.

The Gramme's winding was selected for the ERPMSM's winding type (Fig. 3).



Fig. 3. View of the wound stator.

The winding consist of 8 coils connected in series in each phase winding [3]. The winding scheme of ERPMSM is shown on Fig. 4.

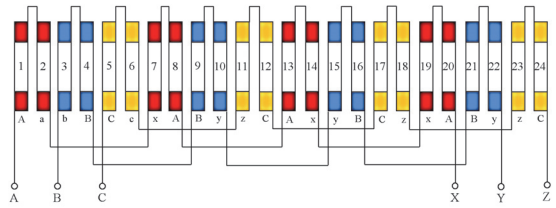


Fig. 4. The winding scheme of Gramme's winding [3].

The ERPMSM's stator slots are cut in the outer and inner parts of the core. This configuration lets the winding coils to be fixed more firmly in the stator slots. The width of the single slot is 8.0 mm, which is significantly wider compared to the tooth diameter of 6.01 mm. The wider surface makes the practical winding easier, as the winding conductors can be installed onto a wider surface (Fig. 5).

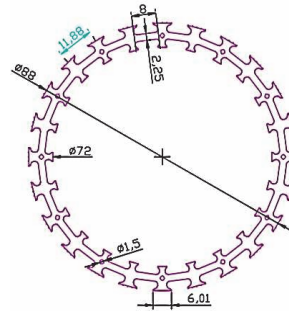


Fig. 5. The layout of the stator [3].

The main technical parameters of the ERPMSM are represented in Table 1.

TABLE I. TECHNICAL PARAMETERS OF ERPMSM

No.	Reference Parameters		
	Symbol	Parameter	Value
1	S_n	Total power	0.89 kVA
2	U_F	Phase voltage (rms)	12.89 V
3	I_n	Nominal current	23.0 A
4	n_n	Nominal speed	5500 rpm
5	Q	Number of slots	24
6	$2p$	Number of poles	20
9	D	Outer diameter	98 mm
10	l	Axial length	24 mm
11	M	Total weight	742 g

III. GENERATOR TESTS

For measuring the ERPMSM's technical parameters, the test bench was constructed. In the bench the ERPMSM is already mechanically linked to a 4-stroke ICE, as its real primary propulsion system on board of the small UAV.

For the mechanical power and torque measurements the test bench is provided with the torque sensor.

To achieve a flexible and precise adjustment of the rotational speed during the tests, a servo drive was implemented. The drive system will be used also as the mechanical load during the ERPMSM's tests in the motor mode. The exterior view of the test bench is shown in Fig. 6.

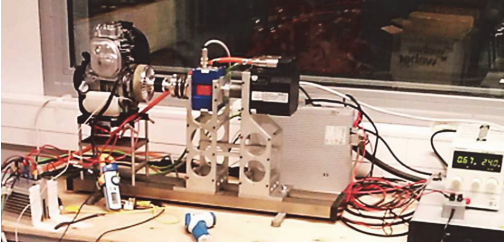


Fig. 6. The external view of the test bench.

A. No-Load Test

The ERPMSM was tested under no-load conditions, which are described in [3]. Based on the recorded values of the phase voltage and line voltage U_{IL} at different rotational speeds the correct linear no-load characteristic was compiled. The U_{IF} result at the nominal speed of 5500 rpm was 15.46 V. The calculated rms value was 15.39 V. The difference between calculated and measured values varies only by 0.45%. The results of U_{IF} and U_{IL} were recorded also over the nominal rotational speed until 7000 rpm. The measured voltage values at that speed continued the linear rising of the no-load characteristic. The registered U_{IF} value was 19.56 V and respective U_{IL} 34.79 V. The no-load characteristic of ERPMSM is shown in Fig. 7 [3].

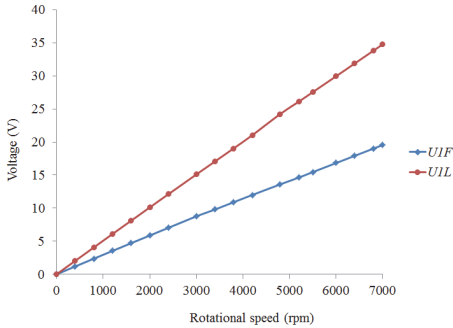


Fig. 7. No-load test results of U_{IF} and U_{IL} [3].

The curves U_{IF} and U_{IL} at different rotational speeds were taken up with an oscilloscope. Fig. 8 shows the correct sinusoidal shape of the phase voltage U_{IF} at the rotational speed of 6000 rpm.

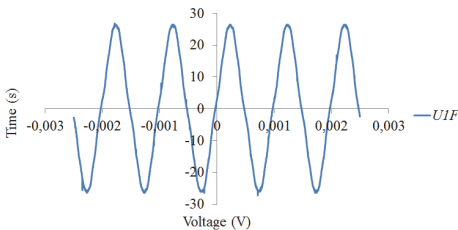


Fig. 8. The waveform of the phase voltage U_{IF} at 6000 rpm.

B. The Impact of the Rectifier

In its operational mode on board UAV the ERPMSM is connected to a full period 3-phase rectifier, which output is further in series connection with a voltage stabilizer (Fig. 9).

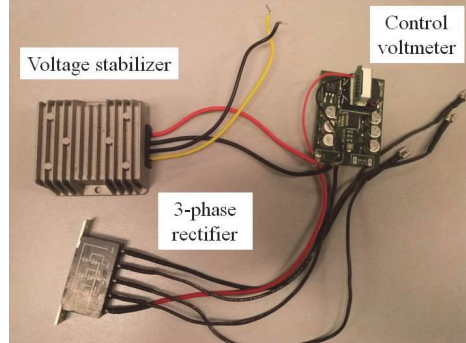


Fig. 9. The rectifier and voltage stabilizer used on UAV for power supply.

Voltage Stabilizer's function is to provide a constant output voltage of 12 V_{DC} from variable rectified values generated by ERPMSM trough the rectifier in the range of 8-40 V_{DC}. For smaller voltages (e.g. 6 V_{DC} for batteries of CCTV cameras) the voltage divider is used. This solution ensures the permissible values of voltage and current for all devices on board the UAV.

For load tests a 50 A full-period 3-phase rectifier bridge B6U was used. Due to the diode bridge the rectifier causes also negative feedback effect in the output circuit of ERPMSM. This effect is shown in Fig. 10 where the shape of U_{IF} is highly distorted compared to Fig. 8.

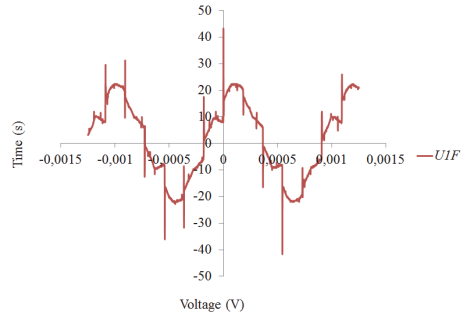


Fig. 10. The distorted waveform of the phase voltage U_{IF} at 5500 rpm.

These distortions of voltage waveforms are caused by diodes during load switching, which induce voltage peaks.

C. Load Tests

Load characteristics determine the dependence $U = f(I)$ showing how the terminal voltage of the generator changes due to the variable load in case of constant magnetic flux of the permanent magnets.

In the real operation the ERPMSM in a generator mode is implemented to ensure enough power for all the equipment on board the UAV. As those devices are active power consumers (e.g. the battery bank, batteries of photo and video devices), the load tests were performed also with active loads. For this the parallel connected cascade of rheostats were used.

ERPMSM's load characteristics were taken based on three rotational speeds. Fig. 11 shows load characteristics between no-load and nominal current at rotational speeds of 3000, 4000 and 5500 rpm.

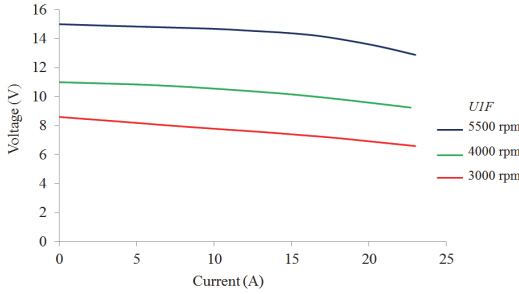


Fig. 11. Load characteristic at 3000, 4000 and 5500 rpm.

During load tests the ERPMSM was loaded with an active load. The increase of the active voltage drop and the armature reaction across the stator caused the continuous decrease of the terminal voltage.

ERPMSM's voltage drop was also influenced by the value of the rectifier's power factor $\cos \varphi$, which varied depending on the load in the range from 0.95 to 0.98.

Comparing load characteristics shown in Fig. 11 is visible the higher linearity at lower rotational speeds 3000 and 4000 rpm.

At the nominal rotational speed 5500 rpm and nominal current 23.0 A the U_{IF} deviation was $\Delta U = 2.57$ V ($U_{IFmax} = 15.46$ V, $U_{IFmin} = 12.89$ V). That gives the voltage increase rate nearly by 20%. This figure is a normal result on the basis of permanent magnet synchronous generators that in use today [8].

D. Short Circuit Test

In case of PM synchronous machines (PMSM) a short-circuit characteristic is taken up with the short-circuited stator winding by determining the dependence $I = f(n)$ and in condition $U = 0$.

In the absence of the load in a short circuit situation the resistance of the stator circuit is determined only by the active resistance of the conductors. For ERPMSM it the winding resistance was measured 0.07Ω at 48°C .

In general short-circuit parameters can be neglected due to their small values and it is generally considered that the total resistance of the stator winding has an inductive nature [9]. During a short-circuit the armature reaction has a strong demagnetizing influence which in case of higher short-circuit currents can damage the rotor magnets by changing their magnetic parameters.

In Fig. 12 is shown the ERPMSM's short-circuit characteristic.

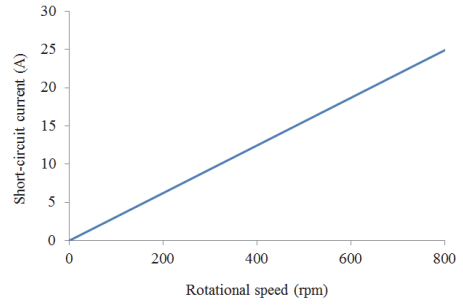


Fig. 12. Short circuit characteristic.

The ERPMSM's nominal current 23.0 A was achieved at 750 rpm.

E. Temperature Field Characteristic

The temperature characteristic of a PMSM expresses a nature of the temperature change during a certain amount of time and at a constant current in the stator windings. The objective of temperature tests is to determine the value of the maximum current at which the PMSM reaches to the maximum stabilized temperature which is permissible to the winding insulation and to the permanent magnets. The measured voltage, current, rotational speed etc. can be considered as nominal values of the PMSM.

ERPMSM was tested until to the current of 23.0 A. At this current the winding temperature stabilized at 106°C . The winding insulation and also the parameters of the permanent magnets would probably tolerate even higher load current, as ERPMSM's impeller can create sufficiently intense cooling. The limiting factor in further testing was ERPMSM's mechanical design feature, which didn't permit to proceed with higher currents, as they were causing too strong electromagnetic forces for the construction. Thus, the nominal current was considered 23.0 A. Fig. 13 represents the ERPMSM's temperature characteristic.

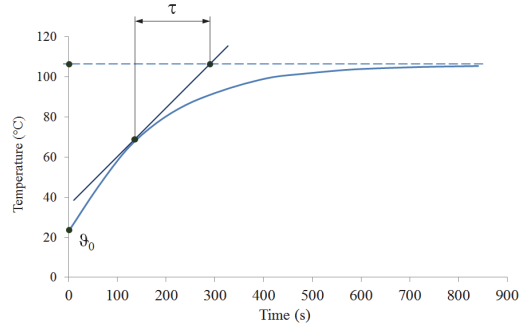


Fig. 13. Temperature characteristic with the thermal constant τ .

The characteristic indicates graphically the thermal time constant τ , which characterizing the approaching velocity rate to the final temperature, as in (1).

$$\vartheta_{(t)} = \vartheta_{(final)} \left(1 - e^{-\frac{t}{\tau}} \right) \quad (1)$$

where $\vartheta_{(final)}$ is a constant temperature ($t = \infty$).

The time constant τ depends mainly on the heat capacity factors of ERPMSM's active materials. In practice, the machine's final temperature is reached within 4-5 time of the constant values. The difference from the final temperature during 4τ is 1.8%, and after 5τ only 0.7%. ERPMSM's time constant $\tau = 2.67$ minutes and the heat transfer process lasts in total approximately 13.3 minutes.

F. Losses

In a PM synchronous generator (PMSG) the mechanical energy is converted into electrical. During that process a part of the mechanical energy is dissipated to the PMSG's various parts and turning into heat. Therefore, the output power of the PMSG is always less than the input power given by its primary mechanical power source. PMSG losses can be divided into four main categories [9]:

- resistive losses,
- iron losses,
- additional losses,
- mechanical losses.

Resistive losses (*Joule losses*) cover copper losses in ERPMSM's windings, and exist only when it is loaded [10].

As copper losses are proportional to the square of the load current and the value of active resistance in winding conductors, it became possible to estimate those losses by measuring across the winding active resistance at different temperatures (Fig. 14).

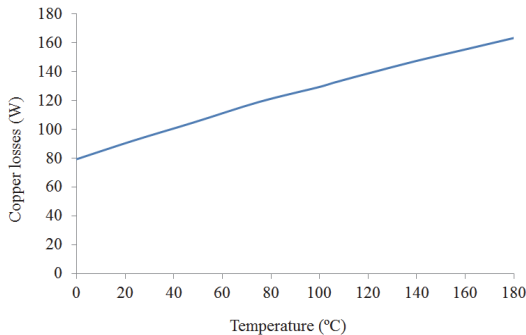


Fig. 14. Resistive losses at nominal operating temperature 106 °C.

By calculations estimated ERPMSM's copper loss at the nominal current 23.0 A is 133 W.

Iron losses are permanent and are not dependent on the losses caused by the generator load. They are directly dependent on the magnetic flux density and on the magnetization frequency in the stator core [10]. This, in turn, depends on the speed of the generator and the number of pole pairs. Iron losses consist of hysteresis and eddy current losses.

In this article ERPMSM is studied as a multi-pole PMSG, which rotates at high speeds, it has the high frequency of magnetization in the stator core. For example, at the rotational speed of 5500 rpm the related frequency is 916.67 Hz. The high frequency leads obviously to significantly higher iron losses as compared to the power grid generators whose operational frequency is 50 or 60 Hz.

To reduce eddy current losses which are directly dependent on the size of the magnetic conductor cross-sectional area, the ERPMSM's stator was constructed from

the electrical steel with a smallest thickness (0.18 mm) that was still possible to mechanically process.

ERPMSM's iron losses were determined analytically. For their calculation the magnetic flux density distribution at the rated load and nominal temperature was modelled using FEM software (Fig. 15).

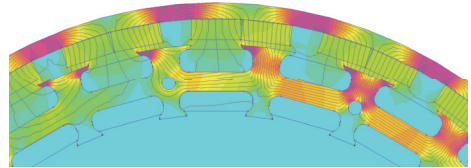


Fig. 15. Distribution of the magnetic flux at rated current and nominal temperature.

Based on the field analysis the estimated value of the magnetic flux density $B = 1.5$ T was taken. The ERPMSM's operating frequencies were compared with the respective power loss values of the electrical steel related to the same frequency rate throughout the stator volume, which formed the total iron loss.

The calculated iron loss at nominal rotational speed of 5500 rpm (916.67 Hz) was 13.5 W (84.0 W/kg). The dynamics of iron losses is shown in Fig. 16.

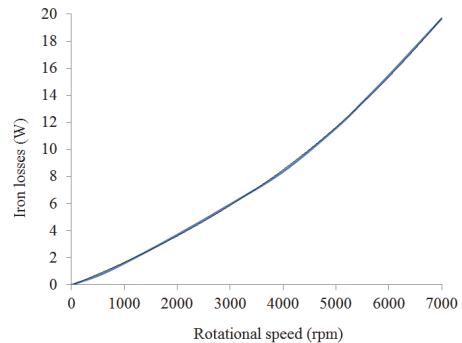


Fig. 16. Iron losses at different rotational speeds [11].

PMSG mechanical losses in general consist of friction losses in bearings and ventilation loss [10].

As ERPMSM has a fast rotational speed, but small diameter, its ventilation losses are not significant. The same applies to the frictional losses in bearings. Thus, these losses are not taken into account in calculations.

IV. PRIMARY ENGINE

ERPMSM's primary power source is 35 cm³ four-stroke ICE which rotates the propeller of the UAV in currently produced models.

Its maximum torque of 1.6 Nm is gained at rotational speed of 5500 rpm [12]. This rotational speed at a maximum torque was taken for the basis for determining the ERPMSM's nominal rotational speed.

In ERPMSM designing process in the generator mode also the rotational speeds of 3000 and 4000 rpm had to be taken account. Those speed values were provided by constructor of the aircraft and are characterizing the ICE's rotational speeds while the UAV is airborne and flies in a stable mode. ERPMSM as a generator must produce enough

energy to supply all the batteries on board at these three rotational speeds.

V. CONCLUSION AND FUTURE WORK

For the conclusion can be stated that ERPMSM fulfils its requirements as a generator.

Mechanical improvements need stator and bearing fixation construction in order to achieve longer endurance particularly during high loads, which generate significant electromagnetic forces.

The measured nominal current of 23.0 A during the load test is close to 26.0 A, which was originally estimated [3]. The last higher current value is theoretically possible, taking into account the parameters of the winding insulation and permanent magnets. This, however, requires the above-mentioned mechanical improvements.

Based on measured nominal current (23.0 A) and voltage (12.89 V) values the obtained apparent power $S = 0.89$ kVA. Taking into account the dimensions of the machine and weight of active materials (742 g) the ERPMSM's specific power is 1.2 VA/g, which is a very good result.

Modelling the distribution of the magnetic flux in the ERPMSM's magnetic circuit with FEM software and analysing it, is obvious that the Gramme's winding scheme does not justify itself completely if permanent magnets are only on one side of the stator winding. In the stator of the ERPMSM the magnetic flux passes mainly through the central radius of the core and through the upper tooth layer. The magnetic flux density in the inner part of the stator is very low or not present at all. Such a stator and winding combination is obviously a lot more efficient if to implement it with the double rotor. One important thing to pay attention to is the magnetic permeability of both rotor and stator core, as those two magnetic fluxes generated by them add up and can cause overheating.

The next step is to continue with the design and working principle study of multi-pole exterior-rotor synchronous PM machines. The next objective is to construct this type of machine with the revised geometry of the stator and winding scheme and test it as a PM synchronous motor.

REFERENCES

- [1] D. L. Gabriel, J. Meyer, F. du Plessis, "Brushless DC motor characterisation and selection for a fixed wing UAV," IEEE Africon. The Falls Resort and Conference Centre, Livingstone, Zambia, 13–15 September 2011.
- [2] http://www.toyota-global.com/innovation/environmental_technology
- [3] R. Nukki, A. Kilk, A. Kallaste, T. Vaimann, and K. Tiimus Sr, "Exterior-rotor permanent magnet synchronous machine with toroidal windings for unmanned aerial vehicles," IEEE Xplore. Electric Power Quality and Supply Reliability Conference, Rakvere, 2014, pp. 215 – 220.
- [4] V. X. Hùng, "Modeling of exterior rotor permanent magnet machines with concentrated windings," Ph.D. Dissertation, Delft University of Technology, the Netherlands, 2012, pp. 26–40.
- [5] J. R. Hendershot Jr and T. J. E. Miller, "Design of brushless permanent-magnet motors," 2nd ed., Ohio: Magna Physics Publishing, New York: Oxford University Press 2011, pp. 1.1–5.1.
- [6] P. Madaan, "Brushless DC Motors – Part I: Construction and Operating Principles," Cypress Semiconductor, 11 February 2013.
- [7] J. F. Gieras and I. A. Gieras, "Recent developments in electrical motors and drives," East Hartford, CT: United Technologies Research Center, Royal Oak, MI: Beaumont Services Company, 2001.
- [8] A. Kilk, "Multipole Permanent-Magnet Synchronous Generator for Wind Power Application," Ph.D. Dissertation, Tallinn University of

Technology, Department of Electrical Engineering, Tallinn, 2008, pp. 112–113.

- [9] J. Pyrhönen, T. Jokinen, and V. Hrabovcová, "Design of rotating electrical machines," Wiley, 2008, pp. 383–386.
- [10] A. Kallaste, "Low speed permanent magnet slotless generator development and implementation for windmills," Ph.D. Dissertation, Tallinn University of Technology, Department of Electrical Engineering, Tallinn, 2013, pp. 22–23.
- [11] <https://www.emetor.com/edit/materials/sura-no18/?cat=6&co=10>
- [12] <http://engines.honda.com/models/model-detail/gx35>

BIOGRAPHIES



René Nukki was born in Pärnu, Estonia, in 1974. He received BSc and MBA degrees from Tallinn University of technology in 2005 and 2012 respectively. His research covers high power-to-weight PM synchronous machines for a small electric aircraft applications.

He has worked in an electrical industry for 16 years, including such companies as ABB and Schneider Electric. Currently he works as a lecturer and the holder of the chair of Electrical Engineering at Faculty of Mechanics at TTK University of Applied Sciences.



Aleksander Kilk was born in Viljandi district, Estonia, in 1946. He received Dipl.Eng, MSci and PhD from Tallinn University of Technology in 1969, 1992 and 2008, respectively, all in electrical engineering.

He has held academic posts of assistant professor, lecturer and associate professor at Tallinn University of Technology in electrical engineering and machines, where he currently works as associate professor of the Department of Electrical Engineering. His research activities cover some different aspects of both electrical PM machines and induction MHD devices.



Ants Kallaste was born in Pärnu, Estonia in 1980 and received his BSc, MSc and PhD degrees in electrical engineering from Tallinn University of Technology, Estonia, in 2004, 2006 and 2013 respectively. He has been an IEEE member since 2013.

He has been working in several companies as an electrical engineer. Presently he is working at the Tallinn University of Technology Department of Electrical Engineering on researcher position and is the Head of Chair of Electrical Machines.

His main research interest includes PM machine design and wind generators.



Toomas Vaimann was born in Pärnu, Estonia, in 1984 and received his BSc, MSc and PhD degrees in electrical engineering from Tallinn University of Technology, Estonia, in 2007, 2009 and 2014 respectively. He has been an IEEE member since 2011.

He has been working in several companies as an electrical engineer. Presently he is working at the Tallinn University of Technology Department of Electrical Engineering on researcher's position.

His main research interest includes diagnostics of electrical machines.



Kristjan Tiimus Sr was born in Tallinn, Estonia, in 1953. His educational background is related to the practical physics and electrical engineering, specialized mainly to electrical machines.

He has been working in several companies as a mechanical and electrical engineer. Presently he is working at Helicam Est OÜ on engineer's position.

His main research includes permanent magnet electric generators and motors for lightweight aircrafts.

[PAPER-III] **Nukki, R.**; Lehtla, T.; Kilk, A.; Kangru, T. (2015). Design of the Exterior-Rotor PM Synchronous Motor for an Electric Powered Paraglider. 56th International Scientific Conference on Power and Electrical Engineering, RTUCON 2015, Riga Technical University, 14.10.2015. IEEE, pp. 1 - 4.

Design of the Exterior-Rotor PM Synchronous Motor for an Electric Powered Paraglider

René Nukki (*Doctoral student, Tallinn University of Technology*), Tõnu Lehtla (*Professor, Tallinn University of Technology*), Aleksander Kilk (*Associate professor, Tallinn University of Technology*), Tavo Kangru (*Lecturer, Tallinn University of Applied Sciences*)

Abstract – This paper presents a study of the application of the exterior-rotor permanent magnet synchronous motor for a single pilot paraglider as the main propulsion device. The results based on analytical calculations are compared with those obtained by SPEED modeling software. The primary magnetic field distribution is simulated with the SPEED sub-module PC-FEA. The acquisition of analytical and modeling results is the basic and important step to design a functional prototype of the PM motor for an electric powered paraglider in the next phase of the study.

Keywords – AC motors, electromagnetic modeling, permanent magnet motors, propellers, propulsion, prototypes.

I. INTRODUCTION

A powered paraglider is a part of an ultralight aviation where a motor provides thrust to take off using an adapted wing. The pilot wears a harness together with a motor on the pilot's back, also called a paramotor (Fig. 1) [1].

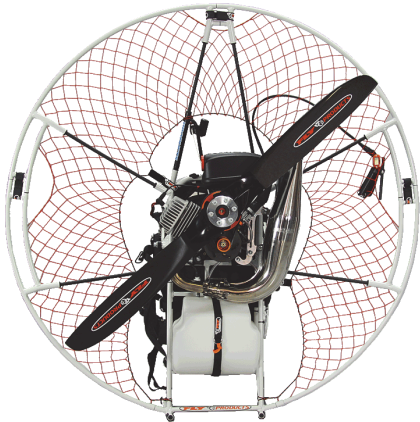


Fig. 1. Paramotor Rider Sprint 200 [1].

Nowadays, mainly internal combustion engines (ICE) are applied in paramotors. A new trend is the use of electric motors that are more reliable, simpler, and provide more economical and quieter flight.

The objective of the first step of the research was to the design of the permanent magnet synchronous motor (PMSM) for an electric powered paraglider (EPP) and to achieve the high power and torque at the low weight and volume by using effective cooling, at the same time optimizing the power loss and the density in the winding conductors.

The operating duty cycle of the PMSM is short-term, applied mainly during the takeoff time. The power supply is provided by the batteries operated by the controller and a DC/AC inverter. The deigned prototype will be used in the existing EPP, where its ICE will be replaced.

II. INITIAL SIZING

To make an appropriate geometry selection of an electric motor for an EPP it is important to have a large torque at low rotational speed. Based on this requirement and on the experience from a similar study of a PMSM constructed for a small unmanned aircraft [2], it was decided to implement the same external rotor geometry also for this prototype. Another practical reason for that decision was a more convenient and easier winding of the stator comparing to an interior-rotor electric machine.

The known mechanical requirement of the designed motor was the nominal rotational speed, which was determined by the aerodynamic properties of the used propeller. Based on this, 3000 rpm was taken as the nominal rotational speed.

One initially known electrical parameter was the output power P_1 of the used controller, which was 12.6 kW. As the power factor $\cos \varphi$ of the controller was 95%, the mechanical power on the shaft P_2 was estimated at 11.0 kW. This set-point satisfied the initial requirement for the P_2 value, which had to be at least 10.0 kW. The requirement was based on the P_2 value of the replaceable ICE. Considering these initial data, the expected mechanical torque $T_m = 35.0$ Nm was calculated.

An important indicator at the initial phase of the motor elaboration is the torque per rotor volume unit K_{trv} . This value describes the amount of torque available for a given rotor total volume [3]. The arithmetical average value of K_{trv} for PM motors with NdFeB magnets is considered 28 kNm/m³ and therefore the expected tangential force per unit rotor surface area σ is equal to 14 kNm/m³ [4], expressed as:

$$\sigma = \frac{T_m}{\frac{\pi}{2} \cdot D_r^2 \cdot L_{stk}} = \frac{K_{trv}}{2}, \quad (1)$$

where D_r is the rotor diameter and L_{stk} is the active stack length.

As high torque per unit rotor volume is an important parameter for the design of PMSM, the radial diameter of the rotor value had to be increased and the length of the rotor decreased. Therefore, the estimated rotor diameter and length ratio was taken approximately 1.5 to create the largest possible

cooling area for the high power density motor. The intensive cooling is provided by the impeller with ventilation openings (Fig. 2).



Fig. 2. The air cooling system with an impeller on the rotor.

As PMSM has only single-sided fixing to the frame, there is an increased mechanical stress on the bearings. Therefore, the active part of the rotor had to be as short as possible. Based on that reason and on the length of the selected magnets, the rotor length 40 mm was selected. Table 1 lists the initially calculated parameters of the PMSM.

TABLE I
INITIAL PARAMETERS OF THE PMSM

No.	Reference Parameters		
	Symbol	Parameter	Value
1	U_n	Rated input voltage of the controller	51.8 V _{DC}
2	I_{max}	Maximum continuous current of the controller	250 A
3	P_2	Nominal shaft power	11.0 kW
4	n_n	Nominal speed	3000 rpm
5	T_m	Mechanical torque	35.0 Nm
6	D_r	Outer diameter	207.2 mm
7	L_{stk}	Axial length	40 mm

III. STATOR GEOMETRY AND POLES

One of the basic requirements was to minimize the cogging torque, which is the lowest when the slot opening is the smallest. The slot opening is limited by the practical winding process [5]. Small PMSM use often rectangular slots to obtain a greater winding area to lower the temperature rise [4]. In common slot types the overhang of teeth tips is used to reduce the effective slot opening without materially reducing the slot area. Fig. 3 shows the slot type of the designed PMSM.

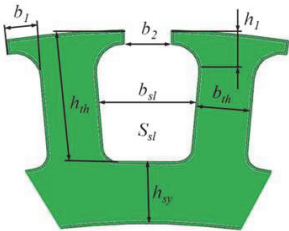


Fig. 3. The geometry of the stator slot and teeth.

Open slots are not widely used in PMSM's because they generate an additional cogging torque [4]. One important aspect for the stator lamination design is the height of the tooth-tips h_1 . In case of too small h_1 , the tooth tip becomes saturated, and gives the same effect as an open slot, which in turn causes the growth of the cogging torque. In practice [6], in order to minimize the saturation, the height of h_1 is taken approximately the same as the width of the tooth b_1 . To minimize the sharp corners, the radius of the slot is also calculated. In the designed machine it was 2.7 mm.

EPP engines are mainly PM motors, which are using large numbers of slots and poles. For the designed PMSM, the number of slots was taken 36, which provides the height to the diameter ratio of 1.3. The thickness of the stator yoke h_{sy} was selected as small as possible to reduce the weight and loss of the active material.

Regarding the number of poles, a higher number of magnet poles create higher torque at the same current level [6]. In contrast, with a smaller number of slots and poles, for example 36 to 12, every magnet passes a slot opening at the same time, which causes a maximum cogging torque, which involves a risk of acoustic resonances and higher noise [3]. Therefore, the number of pole pair p for the PMSM was selected 21, which increases K_{tm} , and consequently the value of σ .

IV. FRACTIONAL SLOT WINDING

In the elaborated PMSM winding, the number of slots Q_s per poles and phase was taken 2/7, which is equal to two winding sections per seven phase zone. In this case, the solenoidal or concentrated fractional slot winding was used where windings of each phase were isolated from each other and concentrated around individual teeth or salient poles. The purpose of the chosen fractional slot winding scheme was also to reduce the cogging torque.

Windings of coil groups were connected in parallel with each other and the ends of the windings were in delta connection, in order to reduce the current values in the windings (Fig. 4).

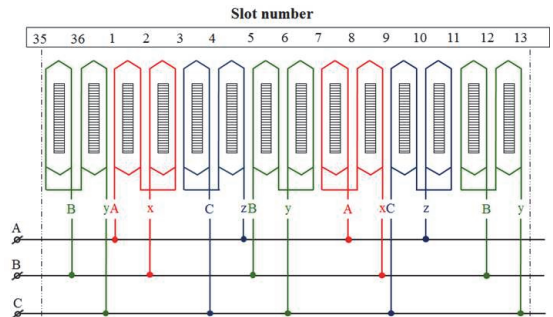


Fig. 4. Winding scheme.

The shift angle α between the two slots of the PMSM is designed at 210 electrical degrees. As it differs from 180°, the used winding is an extended fractional pitch winding. Fig. 5 shows the vector diagram of phase electromotive forces (EMF) in the windings.

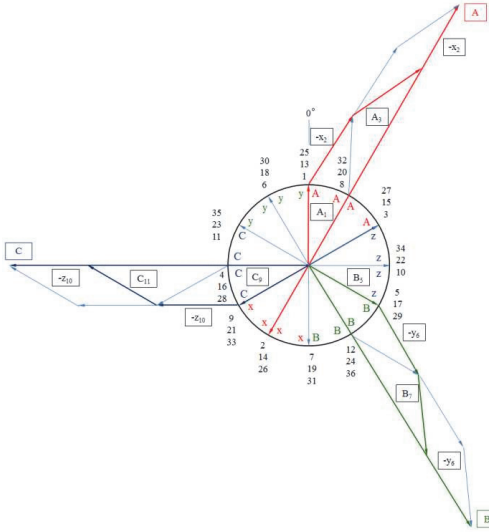


Fig. 5. EMF vector diagram.

The vector diagram shows the overlap between the phase EMFs, which indicates that the used winding is also an overlapped winding. The number of turns was determined based on the voltage provided by 14 cell lithium-ion polymer batteries, which produce 51.8 V_{DC} in total. To obtain such an EMF, the result of the calculation was 17 turns per each coil pair. During practical winding, one coil of the coil pair was wound with 8 and the second coil with 9 turns, accordingly.

As the number of slots for the PMSM machine was selected 36, according to the winding scheme, 6 coil groups are connected in parallel. Each group consists of two series-connected coils (Fig. 4). The increased number of coil groups allowed the distribution of the phase current between the coil groups. This winding structure also decreases the value of the current density J within the winding conductors. The calculated phase current i_{ph} value was 83.3 A. This is divided between 6 coil groups accordingly, which gives the current amplitude value within one conductor of the coil $i_{con} = 13.9$ A.

With a 120° square waveform, the I_{rms} value is $\sqrt{2/3}$ times of the peak value of i_{con} , which is 11.3 A [3].

Conventional fan-cooled electric machines operating in a continuous duty cycle are permitted to use current densities in the range of 5.0-10.0 A/mm² [7]. In intensively cooled high speed PM machines, the applied current densities are significantly higher. For example, copper wire 23AWG with the insulation rating of 180 °C (class H) has the maximum allowable current density of 23.7 A/mm² [8]. In PMSM, the propeller and mechanically machined openings in the rotor plate are used to provide the intensive cooling operating as an impeller. Considering the intensive cooling during the flight, the temperature class of the winding wire insulation and the effect of the demagnetization of permanent magnets at high temperature, the maximum current density $J = 10.0$ A/mm² was determined. Based on the J value, the winding cross section of 1.13 mm² was selected. With this cross section, the

mechanical properties and flexibility of the conductor were still sufficient and allowed to achieve the desired current density.

V. ROTOR WITH MAGNET POLES

In the designed PMSM, the neodymium magnets N45SH with the maximum operating temperature of 150 °C and with the nominal residual flux density $B_r = 1.35$ T are used (Fig. 6) [9].

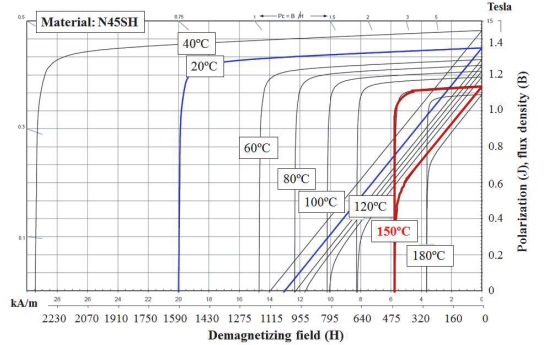


Fig. 6. The magnetic parameters of N45SH magnets [9].

The magnets are all surface mounted. This usually generates more than two times lower cogging torque than the one with embedded magnets [5].

An important parameter for the determination of magnet dimensions is the ratio between the width of the magnet b_m and pole pitch τ_m or the coverage factor k_m (Fig. 7).

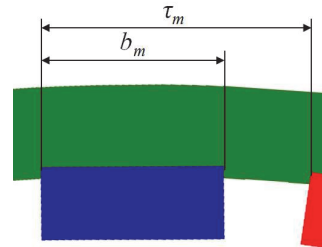


Fig. 7. Pole pitch.

This value is typically in the range between 0.6-0.9. In the designed motor this ratio was calculated 0.68, which remains within this interval.

Rotor magnets were chosen with thickness of 4.0 mm, which was about seven times of the airgap (0.56 mm) length.

VI. MODELING WITH SPEED SOFTWARE

In parallel with the analytical calculations, the studied PMSM was also modeled with the SPEED software, which provided an opportunity to compare the calculations with the simulated results [3]. For example, when comparing the calculated value of the mechanical torque T_m with the result generated by the software, only a marginal difference is present (Fig. 8).

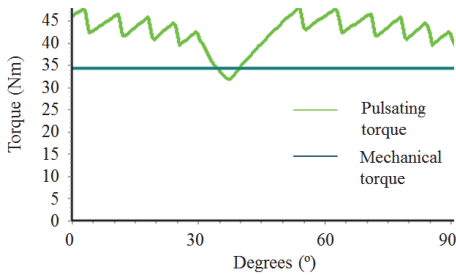


Fig. 8. Torque characteristic with SPEED PC-BDC.

Fig. 9 shows the simulated distribution of the primary magnetic flux density in the magnetic circuit and saturated teeth tips of the motor using SPEED PC-FEA software.

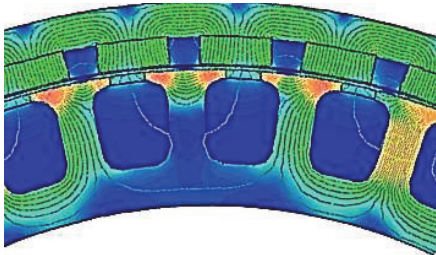


Fig. 9. The distribution of primary magnetic flux in the magnetic ring.

Based on the obtained parameters of the primary magnetic field the air-gap flux density B_g was calculated 0.68T, the average flux density in the stator yoke B_{sy} was 0.76T and the peak flux-density in the teeth B_{max} on the open circuit 1.97T.

VII. CONCLUSIONS

In this paper was represented the first stage of PM exterior-motor, designed as the main propulsion device for a motorized paraglider.

In the next phase of the research, the electromagnetic modeling will be continued and the practical construction will be started.

As the designed motor has a large number of poles, the problems caused by high frequency re-magnetization can be raised, which in turn can lead to increased iron losses. Therefore, in the practical design of the stator lamination material selection must meet these conditions.

In the next stadium the focus will be also aimed to the possibilities to minimize the cogging torque effects.

Another important issue of the study is the cooling problem. Although the current densities in the windings do not exceed the maximum values to the motors with an intensive cooling, high phase currents are still available, which increase copper losses. Therefore, the design of the geometry of the impeller on the rotor is of great importance.

The first step of the research covered the analytical calculations and modeling part of the PM motor for the electric powered paraglider. The initial results were successfully achieved and will be further compared with the practical tests.

REFERENCES

- [1] <http://aerolight.com/A/index.php/products/powered-paragliding>
- [2] R. Nukki, A. Kilk, A. Kallaste, T. Vaimann, and K. Tüimus Sr, "Exterior-rotor permanent magnet synchronous machine with toroidal windings for unmanned aerial vehicles," IEEE Xplore. Electric Power Quality and Supply Reliability Conference, Rakvere, 2014, pp. 215–220.
- [3] T. J. E. Miller, D. A. Saton, "Electric machine design using Speed and Motorcad," Training book, 2013, pp. 9–18.
- [4] J. R. Hendershot Jr and T. J. E. Miller, "Design of brushless permanent-magnet motors," 2nd ed., Ohio: Magna Physics Publishing, New York: Oxford University Press 2011, pp. 5.57–12.2.
- [5] O. Kudrjavtsev, A. Kilk, "Cogging torque reduction methods," IEEE Xplore. Electric Power Quality and Supply Reliability Conference (PQ), Pärnu, 2014, pp. 251–254.
- [6] D. Hanselman, "Brushless motor magnetic design, performance and control," E-Man Press LLC, 2012, pp. 8–31.
- [7] J. Pyrhönen, T. Jokinen, and V. Hrabovcová, "Design of rotating electrical machines," Wiley, 2008, pp. 294.
- [8] W. H. Yeadon and B. M. Frustaglio, "Current density," Yeadon Energy Systems, Inc., SMM Fall Conference, 2010.
- [9] Arnold Magnetic Technologies Corp. "Neodymium-Iron-Boron Magnet Catalogs," 2015. [Online]. Available: <http://www.arnoldmagnetics.com/> [Accessed: Jun. 07, 2015].



René Nukki was born in Pärnu, Estonia, in 1974. He received BSc and MBA degrees from Tallinn University of technology in 2005 and 2012 respectively. His research covers high power-to-weight PM synchronous machines for a small electric aircraft applications.

He currently works as a lecturer and the holder of the chair of Electrical Engineering at Faculty of Mechanics at TTK University of Applied Sciences.



Tõnu Lehtla was born in Estonia 1947. Since 1992 professor of robotics at Tallinn University of Technology, Dean of the Power Engineering Faculty 2006 - 2012, since 2010 to present director of the department of Electrical Engineering.

His research activities are mainly in the field of electrical drives.



Aleksander Kilk was born in Viljandi district, Estonia, in 1946. He received Dipl.Eng, MSci and PhD from Tallinn University of Technology in 1969, 1992 and 2008, respectively, all in electrical engineering.

He currently works as associate professor of the Department of Electrotechnical Engineering.

His research activities cover some different aspects of both electrical PM machines and induction MHD devices.



Tavo Kangru was born in Türi, Estonia, in 1982. He received MSc degree from Tallinn University of Technology, and Dipl.Eng in 2012.

Currently he works as a lecturer and the holder of the chair of Mechanical Engineering at Faculty of Mechanics at TTK University of Applied Sciences.

[PAPER-IV] **Nukki, R.**; Kilk, A.; Saarts, S.; Tiimus, K. (2016). Motor Mode Analysis of Exterior-Rotor PM with the Gramme's Winding. 20th International Conference, Electronics 2016, Kaunas University of Technology in collaboration with Vilnius Gediminas Technical University. IEEE (*Accepted 24.04.2016*).

Motor Mode Analysis of Exterior-Rotor PM Machine with Gramme's Winding

René Nukki^{1,2}, Aleksander Kilk¹, Samo Saarts², Kristjan Tiimus Sr³
¹*Department of Electrical Engineering, Tallinn University of Technology,
 Ehitajate St. 5, 19086 Tallinn, Estonia*

²*Chair of Electrical Engineering, TTK University of Applied Sciences,
 Pärnu St. 62, 10135 Tallinn, Estonia*

³*HeliCam Services Ltd.*

Looduspargi St. 4, 76901 Tabasalu, Estonia

renenukki@gmail.com, aleksander.kilk@ttu.ee, samo@tktk.ee, helicam@helicam.ee

¹**Abstract**— This paper presents the PM electrical machine with the Gramme's winding, which is intended for a small unmanned aircraft. The PM machine is a part of a hybrid drive operating in conjunction with an internal combustion engine. The main study involves operations in the motor mode, where the PM electric machine performs as the main propulsion system, as well as the additional power source or a starter in the hybrid drive. The purpose of the investigation is experimental evaluation of the electric parameters of the PM electric machine in the motor mode; in particular, achievable torque at different speeds on several loads, to compare the results with the initial requirements.

Index Terms—Electric motors, permanent magnet machines, propellers, temperature dependence, testing.

I. INTRODUCTION

Today small unmanned aerial electric vehicles (UAV) are used for a wide range of purposes, like wildlife tracking, traffic monitoring, border patrols, environmental research, geographical mapping, numerous military applications and several more [1]. UAVs are also used for broadcasting and recording various mass events like concerts, demonstrations and sports events. The reason for the increasing trend in the use of UAVs is their simple construction, reliability, easy operation, relative safety and environmental friendliness. The market of electric UAV market has grown into a multi-billion dollar industry [1].

Electric machines (EM) are also used in the UAVs that use an internal combustion engine (ICE) as their main source of power. In the named combination EMs are used mainly as generators. Lately, hybrid drive systems (HDS), which have proven itself in the land and in the maritime transport [2], and have started to expand into the field of UAVs. An HDS is generally an integrated single system, which uses two or more different power sources to move the vehicle. ICE's, also electric motors, have certain strengths and weaknesses. An HDS combines the strengths of both types of motors [2].

There are various types of electrical machines used today

in electric-powered small UAV-s. The most commonly used are PMSM with external AC/DC converters. Mainly used types of these machines are with interior, exterior and axial rotor [3]. Their topologies are shown in Fig. 1.

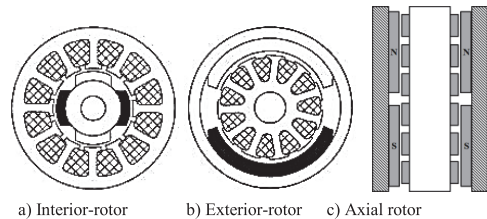


Fig. 1. Three basic machine configurations used in small UAV-s [3].

In this paper, an exterior-rotor multi-pole permanent magnet synchronous machine (ERPMSM) with toroidal winding is used in HDS.

The principle scheme of the HDS with the energy storage elements is shown in Fig. 2.

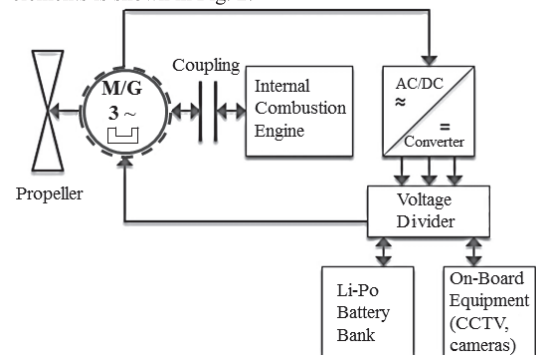


Fig. 2. Principle scheme of the UAV hybrid engine and energy storage system [4].

The choice of the ERPMSM's topology was determined by basic requirements, such as simple construction, low cost, high power-to-weight and power-to-volume ratio, smallest size, good control options and high torque at low speed. In this case the exterior-rotor topology has several advantages. One example is the possibility to install additional

components into the internal opening of the stator, thus obtaining more compact solutions. For ERPMSM it is the mechanical clutch which connects and disconnects ICE from it, which is rather complicated with the axial and interior-rotor design [4].

The other advantages of the exterior-rotor topology comparing for example with the interior-rotor design are higher torque density, better cooling possibilities, reduced copper loss, lower weight and cost [1].

ERPMSM solution is novel in its geometry and functionality as the same EM can be used as a motor and a generator. The operation in the generator mode was discussed already in the previous phase of the research [5]. In this study the main focus is on the ability of ERPMSM to work as a motor. This includes its capability to function as a primary engine which directly rotates a propeller, also operates in parallel with ICE as a starter or giving extra power during UAV's take off.

During the research the prototype of ERPMSM was also constructed (Fig. 3).

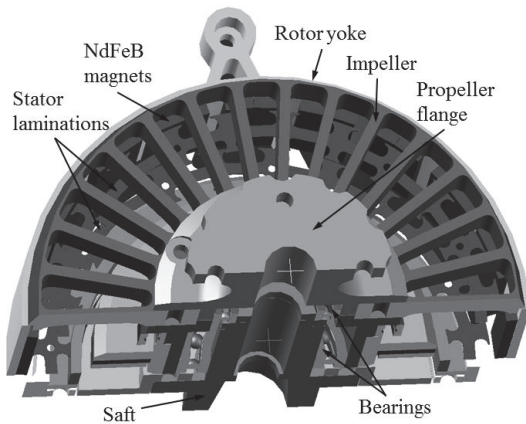


Fig. 3. The section geometry of the exterior-rotor motor-generator with the toroidal winding.

II. INITIAL PARAMETERS

One of the first initial design parameters for HDS was the range of rotational speed between 3000 to 4000 rpm, which meets the efficient operational regime of the propeller at UAVs stable flight situation.

An additional important nuance considered when ERPMSM functions as a motor, was the ability to output enough torque at required speeds of rotation while driving the propeller whilst maintaining the desired thermal parameters.

Various supplementary design parameters were given from ICE technical data, including the starting torque that ERPMSM had to overcome. In addition, manufacturer's requirement for the UAV is to be able to maintain stable flight for minimum of 15 minutes on electric power.

III. LOAD TESTS

During load tests of ERPMSM in motor regime, UAVs

actual wooden propeller with the diameter of 508 mm and pitch of 355.6 mm was used as a load [7].

In Fig. 4 is shown the counter torque of the propeller T_{pr} characteristic in dependence of rotational speeds.

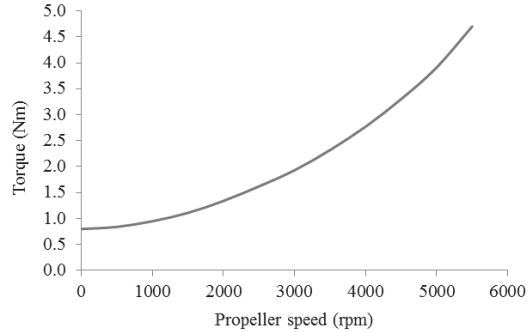


Fig. 4. Measured torque characteristic of the propeller.

ERPMSM load tests in motor operation were conducted in delta configuration to achieve more power at lower rotational speeds. Three primary supply voltages were used, $U_{DC} = 14.8, 18.5$ and 20.9 V. $U_{DC} = 14.8$ V was considered as the minimal voltage at which the rotational speed $n = 3000$ rpm was guaranteed by the specified propeller. Voltage $U_{DC} = 18.5$ V was chosen due to the nominal voltage of 5S-type batteries, which was achieved at the above-mentioned rotational speed in ERPMSMs generator mode in star connection [4]. The chosen voltage level of $U_{DC} = 20.9$ V is equivalent to the voltage output of the battery at fully charged state, at which rotational speed $n = 4000$ rpm was reachable.

While loading ERPMSM with a propeller, using nominal battery voltage $U_{DC} = 18.5$ V the rotational speed of nearly $n = 3500$ rpm was reached. Due to rapid rise from $n = 2500$ rpm the counter torque of the propeller was increasing with the supply current from the batteries. At $n = 3500$ rpm the measured supply current was $I_{DC} = 35$ A at the torque level of $T_{pr} = 1.46$ Nm.

The measured phase current values in the machine after rectification were considerably smaller than the supply currents. As previously noted, the supply voltage from the batteries was $I_{DC} = 35.0$ A. In this case the measured phase current in the machine was $I_{I3} = 16.4$ A, also the phase voltage was only $U_I = 12.2$ V_{AC}. In Fig. 5 the dependency of phase and supply voltages and phase and supply currents at different rotational speed is represented.

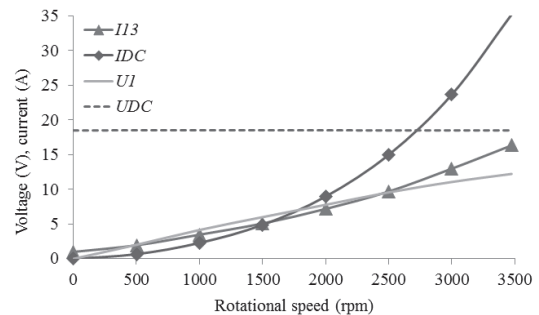


Fig. 5. Current and voltage dependencies of the rotational speed with propeller as the load.

The ratios between the incoming power to inverter P_{DC} and mechanical power P_2 measured by a torque sensor which was connected to the ERPMSM's rotor is characterized in Fig. 6.

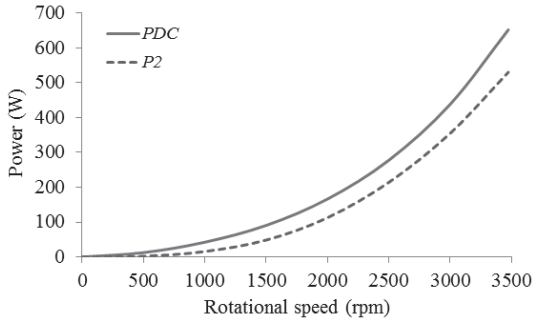


Fig. 6. The relations between the input P_{DC} and output power P_2 in dependence of the rotational speed.

The difference between P_{DC} and P_2 is an expression of the total exponential rise in power loss P_{loss} of the machine while consisting of magnetic, mechanical and residual losses. Losses in semiconductors of rectifying circuits also have a part in those losses. The most significant portion, though, is formed by ERPMSM electrical, in other words, copper losses P_{cu} , which constitute 55% of the total loss in conditions $n = 3500$ rpm, $U_{DC} = 18.5$ V_{DC} and $I_{DC} = 35.0$ A. Almost 30% of P_{loss} value resulted from the higher harmonics by the inverter during switching. Other losses compose of iron losses $P_{fe} = 8.0$ W, which have been previously determined [5], mechanical losses P_{mech} , induced by friction in bearings and aerodynamic losses, generated by aerodynamic drag dependant on rotational speed of the rotor.

Experimental documentation of ERPMSM mechanical characteristics were conducted with the help of a specific test rig with a servo drive for loading the ERPMSM (Fig. 7), enabling torque and rotational speed measurements.

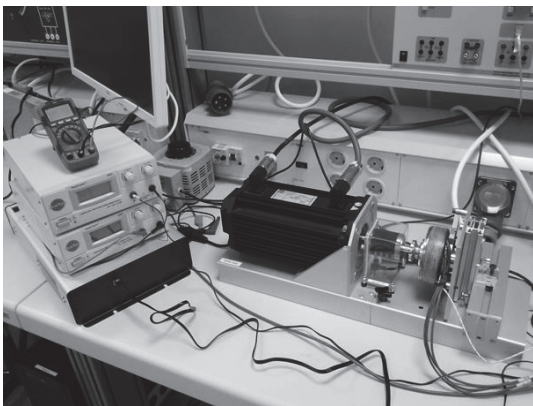


Fig. 7. Test bench of the ERPMSM.

During the load tests, servo drive was configured to be equivalent to the counter torque characteristics of the propeller.

In Fig. 8 based on propeller, the values of the dependence

of the mechanical load T_m values against rotational speeds are given.

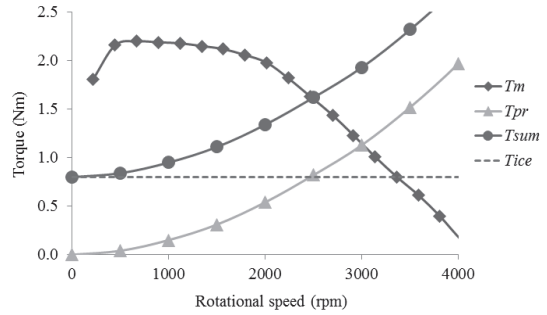


Fig. 8. Measured mechanical torque-speed characteristics at $U_{DC} = 18.5$ V.

At rated voltage $U_{DC} = 18.5$ V ERPMSM was set to rotate at the corresponding no-load speed $n_0 = 4260$ rpm. Further the mechanically coupled servo machine was automatically increasing the load by the preliminary specified time intervals. As T_m was gradually growing during the load test the ERPMSM's rotational speed was decreasing accordingly. This lasted until ERPMSM's torque T_m became equivalent with the counter torque resulted by the load machine. In this method ERPMSM's maximum torque $T_{max} = 2.2$ Nm at $U_{DC} = 18.5$ V and $n = 670$ rpm was measured. At rotational speed $n < 500$ rpm ERPMSM's rotor didn't have enough inertia and power anymore. This caused also the torque reduction in this part of T_m curve.

To identify the load points the counter torque curve of the propeller was included to the ERPMSM's mechanical characteristic. At rotational speed of $n = 3000$ rpm, the counter torque of the propeller was measured $T_{pr} = 1.13$ Nm. On the graph, the crossing point of T_m and T_{pr} can be noted. Correspondingly the mechanical load torque T_m is sufficient for maintaining a stable flight regime of the UAV.

The motor operation of ERPMSM also consists of functioning as a starter, during which torque level and rotational speed must be achieved that should be sufficient for starting an ICE connected with the propeller.

According to previous measurements, the starting torque of ICE can be specified as $T_{ICE} = 0.8$ Nm [8, 9]. Additional to starting torque, propeller counter torque $T_{pr} = 1.13$ Nm at rotational speed of $n = 3000$ rpm must be taken in account. Therefore, the optimal starting torque is the sum of T_{pr} and T_{ICE} and gives a result of $T_{sum} = 1.9$ Nm. Achieving this starting torque at nominal battery voltage of $U_{DC} = 18.5$ V, the reduction in rotational speed at the starting moment was expected.

Corresponding to Fig. 8, crossing of T_m and T_{sum} curves can be observed on rotational speed of $n = 2500$ rpm. Nevertheless, for the reason that the starting interval does not exceed 3 seconds, loss in flight speed caused by loss of rotational speed can be interpreted as marginal.

In addition, in case of fully charged batteries, it would be possible to exploit higher voltages than nominal U_{DC} for starting.

In Fig. 9 on torque characteristic at $U_{DC} = 20.9$ V, at rotational speed of $n = 4000$ rpm is shown.

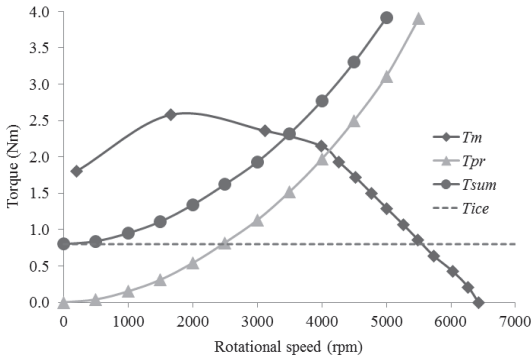


Fig. 9. Measured mechanical torque-speed characteristics at $U_{DC} = 20.9$ V.

The rise in phase voltages ($U_l = 14.6$ V_{AC}), phase currents ($I_{l3} = 25.0$ A) and rotational speed ($n = 4000$ rpm) induces the rise in the ERPMSMs mechanical torque up to $T_m = 2.6$ Nm.

Fig. 9 depicts also the rise of counter torque of the propeller ($T_{pr} = 1.97$ Nm) at this rotational speed. Due to that the torque required to start ICE increases to $T_{sum} = 2.77$ Nm, which exceeds the maximum mechanical torque T_m .

At given conditions, the crossing of $T_{sum} = T_{pr} + T_{ICE}$ with T_m can be marked at rotational speed of $n = 3500$ rpm, which exceeds the minimal rotational speed of the propeller, required for a stable flight by 500 rpm. Therefore, the necessary flight speed is ensured even during the ICE starting period.

At ERPMSM operation as a motor, it is also used for take-offs of the UAV. Ensuring the required rate of increase in flight height, the flight speed of 80 km/h at normal atmospheric pressure must be achieved. Therefore, enough thrust must be generated by the propeller i.e. rotational speed $n = 3800$ rpm reached, without considering the UAVs aerodynamic drag.

At take-off, ICE and ERPMSM work in parallel, being mechanically coupled. Summation of both of the machines output torques T_m and T_{ICE} at various rotational speeds, based on ERPMSM maximal supply voltage $U_{DC} = 20.9$ V, and using counter torque of the propeller T_{pr} as a contrast, total output torque of HDS $T_{sum} = 2.95$ Nm and maximal rotational speed of $n = 4860$ rpm at given conditions could be observed (Fig 10).

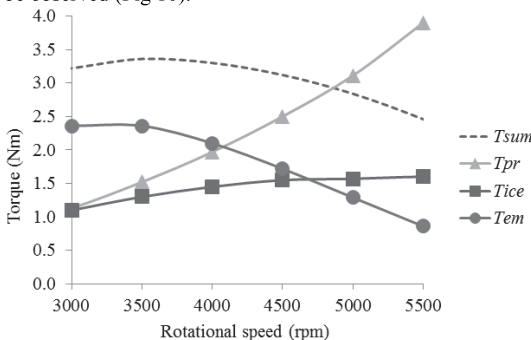


Fig. 10. Torque-speed characteristics during take-off.

At such rotational speed, theoretical flight speed in

relation to earth of 103 km/h could be reached. Although, taking into account the increasing aerodynamic drag of the UAV due to increase in flight speed, the real flight speed would be lower, but nevertheless exceeding minimal take-off speed.

IV. THERMAL CHARACTERISATION

The temperature characteristic of a PMSM expresses the nature of the temperature change during a certain amount of time and at a constant current in the stator windings. The objective of temperature tests is to determine the value of the maximum current where a PMSM reaches the maximum stabilized temperature, which is permissible to the winding insulation and to the permanent magnets [4].

The aim of the current thermal experiments was to determine the maximal temperature of ERPMSMs active parts on steady load. During the experiments, a propeller was used as a load and as a cooling element. Assuming intensive cooling by the propeller, ERPMSM could handle substantially higher supply currents than expected. The first load experiment was made using the propeller at the rotational speed of 4000 rpm and at the supply voltage of $U_{DC} = 20.9$ V, that was near to 5S batteries voltage of $U_{DC} = 21$ V at their fully charged state.

The measured supply current during the experiment reached $I_{DC} = 46.17$ A, while the phase voltage was measured $U_l = 14.6$ V_{AC} and the phase current $I_{l3} = 20.39$ A. Based on that the resulting ERPMSMs apparent power $S = 890$ VA.

At set parameters, the constant temperature of windings was stabilizing after 8 minutes i.e. 480 seconds to the temperature of $\vartheta_{p1} = 64$ °C, resulting as the time constant of $\tau \approx 120$ s. The characteristics in Fig. 11 indicate the thermal time constant τ .

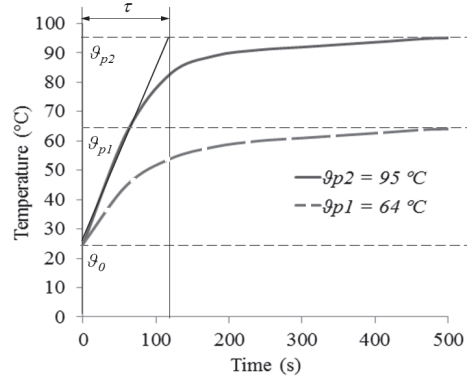


Fig. 11. Temperature characteristics with the thermal constant τ .

As the maximum temperature of the chosen magnets and winding insulations was substantially higher [10, 11], the additional experiment was made at the rotational speed of $n = 5000$ rpm, supply voltage of $U_{DC} = 27.7$ V and current of $I_{DC} = 65.6$ A. At given parameters the phase voltage $U_l = 19.4$ V_{AC} and phase current $I_{l3} = 27.6$ A, was measured, resulting the apparent power $S = 1600$ VA.

Although, at higher power, the constant temperature of $\vartheta_{p2} = 95$ °C was measured. Similarly to previous experiment the winding temperature rose to constant value during 480

seconds and gave the same time constant $\tau \approx 120$ s. The thermal time constant τ characterizes the approaching velocity rate to the final temperature, as in (1) [12].

$$\vartheta_{(t)} = \vartheta_0 + (\vartheta_p - \vartheta_0) \left(1 - e^{-\frac{t}{\tau}} \right), \quad (1)$$

where ϑ_0 is the initial temperature ($^{\circ}\text{C}$) and t is time (s).

The time constant τ depends mainly on the heat capacity factors and weight of ERPMSM's active materials. In practice, the final temperature is reached within 4 times of the time constant values.

The machine can be operated for an indefinite period of time only if the temperatures do not exceed specifications for each part or component of the machine [13]. Therefore, a thermal camera was used for capturing temperatures of various parts of ERPMSM, enabling comparison with results collected by use of a temperature probe. The maximum temperature in windings registered on scale was 97.3°C , being close to the results achieved with the temperature probe.

Considering the measured temperature in windings as maximum, the temperatures of other components in the machine are lower, which ensures that in previous load conditions the allowed maximum temperatures are not exceeded either in permanent magnets.

In previous phase of the research the performed generator tests with ERPMSM were made with the maximal phase current of $I_f = 23.0$ A at rotational speed of $n = 5500$ rpm, therefore the current density in winding conductor reached up to $J = 19.3$ A/mm². The rise in temperature during the experiment stabilized at 106°C . From the perspectives of current density and temperature, the given values are notably high. In the current case though, copper wire with the insulation rating of 180°C (class H) is used, which has the maximum allowable current density of 23.7 A/mm² [14], resulting in even higher allowable rate. According to experiment results, the apparent power of the generator was $S = 890$ VA [4]. During the generator tests, the cooling was only provided by the impeller on the ERPMSMs external rotor.

During the experiments covered with this stage, the forced cooling by using a propeller allowed even higher phase currents I_{f3} as high as 27.6 A at rotational speed of 5000 rpm, resulting in the current density of $J = 23.2$ A/mm² and reaching to the apparent power of $S = 1600$ VA, while the winding temperature was stabilizing already at 95°C .

The performed thermal experiments hence indicated significantly higher power and current density handling capabilities of ERPMSM with forced cooling provided by the propeller while keeping other machine active parts at notably lower constant temperatures.

V. CONCLUSIONS

Based on this experimental work it can be concluded that ERPMSM fulfils the initial requirements set as a primary propulsion element, either working in parallel with ICE or in

starter mode in UAVs stable flying or in take-off regimes at the provided propeller pitch. Experimental work was performed in laboratory conditions at normal atmospheric pressure. Therefore, air mass dynamics in open air, which make an impact on UAV flight speed, were not considered.

It was important to follow UAVs power and mass ratio or the specific power, during the research. As designed HDS exploits the electric machine with its batteries and rectifier circuits in parallel with ICE, it results in additional 1.7 kg i.e. 11% of weight increase. These parameters were added to UAVs standard weight. Using both ERPMSM and ICE in parallel operation during the take-off, the specific power increased nearly by 71% . On the other hand in separate performance of both ICE and ERPMSM the specific power decreased by 10% due to the increased weight. The situation could be improved by increasing the power and torque of both machines, but as for ERPMSM this would result in larger and therefore heavier, accumulator system, which is the main reason of increase in weight of the UAV. Accordingly, the problem must be seen as complex optimization problem with objectives of keeping the mass of every element in the system as low as possible and when possible, research of advanced battery technologies, accumulation devices (super capacitors) or alternative energy resources (solar energy).

The next stage of the research includes also the reliability tests of the HDS in real life situation, mounted on the UAV. Results must be compared to theoretical calculations and with obtained experimental data.

REFERENCES

- [1] D. L. Gabriel, J. Meyer, and F. du Plessis, "Brushless DC motor characterisation and selection for a fixed wing UAV" IEEE Africon. The Falls Resort and Conference Centre, Livingstone, Zambia, 13–15 September 2011.
- [2] http://www.toyota-global.com/innovation/environmental_technology.
- [3] J. R. Hendershot Jr and T. J. E. Miller, "Design of brushless permanent-magnet motors," 2nd ed., Ohio: Magna Physics Publishing, New York: Oxford University Press 2011, pp. 1.1–5.1.
- [4] R. Nukki, A. Kilk, A. Kallaste, T. Vaimann, and K. Tiimus Sr, "Exterior-rotor permanent magnet synchronous machine with toroidal windings for unmanned aerial vehicles," IEEE Xplore. Electric Power Quality and Supply Reliability Conference, Rakvere, 2014, pp. 215–220.
- [5] R. Nukki, A. Kilk, A. Kallaste, T. Vaimann, and K. Tiimus Sr, "Generator mode analysis of exterior-rotor PM synchronous machine with Gramme's winding," IEEE Xplore. IEEE 5th International Conference of Power Engineering, Energy and Electrical Drives (POWERENG), Riga, 2015, pp. 347–352.
- [6] R. K. Pratapa, "Modeling and analysis of radial flux toroidally wound twin rotor permanent magnet motor," MSc. Thesis, Louisiana State University, Agricultural and Mechanical College, 2010, pp. 3–8.
- [7] <http://www.rotomotor.cz/rotomotor/eshop/4-1-Accessories>.
- [8] I. H. Mengistu, "Small internal combustion engine testing for a hybrid-electric remotely-piloted aircraft" MSc. Thesis, Air Force Institute of Technology, 2011, pp. 67–68.
- [9] <http://engines.honda.com/models/model-detail/gx35>.
- [10] http://www.arnoldmagnetics.com/Neodymium_Literature.aspx.
- [11] <http://www.brocott.co.uk/enamelled-magnet-wire/1kg-spoofs/0-355mm-enamelled-copper-winding-wire-1kg-ww0355-1000.html>.
- [12] H. A. Toliyat and G. B. Klimanang, "Handbook of Electric Motors," Marcel Dekker, Inc., New York, 2004, pp. 638–639.
- [13] J. F. Gieras, R. J. Wang, and M. J. Kamper, "Axial flux permanent magnet brushless machines," Springer Science, 2008, pp. 272–273.
- [14] W. H. Yeadon and B. M. Frustaglio, "Current density," Yeadon Energy Systems, Inc., SMMA Fall Conference, 2010.

**DISSERTATIONS DEFENDED AT
TALLINN UNIVERSITY OF TECHNOLOGY ON
*POWER ENGINEERING, ELECTRICAL ENGINEERING,
MINING ENGINEERING***

1. **Jaan Tehver**. Boiling on Porous Surface. 1992.
2. **Aleksandrs Cars**. Woodhips Combustion Technology. 1992.
3. **Endel Risthein**. Electricity Supply of Industrial Plants. 1993.
4. **Tõnu Trump**. Some New Aspects of Digital Filtering. 1993.
5. **Vello Sarv**. Synthesis and Design of Power Converters with Reduced Distortions Using Optimal Energy Exchange Control. 1994.
6. **Ivan Klevtsov**. Strained Condition Diagnosis and Fatigue Life Prediction for Metals under Cyclic Temperature Oscillations. 1994.
7. **Ants Meister**. Some Phase-Sensitive and Spectral Methods in Biomedical Engineering. 1994.
8. **Mati Meldorf**. Steady-State Monitoring of Power System. 1995.
9. **Jüri-Rivaldo Pastarus**. Large Cavern Stability in the Maardu Granite Deposit. 1996.
10. **Enn Velmre**. Modeling and Simulation of Bipolar Semiconductor Devices. 1996.
11. **Kalju Meigas**. Coherent Photodetection with a Laser. 1997.
12. **Andres Udal**. Development of Numerical Semiconductor Device Models and Their Application in Device Theory and Design. 1998.
13. **Kuno Janson**. Paralleel- ja järjestikresonantsi parameetrilise vaheldumisega võrgusageduslik resonantsmuundur ja tema rakendamine. 2001.
14. **Jüri Joller**. Research and Development of Energy Saving Traction Drives for Trams. 2001.
15. **Ingo Valgma**. Geographical Information System for Oil Shale Mining – MGIS. 2002.
16. **Raik Jansikene**. Research, Design and Application of Magnetohydrodynamical (MHD) Devices for Automation of Casting Industry. 2003.
17. **Oleg Nikitin**. Optimization of the Room-and-Pillar Mining Technology for Oil-Shale Mines. 2003.
18. **Viktor Bolgov**. Load Current Stabilization and Suppression of Flicker in AC Arc Furnace Power Supply by Series-Connected Saturable Reactor. 2004.
19. **Raine Pajo**. Power System Stability Monitoring – an Approach of Electrical Load Modelling. 2004.

20. **Jelena Shuvalova**. Optimal Approximation of Input-Output Characteristics of Power Units and Plants. 2004.
21. **Nikolai Dorovatovski**. Thermographic Diagnostics of Electrical Equipment of Eesti Energia Ltd. 2004.
22. **Katrin Erg**. Groundwater Sulphate Content Changes in Estonian Underground Oil Shale Mines. 2005.
23. **Argo Rosin**. Control, Supervision and Operation Diagnostics of Light Rail Electric Transport. 2005.
24. **Dmitri Vinnikov**. Research, Design and Implementation of Auxiliary Power Supplies for the Light Rail Vehicles. 2005.
25. **Madis Lehtla**. Microprocessor Control Systems of Light Rail Vehicle Traction Drives. 2006.
26. **Jevgeni Šklovski**. LC Circuit with Parallel and Series Resonance Alternation in Switch-Mode Converters. 2007.
27. **Sten Suuroja**. Comparative Morphological Analysis of the Early Paleozoic Marine Impact Structures Kärđla and Neugrund, Estonia. 2007.
28. **Sergei Sabanov**. Risk Assessment Methods in Estonian Oil Shale Mining Industry. 2008.
29. **Vitali Boiko**. Development and Research of the Traction Asynchronous Multimotor Drive. 2008.
30. **Tauno Tammeoja**. Economic Model of Oil Shale Flows and Cost. 2008.
31. **Jelena Armas**. Quality Criterion of road Lighting Measurement and Exploring. 2008.
32. **Olavi Tammemäe**. Basics for Geotechnical Engineering Explorations Considering Needed Legal Changes. 2008.
33. **Mart Landsberg**. Long-Term Capacity Planning and Feasibility of Nuclear Power in Estonia under Certain Conditions. 2008.
34. **Hardi Torn**. Engineering-Geological Modelling of the Sillamäe Radioactive Tailings Pond Area. 2008.
35. **Aleksander Kilk**. Paljupooluseline püsimagnetitega sünkroongeneraator tuuleagregaatidele. 2008.
36. **Olga Ruban**. Analysis and Development of the PLC Control System with the Distributed I/Os. 2008.
37. **Jako Kilter**. Monitoring of Electrical Distribution Network Operation. 2009.
38. **Ivo Palu**. Impact of Wind Parks on Power System Containing Thermal Power Plants. 2009.
39. **Hannes Agabus**. Large-Scale Integration of Wind Energy into the Power System Considering the Uncertainty Information. 2009.

40. **Kalle Kilk**. Variations of Power Demand and Wind Power Generation and Their Influence to the Operation of Power Systems. 2009.
41. **Indrek Roasto**. Research and Development of Digital Control Systems and Algorithms for High Power, High Voltage Isolated DC/DC Converters. 2009.
42. **Hardi Hõimoja**. Energiatõhususe hindamise ja energiasalvestite arvutuse meetoodika linna elektertranspordile. 2009.
43. **Tanel Jalakas**. Research and Development of High-Power High-Voltage DC/DC Converters. 2010.
44. **Helena Lind**. Groundwater Flow Model of the Western Part of the Estonian Oil Shale Deposit. 2010.
45. **Arvi Hamburg**. Analysis of Energy Development Perspectives. 2010.
46. **Mall Orru**. Dependence of Estonian Peat Deposit Properties on Landscape Types and Feeding Conditions. 2010.
47. **Erik Väli**. Best Available Technology for the Environmentally Friendly Mining with Surface Miner. 2011.
48. **Tarmo Tohver**. Utilization of Waste Rock from Oil Shale Mining. 2011.
49. **Mikhail Egorov**. Research and Development of Control Methods for Low-Loss IGBT Inverter-Fed Induction Motor Drives. 2011.
50. **Toomas Vinnal**. Eesti ettevõtete elektritarbimise uurimine ja soovituste väljatöötamine tarbimise optimeerimiseks. 2011.
51. **Veiko Karu**. Potential Usage of Underground Mined Areas in Estonian Oil Shale Deposit. 2012.
52. **Zoja Raud**. Research and Development of an Active Learning Technology for University-Level Education in the Field of Electronics and Power Electronics. 2012.
53. **Andrei Blinov**. Research of Switching Properties and Performance Improvement Methods of High-Voltage IGBT based DC/DC Converters. 2012.
54. **Paul Taklaja**. 110 kV õhuliinide isolatsiooni töökindluse analüüs ja töökindluse tõstmise meetodid. 2012.
55. **Lauri Kütt**. Analysis and Development of Inductive Current Sensor for Power Line On-Line Measurements of Fast Transients. 2012.
56. **Heigo Mölder**. Vedelmetalli juhitava segamisvõimaluse uurimine alalisvoolu kaarleekahjus. 2012.
57. **Reeli Kuhi-Thalfeldt**. Distributed Electricity Generation and its Possibilities for Meeting the Targets of Energy and Climate Policies. 2012.
58. **Irena Milaševski**. Research and Development of Electronic Ballasts for Smart Lighting Systems with Light Emitting Diodes. 2012.

59. **Anna Andrijanoviš.** New Converter Topologies for Integration of Hydrogen Based Long-Term Energy Storages to Renewable Energy Systems. 2013.
60. **Viktor Beldjajev.** Research and Development of the New Topologies for the Isolation Stage of the Power Electronic Transformer. 2013.
61. **Eduard Brindfeldt.** Visually Structured Methods and Tools for Industry Automation. 2013.
62. **Marek Mägi.** Development and Control of Energy Exchange Processes Between Electric Vehicle and Utility Network. 2013.
63. **Ants Kallaste.** Low Speed Permanent Magnet Slotless Generator Development and Implementation for Windmills. 2013.
64. **Igor Mets.** Measurement and Data Communication Technology for the Implementation in Estonian Transmission Network. 2013.
65. **Julija Šommet.** Analysis of Sustainability Assessment in Carbonate Rock Quarries. 2014.
66. **Tanel Kivipõld.** Real-Time Electricity Tariff System for Retail Market. 2014.
67. **Priit Uemaa.** Industrial CHP Optimal Management Model in the Energy Market under Incomplete Information. 2014.
68. **Anton Rassõlkin.** Research and Development of Trial Instrumentation for Electric Propulsion Motor Drives. 2014.
69. **Toomas Vaimann.** Diagnostics of Induction Machine Rotor Faults Using Analysis of Stator Signals. 2014.
70. **Aivar Auväärt.** Development of Energy Reserve Optimization Methodology for Households with Renewable Power Systems. 2014.
71. **Raivo Attikas.** Modelling of Control Systems and Optimal Operation of Power Units in Thermal Power Plants. 2014.
72. **Liisa Liivik.** Semiconductor Power Loss Reduction and Efficiency Improvement Techniques for the Galvanically Isolated Quasi-Z-Source DC-DC Converters. 2015.
73. **Victor Astapov.** Technical-Economic Analysis of Distributed Generation Units in Power Systems. 2015.
74. **Tiit Hõbejõgi.** Possibilities to Optimize Low Voltage Network Investments in Rural Areas. 2016.